Development of a Tailor-Welded Hot Stamped Side Frame Member

By

Matthew Tummers

A thesis

presented to the University of Waterloo

in fulfillment of the

thesis requirement for the degree of

Master of Applied Science

in

Mechanical and Mechatronics Engineering

Waterloo, Ontario, Canada, 2019

I hereby declare that I am the sole author of this thesis. This is a true copy of the thesis, including any required final revisions, as accepted by my examiners.

I understand that my thesis may be made electronically available to the public.

Abstract

This thesis investigates the application of hot stamped ultra-high strength steel (greater than 1000 MPa tensile strength) tailor-welded blanks in vehicle frontal crash energy management structures, as well as their potential for weight savings through sheet material thickness down-gauging. The ultra-high strength steels examined in this thesis are Ductibor® 1000-AS and Usibor® 1500-AS. The vehicle frontal crash structure of focus is the side frame member, which is typically comprised of various gauges of 590 MPa advanced high strength steel, such as JAC590R. The suitability of using hot stamping steels in the side frame member is assessed by comparing the frontal crash performance of a production side frame member (baseline front end module) to a side frame member comprised of tailor-welded hot stamped steels (tailor-welded hot stamped side frame member).

The crash performance of the driver's side frame member in a commercial SUV is numerically evaluated in the US-NCAP Full Width Rigid Barrier frontal crash test configuration. A set of design requirements and constraints for the baseline front end module and tailor-welded hot stamped side frame member are developed from the production side frame member evaluation. The evaluation includes: matching the crush response (crush modes), deceleration profile, final crush distance, crush forces, resistance to passenger compartment intrusion and extent of spot weld failure.

A baseline front end module is fabricated from production components and houses the production side frame member. Its development is based on a set of design specifications established from consideration of the full-vehicle model. A key consideration when developing the baseline front end module is to include the least amount of body-in-white components in order to reduce the scope of fabrication and testing. Dynamic crash sled testing at 51 km/hr is used in conjugation with a calibrated numerical model to characterize the performance of the production side frame member. An adaptive test matrix is employed during the nine baseline front end module tests, meaning that test configuration and boundary conditions are changed between sequential tests. Due to these test configuration changes, three different crush responses are observed, only one of which matches the crush response of the side frame member in the full-vehicle model. When a similar crush response to the full-vehicle model is observed in the baseline front end module, it is demonstrated that the velocity history, crush loads, occupant compartment intrusion resistance and extent of spot weld failure meet the design specifications.

The tailor-welded hot stamped side frame member is designed using the boundary conditions developed from the baseline front end module. The high energy absorbing crush section is comprised of Ductibor® 1000-AS, while the high rigidity, anti-intrusion S-rail section is made from Usibor® 1500-AS. It is clear from the design process that using higher strength materials (Ductibor® 1000-AS) in the crush section requires

topological changes to be made to the production side frame member design. In order to capture the desired crush response and reduce spot weld failure severity in the tailor-welded hot stamped side frame member, new enhanced fold initiators, as well as geometric changes to the crush tip spot weld flanges are required. Ultimately, a two-component, 5.5 kg tailor-welded hot stamped side frame member is developed, which demonstrates a 2.1 kg (27.6%) weight reduction compared to the 7.6 kg production JAC590R side frame member. The designed tailor-welded hot stamped side frame member matches the baseline front end module crush response, deceleration profile, crush forces and passenger compartment intrusion resistance, while also exhibiting good parent metal fracture resistance and relatively low severity spot weld failure. Inserting the tailor-welded hot stamped side frame member into a model of the commercial SUV, in place of the production driver's side frame member, further verified the suitability of the proposed side frame member.

Designing and fabricating the tooling for the full-length tailor-welded hot stamped side frame member comes with many complexities. To reduce the complexity, only the crush tip section of the tailor-welded hot stamped side frame member is manufactured. Two crash forming tools are made to hot stamp the channel "main rail" section and a flat "enclosure panel" section. The hot stamping process consisted of soaking multi-gauge (1.0 mm and 1.2 mm) Ductibor® 1000-AS blanks in a 950 °C furnace for 6 minutes, transporting them to the tool for forming and quenching in chilled dies for 10 seconds. The average hardness of the 1.0 mm and 1.2 mm Ductibor® 1000-AS sections in the main rail part are 368.5 HV and 401.2 HV, respectively. In the enclosure panel part the average hardness of the 1.0 mm and 1.2 mm Ductibor® 1000-AS sections are 412.8 HV and 392.8 HV, respectively. A model of the hot stamping process is used to map the predicted thinning due to forming onto a crash suitable mesh.

The crash performance of the tailor-welded hot stamped crush tip is evaluated to determine whether it is a suitable simplification to the full-length tailor-welded hot stamped side frame member. A crash model of the first 491 mm of the full-length tailor-welded hot stamped side frame member is constructed to represent the crush tip section. The inclusion of thinning predictions from the hot stamping model into the tailor-welded hot stamped crush tip crash model are shown to have only a small effect on the predicted crash performance of the crush tip. Evaluating the tailor-welded hot stamped crush tip against the baseline front end module and full-length tailor-welded hot stamped side frame member demonstrates that the crush tip provides valuable information on crush response, parent metal fracture resistance, crush forces and extent of spot weld failure. The tailor-welded hot stamped crush tip is deemed a suitable simplification of the full-length side frame member when evaluating the suitability of Ductibor® 1000-AS in frontal crash applications.

This research to-date supports the use of Ductibor® 1000-AS and Usibor® 1500-AS, in the form of tailor-welded blanks, as a higher strength alternative for conventional 590 MPa strength materials in frontal crash energy management structures. Through sheet material thickness down-gauging significant weight savings

are shown. The results support the use of Ductibor® 1000-AS in high energy absorbing frontal crush structures requiring sequential folding and Usibor® 1500-AS in high rigidity anti-intrusion structures. These findings are tempered by the fact that experimental testing of the crush tips is still pending and that additional load cases need be considered. In future work, crash tests on the tailor-welded hot stamped crush tip will be conducted to support the numerical crash simulations of this thesis.

Acknowledgements

The work conducted in this thesis would not be possible without the effort and support received from all of its contributing members. I would like to thank my supervisor, Dr. Michael Worswick, for providing me the opportunity to work on such an industry applicable thesis project, which has specialized my engineering skill set. His support and guidance throughout the project have improved my analysis skills, made me a better writer and taught me the importance and complexity of material characterization. I would like acknowledge Dr. Clifford Butcher for his guidance in material modelling. Thanks to Dr. José Imbert-Boyd for his support during crash testing, as well as Ryan George for assistance and guidance with hot stamping and component design.

Support for this project from industry sponsors Honda R&D Americas, the Promatek Research Centre (Cosma International), and ArcelorMittal, as well as from the Natural Sciences and Engineering Research Council, the Canada Research Chair Secretariat, the Canadian Foundation for Innovation, the Ontario Advanced Manufacturing Consortium, the Ontario Research Fund, and the Ontario Centres for Excellence is acknowledged and greatly appreciated. I would like to extend special thanks to Skye Malcolm and Jim Dykeman, from Honda R&D Americas, for their continual support and feedback with numerical modelling and crash testing throughout the duration of the project. In addition, I would like to commend Skye Malcolm for his patience in dealing with the countless data transfers to and from the Honda server. Special thanks to the Honda R&D Americas fabrication team for making the integration of the baseline front end module and tailor-welded hot stamped crush tip possible. I would also like to thank Cyrus Yau, Kevin Goulding and Mark Bonello from the Promatek Research Centre for their support in the tooling development and the laser cutting of blanks and formed parts. In addition, Justin Hansen and Monty Hansen from Cosma Die Technology provided valuable hot forming analysis insight for the crush tips. Finally, I thank Ron Soldaat, Willie Bernert and Dan Papalazarou, from ArcelorMittal Dofasco, for their material support and delivery of the tailor-welded blanks necessary to complete this project, as well as Eric Famchon from ArcelorMittal Global R&D Montataire for fabrication of the laser welded blanks.

In the lab, the support and assistance of Eckhard Budziarek, Tom Gawel, Andy Barber and Doug Hirst allowed me to complete my experiments successfully and more important, safely. Thanks to Cameron Tolton for being an excellent morning, mid-morning, after lunch and occasional late afternoon coffee buddy, Sante DiCecco and Brock Watson for the occasional afternoon pints, as well as thanks to Steven Lee, Hossein Pishyar, Raphael Boulis, Pedram Samadian, Alireza Mohamadizadeh and Dylan Budnik.

Most importantly I would like to thank my parents, John and Dianne, my siblings, Mackenzie, Brittany and Rebecca, and my girlfriend, Alexandra Smolak for their unconditional support throughout my studies.

To my parents, John and Dianne for raising me right

Table of Contents

List of Figures

List of Tables

“Iron seemeth a simple metal, in its nature are many mysteries, and men who bend to them their minds shall, in arriving days, gather therefrom great profit, not to themselves alone but to all mankind”

– attributed to Joseph Glanvill (1636 – 1680)

Chapter 1 – Introduction

Regulating bodies around the world continue to push automotive manufacturers to reduce the fuel consumption of their vehicles. Fuel economy standards such as the Corporate Average Fuel Economy (CAFE) in the United States pressure automotive manufacturers to constantly meet increasing fuel standards or be faced with monetary fines. According to a report from the National Highway Traffic Safety Administration (NHTSA) the average required fuel economy of passenger vehicles will increase from 39.6-40.1 miles per gallon (mpg) to 55.3-56.2 mpg (28 percent increase) from 2017 to 2025. Similarly, light trucks (including Sport Utility Vehicles (SUVs)) will see an increase from 29.1-29.4 mpg to 39.3-40.3 mpg (26 percent increase) from 2017 to 2025 [1]. Increases in fuel economy standards have automotive manufacturers researching and developing new technologies to help reduce fuel consumption, including reducing drag through aerodynamics and improving efficiency of powertrains such as hybrid gas-electric vehicles.

Improvements to fuel economy can also be achieved through the reduction of vehicle mass, which is the focus of this thesis. A report from MIT's Laboratory for Energy and the Environment projects a 4.5 to 8 percent reduction in fuel consumption for every 10 percent decrease in vehicle weight [2]. The prospect of reduced fuel consumption has peaked a lot of interest in researching alternative materials that maintain vehicle safety standards and performance but are lighter in weight. Alternative materials considered in vehicle light weighting include fibre reinforced composites, light metals such as aluminum and magnesium, and advanced steels such as Advanced High Strength Steel (AHSS) and Ultra-High Strength Steel (UHSS) [3].

The focus of this thesis is press hardened UHSS sheet, which has enhanced specific strength and thus a great deal of potential for weight savings in body-in-white (BIW) components. Press hardened UHSS uses the hot stamping manufacturing process, which involves the heating of a boron steel sheet in a furnace with simultaneous forming and quenching of the part in a chilled die. Ultimately, a part is produced with a primarily martensitic microstructure, hence the high strength properties. Additionally, hot stamped materials can be formed into complex geometries without worry of springback, which is a source of much complication in the cold forming process, as discussed by Mori *et al.* [4]. Though conventional hot stamped steels (*i.e.* 22MnB5) exhibit high strength they also tend to display relatively low ductility; thus conventional hot stamped steels are often used for occupant compartment intrusion resistance but less attractive for frontal impact energy absorption.

Traditionally, automotive manufacturers have made extensive use of UHSS, such as Usibor® 1500-AS, for anti-intrusion applications, but have been hesitant to adopt such alloys in frontal crash applications due to its susceptibility to fracture at low strains relative to lower strength advanced high-strength steels (AHSS). Recent developments in the realm of hot stamped steels have led to higher ductility options becoming available, namely Ductibor® 1000-AS and Ductibor® 500-AS. These higher ductility hot stamped materials display promising frontal crash characteristics, such as enhanced impact energy absorption and resistance to fracture, while maintaining relatively high strength levels, thus making Ductibor® 1000-AS and Ductibor® 500-AS attractive materials to consider in vehicle light weighting.

Recent developments to UHSS tailoring techniques, namely tailor-welded blanks (TWBs) have made it possible for a single hot stamped part to combine the high strength and rigidity of Usibor® 1500-AS in one region, with the higher ductility and impact energy absorption potential of Ductibor® 1000-AS in another region of the part. This combination of impact energy absorption and passenger compartment intrusion resistance suggests the potential for the use of hot stamped materials in frontal crash energy management structures. In order to demonstrate the appropriateness of using hot stamped steels in frontal crush structures the research presented in this thesis has been conducted.

1.1 Automotive Sheet Steel

In regular automobiles the BIW and chassis typically account for 58 percent of the total vehicle mass according to Tisza and Czinege [5]. On average, steel (of various compositions) makes up 55 percent [3] of the components used to assemble the BIW and chassis, with the next closest material being aluminum alloys at only 9 percent. The steel sheet used in vehicle structures can vary greatly in both tensile strength and elongation at failure, as shown in Figure 1. This figure shows that mild steels with tensile strengths ranging from 250-380 MPa have a very high amount of elongation before failure, whereas hot stamped 22MnB5 steel with tensile strengths of 1300-1600 MPa exhibit a relatively low amount of elongation at failure.

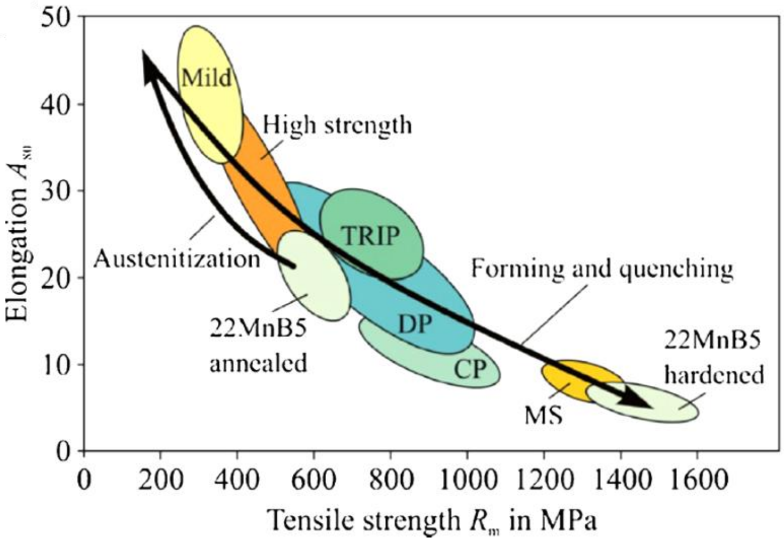

Figure 1. Elongation as a function of tensile strength for various groups of steel, from Karbasian and Tekkaya [6].

The BIW of the 2016 Honda Pilot (Figure 2) illustrates the tensile strength range of steel sheet used in a large SUV. It is observed from this figure that non-crash relevant structural components are made from low strength (270 MPa) mild steel, crash energy absorbing structures such as the front and rear crush rails are made from 590 MPa dual phase steel, and occupant compartment intrusion resistant structures (such as the B-pillar and door sill) are made from steels with 980 MPa and greater strengths. In the occupant intrusion resistant zone one such steel used is hot stamped UHSS with a tensile strength of 1500 MPa. It is quite clear from the strength levels present in the BIW shown in Figure 2 that current vehicles have already undergone significant weight optimization through increased material strengths, however opportunity to further reduce vehicle weight still exists.

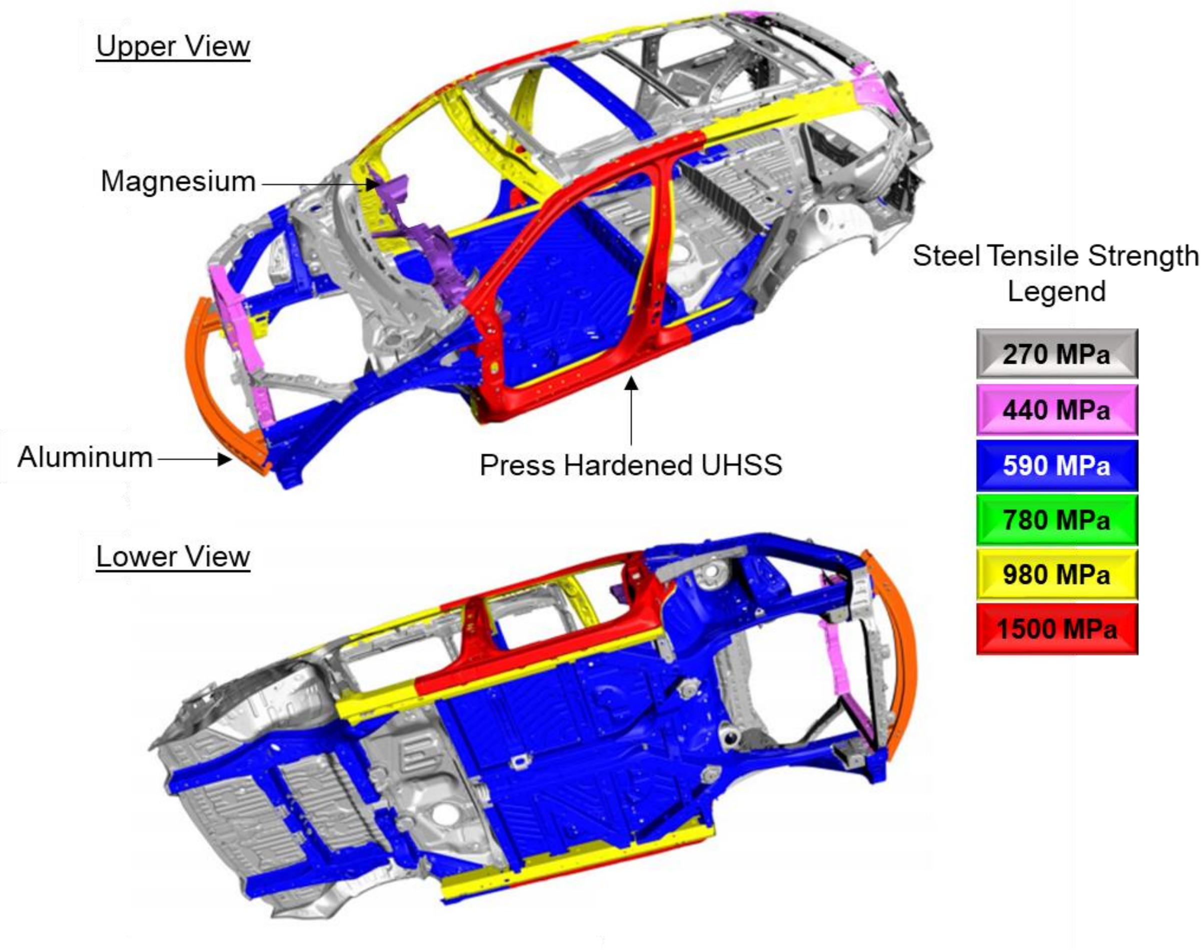

Figure 2. Body-in-white for the 2016 Honda Pilot is mainly comprised of steel, with press hardened UHSS used for the door ring, from Honda [7].

1.1.1 Hot Stamping

The concept of heating steel in a furnace to improve formability has been around for centuries, but Japanese sword makers are attributed with being the first civilization to understand the effects that cooling rate has on the overall characteristics of a steel blade. Layers of a clay mixture (*yakibatsuchi*) were applied to the exterior of the blade prior to heating so that upon submerging in water the quench rates throughout the blade could be locally controlled and the mechanical properties of the sword optimized (martensite at the edge of the blade for edge retention and pearlite/ferrite at the ridge opposite the edge for toughness and ductility) [8].

The modern practice of quenching furnace heated, boron alloy steel, has become a science in which process parameters can be meticulously monitored to achieve optimal microstructures. Today, hot stamped steels are mainly used in the automotive industry for structural chassis components, such as: A-pillar, B-pillar, roof rails, roof side stiffeners and rear crush rails as shown in the 2016 Honda Civic BIW (Figure 3). According to Hu *et al.* [9] the usage of hot stamped boron steel in VOLVO vehicles has gradually risen from 7 percent in the XC90 models to 17 percent in the S60 series, which is expected to reach 45 percent of the total BIW in the future.

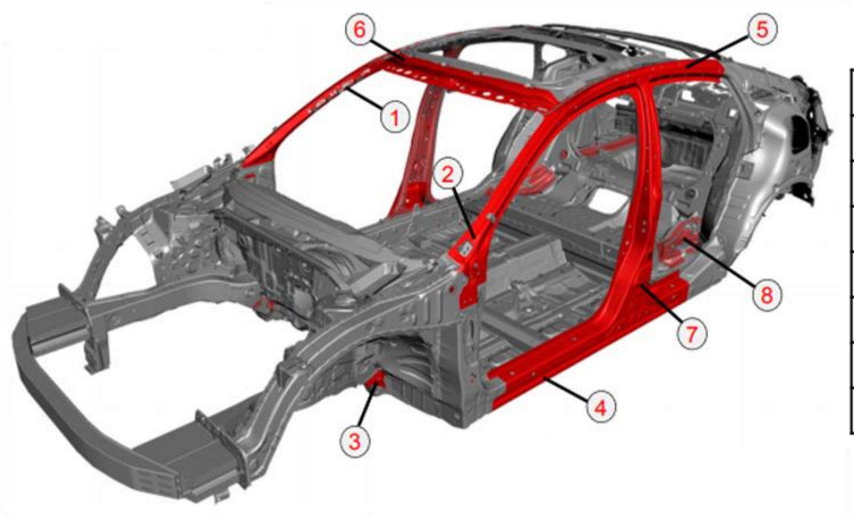

1	Front Inner Upper Pillar
2	Front Pillar Upper Stiffener
3	Front Side Frame Extension
4	Side Sill Reinforcement
5	Roof Side Stiffener
6	Roof Front Rail
7	Center Pillar Stiffener
8	Rear Frame

Figure 3. Application of UHSS hot stamped steel illustrated in the 2016 Honda Civic, adapted from Honda [10].

Hot stamping is differentiated from cold stamping through two distinct processes, namely austenitization and quenching. According to the Fe-Fe$_3$C diagram, the Ac$_1$ (austenite formation temperature on heating) and Ac$_3$ (completed transformation temperature of ferrite to austenite on heating) temperatures of hot stamping steels are 775 °C and 825 °C, respectively [11]. In order to ensure full austenitization, boron steel blanks are heated in a furnace to temperatures between 900-950 °C (well above the Ac$_3$ temperature) and allowed to soak at this temperature for 4-5 minutes. In a study conducted by Zhou *et al.* [12] the austenitization temperature and soak time were investigated. The results of this study showed that austenitizing at 900 °C provided the maximum tensile strength, with temperatures below 900 °C showing large reductions in tensile strength and temperatures above 900 °C showing gradual reductions in tensile strength. The study also showed that an oven soak time of 4 minutes corresponded to the maximum tensile strength, with gradual reductions in tensile strength for times above 4 minutes. Ultimately, higher oven temperatures (greater than 900 °C) and longer soak times (greater than 4 minutes) produce larger grains and coarser microstructures, resulting in lower tensile strength and hardness [12].

There exist two forms of hot stamping in today's processing environment: direct hot stamping and indirect hot stamping (Figure 4). In the direct hot stamping process a boron steel blank is heated in a furnace until full austenitization has occurred. After soaking in the hot oven and until all of the steel's ferrite has transformed to austenite, the blank is transferred to the press, where the part will be formed. Typically, transfer of the blank is done using robotic systems for rapid and repeatable results. It is important during this stage that the blank is transferred relatively quickly as heat loss from the blank will decrease its formability and may result in unwanted phase transformation prior to the forming operation. The only difference between direct and indirect hot stamping up to this point is that the blank is pre-formed in a cold forming operation prior to being austenitized in the indirect hot stamping process.

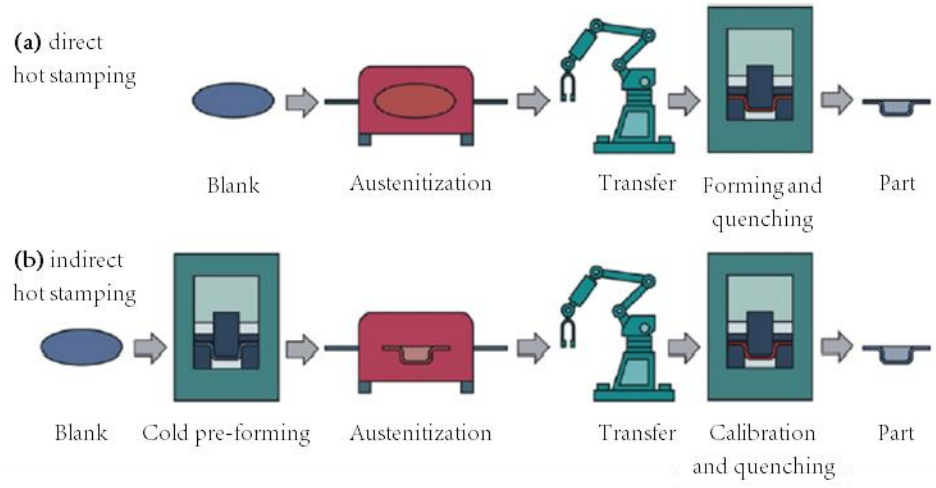

Figure 4. Hot stamping process flow diagrams: **(a)** direct hot stamping, **(b)** indirect hot stamping, adapted from Karbasian and Tekkaya [6].

Once the blank is transferred from the furnace to the water-cooled die set it is formed to the desired geometry, as dictated by the design of the die set (in the case of indirect hot forming only small calibrations are made to the initially cold formed part). The formed part is then held under the press tonnage for 5 to 10 seconds, quenching the hot blank due to contact with the chilled tool. According to Merklein *et al.* [11] if a critical cooling rate of 27 Ks^{-1} is exceeded during the quench, a diffusionless martensitic transformation will be induced. The continuous cooling transformation (CCT) diagram shown in Figure 5 illustrates the complete transformation of austenite to martensite with a cooling rate greater than 27 Ks^{-1}. If however, the critical cooling rate is not achieved (less than 27 Ks^{-1}) a bainitic or ferritic/pearlitic microstructure will be produced depending on the cooling rate obtained [6], [11], [13], [14], [15] and [16].

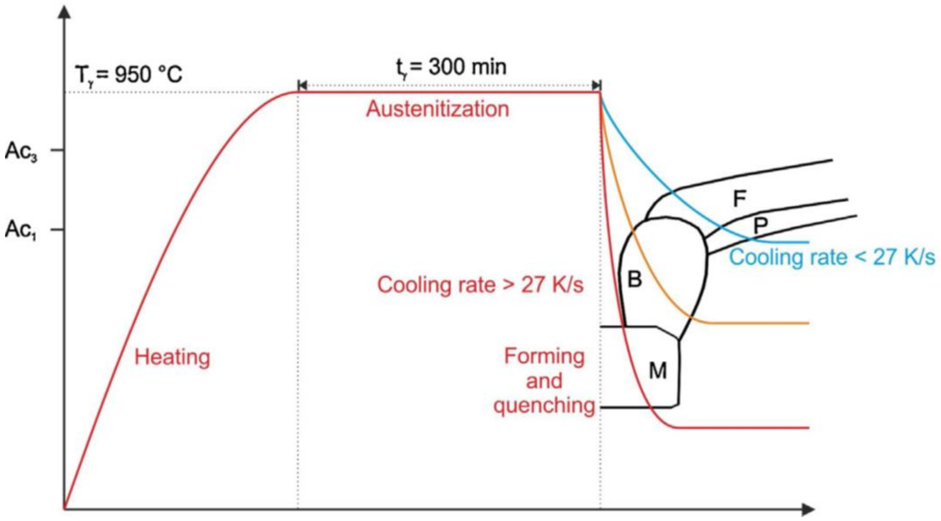

Figure 5. CCT diagram of 22MnB5 under various quenching rates shows the range microstructures that can be achieved through the quenching process, adapted from Merklein *et al.* [11].

Merklein and Svec [17] conducted a study into the effect that deformation temperature, cooling rate, true strain and strain rate have on the transformation of austenite to martensite. They found that the deformation temperature and quench rate had the largest influence on the hardness and microstructure formed. They also found that when plastic deformation occurred in the austenite phase, the phase regions shift leftwards on the CCT diagram (Figure 6), thus requiring higher quench rates to produce a fully martensitic microstructure.

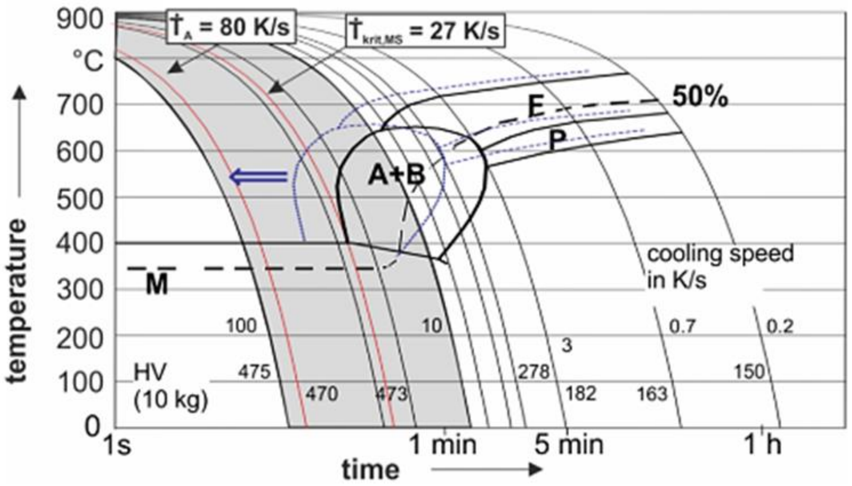

Figure 6. CCT diagram showing the effect of pre-deformation on the phase transformation of austenite, adapted from Merklein and Svec [17].

1.1.2 Hot Stamping Process Tailoring Methods

Safety demands of vehicle body-in-white structures have led to developments in the hot stamping process, such as local adjustment of component mechanical properties. These local adjustments allow for separate regions with excellent intrusion resistance and regions high energy absorption within the same component. Variants of the conventional hot stamping process used to achieve local adjustments are the use of tailored semi-finished products, such as tailor-welded blanks (1.1.2.1) or differential cooling through tailored in die heating (1.1.2.2). Several other methods of achieving local adjustments exist, but will not be covered in detail in this thesis. These adjustment methods include: partial heating of the blanks, variation of thermal properties of the tool, die relief through limiting the blank's contact pressure with the tool and annealing (tempering) the quenched component, as described by Merklein *et al.* [11].

1.1.2.1 Hot Stamped Tailor-Welded Blanks

A tailor-welded blank (TWB) is a single non-homogeneous blank fabricated by joining materials of different gauge, composition and/or mechanical properties together, as illustrated in Figure 7. In a TWB, the proper choice of joining partner controls how the mechanical properties of the component are locally adjusted. TWBs allow for higher strength or thicker material to be used in places where rigidity and structural strength are required and thinner or lower strength material to be placed in less severely-loaded locations for weight savings. In a frontal crush application, lower strength and more ductile alloys may be selected for an energy absorbing crush tip, for example, which can be welded to higher strength and more rigid material for intrusion and collapse resistance. Múnera *et al.* [18] and Peister [19] numerically and experimentally demonstrated the use of TWBs in automotive parts consisting of Ductibor® 500-AS and Usibor® 1500-AS in axial impact energy absorption and intrusion resistant zones, respectively.

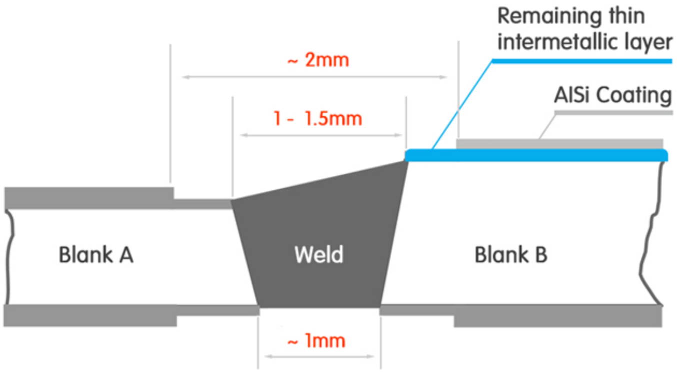

Figure 7. Laser welded blank of Al-Si coated hot stamping material with differing sheet thickness, from ArcelorMittal [20].

The most commonly used joining method is laser welding but mash seam and friction stir welding are other practiced joining options. A difficulty with welding hot stamping material stems from the fact that the sheets are covered with an Al-Si coating to prevent corrosion. According to Ehling *et al.* [21] if the coating is welded without being removed, an FeAl intermetallic phase is produced, which strongly reduces the mechanical properties of the joint. If however, the coating is fully removed, the corrosion resistance potential is heavily diminished. In order to maintain the integrity of the weld, a laser ablation process was developed by Ehling *et al.* [21] to remove exterior free Al-Si coating to avoid the creation of intermetallic phases during laser welding. However, this process does not remove the intermediate layer between the steel and Al-Si coating for corrosion protection during and after heat treatment.

The properties of the laser welded joint between Ductibor® 500-AS and Usibor® 1500-AS was studied by Kang and Kim [22]. In their study they measured the hardness across the laser weld line and found that in the fusion zone the hardness was higher than that of the base metal Ductibor® 500-AS. Samadian *et al.* [23] found, through tensile testing perpendicular to the laser weld line, that fracture always occurred through necking in the weaker Ductibor® 500-AS base metal.

Peister [19] researched the Vickers hardness level of axial hat channel TWBs consisting of Ductibor® 500-AS laser welded to Usibor® 1500-AS. In his study, hardness was measured along the length of the hat channel section from the top, side and flange for 1.2 mm, 1.6 mm and 1.2/1.6 mm material thicknesses. It is observed from Figure 8 that the hardness of the Ductibor® 500-AS section is much less than that of the Usibor® 1500-AS section; hence, Ductibor® 500-AS is the lower strength material in the TWB. It is also apparent from this figure that the transition zone (at the laser weld line) between the two materials is very small and was quantified by Peister to be about 2 mm in length.

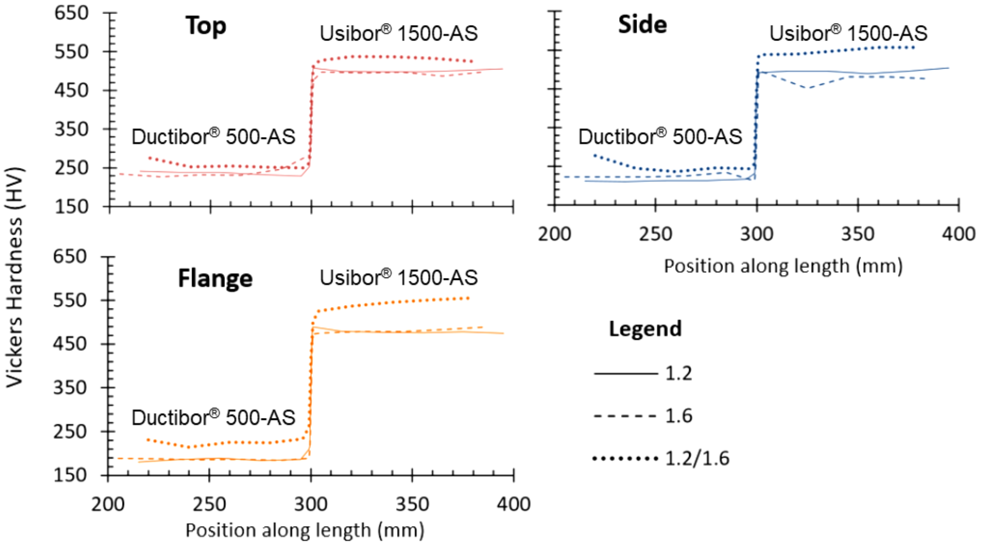

Figure 8. Comparison of the Vickers hardness level along the length of axial hat channel cross-sections taken from the top, side and flange. Adapted from Peister [19].

1.1.2.2 Tailored In-Die Heating

The rate of heat transfer between two contacting bodies is strongly influenced by their difference in temperature [24]. In-Die Heating (IDH) (also known as tailored tempering or heated tool tailoring) is the process of heating the tooling locally to control the cooling rate of the blank. The process works by increasing the temperature of the hot stamping die such that the difference in temperature between the austenitized blank and die are decreased. The decrease in temperature difference directly translates to a reduced cooling rate and, if severe enough (less than 27 Ks^{-1}), the formation of a bainitic and/or ferritic microstructure, as shown by George *et al.* [25] and Omer *et al.* [16]. The bainitic and/or ferritic microstructures produced through IDH exhibit reduced strength and increased ductility when compared with fully martensitic microstructures.

The tooling in the IDH process can be segmented, as shown in Figure 9, to have separate heated and cooled zones. Heating is achieved through embedding cartridge heaters into the tooling that when powered can heat the tooling up to 700 °C. Cooling channels are placed along the length of the other half of the tool, through which chilled water can be run. A 3 mm air gap separates the tool segments, which limits heat transfer from the heated tool to the chilled tool.

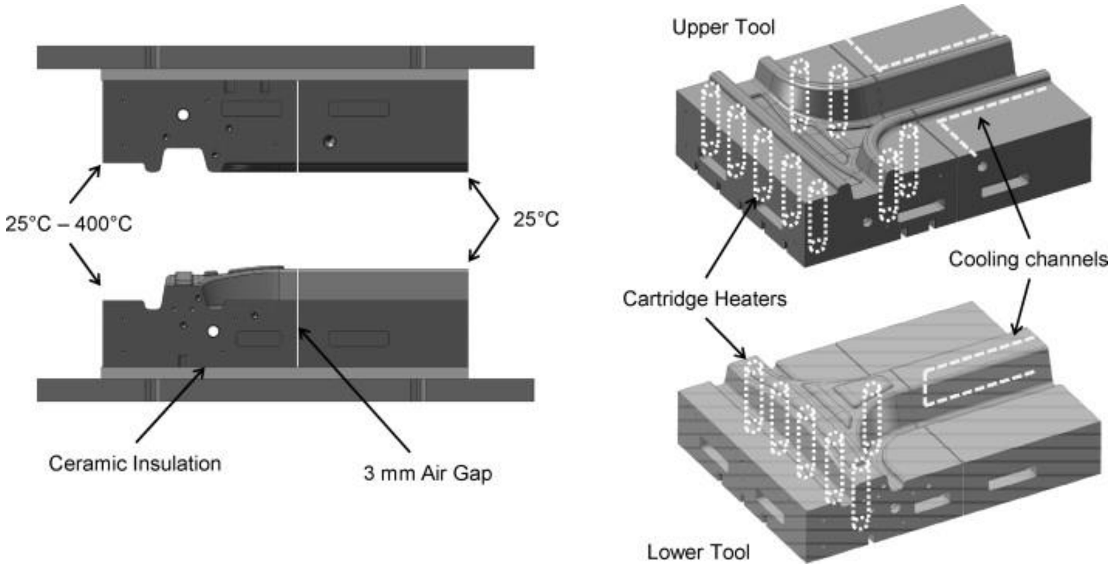

Figure 9. Schematic of segmented B-pillar tooling, from George *et al.* [25].

The IDH process can be used as a local adjustment method by only heating segments of the tooling in which higher ductility and reduced strength (lower hardness levels) are desired, often this local adjustment is called the tailored IDH process. George *et al.* [25] used the tailored IDH hot stamping process on B-pillar geometry to produce parts with two distinct zones, as shown in Figure 10; these zones included a fully quenched martensitic zone (chilled die region) and a quenched bainitic/ferritic zone (heated die region). Just through varying the tool temperature by 400 °C a difference in hardness of as much as 200 HV is observed in the B-pillar.

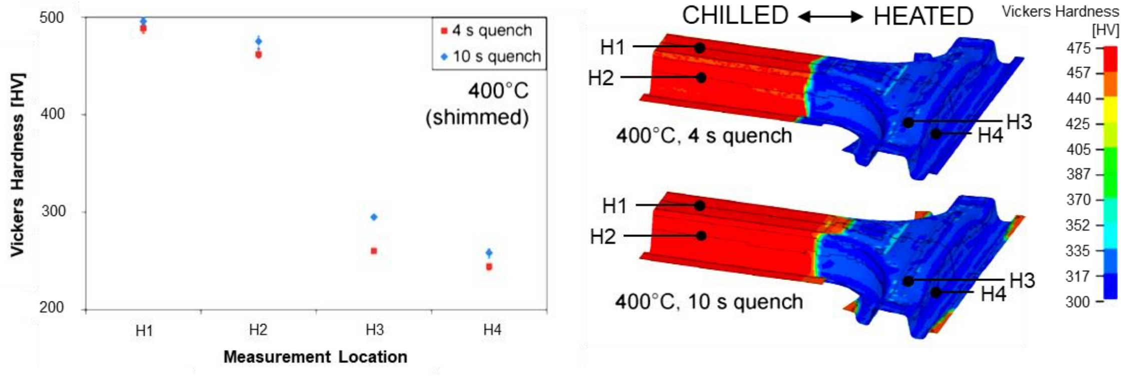

Figure 10. Tailored lab-scale B-pillar by George *et al.* [25] demonstrates the variation in Vickers hardness achieved using the in die heating process with a chilled die section and a 400 °C die section.

The process of tailored IDH was applied to an axial crush rail top hat geometry in a study by Omer *et al.* [16]. In this study, different levels of hardness and microstructure of the hat channel crush tip were produced through the tailored IDH hot stamping process, as shown in Figure 11. The tool temperatures considered in the crush tip region of the tooling were a 20 °C (fully quenched baseline), a 400 °C single soft zone, a 700 °C single soft zone and a 700 °C/400 °C graded soft zone. The study ultimately showed the tailored IDH process is an effective method of locally controlling the final part hardness.

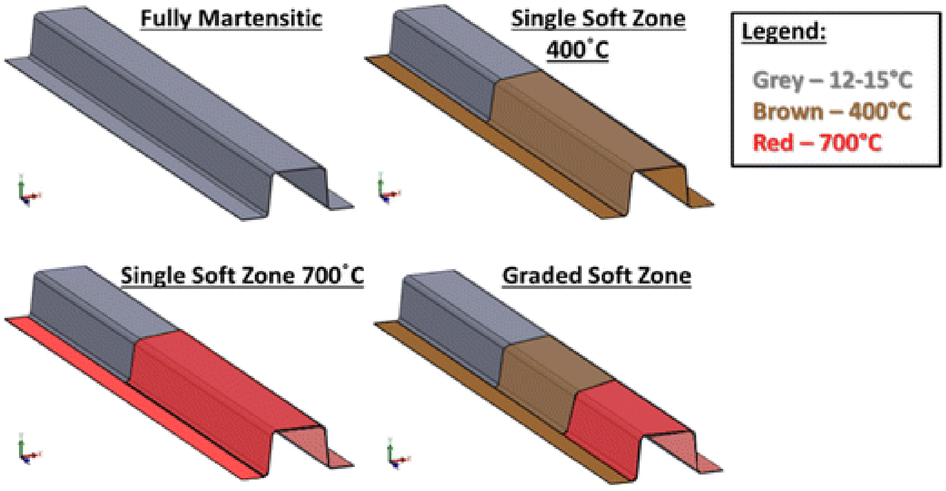

Figure 11. Tailored IDH process applied to axial crush rail top hat geometries, from Omer *et al.* [16].

1.1.3 Hot Stamping Materials

Hot stamping steels produce a fully martensitic or dual phase (ferritic-martensitic) microstructure when a hot forming die quenching operation is performed within a water-cooled tool. To achieve this fully martensitic microstructure special boron containing alloys have been developed. Boron, as an alloying element, acts as a hardening agent during die quenching, providing the material with excellent hardness and high strength. During quenching, heterogeneous precipitation of boron carbide and boron segregation occurs at the grain boundaries causing increased hardenability by suppressing the austenite to ferrite transformation, as demonstrated by Barcellona and Pallmeri [26].

During the austenitization stage of the blank, oxide scale formation occurs when contact with the hot furnace air occurs. A counter measure against surface oxidation and decarburization is to coat the material with an aluminum silicon (Al-Si) coating, which is applied in a continuous hot-dip galvanizing process. Typically the initial (prior to austenitization and quenching) Al-Si coating thickness is 25–30 µm per side, as observed by Fan and De Cooman [27]. Yakubtsov and Sohmshetty [28], found that during austenitization the Al-Si coating forms a Fe-Al intermetallic which grows in thickness as a function of oven soaking time. Due to lower forming limits of the Al-Si coating layer compared to the base material, at room temperature, coated material cannot be used in the indirect hot forming process, as they are not suitable for cold forming [6]. The strength of the Al-Si coating is much lower than that of press hardened UHSS and is therefore typically subtracted from the overall sheet thickness in strength calculations, such as during crash modelling.

The hot stamping steels considered in this research are Usibor® 1500-AS (nominally 22MnB5), Ductibor® 1000-AS and Ductibor® 500-AS, all of which are manufactured by ArcelorMittal. To date, Usibor® 1500-AS has been fully characterized by various researchers including: constitutive characterization by Bardelcik *et al.* [14], [14] and [15] and fracture characterization by ten Kortenaar [13], Golling *et al.* [29] and Östlund *et al.* [30]. The literature is very sparse with material characterization data for the relatively new material, Ductibor® 1000-AS and as a result only crashworthiness characterization has been conducted by Lee *et al.* [31]. Research has been conducted by Samadian *at al.* [32] and [23] on the fracture behaviour of Ductibor® 500-AS and TWB laser weld line between Ductibor® 500-AS and Usibor® 1500-AS, respectively. The chemical composition by maximum weight percent of each of these materials are shown in Table 1. The most obvious trend between the three materials is the declining carbon content from Usibor® 1500-AS through to Ductibor® 500-AS.

Table 1. Chemical composition by maximum weight percent of Usibor® 1500-AS, Ductibor® 1000-AS and Ductibor® 500-AS, from ArcelorMittal [33].

Material	C	Mn	P	S	Si	Cr + Mo	Al	Ti + Nb	B	Fe
Usibor® 1500-AS	0.250	1.400	0.030	0.010	0.400	1.000	0.100	0.120	0.005	Rem.
Ductibor® 1000-AS	0.120	2.000	0.030	0.010	0.800	0.600	0.100	0.120	0.010	Rem.
Ductibor® 500-AS	0.100	1.900	0.030	0.030	0.500	-	0.200	0.240	0.001	Rem.

A summary plot of the yield strength, ultimate tensile strength (UTS) and elongation of these hot stamping steels, as well as a galvanneal coated structural cold stamped steel (JAC590R), is presented in Figure 12. Through observing this figure, there is a clear trend that with increasing ultimate tensile strength, the elongation of the material decreases. In considering only the hot stamping steels, Usibor® 1500-AS has the largest UTS but the smallest elongation, whereas Ductibor® 500-AS has the smallest UTS but the largest elongation. Comparing the hot stamped steels now to the conventional steel it is observed that JAC590R has a very comparable UTS to Ductibor® 500-AS but has almost double the elongation.

The potential for weight savings in automotive structures, through using hot stamping steels becomes apparent when comparing JAC590R with a material such as Ductibor® 1000-AS, which has a UTS almost twice that of JAC590R. The current research investigates the feasibility, in terms of crash performance and formability, of replacing JAC590R with thinner gauge, higher strength hot stamped material (Ductibor® 1000-AS).

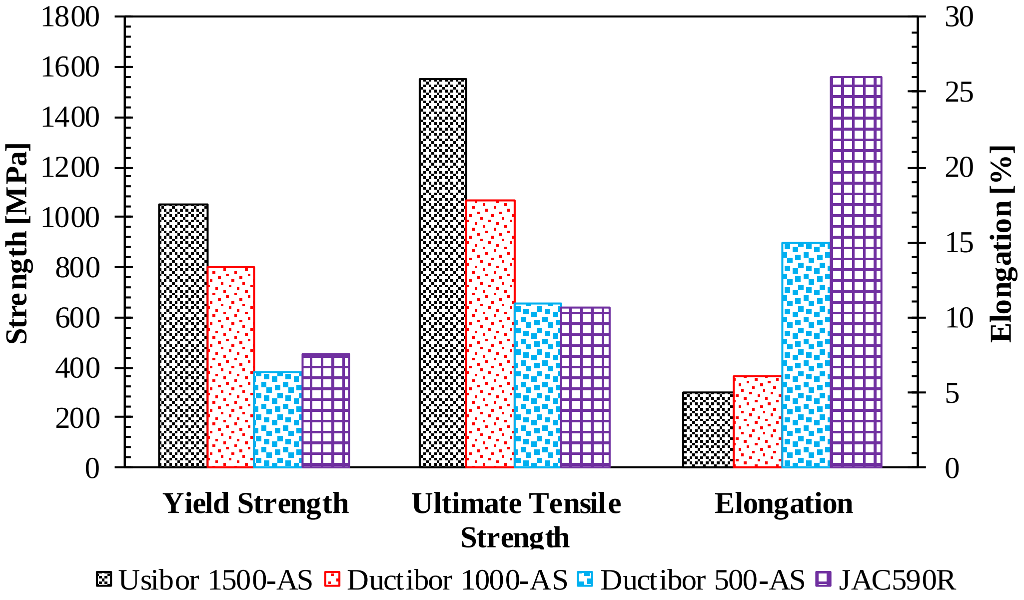

Figure 12. Mechanical property summary of the hot stamping materials (Usibor® 1500-AS, Ductibor® 1000-AS and Ductibor® 500-AS) after hot stamping thermal treatment and a conventional structural automotive steel (JAC590R). Data for Usibor® 1500-AS, Ductibor® 1000-AS and Ductibor® 500-AS from ArcelorMittal [34], [35] and [36]. Data for JAC590R from Kohei *et al.* [37].

1.2 Crashworthiness

Automotive crash safety structures are being designed lighter through the use of higher strength materials, by means of sheet metal down gauging. Designers of these light weight structures must consider crashworthiness requirements to maintain or improve the current occupant safety in crash. Vehicle frontal and rear impact structures should be deformable, yet stiff, with strategically located crumple zones to absorb crash kinetic energy through plastic deformation, while preventing intrusion to the passenger compartment. Side structures such as door pillars must be designed to minimize intrusion during side impacts. Roof rails must be strong to prevent collapse in the case of vehicle rollover. All of these crashworthiness requirements must be met while also accommodating non-crash related constraints, such as: styling considerations, range of occupant sizes and ages, working in harmony with occupant restraint systems, and accommodating various chassis designs and powertrain platforms.

There exist two major considerations in the design of automotive crash energy management structures: 1) absorption of the kinetic energy of the vehicle and 2) crash resistance or strength to sustain the crush process and maintain occupant compartment integrity [38]. The two basic modes of energy absorption are axial collapse and bending, as illustrated in Figure 13. Pure axial collapse can only be achieved during direct front/rear or slightly off angle impacts, therefore front and rear end structures are subject to mixed modes of deformation comprised of axial crush and bending.

Crashworthiness of structural members is measured by the amount of impact energy absorbed and the peak reaction force obtained during a crash event. The larger the impact energy absorption, the safer the structure. However, if the associated peak reaction force is too high, the design is often rejected due to large deceleration values induced on the occupants, which may cause injury [39]. It is therefore the main objective of the design process to increase the impact energy absorption potential, while minimizing the peak reaction force values of automotive structures. An important metric for comparing the efficiency of different crash structures is the specific energy absorbed, which is the impact energy divided by the structural mass. It is often useful to determine the crush force uniformity or efficiency by dividing the average crush load by the peak reaction load. An ideal energy absorbing structure would have a crush force efficiency of unity.

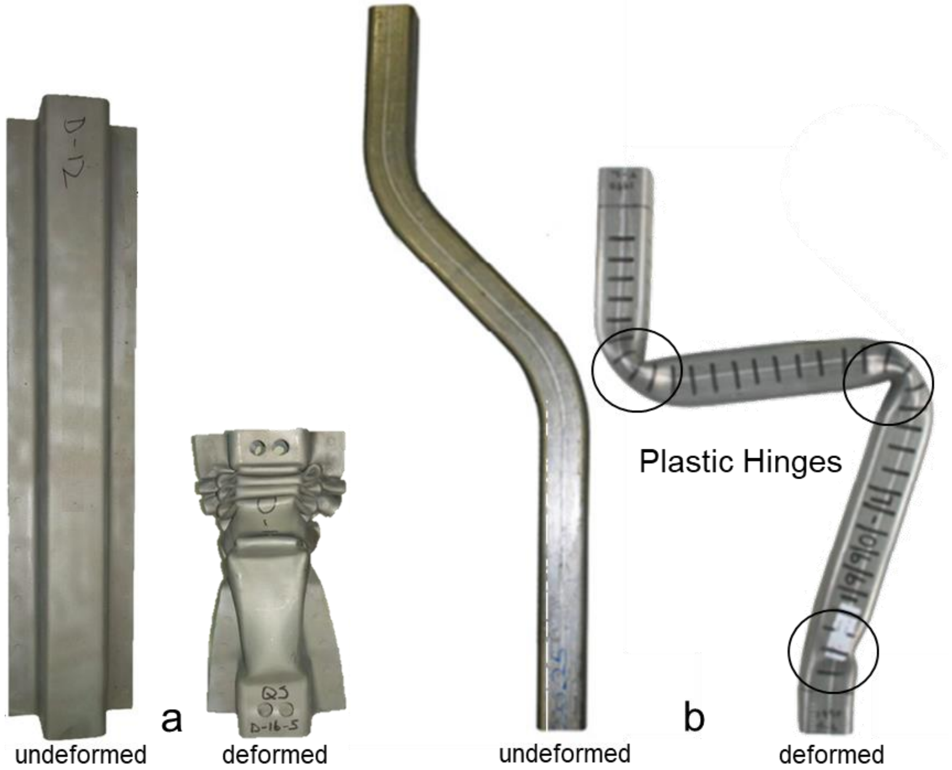

Figure 13. (a) Double top hat channel demonstrating axial collapse mode, adapted from Peister [19]. **(b)** Hydroformed S-rail tube demonstrating bending mode, adapted from Oliveira [40].

1.2.1 Axial Collapse Mechanism

Manufacturer interest in reduced production costs and vehicle light weighting, through using thinner frame constructions, has caused the plastic behaviour of BIW components to become of great importance. However, before analysing complex frontal or rear impact structures it is instructive to first examine the behaviour of less complex components, such as thin walled axial crush structures. These thin walled axial crush structures have historically consisted of circular tubes, as investigated by Alexander [41], rectangular tubes studied by Weirzbicki and Abramowicz [42] and spot welded flanged axial crush geometries reported by White *et al.* [43].

Early analytical work by Ohkubu *et al.* [44], Johnson *et al.* [45], Wierzbicki and Akerstrom [46] and others investigated modelling the mechanics and kinematics of the folding process to derive relatively simple relationships involving component geometry and material properties. In 1983, Weirzbicki and Abramowicz [42] developed the expression,

$$P_m = 9.56\sigma_0 t^{\frac{5}{3}} b^{\frac{1}{3}} \tag{1}$$

for defining the mean static crushing load P_m of thin walled rectangular box columns, where σ_0 is the yield strength of the material, t is the sheet thickness and b is the width of the rectangular section. This equation was developed under the assumptions of an initially planar surface, a rigid-perfectly plastic material and the local buckling wave remains constant throughout the crush event.

In 1999, White *et al.* [43] expanded these relationships to encompass flanged cross-sections, namely the single top hat and double top hat geometries, as depicted in Figure 14 (a) and (b), respectively. Idealization of the actual collapse profiles of these single and double top hat profiles are illustrated in Figure 14 (c) and (d), respectively. The flanged profiles are much more representative of vehicle components, since they can be pictured as abstracted forms of side door anti-intrusion beams, roof rails, front/rear crush rails and door pillars. Expressions were developed for single top hat profiles as,

$$P_m = 8.22\sigma_0 t^{\frac{5}{3}} L^{\frac{1}{3}} \tag{2}$$

and for double top hat profiles as,

$$P_m = 13.05\sigma_0 t^{\frac{5}{3}} L^{\frac{1}{3}} \tag{3}$$

where L is the perimeter of the single or double top hat specimen. It is to be noted that Equations (2) and (3) are derived under the assumption of a rigid-perfectly plastic material. If instead a material with significant strain hardening effect is used, Equations (2) and (3) can be modified by using the ultimate tensile strength σ_u of material instead of the yield strength, which for single top hat profiles is written as,

$$P_m = 8.89\sigma_u t^{\frac{5}{3}} L^{0.29} \tag{4}$$

and for double top hat profiles as,

$$P_m = 14.54\sigma_u t^{\frac{5}{3}} L^{0.29} \tag{5}$$

In Equations (1-5) it is interesting to note that the thickness term has an exponent 5/3 ($t^{\frac{5}{3}}$). In a material down-gauging study for which all of the other parameters remain the same except for the material ultimate tensile strength σ, a strength to thickness ratio,

$$\frac{\sigma_1}{\sigma_2} = \left(\frac{t_2}{t_1}\right)^{\frac{5}{3}} \tag{6}$$

can be formulated. Where σ_1 and t_1 denote ultimate tensile strength and material thickness for the first material, respectively, and σ_2 and t_2 the same for the second material. Equation 6 becomes particularly useful to an automotive crash structure designer when they are considering new materials of differing tensile strength for crash applications. The equation allows them to quickly obtain an initial analytical starting point for material thickness under the pretense they wish to maintain the same mean reaction load.

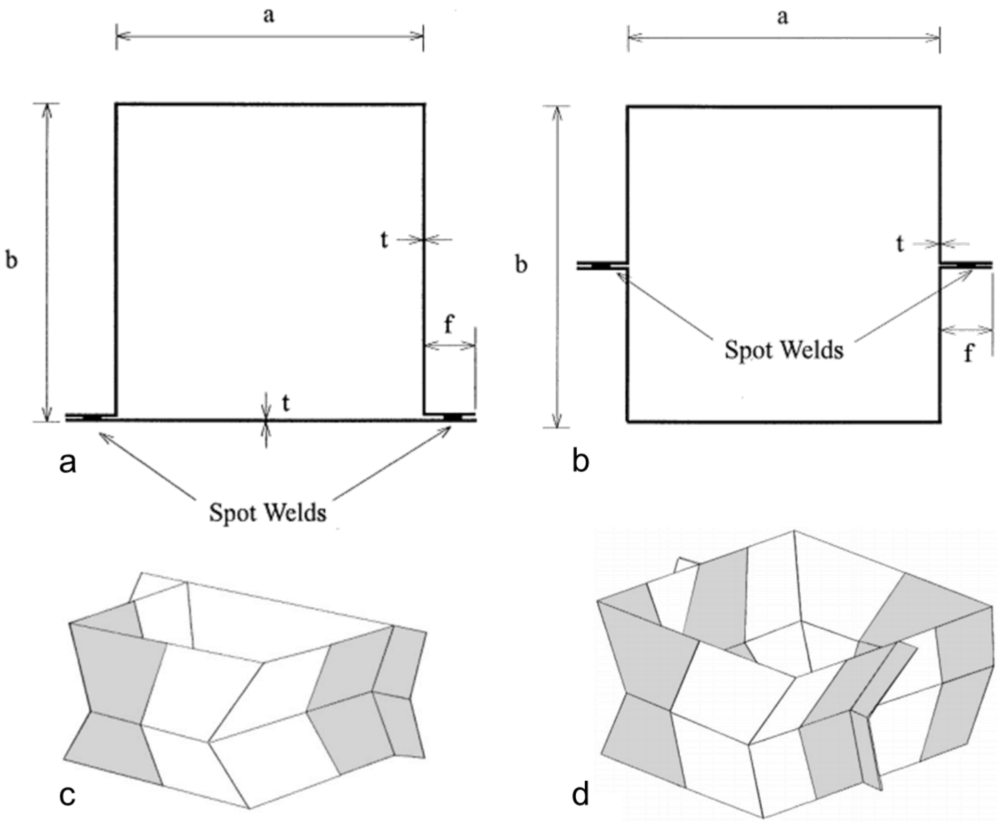

Figure 14. **(a)** Cross-section of a single top hat geometry. **(b)** Cross-section of double top hat geometry. **(c)** Four asymmetric elements forming the single top hat collapse profile. **(d)** Eight asymmetric elements forming the double top hat collapse profile. Adapted from White *et al.* [43].

1.2.2 Bending Collapse Mechanism

Bending as a collapse mode may be designed into the structure as a way of managing impact energy or it can be a consequence of a structure being loaded outside of its intended use. The predominance of the bending collapse mode is the result of the natural tendency of structures to collapse in a mode that requires the least expenditure of energy. It is important in many practical designs to estimate the factor of safety against a global collapse mode, which would lead to large deformations and potentially catastrophic consequences. A schematic of the bending collapse mode is shown in Figure 15.

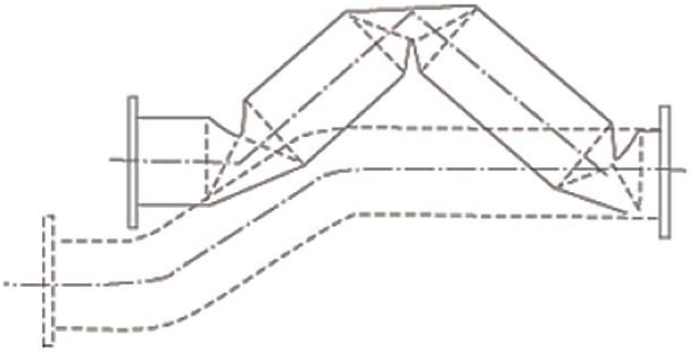

Figure 15. Schematic of the bending collapse mode in a thin-walled box cross-section, from Du Bois *et al.* [38].

The uniaxial bending collapse of thin-walled rectangular and square section tubes were investigated both experimentally and theoretically by Kecman [47], for the design of weight-efficient safety structures. Important findings from this work were: plastic deformation occurs between two undeformed beam segments with clearly defined hinge lines and the folding length and corner angle along the folding length remain almost constant during hinge rotation.

Wierzbicki and Abramowicz [42] expanded on Kecman's model by introduced extensional deformation at the corners of the hinge mechanism and created a three parameter model. Later in 2001, Kim and Reid [48] proposed a new analytical, kinematically admissible folding mechanism for bending collapse, which included extensional deformation at the corner in the deformation mechanism.

Abramowicz and Jones [49] found a relationship,

$$\left(\frac{L}{C}\right)_{cr} = \sqrt{\frac{6n}{2+\sqrt{1+3n}}}\left(\frac{C}{t}\right) \tag{7}$$

to determine the critical length to width ratio $(L/C)_{cr}$ for a thin-walled square tube cross-sectional column of thickness t with plastic properties and hardening parameter n that can predict whether the collapse will either be a local folding mode or global buckling mode. With the formation of a global bending mode there is an abrupt drop off of the force-displacement response for the tested part, followed by large and often uncontrolled deformation.

Oliveira [40] applied bending collapse theory to hydroformed aluminum S-rail tubes, demonstrating their suitability for use in automotive front side rails. It was found through Oliveira's studies that crash energy absorption capability of the S-rail could be increased through decreased offset distance between the two bends of the S-rail, increased wall thickness and work hardening of the material at local hinge locations and decreased bend severity.

1.2.3 Fold Initiation

During a crash incident it is important to achieve maximum energy absorption with the lowest possible peak forces. Automotive frontal crash structures are designed to promote folding instead of bending to more effectively absorb impact energy. One technique employed in frontal crash structures, to improve the tendency to folding, rather than bending is to introduce various types of triggering dents or fold initiators along the length of the frontal crash structure. Examples of some of the geometries used for these fold initiators are shown in Figure 16. According to Eren *et al.* [50] crush initiators are the weakest point in the cross-section of a square column and are deliberately placed on the column to initiate localized folding in order to reduce initial peak load and to ensure a stable failure mode with significant energy absorption.

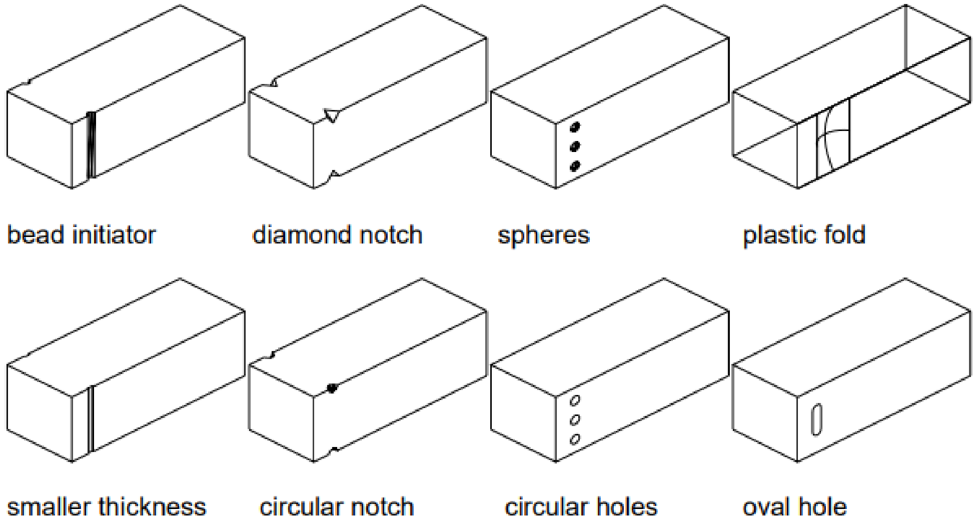

Figure 16. Different types of fold initiators employed on axial crush structures to promote folding, as generated by Witteman [51].

The effect of triggering on the energy absorption of axially compressed rectangular aluminum tubes was studied by Lee *et al.* [52]. They looked at trigger spacing along the length of a rectangular aluminum crush tube and half-dent triggers versus full-dent triggers. From this study it was found that dents introduced at the pitch corresponding to length of the folding wave improved the energy absorption over crush tubes without dents. It was also found that specimens containing half-dents had the same number of plastic hinges as those with full-dent triggers; however, the force required to form those hinges increased, thereby increasing the energy absorption.

The energy absorption potential and reduction of peak reaction force of thin-walled mild steel tubes was improved and could be controlled by Hosseinipour and Daneshi [53] through the introduction of annular groves on the walls of the tubes. Eren *et al.* [50] found that through introducing two rows of convex rib type crush initiators into square cross-sectioned columns, the initial peak reaction load could be reduced by 54 percent and the absorbed impact energy increased by 26 percent.

1.2.4 Relationship between Forming and Crashworthiness

Often the crash performance of sheet metal components is characterized in an ideal state, in which nominal sheet thicknesses without residual forming stresses are used; however, this is not always realistic due to the effect that forming history can have on a stamped component. Through the sheet metal forming process certain areas of a part will experience more thinning than others. In addition, plastic strains, work hardening and residual stresses will accumulate. The combination of these forming history effects can significantly alter the crash performance of a component.

The non-uniform distribution of thickness and effective plastic strain after a forming simulation were considered in a study by Huh *et al.* [54] on the simulated crash performance of a front side member. In this study it was found that if thickness and strain histories were incorporated into the front side member crash model, the initial peak force and energy absorption increased by 12.5% and 17.3%, respectively, when compared to a crash model that neglected forming effects. These predictions demonstrate that the strain hardening resulting from the forming process is dominant in reaction force and energy absorption calculations.

Similarly, the effect of forming process variables on crashworthiness was researched by Oliveira *et al.* [55] on aluminum alloy hydroformed tubes. Simulation of the tube bending process to form an s-rail component was used to account for deformation history including strains, thickness changes and residual stresses that could then be transferred into crash models. The effect of considering the previous forming history in the simulated crash event resulted in an increase in peak force of approximately 25-30% and energy absorption by 18%.

Modelling of the tailored IDH UHSS hot stamping process was conducted by Omer *et al.* [56] on axial crush rail hat channel geometries. In this research, the hot stamping material model created by Åkerström [57] (*MAT_UHS_STEEL or *MAT_244 in LS-Dyna) was used to predict the austenite phase decomposition and final hardness of a hot stamped part. The elemental final hardness levels predicted by the forming model were then placed into five bins of varying hardness range, each having their own constitutive model properties. The axial crush modelling that utilized the hardness level binning showed very close prediction of folding behaviour and impact energy absorption to the tested parts.

1.3 Crush Performance of Hot Stamped Components

A significant amount of component-level research has been conducted into the application of hot stamped steels in side impact structures. Three-point bend tests on 1.6 mm fully martensitic hot stamped steel single top hat cross-sectional geometries, performed by Sato *et al.* [58], demonstrated a 140 kN peak load before bending collapse. Eller *et al.* [59] used the hot stamped IDH process to produce 1.5 mm thick single top hat cross-sectional geometries with tailored properties, which supported a peak load of 45 kN during the four-point bend test before cracking occurred in the martensitic zone of the tailored part. The effect of thermally softening the flanges of otherwise fully martensitic single top hat geometries though the IDH process was studied by Prajogo [60] in the three-point bending configuration. Peister [19] performed three-point bend tests on single hat channels consisting of both 1.2 mm and 1.6 mm Ductibor® 500-AS with a JAC590R closure panel. In the study two different deformation modes were observed, folding and wrapping. The wrapping mode absorbed 72% more impact energy then the folding mode over 120 mm of crash sled travel.

The focus of this thesis however is on frontal crash structures, which are best represented using axial crush experiments. The performance of these axial crush experiments can be evaluated through: total energy absorption, peak reaction load, sustained average reaction load and the deformation behaviour. Common geometries used to evaluate axial crush performance are single or double top hat cross-sections, as illustrated in Figure 17. The single hat channel geometry consists of one hat channel with a back plate welded onto the open face, whereas the double hat channel consists of two hat channels welded to each other.

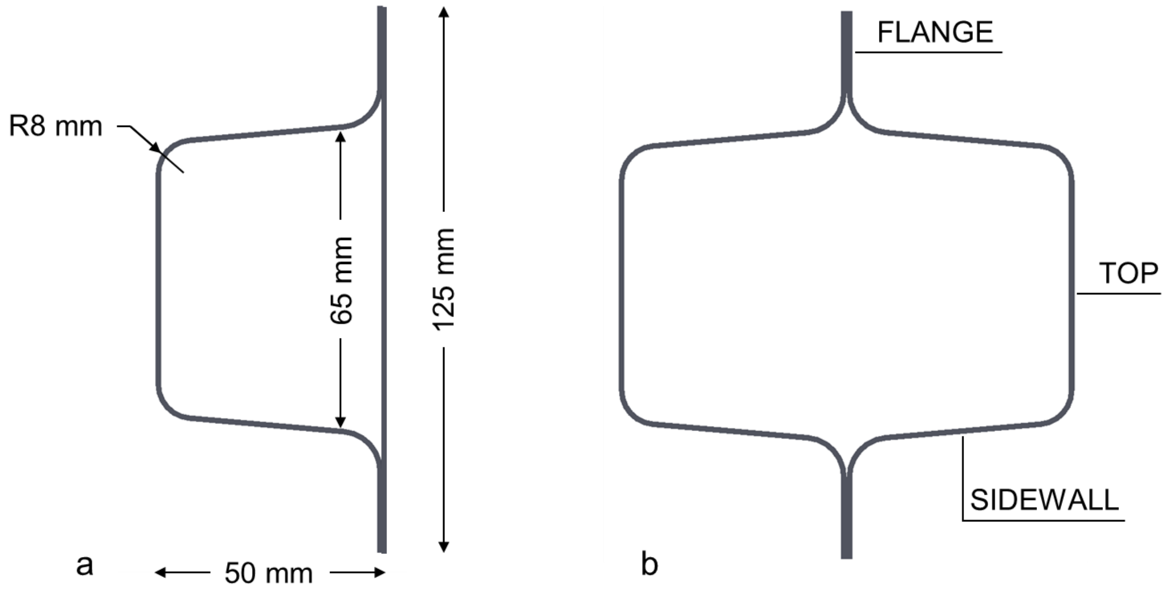

Figure 17. Axial crush rail cross-sections of **(a)** single top hat channel and **(b)** double top hat channel. Dimensions from Peister [19].

Múnera *et al.* [18] formed single top hat channel sections from 1.5 mm monolithic TWBs comprised of Usibor® 1500-AS and Ductibor® 500-AS to be used in axial crush, as shown in Figure 18a. The rails were tested with two different crush distances, 100 mm (engaged only the Ductibor® 500-AS section) and 150 mm (engaged both the Ductibor® 500-AS and Usibor® 1500-AS sections), and were impacted by a mass of 350 kg at a speed of 16 ms^{-1}. The result of the 100 mm crush test shown in Figure 18b illustrates the stable deformation of Ductibor® 500-AS and absence of failure in the laser weld line or parent metal. Based on average crush force, the 100 mm crush test Ductibor® 500-AS ranked similarly to DP600 and demonstrated 6.8 kJ of energy absorption and a peak load of 250 kN. In the 150 mm crush distance test, the Usibor® 1500-AS was engaged as well as the Ductibor® 500-AS causing the peak load and energy absorption to be higher than the 100 mm crush distance test. They examined the potential for weight reduction of a high strength steel (HSS) vehicle front rail using a numerical study, in which the HSS material was substituted with a Ductibor® 500-AS crush tip and fully martensitic boron steel elsewhere. The predictions indicated that a reduction in component weight by 43% was possible while matching performance of the HSS reference rail.

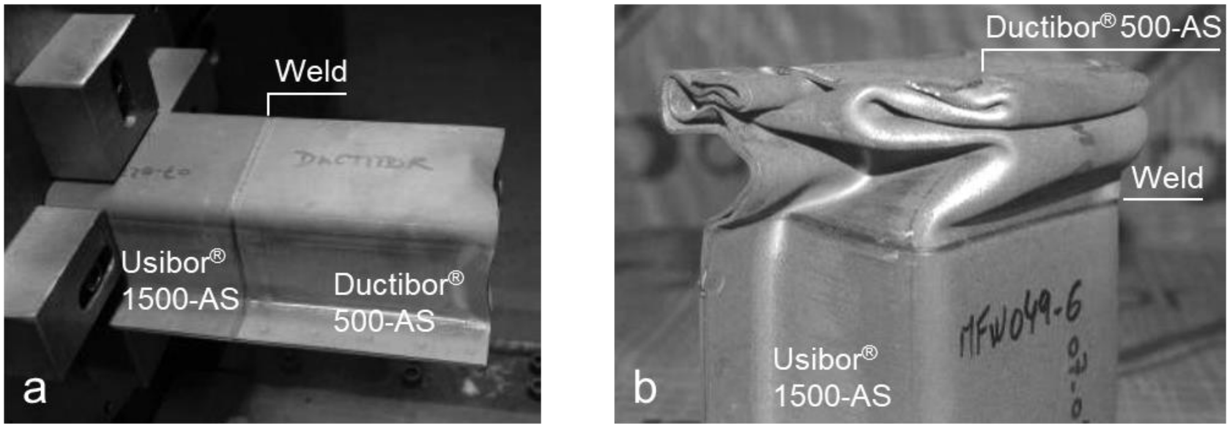

Figure 18. (a) Single hat channel geometry axial crush experiment setup. **(b)** Single hat channel geometry after axial crush experiment, showing impact energy absorption potential of Ductibor® 500-AS. Adapted from Múnera *et al.* [18].

The axial crush performance of tailored IDH hot stamped 1.2 mm and 1.8 mm Usibor® 1500-AS double hat channel crush rails was investigated by Omer *et al.* [56]. In this study, the strength level of the crush tip was tailored through selectively heating sections of the tool, while the remainder of the crush rail was fully martensitic. The crush tip quenching conditions consisted of fully quenched (martensitic) case, configurations with either 400 °C or 700 °C single heated tool zones, and a graded two-zone configuration with tool temperatures of 700 °C and 400 °C to create a graded soft zone. A variety of crush modes were observed (Figure 19) through testing the range of crush tip conditions. Extensive failure was displayed in the fully cooled or martensitic condition, which interestingly also had the highest average impact energy absorption, as shown in Figure 20. A mixed buckling/folding mode was dominant in the 400 °C quench condition and was even present in the 700 °C quench condition. The graded soft zone configuration was dominated by progressive folding

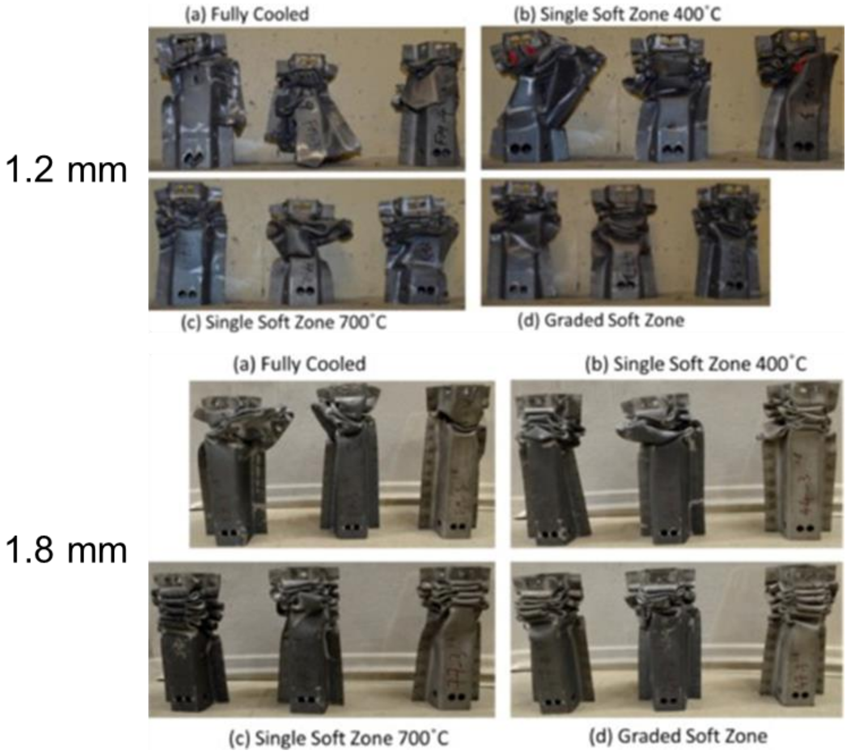

Figure 19. Crush modes observed from the various tailored IDH crush tip configurations, from Omer *et al.* [56].

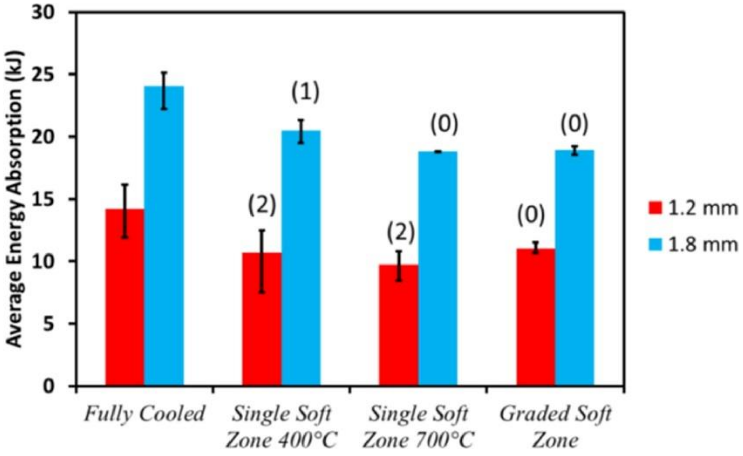

Figure 20. Average energy absorption, and scatter for the various tailored IDH crush tip configurations. The numbered parenthesis above the bars indicate the number of rails that exhibited mixed buckling folding response, from Omer *et al.* [56].

The crash performance of crush members made from monolithic Ductibor® 500-AS and from TWBs comprising Ductibor® 500-AS welded to Usibor® 1500-AS were studied by Peister *et al.* [19], [61] and [62]. Axial crush experiments in that research was conducted on 500 mm long double hat channel sections, allowing for 160 mm of free crush (crush distance prior to engaging honeycomb attenuators). A sled mass of 855 kg at a speed of 38.2 km/hr was used. The experiments conducted by Peister showed that hot stamped TWBs have performance advantages over monolithic parts, as demonstrated in Figure 21. The monolithic Ductibor® 500-AS specimens had a tendency to buckle globally due to their low stiffness and long length. However, introducing a Usibor® 1500-AS end section in the TWB stabilizes the rail section, allowing for progressive axial crush of the Ductibor® 500-AS energy absorption section. The stabilizing effect of the higher strength material added to the end section of the rail is explained by Omer *et al.* [56], who theorizes that the increased strength end section reduces the effective column length of the rail, hence making it less likely to buckle globally.

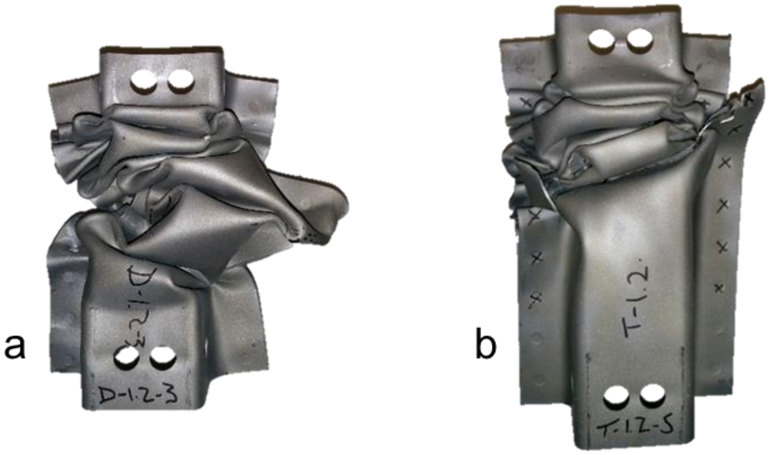

Figure 21. (a) 1.2 mm Ductibor® 500-AS base metal axial crush displays global buckling mode. **(b)** 1.2 mm Ductibor® 500-AS to Usibor® 1500-AS TWB displays progressive folding. Adapted from Peister [19].

Using the double hat channel cross-section, Lee *et al.* [31] studied the axial crush performance of Ductibor® 1000-AS rails in dynamic impact. In this study it was found that rails incorporating only a single fold initiator on the top of the rail (65 mm from the impacted end), were susceptible to failure and the rail was more likely to buckle globally. Failure of the rails was often triggered by spot weld failure. If however, fold initiators were added more strategically along the length of the top of the rail, as well as along the length of the flanges, the number of spot weld failures could be reduced and stable progressive folding of the rail induced.

From the foregoing discussion, the available literature provides extensive knowledge of the axial crush behaviour of simplified hot stamped components (channel sections). However, there are very few studies that exist in which realistic automotive frontal crash structures, consisting of hot stamped components have been tested. The crash behaviour of such realistic hot stamped frontal structures is the focus of the current thesis.

1.4 Resistance Spot Welding

Resistance spot welding (RSW) is a sheet metal joining method commonly used in the automotive industry due to its relatively low cost and quick joining rate, explained by Aknas *et al.* [63]. The RSW process joins two sheets together, without the addition of filler metal (massless) by applying electrical current and clamping force at a point. The area of sheet metal between the two clamped electrodes turns molten, however the adjacent material surrounding the electrodes does not reach melting temperatures and as a result is only locally tempered. The region of local tempering of the adjacent material is known as the heat affected zone (HAZ). In martensitic steels it has been shown by Baltazar Hernandez *et al.* [64] that heating martensite grains close to the lower critical transformation temperature softens them due to the diffusion of carbon. In the same study it is shown that the subcritical HAZ experiences a significant reduction in hardness (Figure 22), with respect to the base material. The strength of martensitic steel spot welds is limited to the strength of the HAZ created during the RSW process, since fracture will initiate in this softened area.

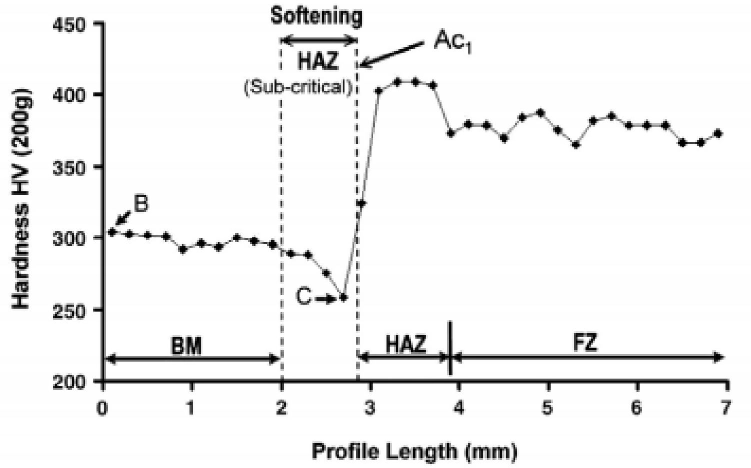

Figure 22. Significant decrease in hardness shown in the subcritical HAZ region with respect to the base material (BM), from Baltazar Hernandez *et al.* [64].

1.4.1 Performance of Hot Stamped Steel Resistance Spot Welds

The performance of tailored IDH Usibor® 1500-AS resistance spot welds was researched by O'Keeffe *et al.* [65] and [66]. The testing included single weld specimens in lap shear and cross tension, as well as Mode I (tensile loading) group weld specimens. The single weld tests showed that the highest overall weld failure force was achieved with the fully quenched base metal condition, however the weld toughness was improved through the tailored IDH process. The fully martensitic material offers the highest parent metal strength, but through spot welding a softened HAZ is produced. Strain localizes in this softened HAZ and results in failure at relatively low displacements, corresponding to low fracture toughness of the welded joint. The lower strength tailored IDH parent metal conditions had HAZ strengths similar to the base metal, which promoted more plastic work in the parent metal prior to failure, resulting in increased fracture toughness of the welded joint.

To test weld groups under Mode I (pull-out) loading, O'Keeffe [65] developed a specimen which consisted of two top hat channels spot welded along the flanges at constant spacing. The two channels are then pulled apart creating a tensile load on the group of spot welds, as shown in Figure 23. In the Mode I group spot weld tests the weld toughness was reflected in the rate of spot weld failure propagation. In the fully martensitic parent metal case, which had a relatively low fracture toughness, a high rate of weld failure propagation was observed. In the tailored IDH cases, the softer parent metal and higher weld toughness causes a lower rate of weld failure propagation.

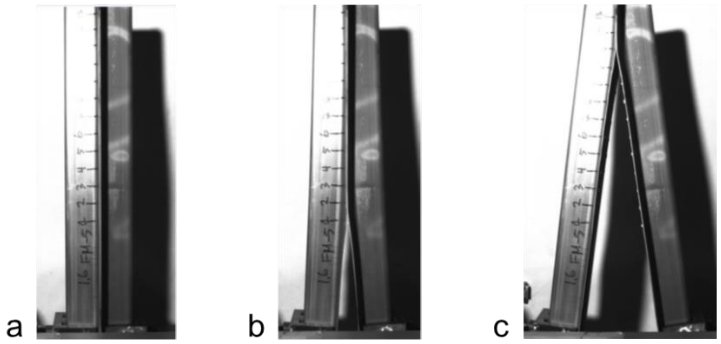

Figure 23. Quasi-static Mode I group spot weld test at the **(a)** start of test, **(b)** first weld failure and **(c)** end of the test. Adapted from O'Keeffe [65].

The success of the Mode I (tensile loading) group weld specimens led the way for the development of a Mode III (shear loading) weld group test. The Mode III weld group test, developed by Tolton *et al.* [67] uses a complex arrangement of die quenched flat panels that are spot welded together along the length and made into a closed channel using a series of C-channel reinforcements (Figure 24). In the test, spot welded specimens are pulled apart from one end using bosses and pins, creating a shear loading condition on the welds. The test allows the performance of hot stamped steel spot welds to be evaluated in a group shear loading condition.

Work has been done to characterize the weld performance of Usibor® 1500-AS in the fully quenched condition, as well as various tailored IDH conditions. It is well understood that the higher the strength of the parent metal, the lower the weld fracture toughness will be. The literature is currently void of research in the weld performance of Ductibor® 1000-AS resistance spot welds.

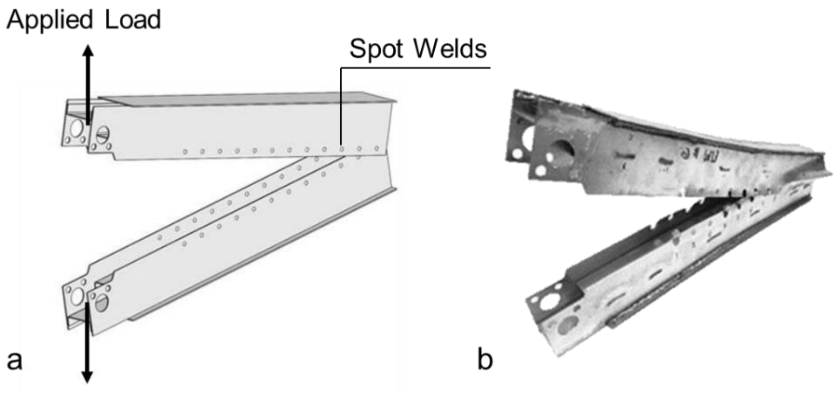

Figure 24. **(a)** Schematic of the Mode III group spot weld failure test. **(b)** Proof of concept test article consisting of as-received Usibor® 1500-AS. Modified from Tolton *et al.* [67].

1.5 Numerical Modelling of Hot Stamped Components and Structures

The use of numerical simulation software allows for the design of structural components to be iterated on in a relatively quick and inexpensive fashion. The areas in which numerical simulation is typically applied include: modelling of the hot forming and subsequent crash performance of hot stamped components and structures, as reviewed in the following sections.

1.5.1 Hot Forming Process Simulation

The hot forming process is much more difficult to model when compared to conventional cold stamping because, during hot stamping, the mechanical properties of the material vary over time due to the change in temperature and microstructure. Thus, in order to numerically model the hot stamping process, a coupled thermal-mechanical solver must be implemented. The thermal-mechanical solver flow is outlined in Figure 25.

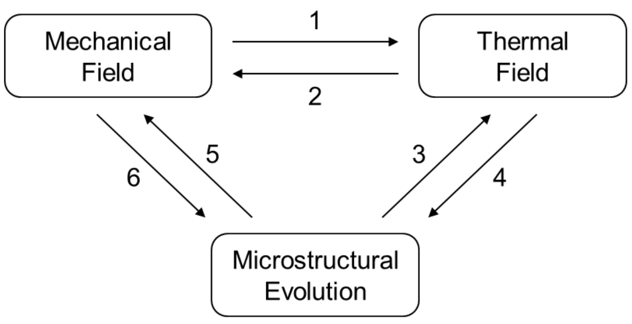

1. Thermal boundary conditions depend on deformation and heat generation due to plastic deformation.
2. Thermal expansion.
3. Thermal material properties depend on microstructure evolution and latent heat due to phase transformations.
4. Microstructure evolution depends on temperature.
5. Mechanical properties depend on microstructure evolution.
6. Phase transformations depend on stresses and strains.

Figure 25. Couplings between mechanical field, thermal field and microstructure evolution, adapted from Bergman [68].

The heat transfer between the blank and tooling is critical in determining the cooling rate of the blank as it is formed and quenched. It is therefore necessary to understand thermal mechanisms and interactions that occur during the process. At the microscopic level, the surface of both the blank and tool are not flat, rather they are comprised of peaks and valleys of varying depth (Figure 26). In areas of direct contact, between the blank and tool, the governing heat transfer mode is conduction; however, in areas where a gap exists heat transfer is governed by radiation and conduction through quiescent air, which are associated with lower heat transfer rates than direct conduction. Increasing the pressure between the tool and blank causes the surfaces to deform, flattening them out, which creates better contact. When the forming process is simulated numerically the interface between the blank and tooling is not modelled directly; instead, a heat transfer coefficient (HTC) is used to encompass all of the heat transfer modes that exist. Extensive research has been conducted by Chang *et al.* [69], Bosetti *et al.* [70] and George *et al.* [25] to determine the interfacial HTC for hot stamped blanks, which demonstrates the dependency of HTC on the contact pressure.

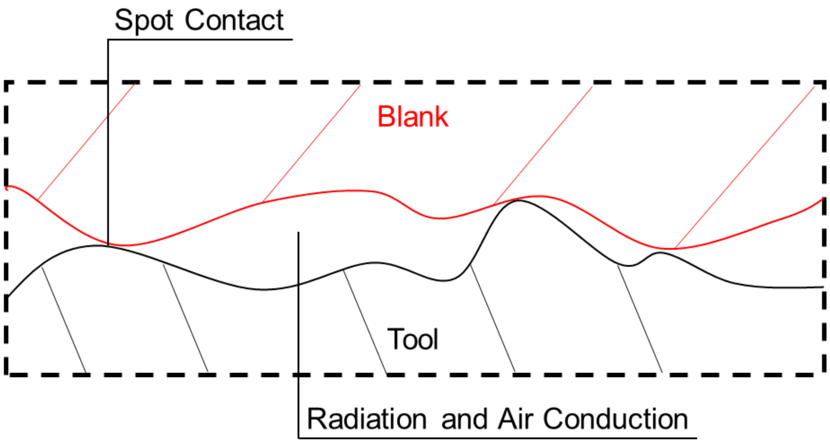

Figure 26. Schematic of the contact surface between tooling and blank at the microscopic level.

Another important parameter used in modelling the forming process is the coefficient of friction between the tooling and blank. If the coefficient of friction in the model is too high, blank thinning will be over predicted, whereas if the coefficient of friction is too low blank thinning will be under predicted. Azushima *et al.* [71] used the strip drawing test on Al-Si coated 22MnB5 hot stamping steel in both lubricated and dry conditions. The coefficient of friction was found to be 0.2-0.35 and 0.55, in the lubricated and dry conditions, respectively.

1.5.2 Hot Stamping Material Models

The material model required for hot forming simulations is far more computationally expensive and complex due to the temperature and microstructure dependency. In LS-Dyna, Olsson [72] implemented *MAT_244, which is based on scientific work done by Åkerström [57]. The hot stamping steel material model includes four phase transformations: austenite-ferrite, austenite-pearlite, austenite-bainite and austenite-martensite. The latent heat, transformation induced plasticity and plastic effects are also captured in the UHSS material model. The set of equations which model the austenite decomposition into its daughter phases, developed by Åkerström *et al.* [73] can be written as,

$$\dot{X}_k = F_G F_C F_T F_{X_k} \tag{8}$$

where $\dot{X}_k$ is the rate of the normalized phase evolving (k being one of the phases ferrite, pearlite or bainite), F_G is the effect of austenite grain size, F_C is the effect of chemical composition, F_T is a function of temperature and F_{X_k} is the effect of the current normalized fraction formed. The true volume fraction of each phase is denoted by x_k and written as,

$$x_k = x_1\left(1 - e^{-\alpha(T_s - T)}\right) \tag{9}$$

where x_1 is the volume fraction of retained austenite from previous reactions, α is a material dependent constant and $T_s - T$ is the undercooling below the starting temperature of the transformation of concern.

The final Vickers hardness of the blank is calculated by a weighted average of each particular phase's Vickers hardness (HV), as developed by Maynier *et al.* [74]. The formula is as follows,

$$HV = X_b HV_b + X_f HV_f + X_p HV_p + X_m HV_m \tag{10}$$

where X is the volume fraction of the particular phase and the subscripts b, f, p and m denote bainite, ferrite, pearlite and martensite, respectively.

George *et al.* [25] used the hot stamping material model in LS-Dyna, *MAT244 to simulate the tailored IDH hot stamping of a Usibor® 1500-AS B-pillar. Through using this hot stamping material model they were able to predict the Vickers hardness and microstructure of the formed part with relatively good accuracy to the experiments. Omer *et al.* [16] altered the hot stamping material model by calibrating the activation energies, which are used to calculate the rate at which the austenite phase decomposes. They were then able to use the model to accurately predict the Vickers hardness of top hat channel, axial collapse specimens for various tailored IDH conditions. Prajogo [60] expanded on this by applying the hot stamping material model to top hat channel flanges for the purpose of three-point bend testing.

A competing forming software, AutoForm has their own hot stamping material model, which has its phase transformation kinetics based off of the work by Merklein and Svec [17]. In this model, a transformation kinetics modelling approach accounts for deformation temperature, cooling rate, true strain and strain rate. The simulation of a hot stamped TWB B-pillar was performed by Graff *et al.* [75] using AutoForm as a simulation tool. In this study they were able to analyse the effect of hot forming process conditions such as press velocity and blank material thickness.

1.5.3 Simulation of the Crash Response of Hot Stamped Components

Crash simulation is a very important part of the vehicle design cycle because it allows for potential safety related issues to be recognized prior to expensive full vehicle testing commencing. The most popular commercial FE package for solving crash problems is the LS-Dyna explicit solver, which uses an explicit dynamic scheme to integrate the equations of motion. In the explicit solving scheme the critical time step (Δt_{min}), or maximum time step that can be taken in order to maintain stability is given by the Courant-Friedrichs-Levy condition.

Axial crush simulations using the double hat channel geometry have been modelled by Omer *et al.* [56], Prajogo *et al.* [76] and Tummers *et al.* [77] for the tailored IDH material condition of Usibor® 1500-AS. Similar modelling was done by Peister [19] for tailor welded blank conditions consisting of Ductibor® 500-AS laser welded to Usibor® 1500-AS. In all of these axial crush simulations a 2.5 mm mesh of fully integrated shell elements with 7 though thickness integration points was used. A fold initiator 4 mm deep was located 65 mm from the free end of the crush rail to promote sequential folding. The last 50 mm of nodes on the mounted end of the rail were fully constrained, while the free end was tied to a rigid boss assembly. The boss assembly is impacted by a rigid plate with initial velocity 10.6 ms^{-1} and mass 855 kg.

An S-rail geometry was numerically simulated by Peister *et al.* [78] to represent a simplified front side rail component, as illustrated in Figure 27. A 5 mm fully integrated quadrilateral shell element mesh with 7 through thickness integration points was used. The rail was sectioned into two distinct zones: an axial zone comprised of Ductibor® 500-AS and an S-rail zone comprised of Usibor® 1500-AS. A fold initiator was located at the free end of the rail in the axial zone to promote sequential folding. An initial velocity of 10.6 ms^{-1} and sled mass of 855 kg were prescribed to the rearmost 75 mm of nodes on the s-rail section, which caused the rail to impact a stationary rigid wall. A numerical parametric study was performed on the aspect ratio of the rail's cross-section, which concluded that with only changing the aspect ratio, sequential folding of the axial zone and intrusion resistance in the S-rail section could not be achieved. Upon changing the thickness ratio between the axial zone and S-rail section they found that as the S-rail section thickness increased relative to the axial zone sequential folding and intrusion resistance could be achieved.

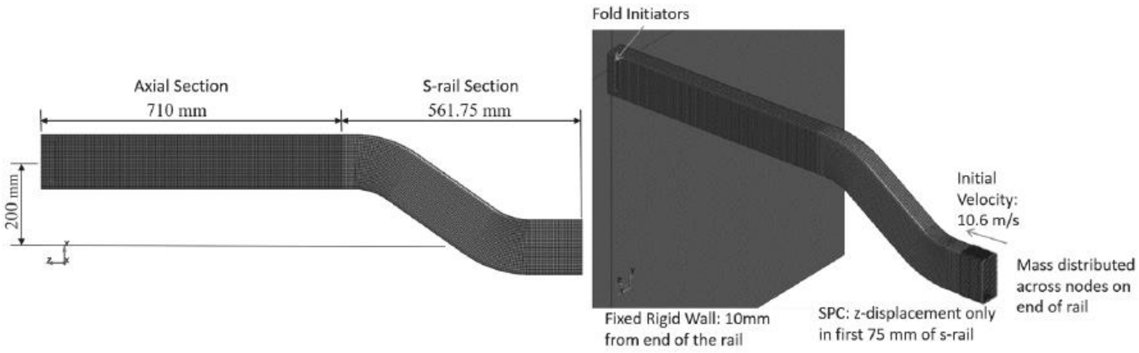

Figure 27. S-rail geometry and the boundary conditions imposed on it, from Peister *et al.* [78].

Peister [19] performed a numerical study on a production front side frame member crush tip made from 1.4 mm JAC590R. The purpose of the study was to assess whether like-gauge, hot stamped Ductibor® 500-AS could be a replacement for JAC590R. The side frame member crush tips were modelled using 5 mm fully integrated shell elements with 5 through thickness integration points. The first three rows of nodes across the part cross-section, located 340 mm from the impacted end were fully constrained to simulate being welded onto a steel plate. The crush tip is then impacted by a rigid plate with initial velocity of 7.5 ms^{-1} and mass of 855 kg. Figure 28 shows the comparison between the production JAC590R crush tip and the replacement Ductibor® 500-AS crush tip. It is quite clear from these images that the crush modes between the two alloys are very similar. Furthermore, the crush forces and energy absorptions predicted for the two were almost identical. From these observations, Peister was able to recommend Ductibor® 500-AS as a suitable replacement for JAC590R.

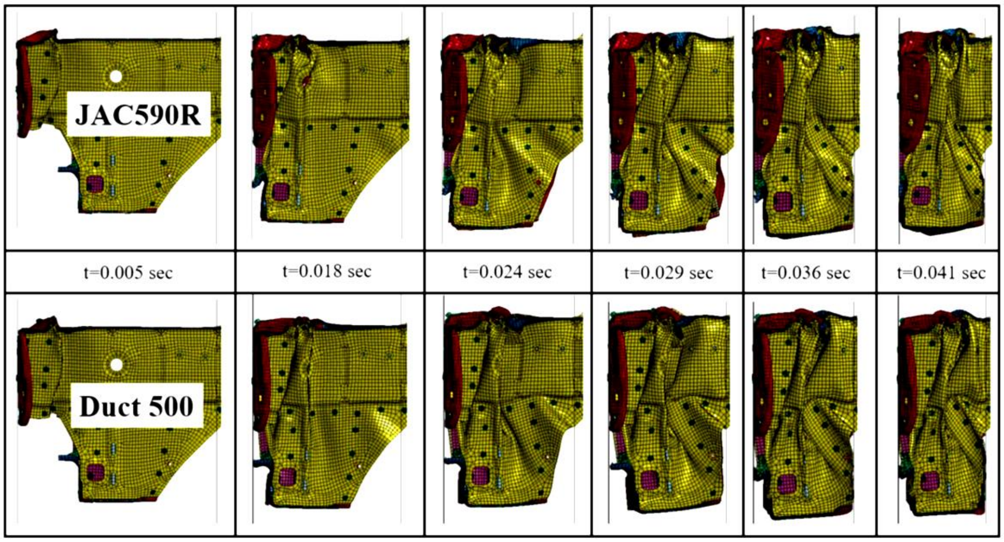

Figure 28. Comparison of the crush mechanics predicted for the production JAC590R crush tip and hot stamped Ductibor® 500-AS crush tip, from Peister [19].

1.5.4 Material Modelling of Tailored Hot Stamped Steel

The material models for tailored hot stamped steels are complex to develop because the material is not homogeneous throughout. In the case of tailored IDH hot stamping, the phase composition of ferrite, pearlite, bainite and martensite in each element must be known as the constitutive response varies with the hardness of the phase present. When using TWBs as a tailoring technique, the phase composition at each element is not as important to be known because the materials are being fully quenched. Information regarding the phase composition and Vickers hardness of each element would come from a forming model using commercial FE codes such as LS-Dyna or AutoForm.

A model known as the Tailored Crash Model (TCM) was developed by Bardelcik *et al.* [79] to characterize the strain rate-sensitive constitutive response of quenched Usibor® 1500-AS. The model approximates the flow stress curves based on the Voce hardening response and is a function of the true strain, strain rate and the Vickers hardness level. This model however only accounts for phase compositions of martensite and bainite, which led Bardelcik *et al.* [15] to develop of the Tailored Crash Model II (TCM II) that also accounts for ferrite in the microstructure. The TCM II model is a function of the area fraction of martensite, bainite and ferrite in the microstructure, instead of Vickers hardness level as in the TCM. Omer *et al.* [56] expanded on the TCM II with the extended TCM (eTCM), which uses an inverse modelling approach to determine the post-necking material response. The constitutive response of a particular elemental hardness is interpolated from three flow stress curves of varying hardness levels.

In high strength materials with low ductility it is crucial to include a failure criterion to accurately predict the crash response of the material. The Generalized Incremental Stress-Strain Model (GISSMO) [80] is a stress-state dependent failure criterion that uses an incremental approach to calculate the damage parameter (D) according to the following formula,

$$\Delta D = \frac{n D^{1-\frac{1}{n}}}{\varepsilon_f(\eta, \xi)} \Delta \varepsilon_p \tag{11}$$

where ε_f is the failure strain as a function of triaxiality (η) and lode parameter (ξ), n is the material dependent damage exponent and $\Delta\varepsilon_p$ is the change in plastic strain. Initially the damage parameter is set to zero and accumulates according to Equation 11. When the damage parameter equals one, the associated element is deleted from the FE model, signifying fracture.

Fracture models (fracture *loci*) are used to determine the failure strain at a given triaxiality and normalized Lode angle parameter ($\bar{\theta}$), given by,

$$\bar{\theta} = \frac{1 - 6\theta}{\pi}, \quad 0 \leq \theta \leq \frac{\pi}{3} \tag{12}$$

Numerous fracture models have been presented in the literature and an example of one such fracture model developed by Bai and Wierzbicki [81] is given by,

$$\hat{\varepsilon}_f(\eta, \bar{\theta}) = \left[\frac{1}{2}\left(D_1 e^{-D_2 \eta} + D_5 e^{-D_6 \eta}\right) - D_3 e^{-D_4 \eta}\right]\bar{\theta}^2 + \frac{1}{2}\left(D_1 e^{-D_2 \eta} - D_5 e^{-D_6 \eta}\right)\bar{\theta} + D_3 e^{-D_4 \eta} \tag{13}$$

where the six parameters D_1, D_2, D_3, D_4, D_5 and D_6 need to be calibrated from at least six different fracture calibration tests. Calibration of the Bai and Wierzbicki fracture criterion was done for Usibor® 1500-AS in five different IDH quench conditions by ten Kortenaar [13], as shown in Figure 29. The test specimen geometry used to calibrate the model include: uniaxial tensile, notched uniaxial tensile, hole tensile, hole expansion, hemispherical domes, plane strain domes, butterfly and mini shear.

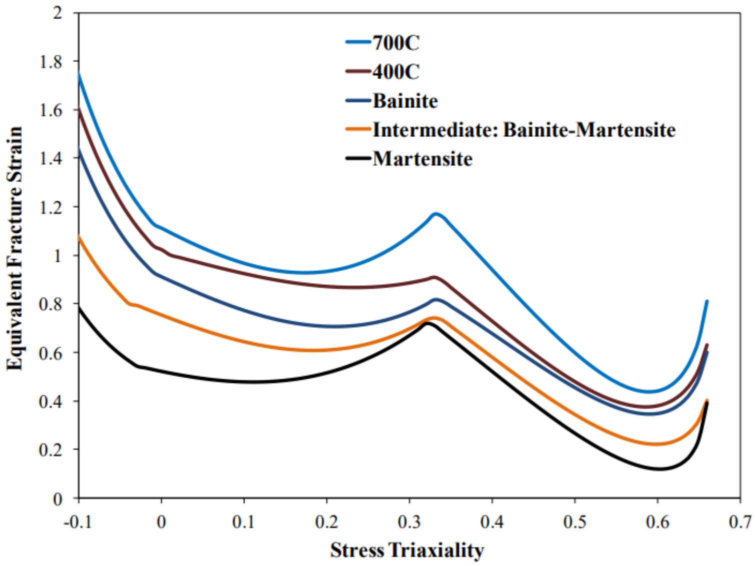

Figure 29. Fracture *loci* for Usibor® 1500-AS in five different quench conditions show higher fracture strain for softer material conditions, from ten Kortenaar [13].

Failure curves are often calibrated using fine meshes (less than 1.0 mm), however most industry applications require the use of coarser meshes (greater than 1.0 mm). Eller *et al.* [59] demonstrated that plastic strain does not accumulate as quickly in larger elements as it does in smaller ones (Figure 30a), so it is therefore required that a mesh regularization scheme be implemented. The fracture curves are scaled as a function of mesh size (Figure 30b) to accurately predict failure, especially in necking zones, where high strain gradients are found.

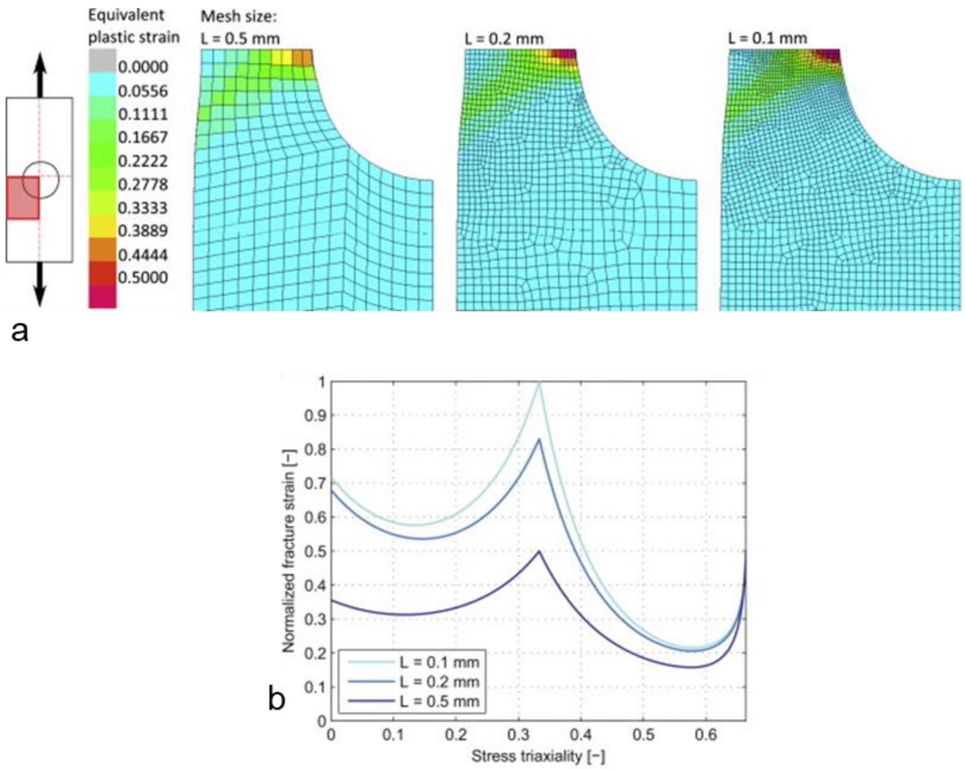

Figure 30. (a) Mesh size dependent strain field of the uni-axial fracture test, showing the difference of accumulated plastic strain with mesh size. **(b)** Calibrated fracture models for different mesh sizes. Adapted from Eller *et al.* [59].

1.5.5 Resistance Spot Weld Modelling

The most commonly used joining method in automotive sheet metal structures are resistance spot welds. It is therefore important that spot welded joints between sheet metal structures be modelled accurately, but with relatively inexpensive computational models for full-vehicle crash analysis. The simplest and computationally least expensive method is inserting a rigid link to connect adjacent thin shell element sheets at the location of a spot weld; however, this method requires different sheets to be aligned, which is not feasible in complex models. A more robust method that also allows for spot weld failure is to use spot weld beam elements with the *CONTACT_SPOTWELD contact definition to tie the spot weld elements to the thin shell mesh sheets. This method creates a spot weld definition that is independent of the surrounding sheet metal mesh and can be represented as solid hexahedral elements using the *CONTROL_SPOTWELD control card. Another method is mesh-dependent hexahedral elements that share nodes to adjoining shell elements and according to Lee *et al.* [82] captures both interfacial and button pullout weld separation modes.

Solid hexahedral elements used to represent spot welds can consist of 1, 4, 8 or 16-Hex element configuration, as illustrated in Figure 31. By modelling a spot weld in shear, Malcolm and Nutwell [83] found the internal forces of the 8-Hex spot weld were within 1 percent of the 16-Hex configuration, indicating that the refinement of eight elements for a spot weld was sufficient. They concluded that beam and single hexahedral element spot welds should not be considered if a resultant force failure method is used.

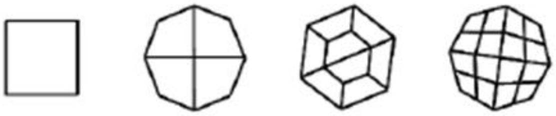

Figure 31. Hexahedral spot weld mesh refinement ranging from 1-Hex to 16-Hex configurations, from Malcolm and Nutwell [83].

1.6 Current Work

In reviewing the literature on the current state of the art it is evident that the hot stamping process has been well researched and already benefits from an abundance of knowledge. Automotive manufacturers have demonstrated an understanding of how to successfully implement fully martensitic components into intrusion resistant crash structures, such as B-pillars, for the purpose of reducing vehicle weight and improving crashworthiness. Hot stampers have shown their capability of controlling the microstructural properties of hot stamped boron steel through tailoring techniques.

Tailoring strategies such as IDH to create local soft zones and TWBs consisting of Ductibor® 500-AS laser welded to Usibor® 1500-AS have been the subject of many numerical and experimental studies. Using these tailoring techniques it has been demonstrated through simplified single component crash tests that hot stamped steels can be made suitable for both axial collapse and occupant compartment intrusion protection.

Automotive manufacturers have particular interest in higher strength hot stamped materials that still exhibit relatively high levels of ductility, such as Ductibor® 1000-AS. The high strength of this material is attractive because it allows automotive manufacturers the ability to down-gauge the sheet metal, while maintaining structural functionality. Down-gauging sheet metal structures is an important exercise that auto makers must undertake in order to light weight their vehicles. This thesis will examine the potential weight savings, through sheet metal down-gauging, offered by Ductibor® 1000-AS when it is applied to replace a 590 MPa strength material such as JAC590R.

There exists a need on the part of automotive OEMs to understand the implications of introducing hot stamped materials into frontal crash energy management structures, especially at strength levels of 1000 MPa and greater. Hot stamped materials have been widely accepted for use in side impact structures due to their high strength and resistance to collapse, ultimately protecting from intrusion. However, the low ductility associated with fully martensitic hot stamped materials have deterred crash engineers from their use in frontal impact structures. The goal of this thesis is to assess the potential of hot stamped Ductibor® 1000-AS as a light weight material in frontal impact structures. The potential to replace the production (driver's side) JAC590R side frame member, shown in Figure 32, with a TWB component consisting of Ductibor® 1000-AS laser welded to Usibor® 1500-AS will be assessed using a numerical simulation approach.

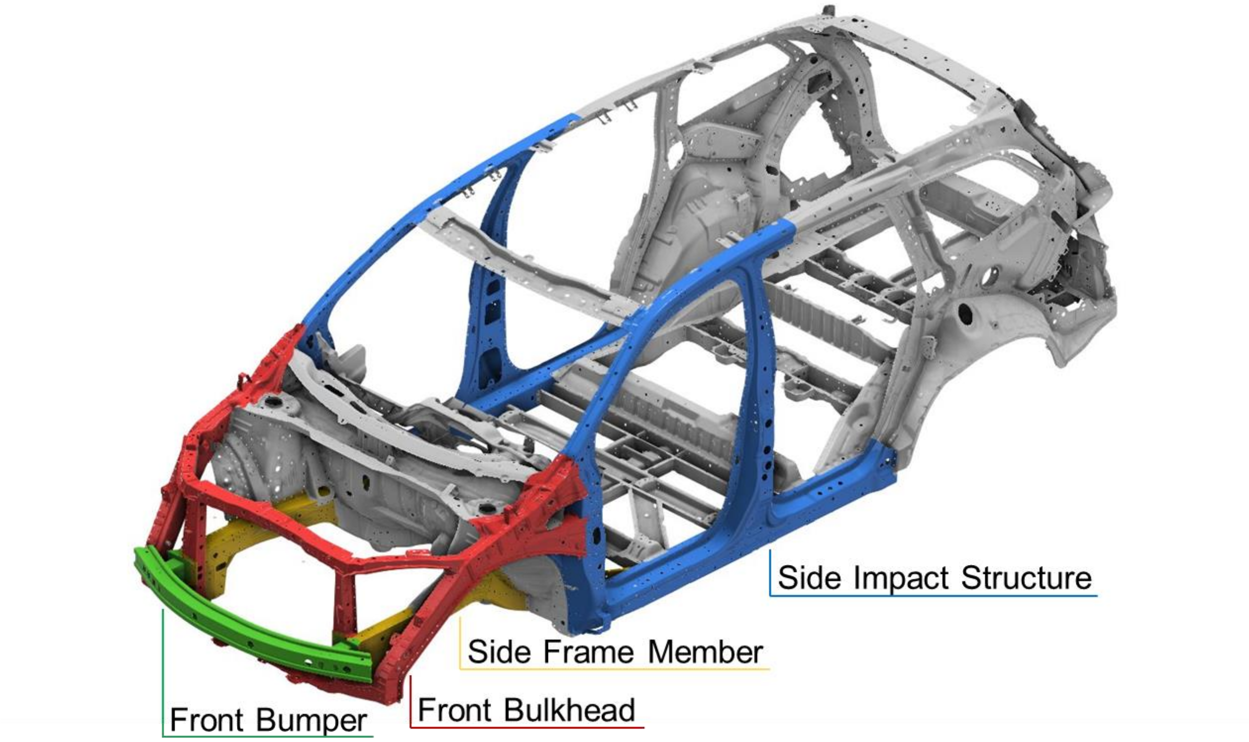

Figure 32. SUV body-in-white structure showing the location of the front bumper (green), front bulkhead (red), side frame member (yellow) and side impact structure (blue).

1.6.1 Scope of Work

The work flow of designing a tailor-welded hot stamped side frame member is outlined in Figure 33, which also highlights the thesis chapters associated with each stage of the design process. The development starts by understanding the crush behaviour of the production side frame member within the full-vehicle SUV model, allowing for the development of a set of requirements the tailor-welded hot stamped side frame member must meet. A number of crash tests exist from the governing crash rating agencies, including: the Insurance Institute for Highway Safety (IIHS), US New Car Assessment Program (US-NCAP) and the Federal Motor Vehicle Safety Standards (FMVSS); however, the scope of this thesis is limited to only evaluating the side frame member in the US-NCAP Full Width Rigid Barrier frontal crash test, due to available project resources.

Full-vehicle crash testing is not feasible in this thesis project and therefore a simplified assembly level structure must be developed. The intention of this assembly is to accurately represent the crash performance of the SUV model side frame member (driver's side), with as little of the body-in-white structure included as possible. It is important to simplify this assembly so that crash sled testing is feasible and within the resources of the project. The SUV model side frame member representative assembly will be termed, "baseline front end module". Through this baseline front end module the production JAC590R side frame member crash performance will be evaluated and compared to the SUV model side frame member.

The tailor-welded hot stamped side frame member is designed based on the boundary conditions imposed from the baseline front end module. The performance of the tailor-welded hot stamped side frame member is numerically evaluated against the production JAC590R side frame member, within the developed baseline front end module, as well as in the SUV model. The objective is to design the tailor-welded hot stamped side frame member with crash response, formability and fabrication in mind.

A large amount complexity is associated with the tooling development and fabrication of the tailor-welded hot stamped side frame member, due to the size and amount of body-in-white components required. Therefore, the scope of the thesis is reduced to only fabricating a portion of the tailor-welded hot stamped side frame member. The section of focus is the tailor-welded hot stamped crush tip.

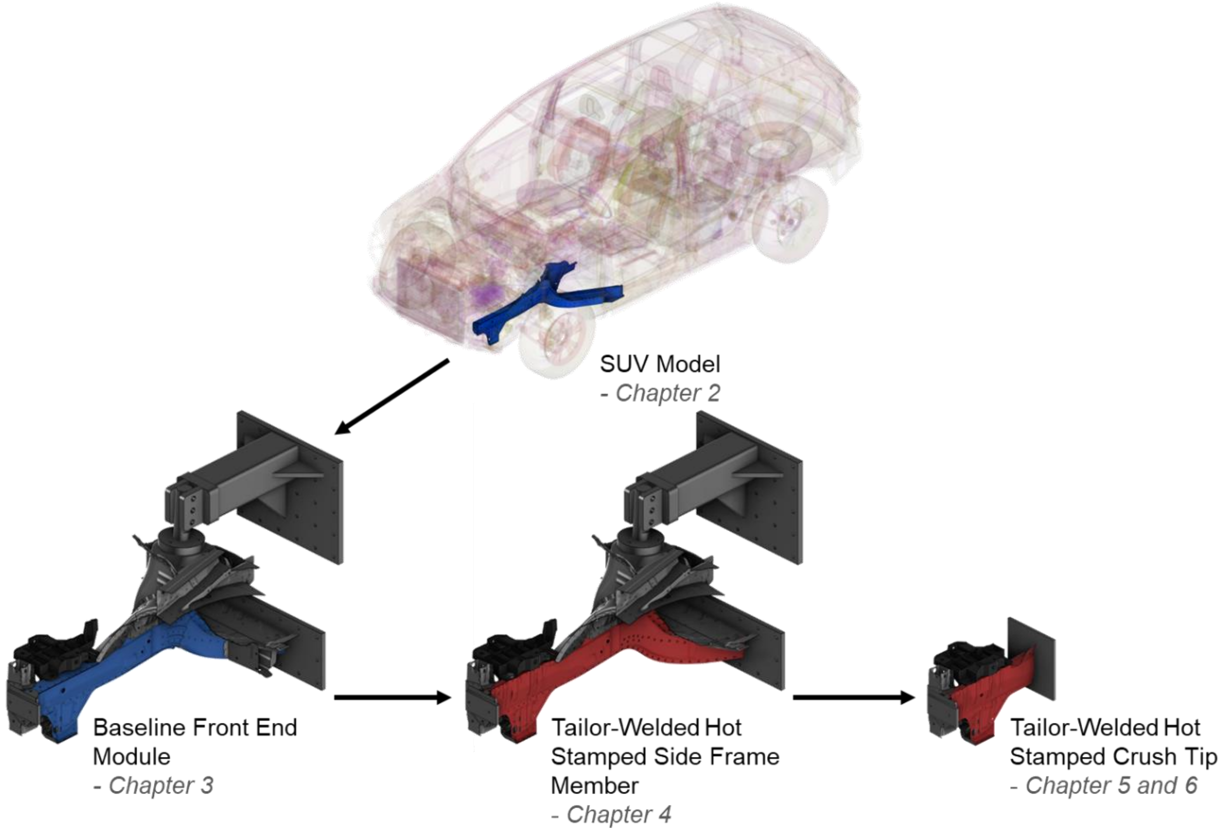

Figure 33. Process flow for developing a tailor-welded hot stamped side frame member.

1.6.2 Thesis Organization

This thesis has been organized into seven chapters to document the development of a tailor-welded hot stamped side frame member. The first chapter comprises this literature review, statement of objectives and scope.

Chapter 2 focuses on establishing design requirements for the tailor-welded hot stamped side frame member from the crush mechanics, vehicle deceleration, crush forces and spot weld failures observed in the US-NCAP Full Width Rigid Barrier full vehicle frontal crash model.

The development of a lab scale assembly to constrain the driver's side frame member for frontal crash testing is developed in Chapter 3. The chapter explains how simulation was used to transition from the SUV frontal crash model to a much less complex structure that could be tested on a component level crash sled while still capturing the relevant loading and structural response of the side frame member. The baseline production side frame member test results are then correlated with the full vehicle model predictions.

In Chapter 4 the tailor-welded hot stamped side frame member design is discussed in detail along with the crash considerations associated with it. The tailor-welded hot stamped side frame member is numerically correlated with the baseline front end module test results and predictions. Additional validation is conducted by inserting the tailor-welded hot stamped side frame member into the SUV model, to make full-vehicle comparisons to the production side frame member.

A plan to simplify the manufacturing and assembly of the tailor-welded hot stamped side frame member is presented in the form of a simplified tailor-welded hot stamped crush tip. The hot stamping process and tailor-welded hot stamped crush tip specimen fabrication are discussed in Chapter 5. The numerically simulated forming process is validated through post hot forming thickness and hardness measurements. The adjustments made to production components during the fabrication of tailor-welded hot stamped crush tips are documented.

Chapter 6 contains the final comparisons of the tailor-welded hot stamped crush tip crash model predictions to the baseline production side frame member. In this section, it is examined whether the hot stamped replacement side frame member meets the design requirements established in Chapter 2.

The thesis is concluded in Chapter 7 with a detailed discussion of the main findings, as well as recommendations made for future work.

Chapter 2 – Side Frame Member Crush Response within the Full-Vehicle – Establishing Performance Criteria

The starting point for developing a tailor-welded hot stamped side frame to replace the production JAC590R side frame member is to understand the crush mechanics at work within the US-NCAP Full Width Rigid Barrier frontal crash model of the SUV. At this stage in the development, it is important that key structural components in the frontal crush structure be examined so their contribution to the overall crash energy management can be assessed. Understanding the underlying mechanics in the crash event allows establishment of performance requirements and criteria that can be used to bound the design space of the tailor-welded hot stamped side frame member development.

The purpose of this chapter is to closely examine the full-vehicle SUV crash model so that a clear set of performance targets can be identified. Note that the actual SUV crash test data was not available for this effort; however, the model was validated against actual crash tests as part of the vehicle development process. The performance targets defined at this stage directly and indirectly affect each stage of the development of the tailor-welded hot stamped side frame member. The design of the demonstrator baseline frontal crash structure or front end module will be driven by the performance targets. The crash results of the baseline front end module will be used as a benchmark for the crash performance of the tailor-welded hot stamped side frame member, which will be evaluated using the front end module used in the baseline study.

2.1 Key Components and Assemblies

Throughout this thesis there are many terminologies used to describe various components and assemblies of the SUV BIW structure. It is therefore quite important to the reader’s understanding that the key components of the BIW be highlighted in this subsection.

Recalling Figure 32 in section 1.6, the SUV BIW has been coloured to illustrate the various crash energy management structures. The crash component of focus in this thesis is the front crush rail or side frame member, depicted in a side view in Figure 34. It is evident from this image that the side frame member contributes a significant fraction of the frontal crash energy absorption. It is also quite clear from Figure 34 that the side frame member is supported by many other sub-structures within the BIW. In this thesis, the side frame member and its supporting sub-structures will be called the “front end module”.

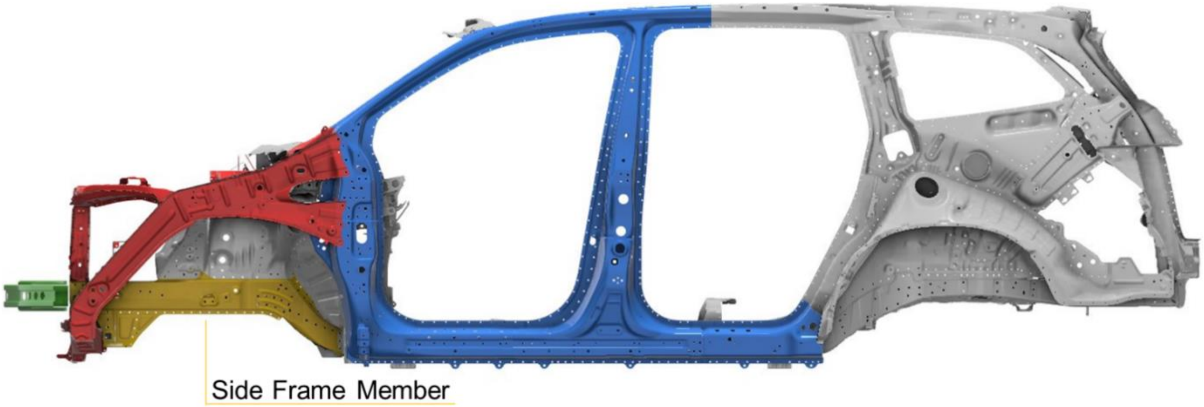

Figure 34. Driver's side view of an SUV BIW structure highlighting the side frame member location within the large structure.

2.1.1 Front End Module

The front end module is the entire sub-assembly which houses the side frame member and provides the support necessary for the side frame member to manage the frontal crash energy. Components relevant to the side frame member are depicted in Figure 35; the structure shown will be referred to as the front end module in this thesis. Only the driver's side half of the front bumper assembly (green) is shown and is attached to the front of the side frame member (yellow) through Metal Inert Gas (MIG) welding of an aluminum crush box onto a bolt-on aluminum plate. The small portion of the front bulkhead (red) shown is spot welded to the side frame member near the front of the crush zone. The shock tower (peach) is spot welded to the side frame member and given extra support through the two shock tower support members, shown in orange. A stiffener (blue) is run through the middle of the rear section of the side frame member for added rigidity. Finally, the additional BIW structures (white) help to support the side frame member during crash loading. In this figure, the floor panel and lower dashboard panel are not shown so that internal components can be seen; however, these two components close off the side frame member S-rail, providing additional stiffness.

The front end module is almost entirely comprised of JAC590R sheet steel with thicknesses ranging from 1 mm to 2.3 mm. Some of the weld-on components that serve non-structural functions are stamped from lower strength materials such as JAC270C and JAC440W. The stiffener that runs along the S-rail section of the side frame member is made from higher strength JAC980Y and has a thickness of 1.6 mm. The relatively high strength and increased thickness of the stiffener provide additional rigidity to the S-rail section of the side frame member, which is where the occupant's feet would reside in the vehicle.

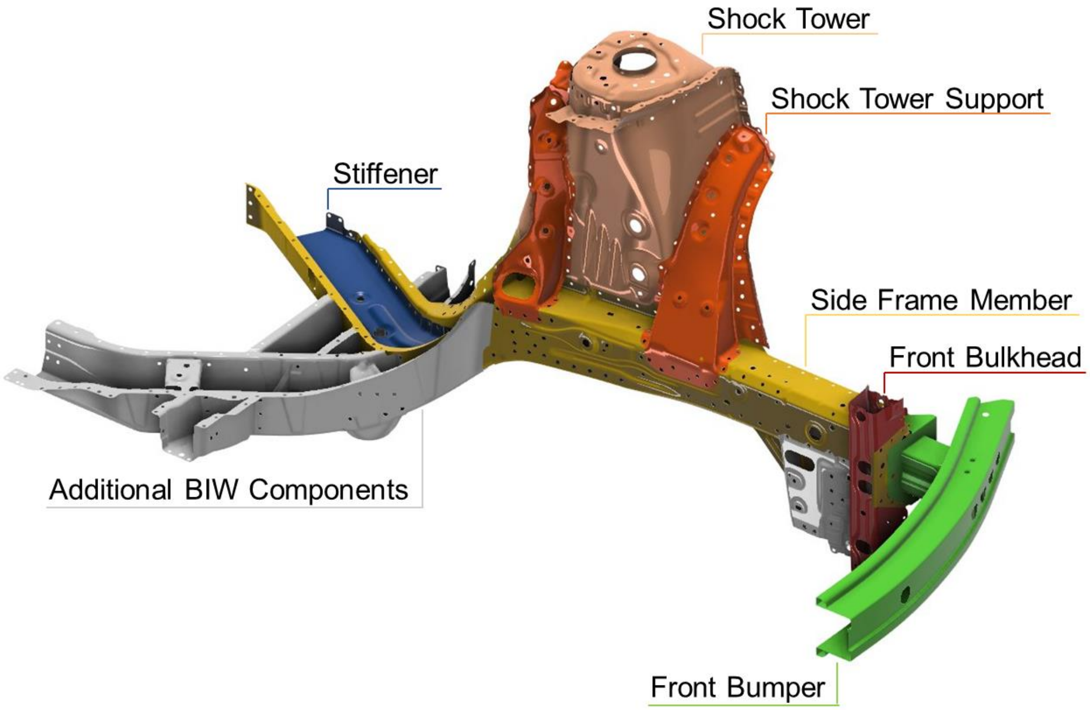

Figure 35. Driver's side front end module highlighting the front bumper (green), front bulkhead (red), side frame member (yellow), shock tower support (orange), shock tower (peach), stiffener (blue) and the additional BIW components (white).

2.1.2 Side Frame Member

The assembly of interest in this high strength material down-gauging study is the side frame member, which is also commonly referred to as the front crush rail. The side frame member from the production SUV is shown in Figure 36, where each distinct zone has been assigned a specific colour scheme and distinct name. The crush tip (yellow) is formed from 1.4 mm JAC590R sheet steel. The side frame member crush tip is where sequential folding occurs during frontal crash and consequently is where majority of the crash energy is absorbed. The middle section (green) is produced from 1.6 mm JAC590R since it must be stiffer than the crush tip. The primary crush mode of the middle section is bending, which is further discussed in section 2.3. The enclosure panel (white) is fabricated from 1.4 mm JAC590R and is used to cap off the crush tip and middle sections. Finally, the S-rail section is the most rigid of all the sections, since it must protect the passenger compartment from intrusion of structural members, and is comprised of 1.8 mm JAC590R. The total mass of the production JAC590R side frame member is 7.6 kg.

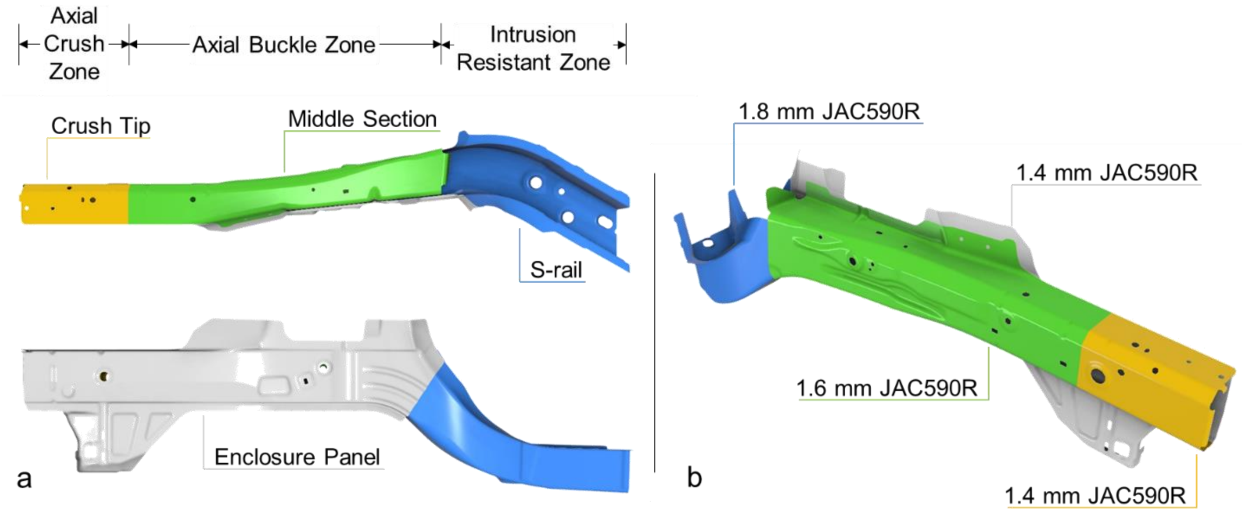

Figure 36. (a) Terminology used to describe the various zones within the side frame member. **(b)** JAC590R sheet steel thicknesses used in each zone of the side frame member.

The internal weld-on components along the length of the side frame member are illustrated in Figure 37. It is observed from this figure that many intricate bulkheads and stiffeners are positioned along the length of the side frame member. The tailor-welded hot stamped side frame member must be designed to interface with each of these internal components.

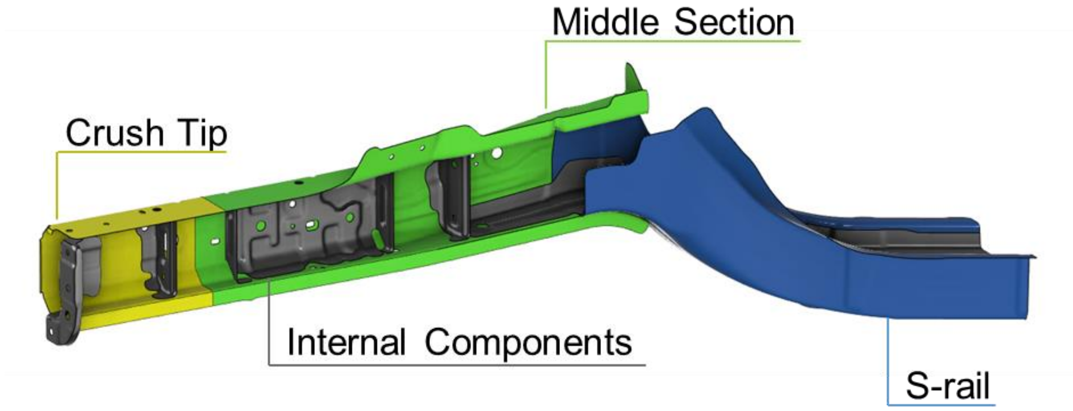

Figure 37. Internal weld-on components along the length of the side frame member.

2.2 US-NCAP Full Width Rigid Barrier SUV Frontal Crash Model

A commercial US-NCAP Full Width Rigid Barrier frontal crash model of an SUV (Figure 38) is used in this thesis. The provided model contains proprietary modelling intellect, and therefore each detail will not be discussed, rather only global boundary conditions applied to the model that are pertinent to the readers understanding of the modelling effort.

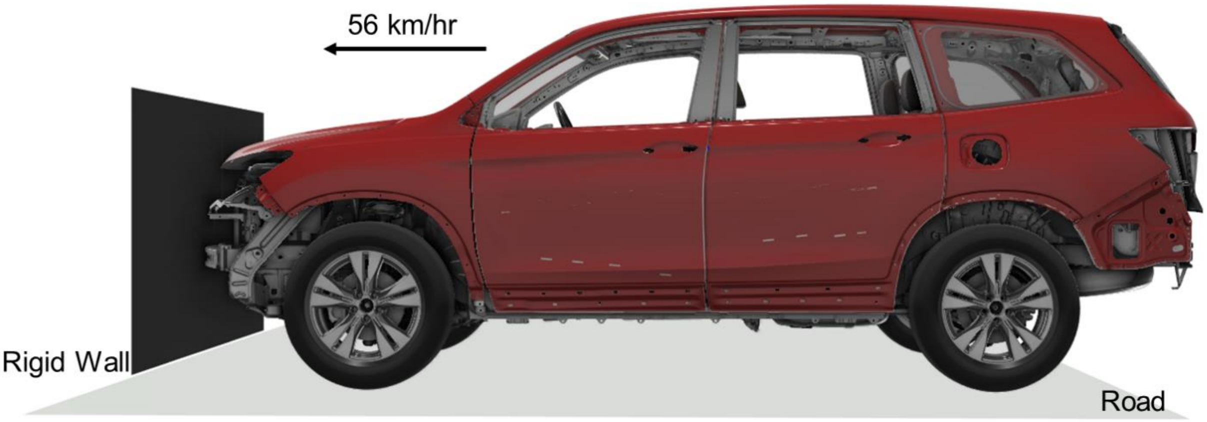

Figure 38. US-NCAP Full Width Rigid Barrier frontal crash model of an SUV at 56 km/hr.

The deformable structural components made of sheet material are modelled with fully integrated, type 16 elements with 5 through thickness integration points. A Flanagan-Belytschko viscous form of type 3 hourglass control is applied to the fully integrated shell elements. The average element size in the model is 3 mm. Non-sheet metal components such as the engine, battery plate, etc. are modelled with single integration point solid elements.

The frontal crash simulation is run to an end time of 0.1 seconds, which allows for all of the kinetic energy to be transferred into plastic work, as well as some elastic recovery to occur. A selective mass scaling factor of 4.6E^{-7} is globally applied to the model. The small selective mass scaling factor only adds mass to solid hexagonal spot weld elements, which are much smaller than the average element in the model.

In the model the vehicle is prescribed an initial velocity of 56 km/hr using the *INITIAL_VELOCITY boundary condition card. The modelled vehicle travels towards a full width rigid barrier wall given the elastic properties of steel. Impact between the rigid barrier wall and the vehicle is possible through the use of the *CONTACT_AUTOMATIC_SINGLE_SURFACE contact card which is supplied a slave part set consisting of all the parts in the vehicle as well as the rigid barrier wall. The single surface contact algorithm looks for contact with differing contacting parts in the slave set as well as self contact within the same part. Important input parameters used in the contact card are provided in Table 2. These parameters include: the static coefficient of friction (μ_S), the dynamic coefficient of friction (μ_d), the coefficient of viscous friction (V_C) and the viscous damping coefficient (V_{DC}). The total force of the vehicle impact with the rigid barrier wall is measured using the *CONTACT_FORCE_TRANSDUCER_PENALTY contact force measurement card, which provides contact forces for the components that come into direct contact with the wall. The vehicle is subject to gravity (9.81 m/s^2) and is constrained from falling by a rigid "road" that is in contact with the tires of the vehicle.

Table 2. Parameters used to define the single surface contact definition in LS-Dyna.

μ_s	μ_d	V_C	V_{DC}
0.15	0.15	177	20

To determine the crush forces acting on the side frame member, cross-sectional planes are defined along the length of the SUV side frame member, as shown in Figure 39. In total, eight cross-sectional planes were positioned along the length of the side frame member. The planes cut through the center of the deformable shell elements and calculate the resultant force transmitted through the plane, which can be used to determine the axial crush force in the side frame member at each plane.

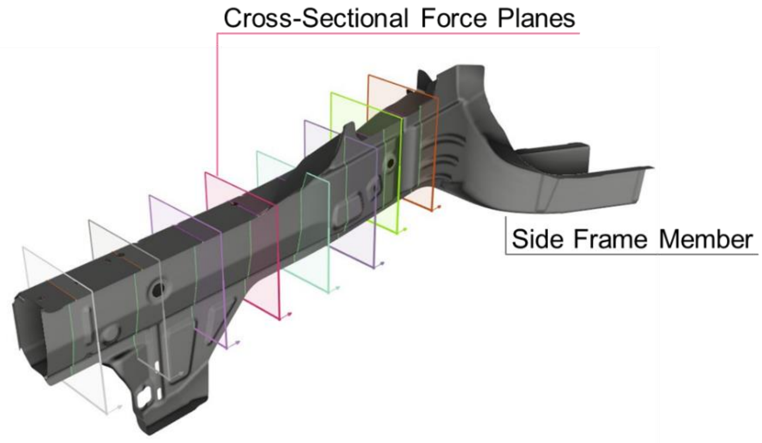

Figure 39. Cross-sectional force planes situated along the length of the side frame member.

2.2.1 Material Modelling

The BIW structure is comprised of many material types, grades and thicknesses; however, the side frame member is made solely from varying gauges of JAC590R. The constitutive properties of JAC590R are proprietary to its owner, but the approach to modelling this material are described in this section.

The JAC590R sheet steel is modelled using an elasto-plastic material model (*MAT_PIECEWISE_LINEAR_PLASTICITY), which is provided stress *versus* strain curves for a variety of strain-rates, to define the hardening behaviour of the material and its strain-rate sensitivity. Though the flow curves for JAC590R used in this model cannot be published, Prajogo [60] published a quasi-static flow curve for JAC590R, as shown in Figure 40. Due to the relatively ductile nature of this material, fracture has not been defined.

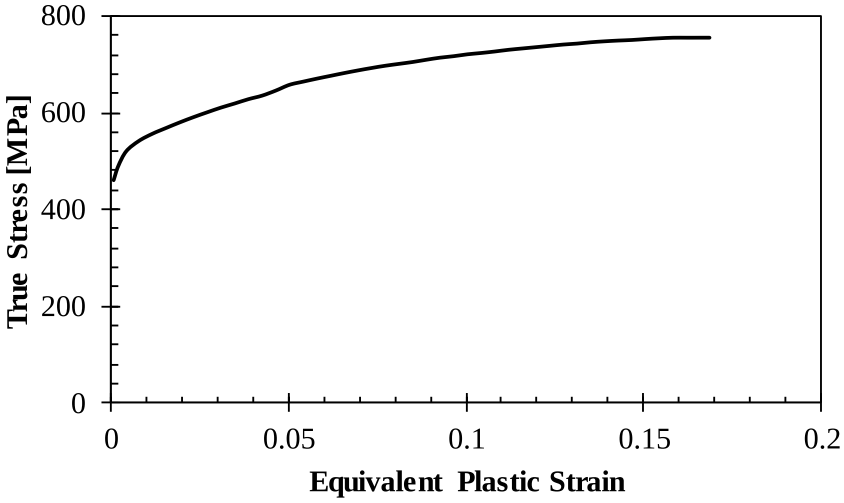

Figure 40. Quasi-static stress-strain curve for JAC590R, from Prajogo [60].

2.2.2 Spot Weld Modelling

Spot welds have been modelled using *MAT_SPOTWELD_DAMAGE-FAILURE spot weld material card, which is a spot weld model available in LS-Dyna. The spot weld material is modelled with isotropic hardening plasticity coupled to a failure model. The failure option selected is OPT = 0, which is a resultant-based failure criterion that fails the weld if the resultants are outside of the failure surface defined by,

$$\left[\frac{\max(N_{rr},0)}{N_{rr_F}}\right]^2+\left[\frac{N_{rs}}{N_{rs_F}}\right]^2+\left[\frac{N_{rt}}{N_{rs_F}}\right]^2+\left[\frac{M_{rr}}{M_{rr_F}}\right]^2+\left[\frac{M_{ss}}{M_{ss_F}}\right]^2+\left[\frac{M_{tt}}{M_{tt_F}}\right]^2=1 \tag{14}$$

The parameters of this equation are best described through observing the depiction of a spot weld and its coordinate system (Figure 41). In Equation 14, parameters denoted with N represent forces and those with M represent moments about a particular axis. From the coordinate system it is clear that subscript r denotes the out of plane or axial loading axis and that s and t denote the in plane shear loading axis. Therefore, N_{rr} is an axial load, N_{rs} and N_{rt} are shear loads, M_{rr} is a torsional moment, and M_{ss} and M_{tt} are peeling moments. In this equation the numerators are the resultants calculated in the local coordinates of the cross section and the denominators with subscript F are the specified input failure load/moment values. The input failure loads and moments are dependent on three variables: the material, sheet thickness and how many connections between sheets there are (number of sheet layers welded together, typically two or three). The SUV frontal crash model and front end module model are comprised of many different combinations of these three variables and therefore the failure loads and moments will not be quantified for each connection. It should be noted that the torsional failure of the weld is suppressed by specifying an exaggerated large number so that failure will never occur due to torsional loading.

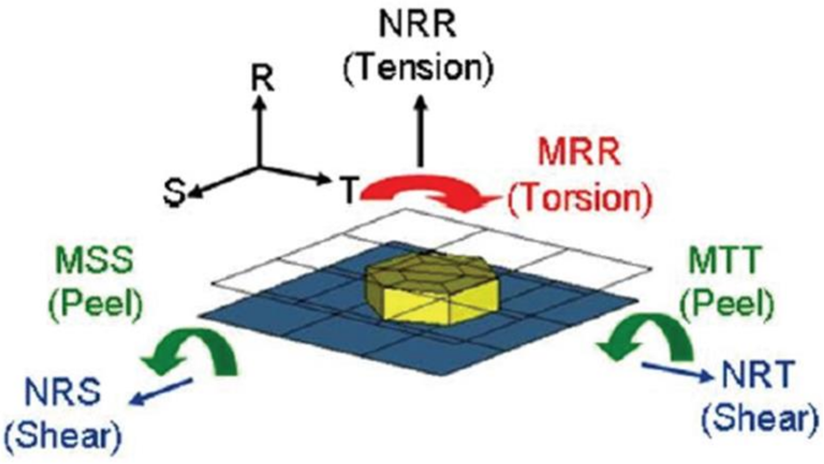

Figure 41. Demonstration of the forces and moments acting on a spot weld along with the coordinate system based on Equation 14, from Malcolm and Nutwell [83].

Upon the failure criterion being met and the failure flag being activated, damage in the spot weld begins to accumulate based on the selected damage option (DMGOPT = 11). The constitutive properties for the damaged material are based on the undamaged material properties. In this damage model the damage variable ω is a function of the effective plastic strain ε_{eff}^{p} in the weld,

$$\omega = \frac{\varepsilon_{eff}^{p}}{\varepsilon_{rupture}^{p}} \tag{15}$$

when the effective plastic strain equals the rupture strain $\varepsilon_{rupture}^{p}$ (where $\varepsilon_{rupture}^{p}$ is specified as 1.5), the damage parameter becomes equal to unity and at this point the spot weld elements are deleted. Deletion of a spot weld elements is analogous to the complete failure of the spot weld.

The spot welds are meshed using eight, single integration point (type 1) solid elements arranged into a hexagonal pattern, as recommended by Malcolm and Nutwell [83] and shown in Figure 42. The spot welds are modelled with mesh dependence, meaning that the nodes of the sheet steel mesh and the hexagonal spot weld elements are coincident. The spot welds are modelled with a true thickness of 1E^{-6} mm, which means that even though they are represented as solid elements that fill the gap between the two sheets, they are evaluated based on the true thickness value. This true thickness is especially important for shear loadings which would create artificially high bending moments if the modelled element thickness was used.

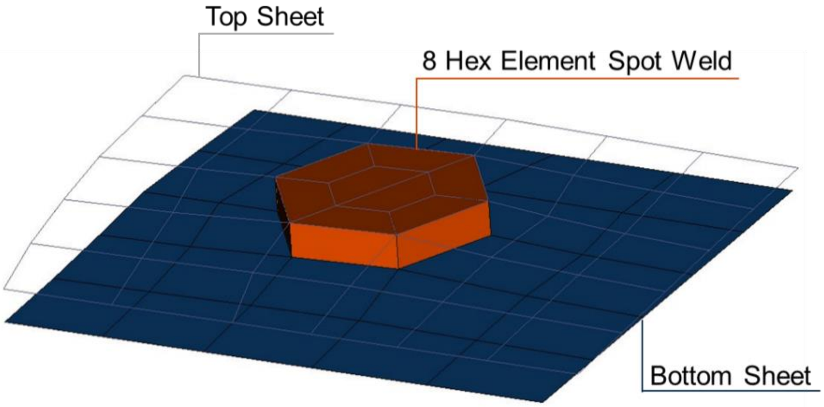

Figure 42. Eight element hexagonal spot weld between two steel sheets, demonstrating the coincidence of nodes between the sheet steel mesh and spot weld elements (mesh dependence).

2.3 Predicted Crush Response

The crush response of the frontal crash energy absorption structure is made up of a combination of axial collapse and bending modes. The frontal impact structure in the SUV absorbs energy and provides passenger compartment intrusion protection by taking advantage of the two crush modes. In the front end module structure, the bulk of the energy absorption is accomplished through the axial collapse mode that occurs during the initial stages of the crush. The bending mode is used to protect the passenger compartment from intrusion of structural members, while absorbing additional energy, and is enabled after the axial collapse mode has reduced the kinetic energy of the vehicle.

The various crush modes observed in the side frame member using the US-NCAP Full Width Rigid Barrier frontal crash model of the SUV are shown in Figure 43. In Figure 43 the driver's side front end module of the SUV has been isolated by hiding surrounding components in the post-processor to better illustrate the crush modes of the side frame member. Before the crash instance, the front end module is shown in its undeformed state at 0 mm of crush distance and has a total kinetic energy of 250 kJ. After the first 160 mm of crush distance the kinetic energy of the vehicle is reduced to 148 kJ. It is observed that the bumper has flattened and the foremost crush tip (see arrow) of the side frame member is fully consolidated and has rotated inboard towards the center plane of the vehicle, which places a rotational moment on the side frame member. At 220 mm of crush distance the kinetic energy of the vehicle is further reduced to 119 kJ and a plastic hinge begins to form in front of the shock tower support (arrow), as the crush tip continues to consolidate. When the crash is progressed further to 300 mm of crush distance the entire crush tip has consolidated. At this point in the crash the axial crush energy absorption mechanisms of the side frame member are largely exhausted and the kinetic energy of the vehicle has been significantly decreased (from 250 kJ to 72 kJ). At this stage, the plastic hinge in front of the shock tower further develops, causing the consolidated crush tip to pivot inboard, creating outward force and bending load on the middle section of the side frame member between the shock tower and S-rail section. The function of this inboard pivot of the crush tip becomes more obvious at 420 mm of crush distance, where the outwards loading caused by the first plastic hinge before the shock tower support creates a new plastic hinge after the shock tower support in addition to the one that forms in front of the S-rail section (two arrows). The purpose of creating these additional bending modes is to transfer the function of the side frame member from largely energy absorption to focusing on protecting the passenger compartment from intrusion of structural members. The reduces the rate of energy absorption but also prevents the rigid S-rail section from being overloaded by the forces transmitted through the side frame member, ultimately ensuring it does not collapse and enter the occupant's seating envelope.

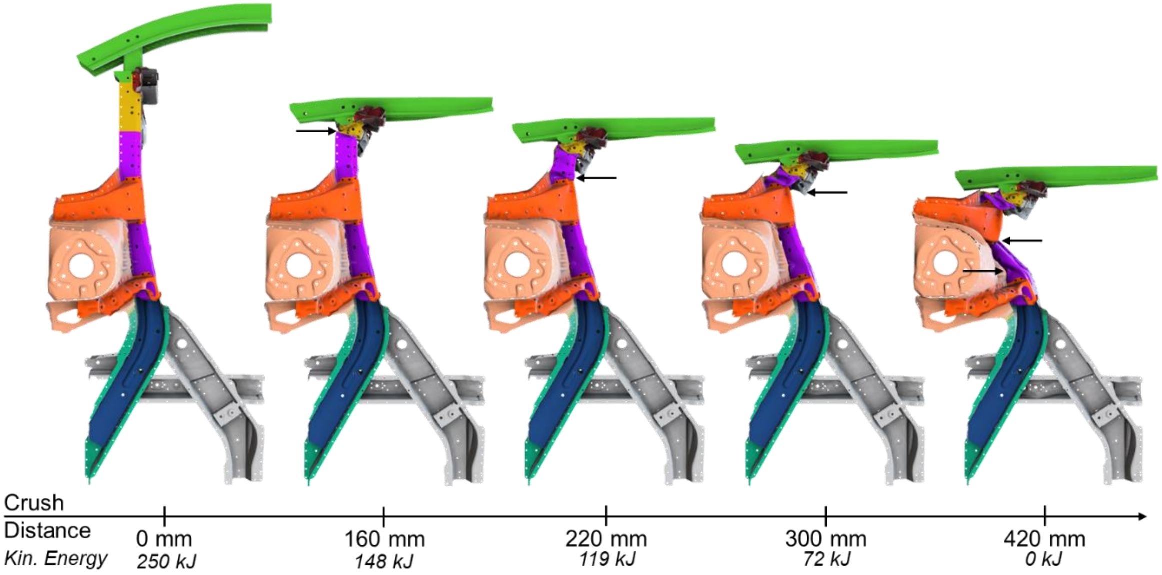

Figure 43. SUV front end module crush modes at various amounts of crush distance. Note that the side front end module has been isolated from the SUV model to better illustrate the crush modes.

It is important to note that there are some complex loading conditions imposed on the side frame member by the SUV bumper structure prior to any appreciable deformations occurring in the side frame member. In Figure 44 it is shown that as the SUV frontal crash progresses, the bumper beam flattens out (as noted by the bumper profile in white), which imposes a load on the side frame member, pushing it to the outboard of the vehicle.

The initial deformation of the side frame member (Figure 45) shows that folding in the crush tip begins by buckling the outboard side of the enclosure panel. The irregular start of the folding on the enclosure panel is attributed to the flattening out of the bumper beam during the initial stages of the SUV frontal crash. The flattening out of the bumper beam puts an outboard shearing load on the bumper crush box, which causes the bumper crush box to initially transmit load to the outboard side of the enclosure panel.

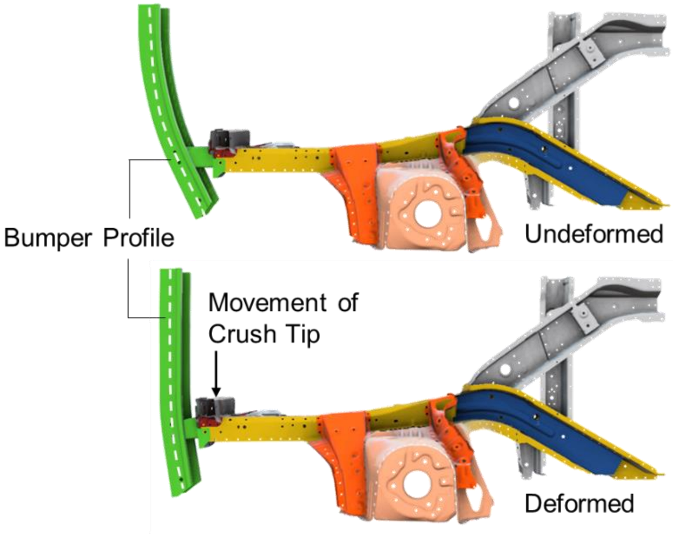

Figure 44. Complex loading created by the flattening out of the bumper beam during the initial stages of the crash event. Both the undeformed (top) and deformed (bottom) side frame members are shown for comparison.

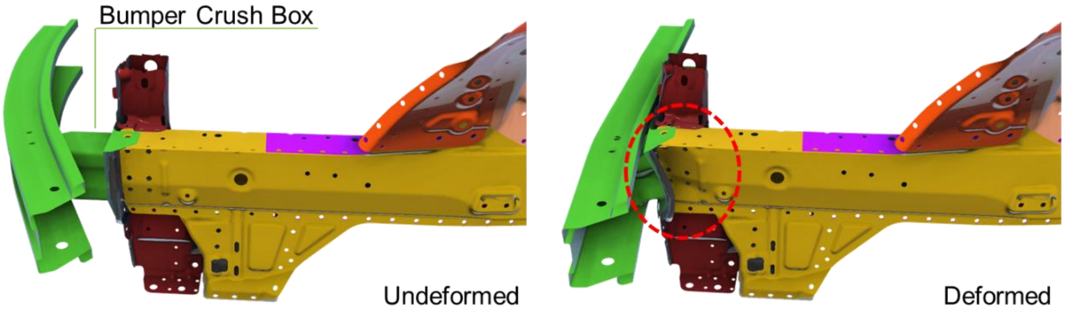

Figure 45. During the initial deformation of the side frame member it is noted that the folding begins on the outboard side of the enclosure panel.

2.3.1 Fold Initiators

The side frame member crush modes identified are initiated through the use of special mechanisms that are directly formed into the rail geometry. These mechanisms take the form of fold initiators that are either oriented to intrude or extrude the cross-section of the rail. The orientation of these fold initiators and the purpose they serve will be described in the following paragraphs.

On the outboard of the side frame member, a fold initiator, extruded outwards from the rail (during manufacturing), is located in the first few centimeters of the crush zone, as seen in the undeformed geometry of Figure 46. The purpose of this early fold initiator, running the width of the side frame member enclosure panel, is to direct the material into controlled sequential folding for optimal kinetic energy absorption in the early stages of the crash, which is observed in the deformed geometry shown in Figure 46.

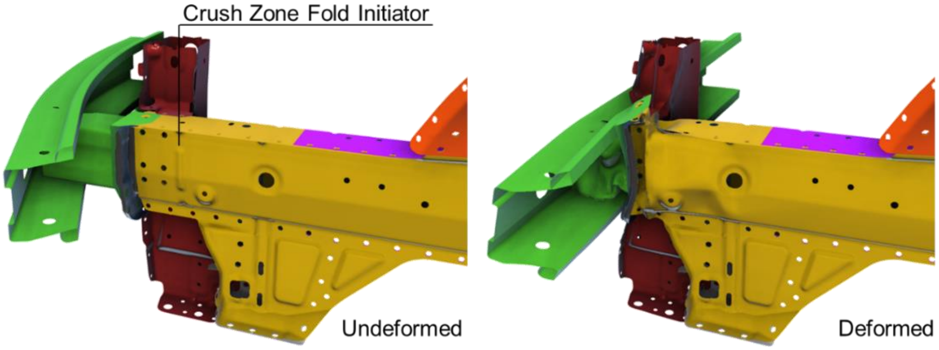

Figure 46. Undeformed (left) and deformed (right) geometry of crush tip fold initiator illustrating controlled fold initiation.

Now moving to the inboard of the side frame member it is noted in the undeformed geometry, shown in Figure 47 that small indentations are made into the corners of the side frame member main rail section. Though relatively small, these indentations are fold initiators that serve the important function of controlling the folding behaviour of the side frame member, inducing preferential sequential folding. In addition, the set of dimple initiators denoted as number 3 in Figure 47 are responsible for creating a bending mode that pivots the side frame member towards the inboard of the vehicle (see Figure 43, 420 mm). The inboard buckle is the first reaction of two that are utilized to protect the S-rail section from being overloaded and intruding into the occupant compartment.

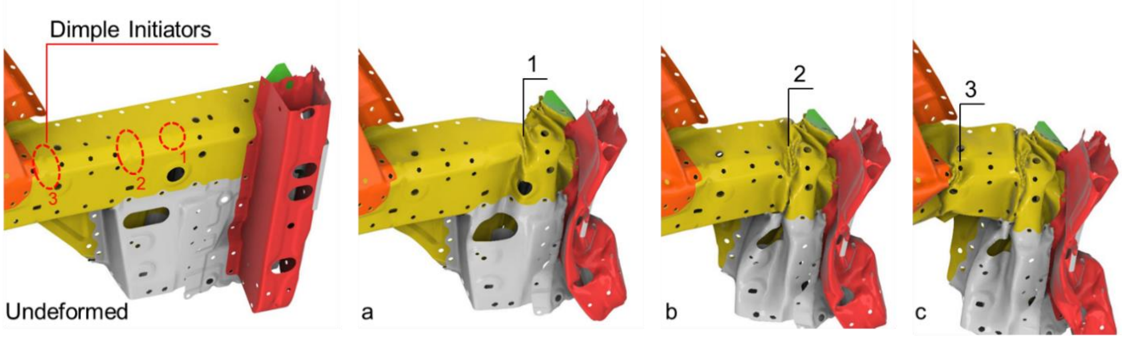

Figure 47. Undeformed geometry of the side frame member’s main rail showing the dimple initiator locations (left). Folds created by the **(a)** first fold initiator, **(b)** second fold initiator and **(c)** third fold initiator during the sequence of the crash event.

A large buckle initiator is located on the outboard of the side frame member, just before the S-rail section, under the shock tower housing, as shown in Figure 48. The buckle initiator creates a local weak point in the side frame member cross-section. Once the loads reach a critical value the buckle initiator will be triggered, creating an additional plastic hinge. The large buckle initiator ensures the occupant compartment remains intact throughout the crash by creating a plastic hinge and preventing the S-rail from being overloaded.

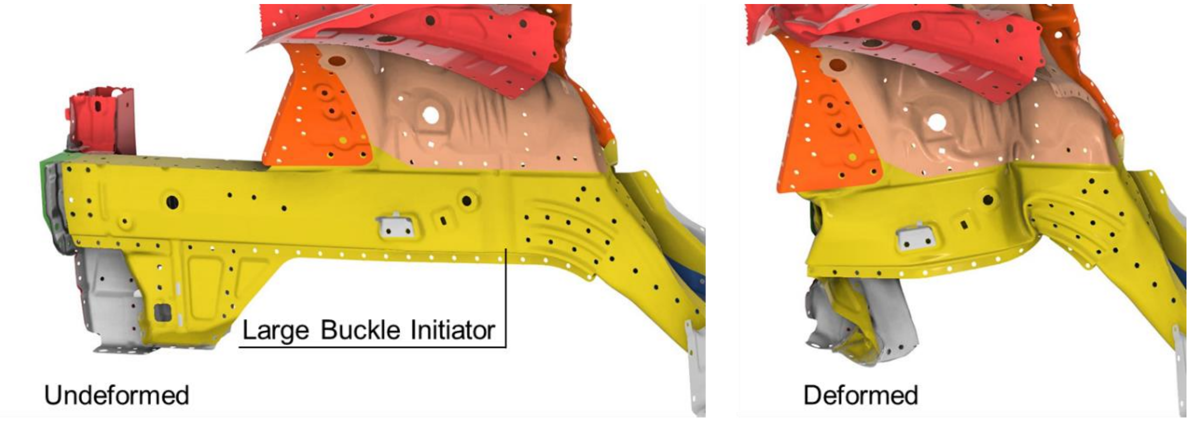

Figure 48. Undeformed geometry (left) of the side frame member illustrating the large buckle initiator. Deformed geometry (right) demonstrates the buckle created in order to protect the S-rail from overloading.

2.4 Vehicle Deceleration

The purpose of the frontal crash structure and more importantly the side frame members are to reduce the speed of the vehicle at a rate safe for the operator and passengers. The materials currently used in the production side frame member (JAC590R) and the hot stamped tailor-welded side frame member (Ductibor® 1000 and Usibor® 1500), to be developed in this work, are strain rate sensitive. This means that their constitutive responses are dependent on the strain rate or speed of deformation in the vehicle at that particular moment in the crash. Therefore it is important that the velocity history of the SUV be considered when determining the requirements for the hot stamped tailor-welded side frame member.

The plot in Figure 49 shows the velocity of the side frame member as a function of its displacement. The velocity of the side frame member was extracted from the SUV frontal crash model by taking an average of the velocity of five nodes at the furthest rearward section of the side frame member and subtracting the average of the velocity of five nodes on the foremost section of the side frame member. The rearmost section of the side frame member is not deformed by the crash and is essentially equivalent to the vehicle speed. The tip of the side frame member has equivalent velocity to the vehicle up until it impacts the wall at which point its velocity becomes zero. Upon subtracting the tip velocity profile of the side frame member from the rear velocity profile, the speed of the side frame member can be isolated. The crush distance is determined in the same way as the velocity, where the displacement of the tip of the side frame member is subtracted from the displacement of the rear. This calculated crush distance difference provides the displacement of the side frame member relative to the vehicle movement.

The plotted velocity illustrates that the speed of the SUV, when the side frame member is first activated, is 51 km/hr. The vehicle decelerates almost linearly from 51 km/hr to 30 km/hr in approximately 300 mm of crush distance. After the first 300 mm of crush, the deceleration increases steadily until the vehicle comes to a stop. The crash incident is completed at 422 mm of crush distance, which is noted by the rapid drop of the vehicle speed to 0 km/hr.

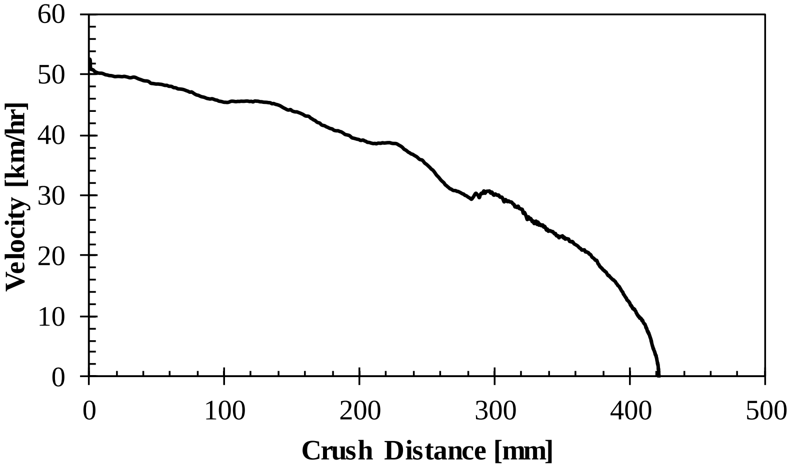

Figure 49. Deceleration profile of the SUV model side frame member plotted as a function of the vehicle crush distance.

2.5 Crush Forces

The crush force has been plotted against the crush distance for each cross-sectional force plane along the length of the side frame member in Figure 50. The crush distance is calculated as the difference between the displacement of the side frame member tip and rearmost points, as explained in the previous section (2.4). In the cross-sectional force plane plots it is observed that the force transmitted through the rail accumulates with each consecutive force plane. It is also pertinent to note that anywhere that the crush force has a peak corresponds to a time during the crash when the deceleration felt by the occupants would increase. Therefore, monitoring the load peaks during the design of the hot stamped tailor-welded side frame member will be critical. In the first three cross-sectional force planes the initial, second and third crush force peaks have been highlighted with an arrow. These three crush force peaks will be used to determine whether acceptable peak forces are measured in the baseline front end module and tailor-welded hot stamped side frame member.

Ultimately, the baseline front end module and hot stamped tailor-welded side frame member must visually match the global crush force trend, as well as the magnitude and location of the peak forces.

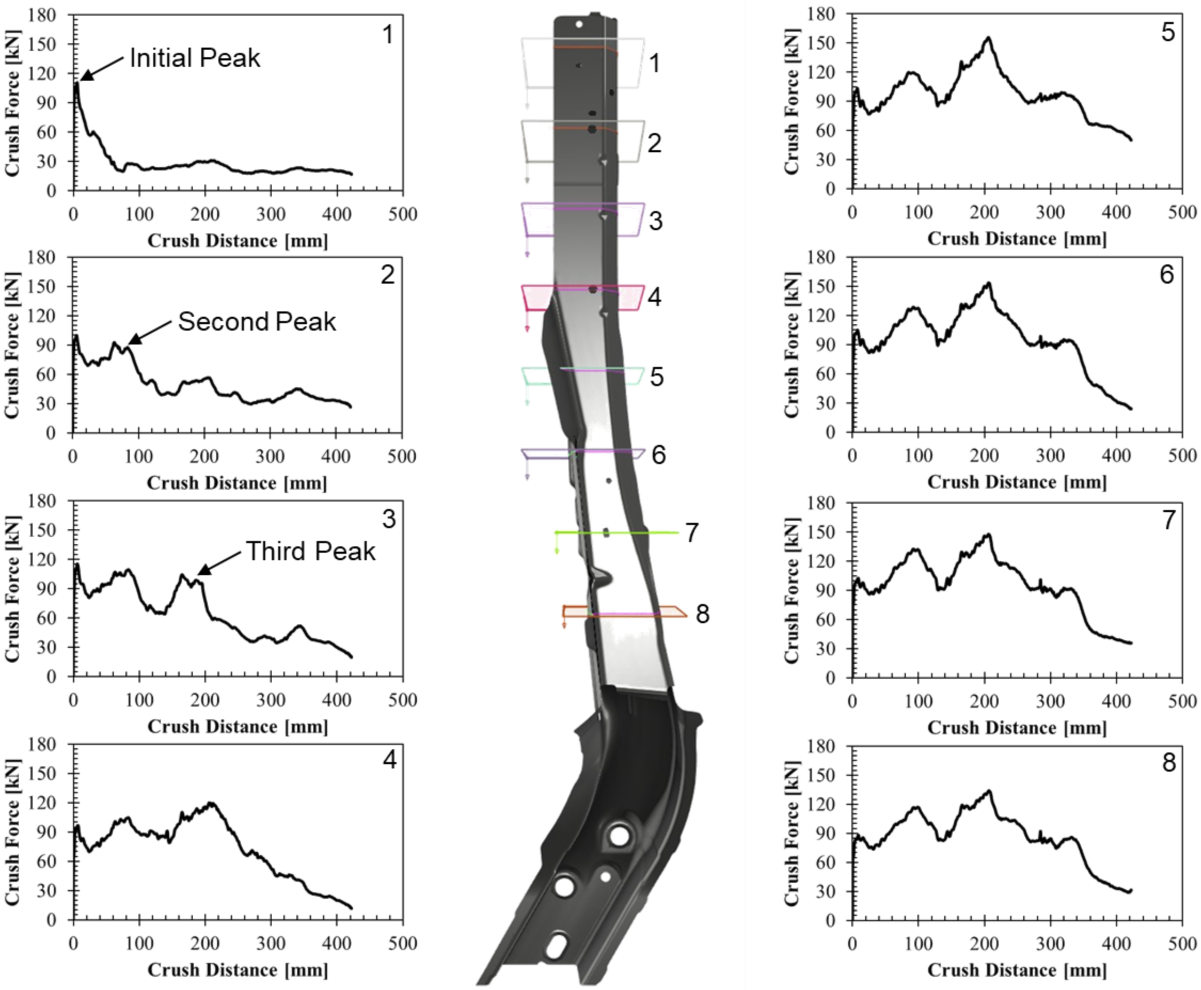

Figure 50. Crush forces in the SUV side frame member calculated with cross-sectional force planes along the length of the side frame member.

2.6 Occupant Compartment Intrusion

One of the major functions of the SUV BIW structure is to safely house occupants within a seating envelope, as illustrated in Figure 51. It is therefore crucial in crash events to limit the amount of intrusion of structural members into the occupant zone. In frontal crash, some of the structural members at risk of intruding on the occupant zone are the A-pillar, dashboard panel, floor panel and S-rail of the side frame member. In this thesis the S-rail will be the only structural member analysed for occupant compartment intrusion, since only the side frame member is being considered in the material down-gauge study. The S-rail of the side frame member is located approximately adjacent to the occupant's feet, so it is critical that intrusions be limited.

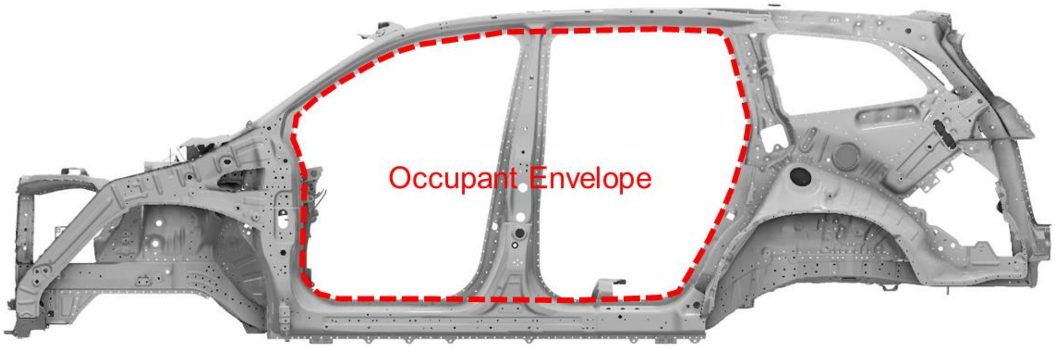

Figure 51. Side view of the BIW structure highlighting the occupant seating envelope.

The displacement of the S-rail is measured from the top of the section (Figure 52) where the largest displacements will be measured. It is observed from Figure 52 that the current production SUV model predicts that the S-rail will displace 25.9 mm along the x-coordinate and 3.0 mm along the z-coordinate. This relatively small amount of intrusion into the occupant zone has been deemed acceptable; therefore, intrusion of the hot stamped side frame member should not exceed this by an excessive amount.

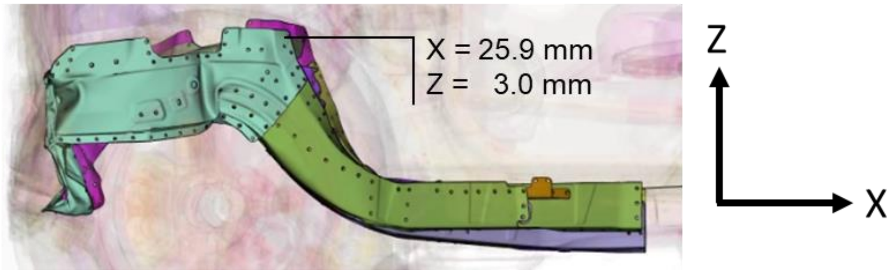

Figure 52. Side view of the driver's side frame member at peak impact showing the amount of intrusion into the occupant compartment.

2.7 Extent of Spot Weld Failure

Spot weld failure is not desired in crash engineering because of the level of uncertainty it brings to the crash response of the assembly. Therefore, it is important that the amount of spot weld failure (if any) occurring in the SUV frontal crash model be assessed to better understand some of the high stress weld locations. Analyzing the weld failure that occurs in the SUV model also provides a target for the acceptable amount of spot weld failure that can occur in the tailor-welded hot stamped side frame member.

The areas of interest for analyzing spot weld failure in the SUV side frame member are the top and bottom flanges of the crush tip. These particular locations exert high loadings, tough on the spot welds during crash, due to the tight folding that occurs in the front rail during axial crush. The spot weld failure parameters are plotted against crush distance for both the top and bottom flanges of the crush tip section of the side frame member in Figure 53 and Figure 54, respectively. It is observed in both the top and bottom flanges of the driver's side crush tip that three spot welds fail in each flange (highlighted with colour). The spot welds shown to fail in the flanges from the SUV model are indicated in Figure 53 and Figure 54 and are denoted as high-stress weld locations. These high-stress weld locations will be closely examined during the baseline and tailored hot stamped side frame member weld failure analysis.

It should be noted that the failure parameter reaching unity does not trigger spot weld element deletion; rather, damage accumulation begins at this point and when the damage parameter reaches unity the elements will be deleted. The failure parameter has been chosen as a metric of quantifying which welds fail (instead of the damage parameter) since failure parameter provides a more condensed analysis of which welds are likely to rupture in the model than viewing the damage parameter of each individual weld element.

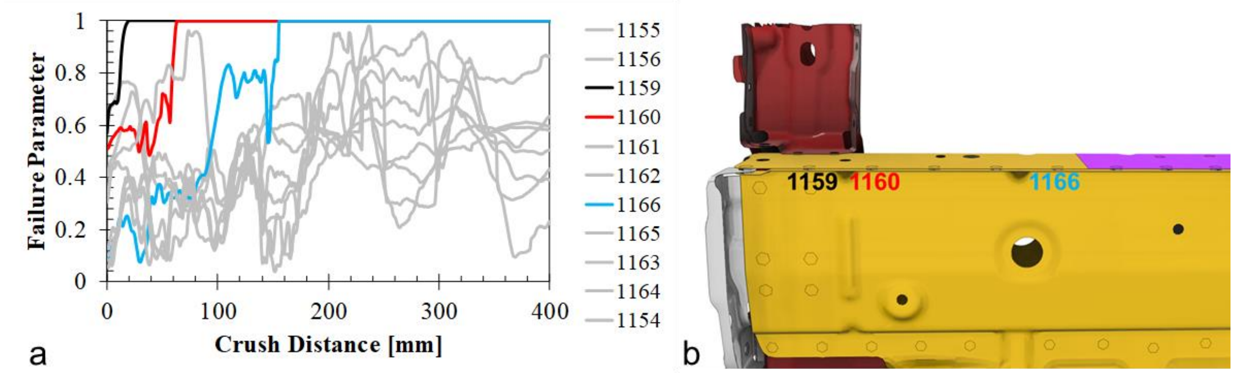

Figure 53. (a) Top flange weld failure parameter shows three welds that undergo failure initiation. **(b)** Close-up of the crush tip shows the location of each spot weld failure initiations by colour.

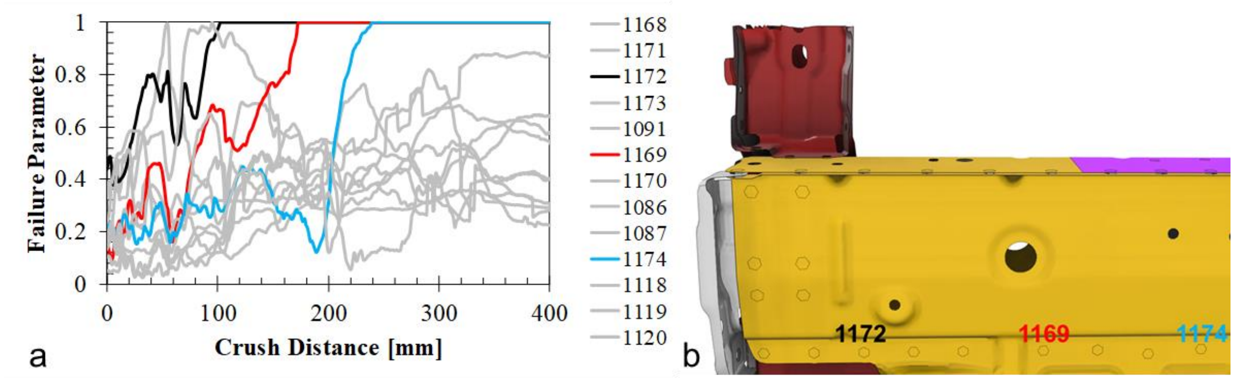

Figure 54. (a) Bottom flange weld failure parameter shows three welds that undergo failure initiation. **(b)** Close-up of the crush tip shows the location of each spot weld failure initiations by colour.

During the folding crush mode, spot welds are subjected to combined loading conditions comprised of axial and shear loading, as well as a peel moment. The loading on each modelled spot weld assembly along the top flange of the side frame member crush tip are shown in Figure 55 for their respective loading condition (axial, shear and peel moment). The respective failure load for a 1.4 mm JAC590R spot weld with two connections has also been plotted for each to demonstrate which loading condition contributes the most to spot weld failure. It is quite clear from these graphs that the dominant loading condition is the peel moment since it comes the closest to its failure load for many different spot welds.

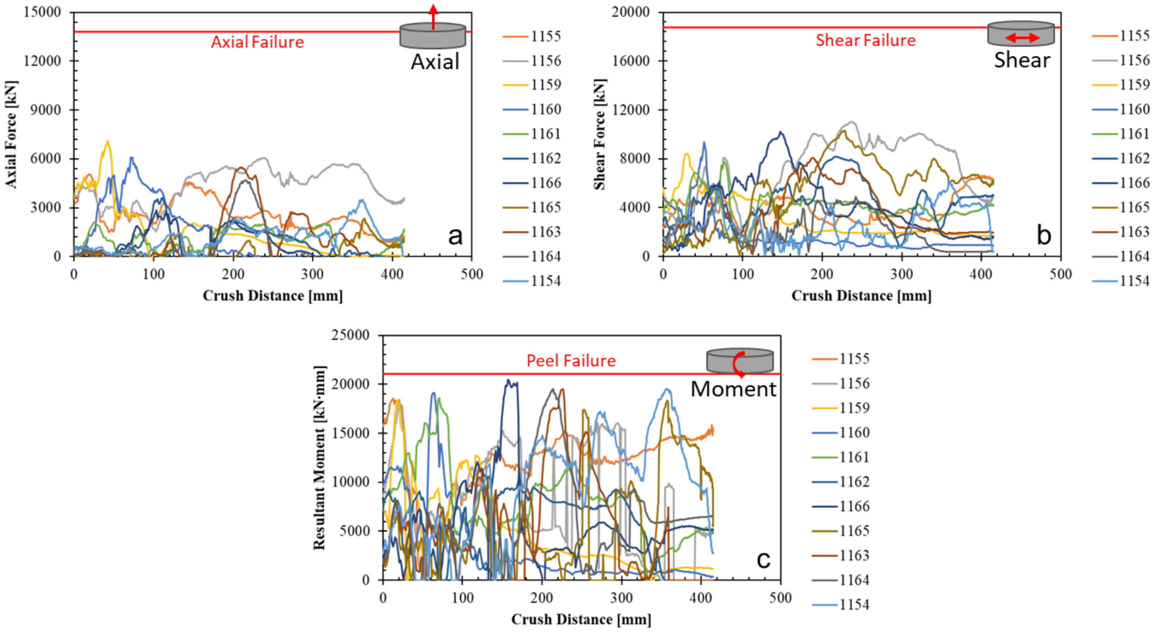

Figure 55. Spot weld forces along the SUV model's crush tip top flange, demonstrating failure loads for **(a)** axial loading, **(b)** shear loading and **(c)** peel moment loading.

2.8 Design Requirement Summary

Figure 33 outlines the steps pursued in this thesis to develop a tailor-welded hot stamped side frame member. This chapter has served to present the numerical model of the full SUV and the predicted side frame member response within the vehicle. The next step in the development path is to design and fabricate a representative baseline front end module that captures the crush response of the side frame member in full SUV model. A key requirement in developing the baseline front end module is to establish a series of design requirements or specifications that will ensure that the baseline front end module behaves in a manner equivalent to that predicted by the full SUV model. The design specifications that will be used to assess the appropriateness of the baseline front end module are presented in Table 3.

Table 3. Design specifications to evaluate the baseline front end module and tailor-welded hot stamped (TW-HS) side frame member.

⬛ **SUV Model**
🟥 **Baseline Front End Module**
🟦 **T-W HS Front End Module**
🟪 **T-W HS SUV Model**
🟨 **T-W HS Crush Tip**

	Numerical (N) Experimental					Qualitative Quantitative	Target	Upper Bound	Lower Bound
	⬛	🟥	🟦	🟪	🟨				
Crush Response									
Consolidation of crush tip (Fig. 56)	N	E	N	N	N	Qualitative	Match	-	-
Buckle in front of shock tower support (Fig. 56)	N	E	N	N		Qualitative	Match	-	-
Buckle behind shock tower support (Fig. 56)	N	E	N	N		Qualitative	Match	-	-
Parent material fracture severity			N	N	N	Qualitative	Minimize	-	-
Vehicle Decleration									
Velocity history	N	E	N	N	N	Quantitative	Match	+ 10%	- 10%
Final crush distance	N	E	N	N		Quantitative	422 mm	+ 30 mm	- 30 mm
Deceleration profile	N			N		Quantitative	Match	+ 15 g	-15 g
Crush Forces									
Sectional force plane (SFP) - global trend	N	N		N		Qualitative	Match	-	-
SFP - peak forces (1st, 2nd, 3rd)	N	N		N		Quantitative	Match	+ 15%	- 15%
Total Force (TF) - global trend		E	N		N	Qualitative	Match	-	-
TF - peak forces (1st, 2nd, 3rd)		E	N		N	Quantitative	Match	+ 15%	- 15%
TF - average force		E	N		N	Quantitative	Match	+ 20%	- 20%
Occupant Compartment Intrusion									
x-coordinate displacement	N	N	N	N		Quantitative	25.9 mm	+ 30 mm	-
z-coordinate displacement	N	N	N	N		Quantitative	3.0 mm	+ 40 mm	-
Extent of Spot Weld Failure									
Weld locations	N	N	N	N	N	Quantitative	Match	-	-
Quantity	N	N	N	N	N	Quantitative	Match	-	-
Severity			N	N	N	Qualitative	Minimize	-	-
Side Frame Member Characteristics									
Mass Reduction	N		N			Quantitative	< 7.6 kg	15%	-
Total number of spot welds	N		N			Quantitative	≤ 245	-	-
Total number of components	N		N			Quantitative	≤ 3	-	-

It is a design requirement that the crush response (collapse modes) of the baseline and tailor-welded hot stamped front end modules be similar to those found in the production side frame member in the SUV model. To be more precise, the location and deformation trajectory of sequential folding in the crush tip, global buckling in the middle section and rigidity of the S-rail section must correspond to that observed for the side frame member within the SUV model. The key crush modes to match in the hot stamped tailor-welded side frame member design are shown in Figure 56. It is also pertinent that the extent of the parent metal fracture in the tailor-welded hot stamped side frame member be minimized in the design process.

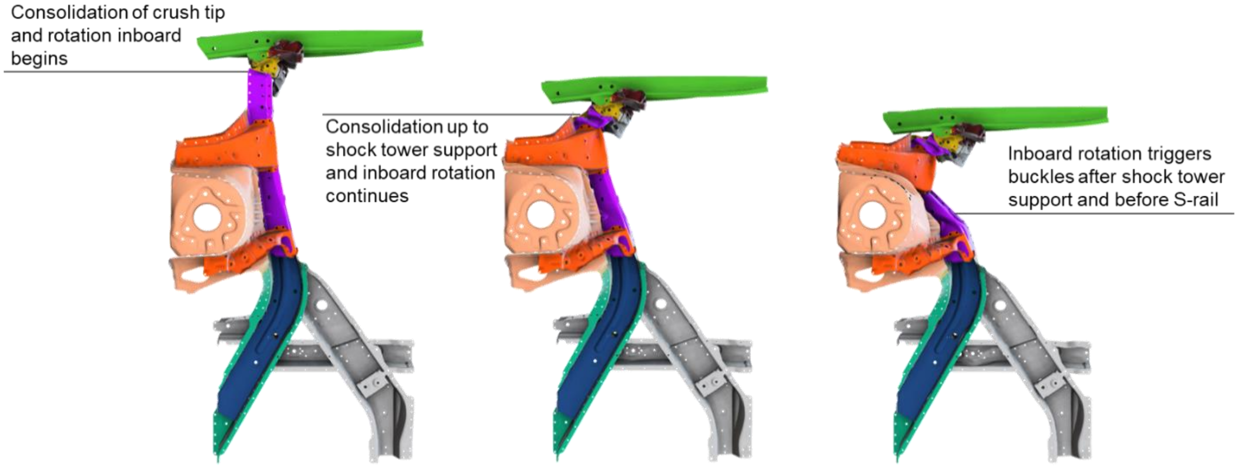

Figure 56. Key crush modes of the production JAC590R side frame member in the SUV model to be matched in the design of the baseline front end module.

The global trend of the crush forces in each cross-sectional force plane of the baseline front end module must match those from the SUV model side frame member. In addition, the first three peak crush forces (highlighted in Figure 50) should be similar in magnitude and instance in the crash event, with a maximum error of 15%. The overall trends in the force-time history of the tailor-welded hot stamped front end module must match that of the baseline front end module. The error in average crush force between the tailor-welded hot stamped front end module and baseline front end module should not exceed 20%.

Components of the BIW structure are designed to keep the occupants safe in the event of a crash. The side frame member in the SUV model demonstrated a small intrusion into the passenger compartment of 25.9 mm in the x-coordinate and 3.0 mm in the z-coordinate. An acceptable level of intrusion is determined by adding a tolerance to the SUV model predicted occupant compartment intrusion. A tolerance of 30 mm in the x-coordinate direction and 40 mm in the z-coordinate direction are added (coordinate systems are based on Figure 52). A higher tolerance is assigned in the z-direction since intrusion in this direction does not travel directly towards the occupant's feet, such as in x-direction intrusion, implying intrusion in the z-coordinate is less severe than x-direction intrusion.

The number of spot weld failures predicted in the production side frame member SUV model was quite limited and the welded flanges in the crush tip remain intact throughout the entirety of the crash event. (Recall that "failure" is defined herein as the initiation of damage as opposed to complete separation of a spot weld.) The extent of spot weld failure in the hot stamped tailor-welded side frame member must be maintained at this low level. Spot weld failure will be quantified through the individual predicted weld failure parameters to identity rupture hot spots and visual checks for element deletion will be used to identify complete weld failure. Most importantly, the severity of spot weld failure and the impact of any spot weld failures on crash safety will be evaluated based on whether controlled folding behaviour follows spot weld failure. Absolutely no spot weld flange "unzipping" may occur during the crash event.

One of the main goals of investigating higher strength hot stamping materials in frontal crush applications is to determine the potential mass savings that can be achieved through sheet steel down-gauging. It is deemed that replacing the production JAC590R side frame member with hot stamped materials is not worthwhile, unless a weight reduction of at least 15% is realized. In addition, the total number of major stamped components that make up the side frame member should not exceed three and the total number of spot welds to fabricate the side frame member should not exceed 245 (the number in the current assembly). Ideally, a reduction in the number of major components and number of spot welds would be desirable.

The development and testing of the baseline front end module is presented in the following chapter of this thesis. Note that the ultimate goal of this thesis is to develop a tailor-welded hot stamped side frame member and this new side frame member will also be evaluated using the design requirements listed in Table 3.

Chapter 3 – Baseline Front End Module Development

Conducting a US-NCAP Full Width Rigid Barrier SUV frontal crash test requires many resources that are outside of the scope of this thesis project. For this reason, the evaluation of the hot stamped tailor-welded side frame member is conducted at the assembly level and will only consider the left hand (driver's side) side frame member. The assembly of interest in this thesis is the front end module, which includes the structural components that house and support the side frame member. The components of the front end module provide the side frame member with adequate support to absorb the kinetic energy of the vehicle. The crash performance of the production JAC590R side frame member will be evaluated using the requirements from the front end module developed in this section, which will be termed the baseline front end module. The same front end module requirements developed in this chapter will be used to evaluate the hot stamped tailor-welded side frame member, as discussed in chapter 4.

The development of the experimental method for testing the baseline front end module is a combined work effort of Peister [19] in his own thesis and the author of this thesis. The numerical studies to determine which components from the BIW structure are required to match the performance of the production JAC590R side frame member, from the SUV model, are discussed in this thesis. Peister [19] is credited with designing the crash sled test fixture for the baseline front end module, as well as performing the first three experiments on the baseline front end module. An additional six baseline front end module experiments are conducted as part of the work of this thesis.

This chapter details the development of the baseline front end module, including the experimental crash test results, numerical predictions and their correlation to the production JAC590R side frame member from the SUV model. The chapter opens with discussing the iterative numerical simulation process used to determine which components of the BIW structure are relevant in reproducing the boundary conditions imposed on the side frame member by the rest of the BIW. The test methodology and the results from the dynamic sled testing are then discussed. The test setup is numerically modelled and correlated to the baseline front end module test results. To conclude this chapter, the baseline front end module is evaluated against the design requirements developed in section 2.8 to ensure the side frame member is properly constrained by the additional BIW supporting members and that a fair comparison can be made to the hot stamped tailor-welded side frame member.

3.1 Development of a Reduced Body-In-White Structure

The starting point for developing the baseline front end module was to determine which components from the SUV BIW (Figure 34) structure should be included to produce an impact response of the driver's side frame member within the full-vehicle. The goal is to reduce the BIW structure as much as possible, such that the remaining structure can be tested on a components level crash sled, without severely altering the crash response of the side frame member. In this sub-section all decisions to remove components are validated through simulating crash of the front end module and checking whether the requirements from section 2.8 are met.

The component of interest in this thesis is the driver's side frame member, therefore all of the components of the BIW structure aft the S-rail section of the side frame member are removed. The remaining structure, shown in Figure 57, is referred to as the frontal BIW structure. The frontal BIW structure is the first large reduction of components, however this is still a very complex and large structure to be fabricated and tested on the crash sled. Further reduction of components are made, since it is observed that there is still potential to further isolate the driver's side frame member.

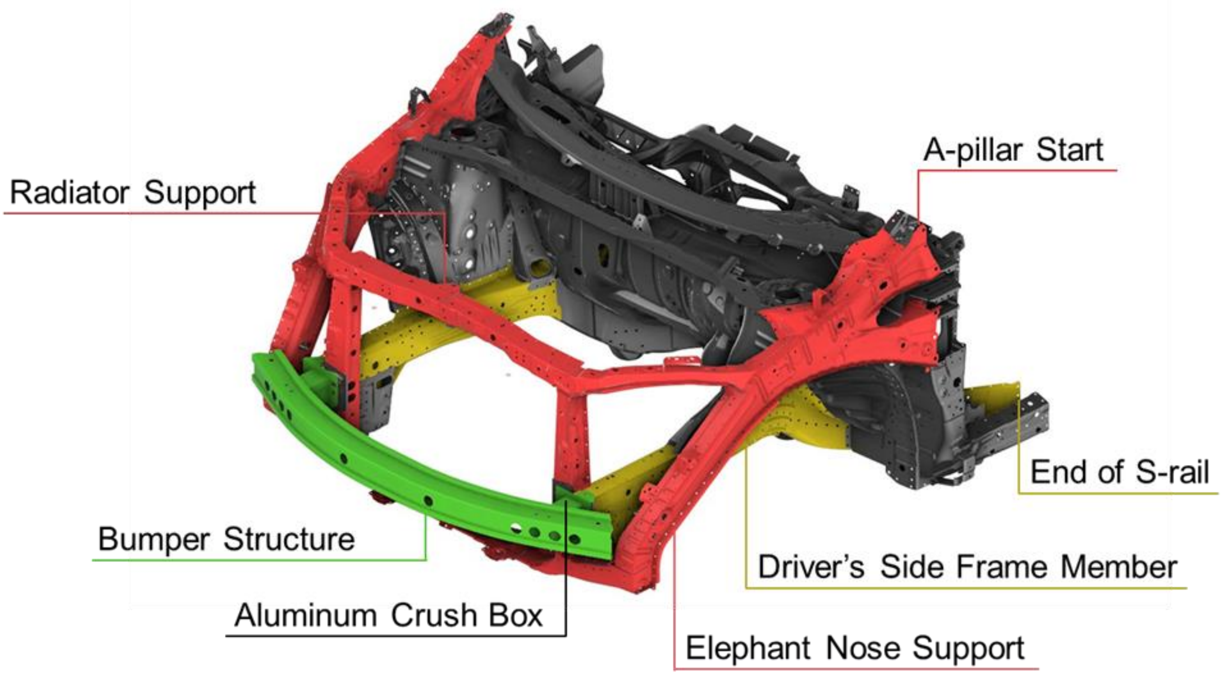

Figure 57. Frontal BIW structure isolated from the SUV model.

The scope of this thesis work is to only evaluate the driver's side hot stamped tailor-welded side frame member. This requirement enables further reduction of the frontal BIW structure by eliminating the passenger side components from the frontal BIW structure (Figure 58a). It is noticed from the half frontal BIW structure that the front bulkhead members that would support the radiator no longer contributes lateral support to the side frame member. Similarly, the half front bumper structure will impose a large moment on the side frame member upon impact without its other half to balance out the forces. For these reasons, both the front bulkhead lateral members and the bumper structure are removed. Additionally, the dashboard support components do not directly constrain the side frame member and are therefore eliminated from the front end module structure. The remaining structure after the passenger's side components, lateral radiator support, bumper structure and dashboard supports are removed is shown in Figure 58b.

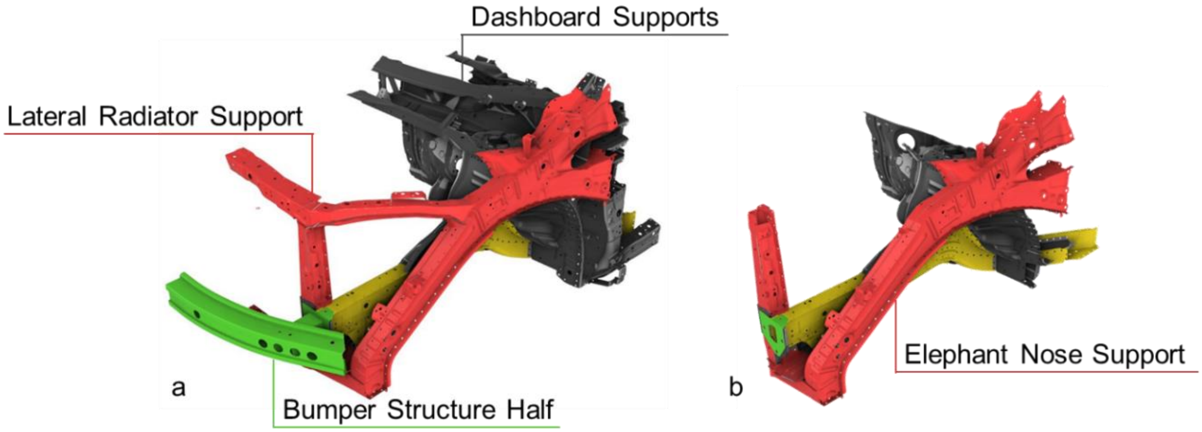

Figure 58. (a) Passenger side components removed from the frontal BIW structure. **(b)** Lateral radiator support components, bumper beam and dashboard supports removed.

The untrimmed floor panel and dashboard panel, shown in Figure 59, are relatively large and do not provide structural support in locations they are not connected to the side frame member S-rail section. For this reason, it is beneficial to trim both of these panels such that they conform to the flanges of the front end module, as shown in the trimmed version in Figure 59. The as-trimmed portions of floor and dashboard panels are retained in the reduced structure since they weld to the driver's side frame member, shock tower and center frame connector bracket and serve to close the cross-sections of these members.

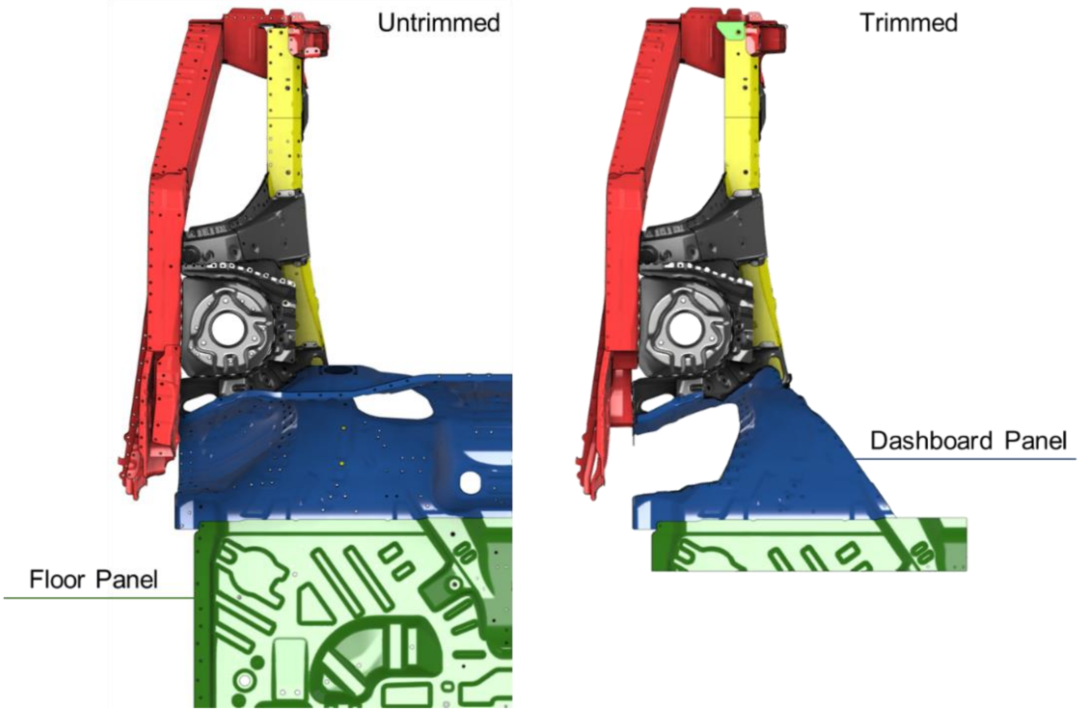

Figure 59. Schematic of the front end module showing the untrimmed (left) and trimmed (right) dashboard panel and floor panel.

The purpose of the elephant nose support shown in Figure 60 is to protect the occupants in the event of a small overlap/oblique crash, similar to the test procedure described by NHTSA [84]. The scope of this thesis is to only evaluate the side frame member in full frontal impact, therefore the inclusion of the elephant nose support is not necessary if it does not significantly affect the driver's side frame member response during full frontal crash.

To determine whether the elephant nose support is relevant to the crash performance of the side frame member numerical simulation is used. The boundary conditions for the simulation are shown in Figure 60, where it is observed that the last 50 mm of nodes at the end of the side frame member are constrained. The nodes at the top of the shock tower, where the shock strut would be mounted, are also constrained to support the upwards loads from the side frame member deformation. The fixed front end module is then impacted by a rigid wall with a mass of 855 kg and a speed of 56 km/hr. The remainder of the boundary conditions are the same as in the SUV model described in section 2.2.

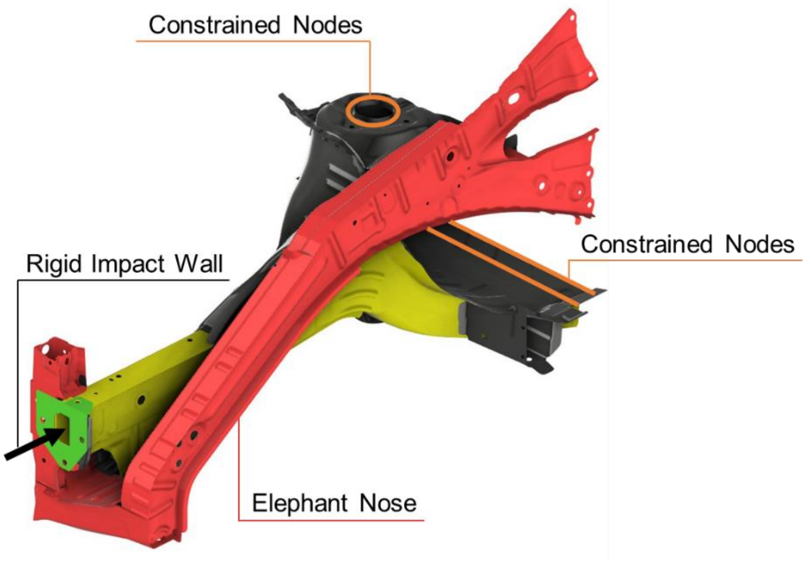

Figure 60. Boundary conditions used to simulate the front end module with elephant nose.

Upon simulating the front end module structure, it is found that the elephant nose support actually negatively effects the crash performance of the side frame member when its surrounding structural members are removed. It is observed in Figure 61 that the inclusion of the elephant nose support in this reduced structure creates a counter-clockwise rotation of the side frame member crush tip causing the crush tip to buckle on the underside of the rail. The buckle on the underside of the rail forces the later portion of the rail upwards, which collapses the S-rail section as the crash simulation progresses. Due to the simulation results the elephant nose and its associated front bulkhead components are removed from the reduced front end module structure.

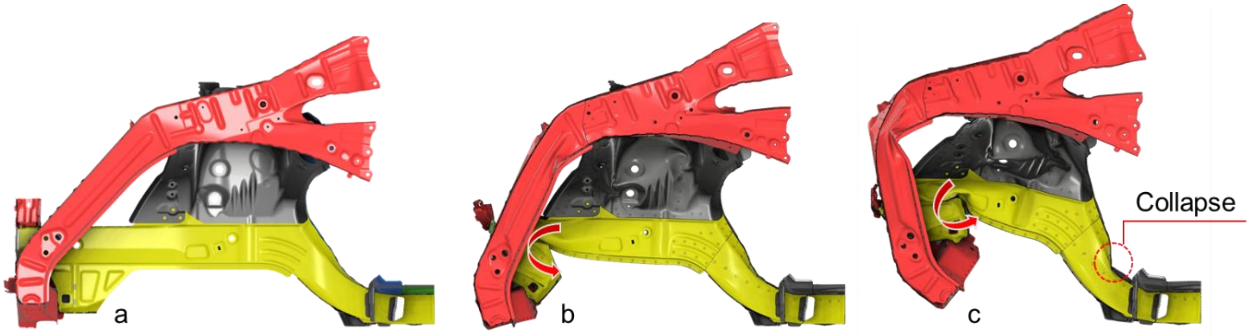

Figure 61. Effect of elephant nose in front end module crash simulation, starting with the **(a)** undeformed state, **(b)** start of side frame member counter-clockwise rotation and **(c)** continued rotation and collapse of the S-rail.

Secondary components, such as the glass fiber reinforced battery base and front bulkhead brace, were then added into the front end module model to observe their effect in crash performance. The battery base supports the battery within the vehicle and bolts directly onto the side frame member. The front bulkhead brace provides lateral support to the side frame member through a connection from the side frame member to the lower radiator support. The radiator support has been removed from the reduced structure and therefore the front bulkhead brace no longer provides lateral support, however it does provide a locally stiffened region that alters the sequential folding in the crush tip where it is bolted on. It is observed in Figure 62 that when the battery base and front bulkhead brace are included into the model, more desirable progressive folding occurs in the crush tip than when these components are not included. It is to be noted in Figure 62 that the battery base has been hidden from its respective image to better examine the crush tip folding. Note also that the battery base fractures and is shears off the side frame member at approximately 14 ms after impact.

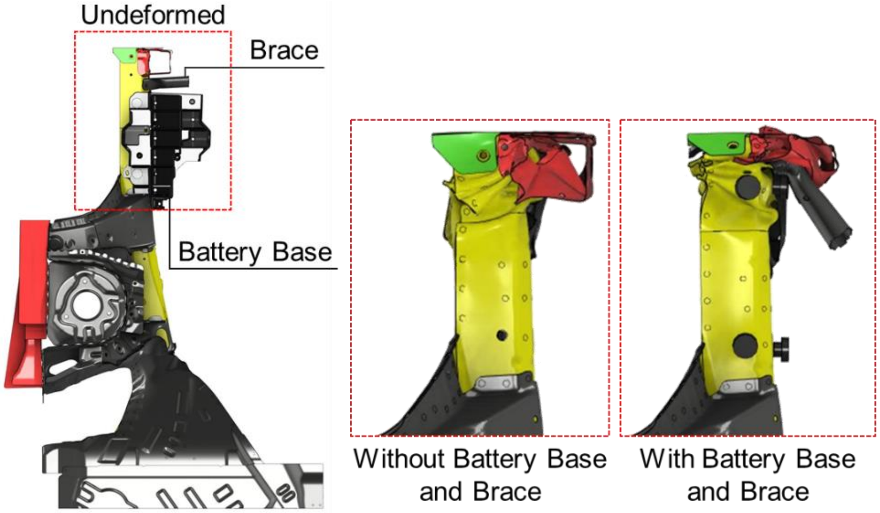

Figure 62. Effect of including the front bulkhead brace and battery base into the simulation illustrates sequential folding. Note that the battery base is hidden so that the folding may be examined.

The final components utilized in the baseline front end module are shown in Figure 63. It is evident from this figure that the baseline front end module is much more manageable from a fabrication and testing perspective than the frontal BIW structure shown in Figure 57. In the proceeding sections of this chapter the crash test results and numerical simulation predictions will be examined and compared to the SUV model predictions to establish whether the baseline front end module suitably constrains the side frame member in frontal crash.

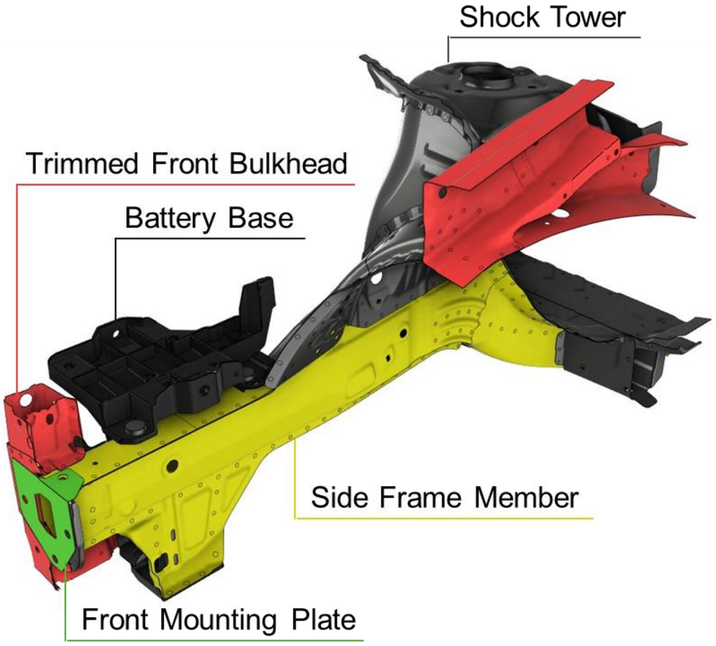

Figure 63. Finalized components necessary to constrain the production side frame member as the SUV model BIW does. The structure is hereafter referred to as the baseline front end module.

3.2 Baseline Front End Module Crash Testing Method

The baseline front end module assemblies are fabricated by the fabrication group at Honda Research and Development Americas (HRA), using production components and assembly methods. This approach ensures that the baseline front end modules being produced are consistent to those sent to the production lines to build into SUV bodies. HRA fabricated and shipped ten driver's side baseline front end modules for dynamic crash sled testing conducted at the University of Waterloo.

The design of the crash test fixtures for the baseline front end module was developed as part of a related thesis by Peister [19]. In that work, a test fixture was designed to mount and impact the baseline front end module (Figure 63) within the Seattle Safety D780-3.7 crash sled [85] facility at the University of Waterloo. In order to fasten the baseline front end module to the rigid wall a steel mounting plate (Figure 64a) is MIG welded onto the end of the S-rail section, which was trimmed in a plane parallel to the fixed barrier wall, as shown in Figure 64b.

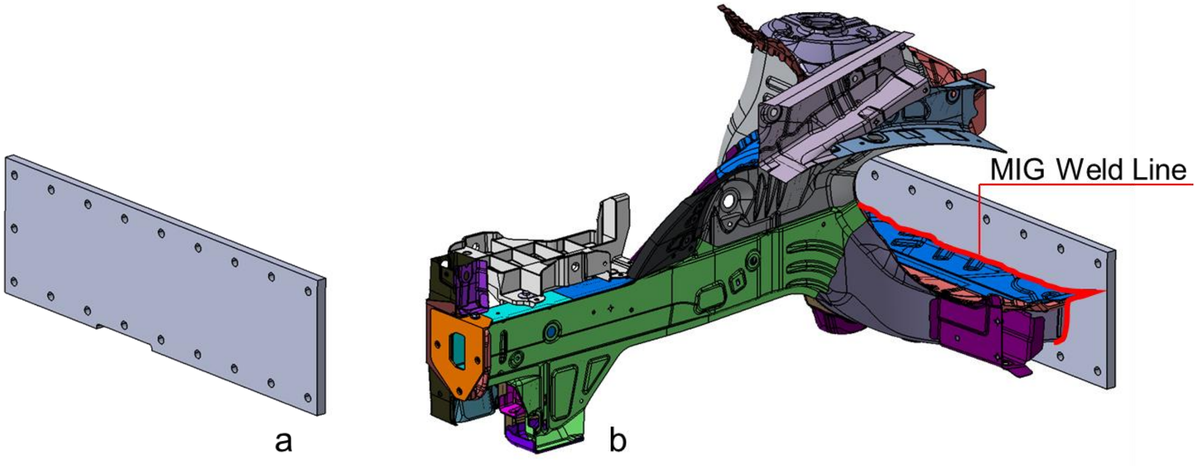

Figure 64. **(a)** The steel mounting plate and **(b)** the baseline front end module assembly that is MIG welded to the mounting plate.

A CAD generated schematic of the test setup is shown in Figure 65. The welded baseline front end module and mounting plate assembly is mounted to the fixed barrier wall with M12 bolts around the perimeter of the mounting plate. In this configuration the crush tip of the side frame member is extended forward to meet with the crash sled impact wall during the test. A large beam (shock tower support) is bolted to the fixed barrier wall and extends outwards toward the shock tower of the baseline front end module, where it is connected with three bolts. The shock tower support reacts the moment induced by the vertical offset of the S-rail and resulting uplifting force that would cause the side frame member to buckle. It was decided to constrain the shock tower over the A-pillar support, which is what would be constrained in the vehicle, to simplify the test fixture design. This simplification is justified, since the displacements of the shock tower in the SUV model during deformation are insignificant due to the amount of reinforcement surrounding it.

Honeycomb arrestors are used for two purposes in the crash experiment: 1) to control the deceleration of the crash sled so that the velocity profile of the side frame member in the SUV model can be matched in the experiment and (2) to dissipate excess kinetic energy (not absorbed by the test article) and decelerate the crash sled to avoid damage to the sled or the fixed barrier wall. The configuration of the honeycomb stack will be adjusted throughout the testing to fine tune the deceleration profile crash sled to match the SUV model response.

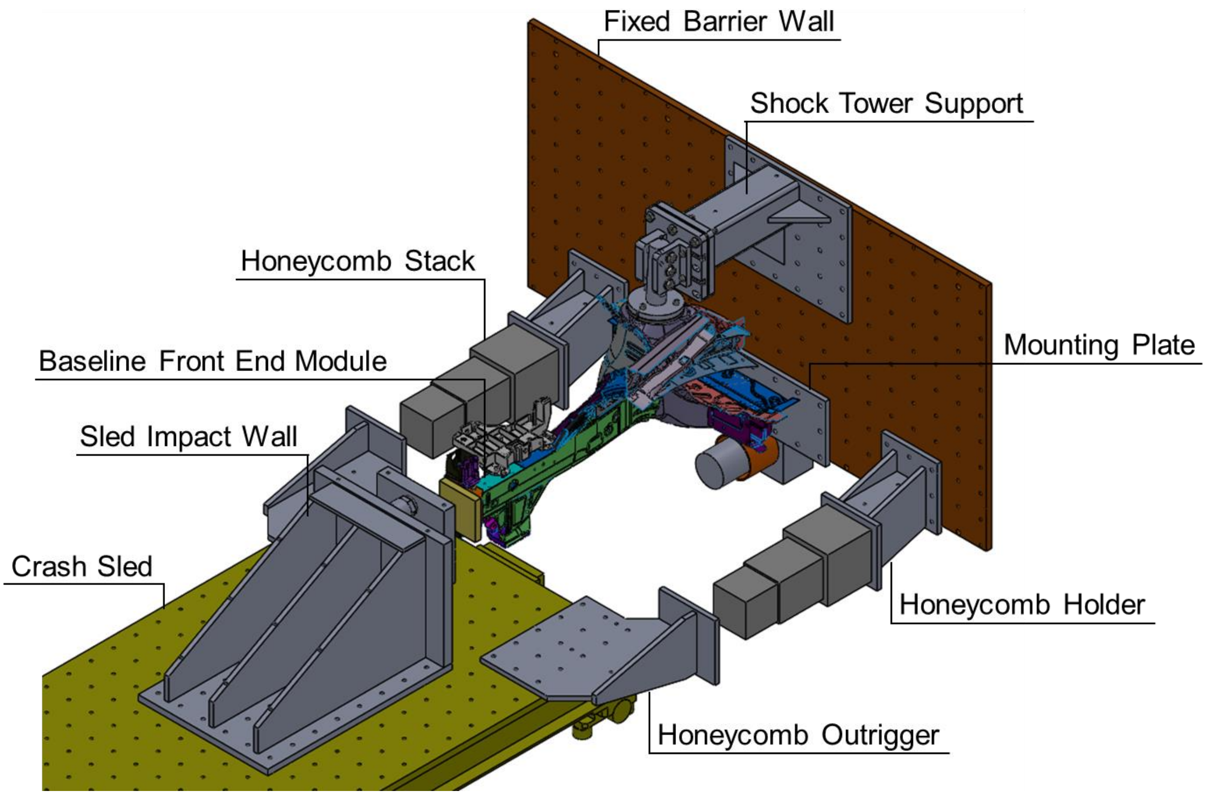

Figure 65. Finalized test setup for the baseline front end module, designed by Peister [19].

3.2.1 Experimental Setup

The baseline front end module structures are impacted using a Seattle Safety D780-3.7 crash sled [85] (Figure 66). The sled has a maximum velocity of 91 km/hr and can carry a payload of 1400 kg. The maximum impact energy the sled can deliver is 165 kJ. The crash sled travels toward the test article along steel rails using a wheeled assembly. Wheel assemblies are mounted on all four corners of the sled and have wheels above and below the rail to react the downward and uplifting forces, while wheels along the side of the rail react the lateral loads. The sled is propelled towards the test specimen by opening a butterfly valve that releases compressed air from a reservoir, pushing a piston, which then pulls the rope attached to the sled.

The sled alone weighs 356 kg and must be accompanied by a 23 kg crush can, which is mounted to the front. Two honeycomb outriggers weighing 49 kg each are mounted on either side of the sled. An impact wall with three load cells and impact face plate are mounted to the sled and weigh a total of 326 kg. Therefore, the total mass of the impact sled is 803 kg. The initial velocity targeted in this crash experiment is 51 km/hr, which is the speed of the vehicle when the side frame member begins to deform, as described in section 2.4. The total energy associated with this test is calculated to be 80.6 kJ, well under the sled's maximum impact energy.

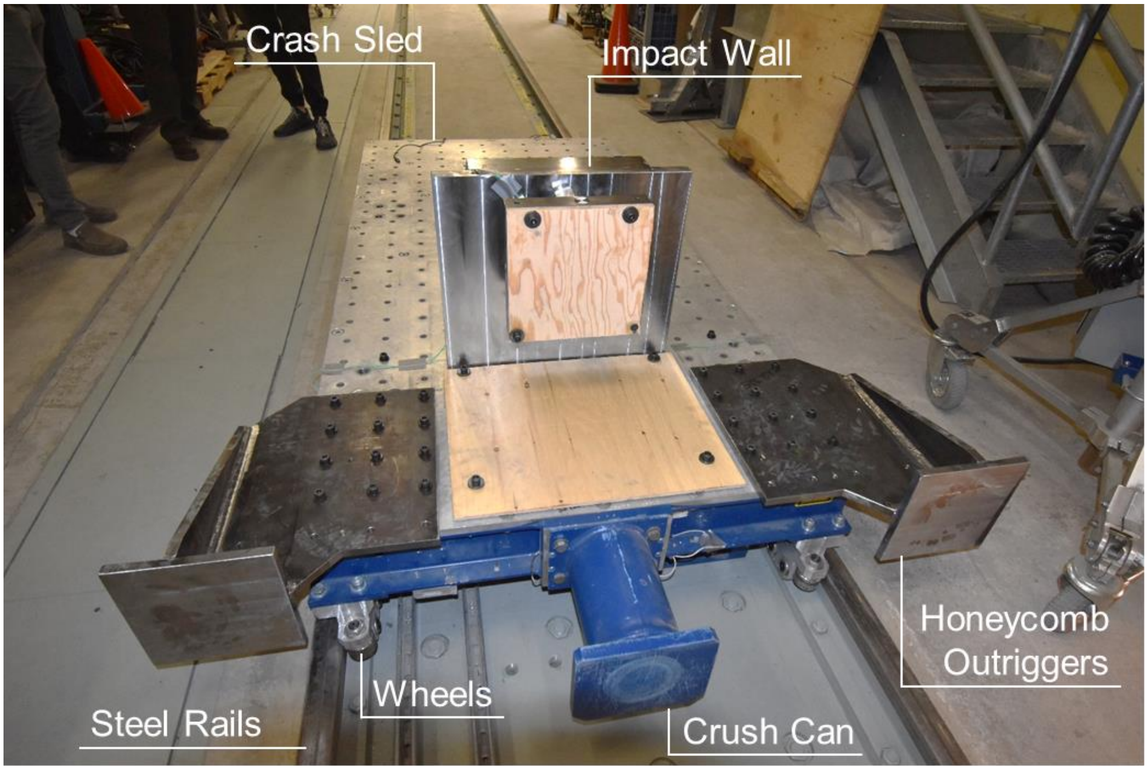

Figure 66. Crash sled experimental setup for baseline front end module.

The kinetic energy of the crash sled is greater than the baseline front end module can absorb on its own. For this reason honeycomb stacks (Figure 67) are used to dissipate the remainder of the crash sled's energy that the test article could not absorb. The honeycomb stacks are made from Plascore 5056 aluminum honeycomb (PACL-XR1-6.1-1/8-15-P-5056) with 3.2 mm (1/8") cells and a crush strength of 3.69 MPa (535 psi) [86]. In addition to dissipating the residual kinetic energy of the crash sled the honeycomb arrestors also play an important role in controlling the deceleration profile of the crash sled. The ability to control the deceleration profile of the crash sled is crucial if the experiment is to match the deceleration profile of the SUV model, as discussed in section 2.4. An additional high stiffness tubular honeycomb is mounted beneath the specimen as a fail safe feature and will be crushed by the crash sled crush can in the event that the honeycomb stacks and specimen fail to stop the sled.

Honeycomb stacks are made by first cutting the honeycomb to size. The dimensions are based on the target crush force, which is easily calculated from the crush strength. The cut honeycomb blocks are then placed into a hydraulic press to adjust their length, as well as pre-crush the honeycomb so that the initial spike in crush peak is removed and the crush is predictably initiated at the impacted end. For resistance to buckling in this long honeycomb assembly the smaller blocks are embedded into the larger blocks with the hydraulic press. The stack is then assembled by duct taping the blocks together and finally by securing them to the honeycomb holders with duct tape.

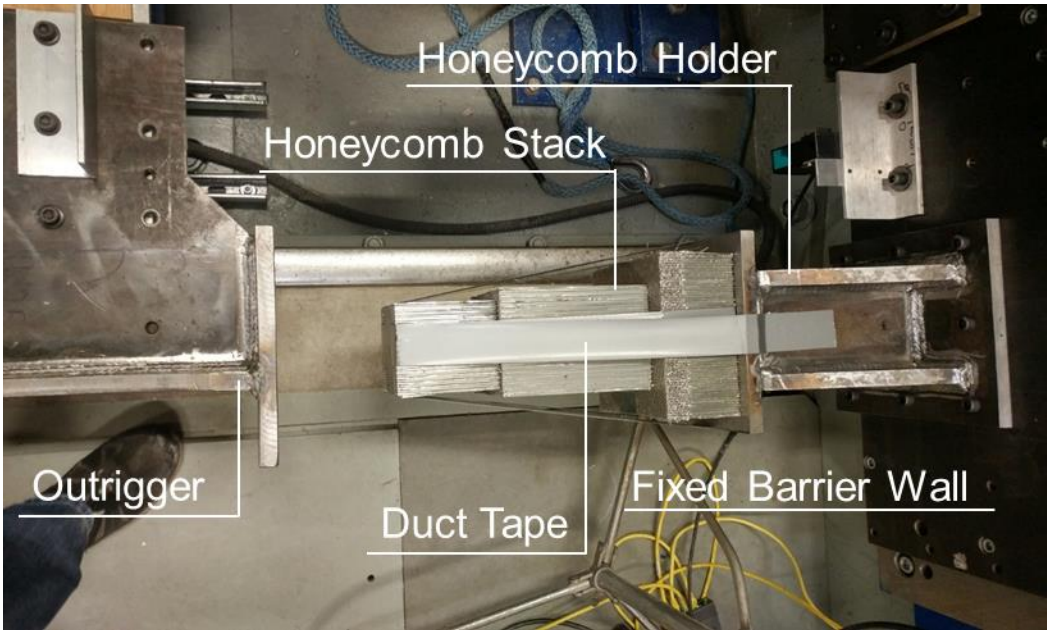

Figure 67. Top view of honeycomb stacks mounted to the honeycomb holders using duct tape.

The crash sled is equipped with an accelerometer on each side and has three 120 kN Kistler 9731B piezoelectric load cells mounted between the impact face plate and sled impact wall, as shown in Figure 68. The data from the accelerometers on either side is averaged to determine the deceleration *versus* time history. Data from the three load cells is summed to measure the force transmitted through the baseline front end module. A Keyence LK 507 laser displacement sensor is used to measure the position of the crash sled during the test. This sensor can measure distances in an envelope starting at 250 mm and ending at 1,000 mm from the sensor. Prior to the sled coming into contact with the test article it crosses the path of a laser trigger, which sends a signal to the data acquisition (DAQ) system, triggering recording the force and acceleration data. Force, acceleration and displacement data are logged at a frequency of 10,000 Hz for a duration of 1 second from when the DAQ is triggered.

A consequence of mounting the load cells on the sled is that the deceleration of the crash sled will have an inertial effect on the relatively heavy impact face plate mounted to the front on the load cells, which will alter the force measurement of the load cells. To account for this inertial effect, the mass of the impact face plate is multiplied by the acceleration of the sled and then subtracted from the measured load for each time step in the data sample.

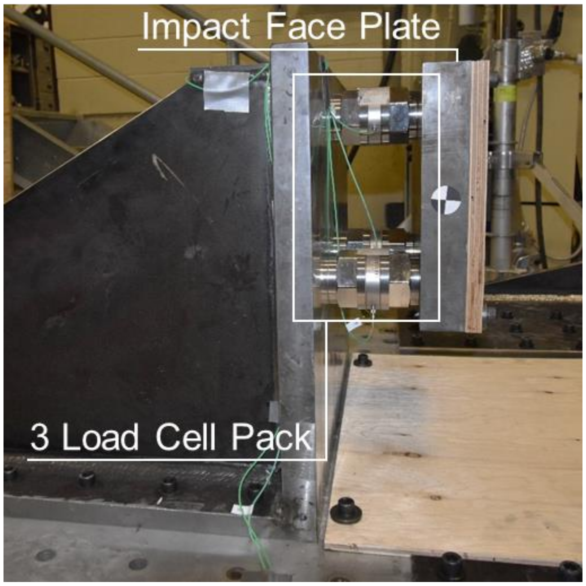

Figure 68. Three-load cell pack mounted between the sled impact wall and the impact face plate.

The entirety of the triggered crash event is captured at 10,000 frames per second with a series of high speed cameras. The cameras and configurations used are changed between tests due to camera availability and desire for different views of the baseline front end module collapse. The cameras consist of Photron SA-1, Photron SA-4, Photron SA-5, Photron SA-Z and AX-100 G-Hardened high speed optical cameras. The placement and use of these cameras changes per test and will therefore be catalogued in section 3.2.2.2. In addition to optically recording the high speed deformation of the side frame member, the crash event is also recorded with a Telops FAST-IR 2K infrared red (IR) thermal imaging camera. The thermal camera records at 5,000 frames per second and is very useful for capturing heat generated from folding and spot weld failure, due to the adiabatic heating from plastic work being generated at a relatively high strain rate.

A total of six baseline front end modules are tested during this thesis and three have been tested by Peister [19] in his own thesis. It should be noted that as each baseline front end module crash experiment was conducted, small changes were made to the setup to try and fine tune the experiment. The details of each change to the testing procedure are documented in the following section.

3.2.2 Experimental Program

Through the work of this thesis and Peister's [19] an experimental methodology is developed to evaluate production side frame member crash performance in frontal impact. Being developmental experiments however, means that improvements to the test method were made using the prior knowledge of each previous test. This sub-section aims to catalogue the experimental conditions used in each of the nine baseline front end modules tested.

The order of testing and the associated specimen identification is shown in Table 4. This table also clearly outlines the experimenter responsible for performing each of the test. In the first test (Bd-1) an initial velocity of 56 km/hr was targeted, whereas for the remainder of the tests the target initial velocity was 51 km/hr.

Table 4. Order of testing, the associated specimen identification and key features from each of the tests. Note that "Bd" refers to "Baseline demonstrator".

Test Number	Specimen	Responsible	Sled Velocity		End Condition				Honeycomb Configuration				
			1	**2**	**A**	**B**	**C**	**D**	**1**	**2**	**3**	**4**	**5**
1	Bd-1	Peister [19]	✓		✓				✓				
2	Bd-5			✓	✓					✓			
3	Bd-4			✓	✓						✓		
4	Bd-7	Tummers (current thesis)		✓		✓					✓		
5	Bd-2			✓			✓					✓	
6	Bd-3			✓			✓					✓	
7	Bd10			✓			✓					✓	
8	Bd-9			✓				✓				✓	
9	Bd-6			✓			✓						✓

1 - 56 km/hr

A - No end plate, plywood
B - 1" thick end plate, plywood
C - 1/2" thick end plate, pine

1 - Honeycomb config. 1
2 - Honeycomb config. 2
3 - Honeycomb config. 3
4 - Honeycomb config. 4

3.2.2.1 Honeycomb Stack Configurations

The configuration of the honeycomb stacks used for matching the SUV model deceleration profile and attenuating residual crash sled energy were varied considerably over the test campaign. The different configurations used for each test specimen are illustrated in Figure 69, in which the position of the honeycomb outrigger and holder are shown along with each set of honeycomb block dimensions. In the default outrigger position (Bd-1), the total honeycomb crush distance is 643 mm, however for the remainder of the tests the distance is 543 mm. The outrigger position was changed to 543 mm to closer represent the velocity history of the SUV model. In this figure, "free crush" is the distance of sled travel after impact between the sled face and the specimen, but prior to the sled contacting the honeycomb stack. It is important to note that the crush loads measured by the load cells are independent of the honeycomb, therefore, other than strain rate effects, the honeycomb configurations should not affect the measured crush loads. In the final test (Bd-6) the free crush distance was increased 20 mm by decreasing the length of the large honeycomb block by 20 mm. Increasing the free crush distance was done to try and better match the SUV model velocity history and final crush distance.

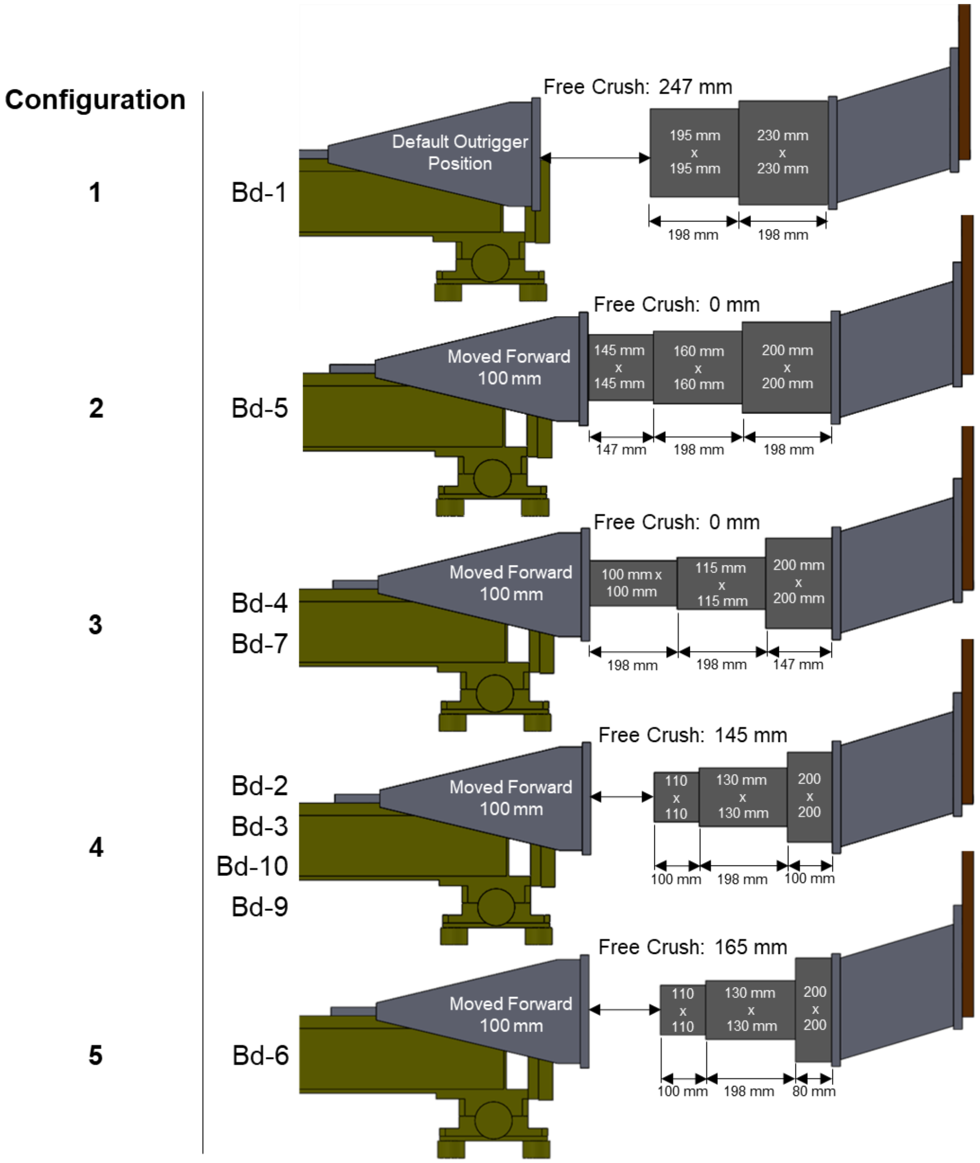

Figure 69. Honeycomb stack configurations with their respective specimen identification.

3.2.2.2 Lighting and Camera Configurations

Due to the rapid frame rate required to capture high speed crash experiments, a great deal of lighting is required to illuminate the specimen. Light positioning was based on the layout and number of cameras used in each individual test. The number and type of cameras used in each test was dictated by availability at the time of the experiment. Another important variable associated with the cameras was their views and focus on particular sections of the rail. During the series of baseline front end module testing the light location, cameras and views were changed from test to test.

The lighting and camera setup for the first test (Bd-1) conducted by Peister [19] is shown in Figure 70. The Photron cameras are used to capture perpendicular views of the specimen from the sides and top as well as an isometric view. The Telops FAST-IR 2K high speed thermal camera is positioned to capture the first few welds of the side frame member crush tip. The views captured by each of the cameras at the first point of contact are observed in Figure 71.

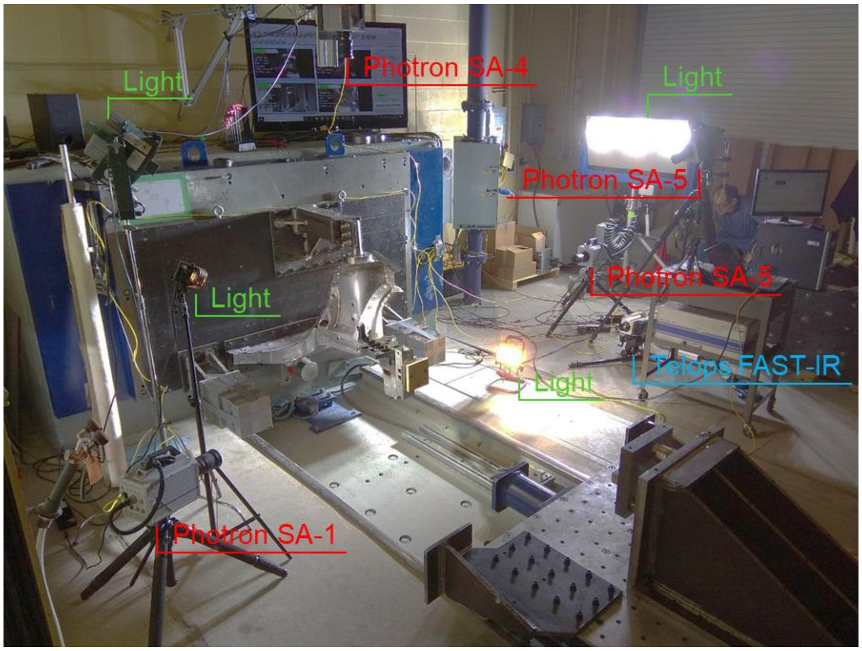

Figure 70. Arrangement of high speed cameras and lighting around the specimen for the first baseline front end module test (Bd-1). Image due to Peister [19].

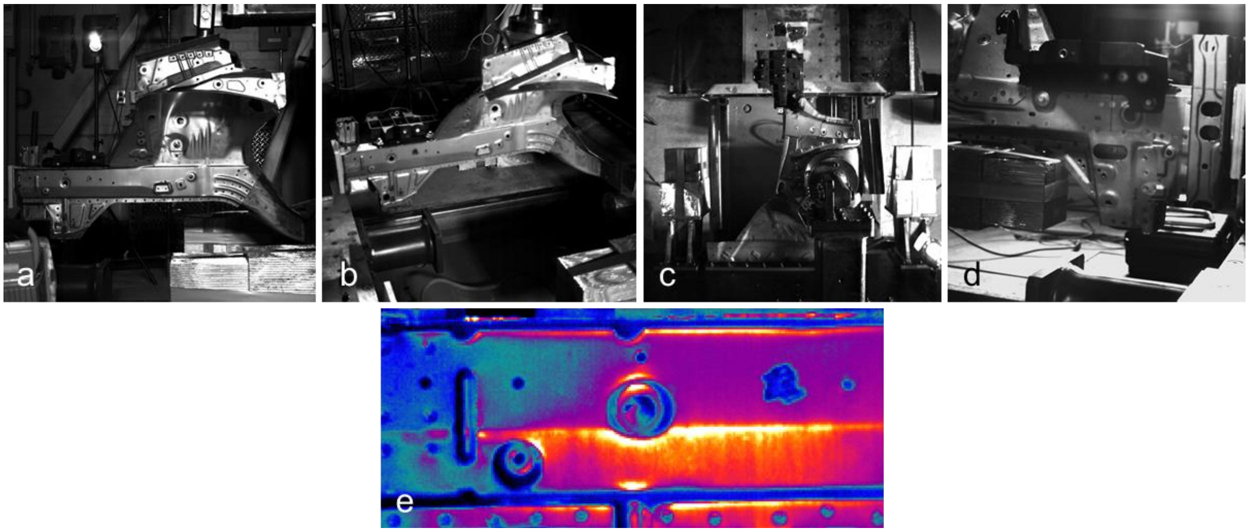

Figure 71. Views from the cameras used in the first baseline front end module test (Bd-1) including: **(a)** vehicle outboard side view (Photron SA-5), **(b)** vehicle outboard isometric view (Photron SA-5), **(c)** top view (Photron SA-4), **(d)** vehicle inboard side view (Photron SA-1) and **(e)** outboard enclosure panel flange (Telops FAST-IR 2K). Images due to Peister [19].

In the second to fourth experiments (Bd-5, Bd-4 and Bd-7) the lighting arrangement was altered by moving the largest light from the vehicle outboard side to the vehicle inboard side of the specimen. The new camera and lighting arrangement is illustrated in Figure 72. The angle of the vehicle inboard high speed camera was changed to better capture the folding behaviour of the rail during folding as shown in the camera views (Figure 73).

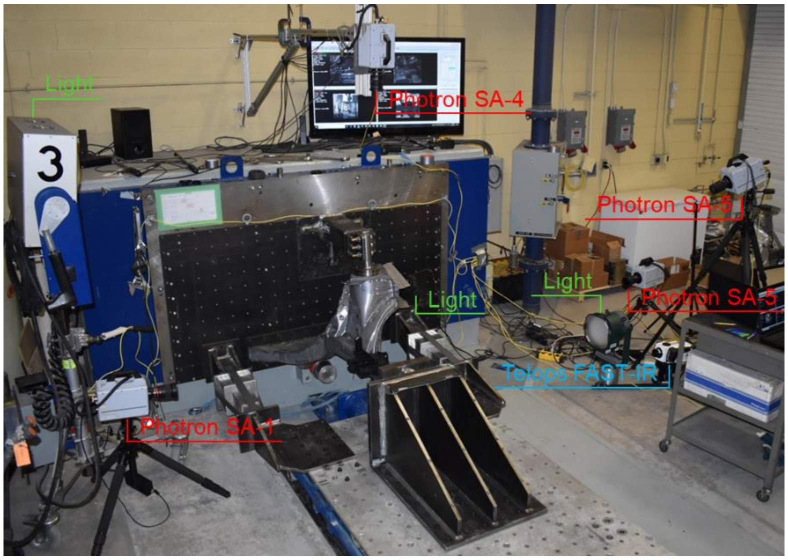

Figure 72. Arrangement of high speed cameras and lighting around the specimen for the second to fourth baseline front end module tests (Bd-5, Bd-4 and Bd-7). Image due to Peister [19].

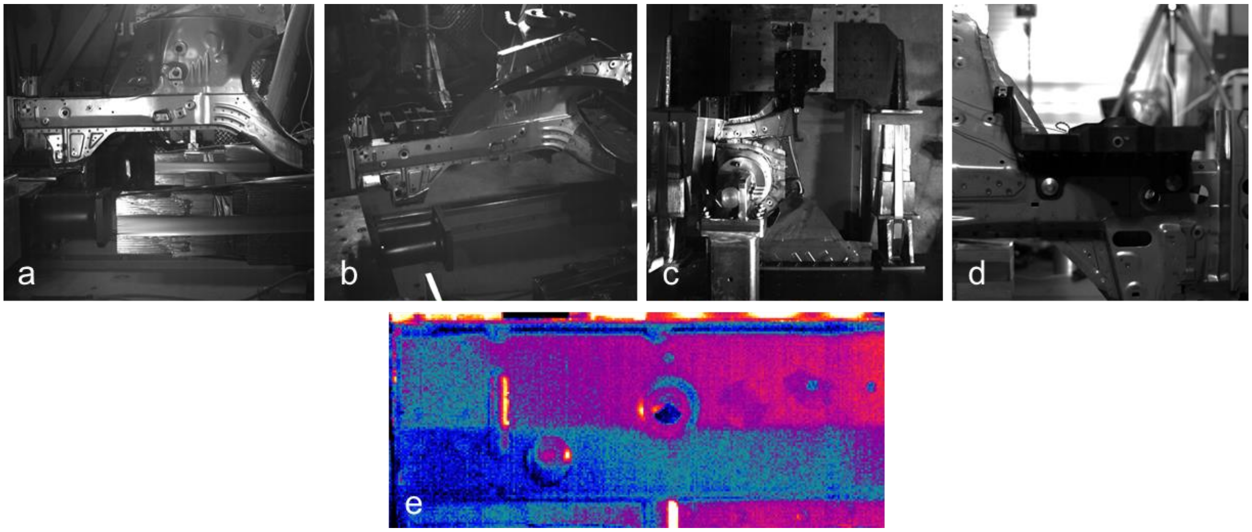

Figure 73. Views from the cameras used in baseline front end module tests Bd-5, Bd-4 and Bd-7 including: **(a)** vehicle outboard side view (Photron SA-5), **(b)** vehicle outboard isometric view (Photron SA-5), **(c)** top view (Photron SA-4), **(d)** vehicle inboard side view (Photron SA-1) and **(e)** outboard enclosure panel flange (Telops FAST-IR 2K). Image due to Peister [19].

The Photron SA-1 high speed camera was not available for the fifth to seventh baseline front end module experiments (Bd-2, Bd-3 and Bd-10). To make do with the available cameras, the vehicle outboard side view was omitted from the camera configuration for these tests. The camera and lighting orientation used is shown in Figure 74. It is observed in this figure that an additional large light is positioned on the vehicle outboard of the side frame member to completely illuminate the specimen. The views captured by each of the cameras are shown in Figure 75. It is clear from this figure that the thermal camera is zoomed in much closer on the first five spot welds of the crush tip along the top flange.

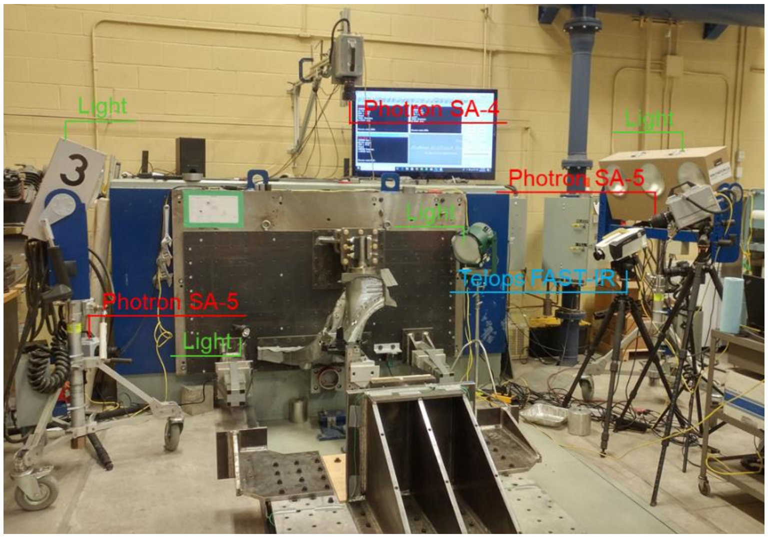

Figure 74. Arrangement of high speed cameras and lighting around the specimen for the fifth to seventh baseline front end module tests (Bd-2, Bd-3 and Bd-10).

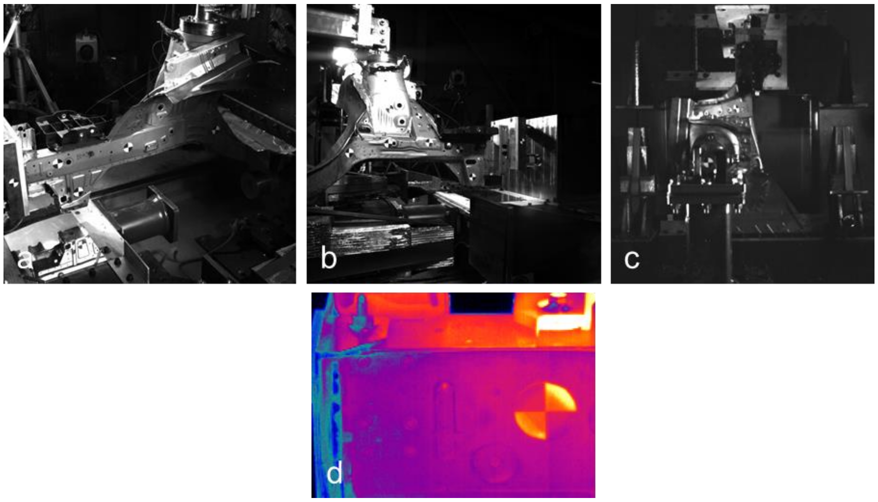

Figure 75. Views from the cameras used in baseline front end module tests Bd-2, Bd-3 and Bd-10 including: **(a)** vehicle outboard isometric view (Photron SA-5), **(b)** vehicle inboard side view (Photron SA-5), **(c)** top view (Photron SA-4) and **(d)** outboard enclosure panel top flange (Telops FAST-IR 2K).

In the eighth baseline front end module test (Bd-9), two Photron SA-Z cameras and an AX-100 G-Hardened camera were added in the experimental setup, as shown in Figure 76. The five high speed camera views and thermal optic view are shown in Figure 77. It is observed from this figure that the additional camera view allowed for a close up shot of the rail crush tip to be captured. The top view was captured diagonally in the lens in order to fit the entire specimen in the view without sacrificing resolution.

Figure 76. Arrangement of high speed cameras and lighting around the specimen for the eighth baseline front end module test (Bd-9).

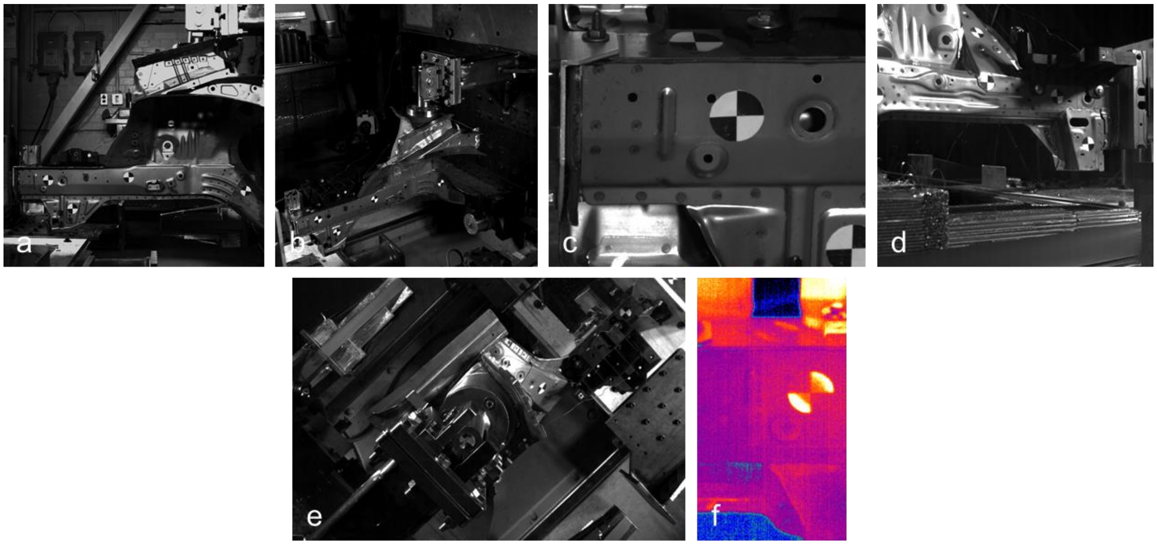

Figure 77. Views from the cameras used in baseline front end module test Bd-9 including: **(a)** vehicle outboard side view (AX-100 G-Hardened), **(b)** vehicle outboard isometric view (Photron SA-Z), **(c)** close-up of crush tip (Photron SA-Z), **(d)** top view (Photron SA-4), **(e)** vehicle inboard side view (Photron SA-5) and **(f)** outboard enclosure panel flange (Telops FAST-IR 2K).

In the ninth baseline front end module test (Bd-6), one Photron SA-Z camera, two Photron SA-5 cameras and one Photron SA-4 camera were used in the experimental setup, as shown in Figure 78. The four high speed camera views are shown in Figure 79. Unfortunately the high speed thermal image was not focused correctly and the deformation cannot be distinguished in this test.

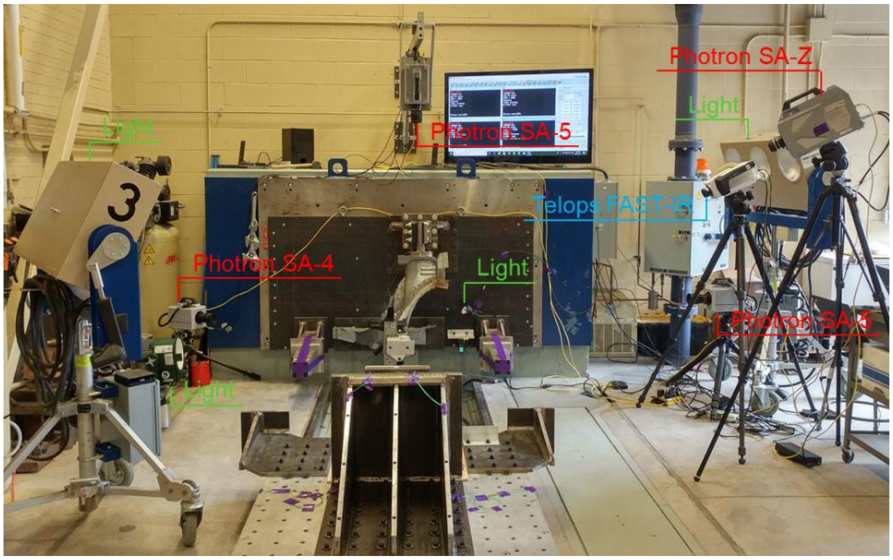

Figure 78. Arrangement of high speed cameras and lighting around the specimen for the ninth baseline front end module test (Bd-6).

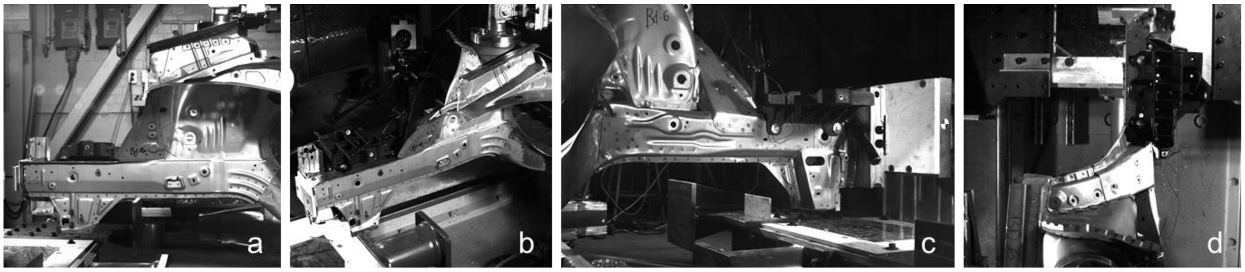

Figure 79. Views from the cameras used in baseline front end module test Bd-6 including: **(a)** vehicle outboard side view (Photron SA-5), **(b)** vehicle outboard isometric view (Photron SA-Z), **(c)** vehicle inboard side view (Photron SA-4) and **(d)** top view (Photron SA-5).

3.2.2.3 Impacted End Boundary Condition

The boundary condition between the crash sled impact face and the free end of the specimen proved to be critical in controlling the crash response of the baseline front end module. Therefore, considerable effort was expended to find the configuration that yielded a crush response close to the full vehicle behaviour. The boundary condition used at the impacted end of the baseline front end module is updated with each successive experiment.

A sheet of wood is used as a vibration attenuator between the crash sled impact face and the impacted end of the specimen. In this series of experiments, the location of the wood, how it is secured and the type of wood used are all variables in the testing program. In experiments 1, 2 and 3 (Bd-1, Bd-5 and Bd-4) a sheet of ¾” plywood is glued onto the aluminum mounting plate on the impacted end of the baseline front end module, as shown in Figure 80. The plywood sheet is cut to the size of the aluminum mounting plate and three clearance holes are drilled into the wooden sheet to accommodate the three mounting bolts on the impacted end.

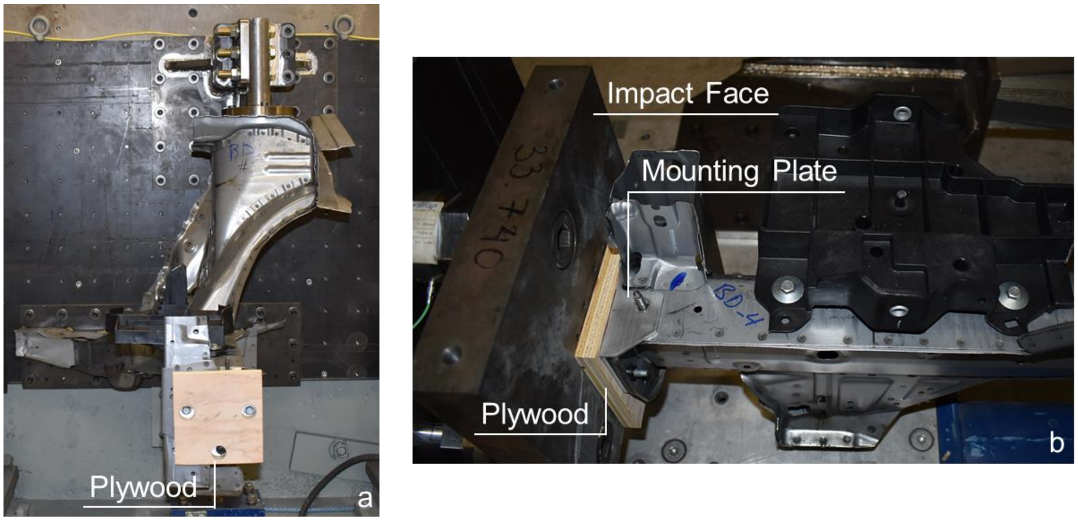

Figure 80. Plywood configuration for baseline front end module tests Bd-1, Bd-5 and Bd-4 shown in the **(a)** front view and **(b)** vehicle outboard side view. Images due to Peister [19].

In experiments 4, 5, 6, 7, 8 and 9 (Bd-7, Bd-2, Bd-3, Bd-10, Bd-9 and Bd-6) the wood is instead mounted to the impact face of the crash sled using four countersink M12 bolts, as shown in Figure 81. There are two types of wood used to attenuate the vibrations in this wood mounting method. In test 4 (Bd-7) the ¾” plywood is used to attenuate, however in the remainder of the tests (Bd-2, Bd-3, Bd-10, Bd-9 and Bd-6) ¾” pine board is used to attenuate the vibrations. The pine board has the advantage of having material properties readily available through MAT_WOOD_PINE in LS-Dyna, making it much easier to model. This material model includes compressibility effects which proved important in accurate predicting the impact and crushing response of the wood and subsequent crush behaviour of the side frame assembly.

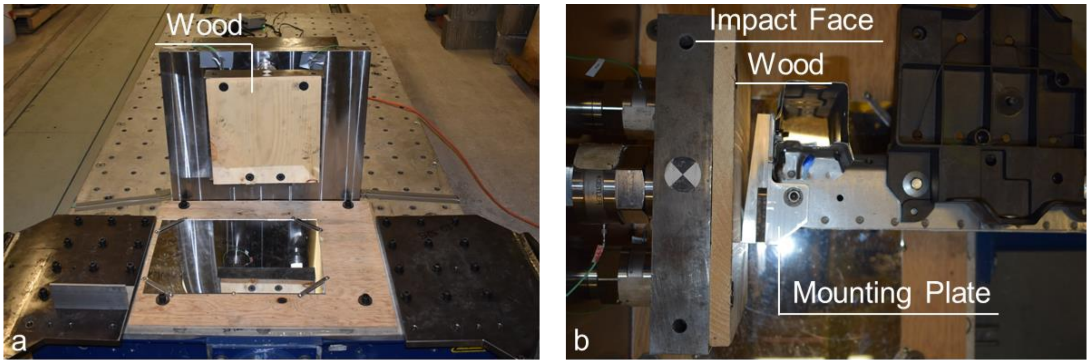

Figure 81. Wood attenuator configuration for baseline front end module tests Bd-7, Bd-2, Bd-3, Bd-10, Bd-9 and Bd-6 shown in the **(a)** front view and **(b)** top view.

The impacted end of the baseline front end module was also subject to boundary condition changes through the use of various aluminum end plates. In the tests conducted by Peister [19] (Bd-1, Bd-5 and Bd-4), no additional end plate was used to alter the impacted end boundary condition. The plywood pieces were simply glued to the production aluminum mounting plate on the front of the front end module. To better replicate the complex loading behaviour caused by the front bumper structure (section 2.3) end plates were added onto the impacted end of the baseline front end module.

The end plate configurations used for test numbers 4, 5, 6, 7, 8 and 9 (Bd-7, Bd-2, Bd-3, Bd-10, Bd-9 and Bd-6) are illustrated in Figure 82. In test number 4 (Bd-7), a 1" thick AA6061-T6 aluminum plate was bolted to the front of the mounting plate. This 1" thick, wide aluminum plate configuration provided the most rigid end condition out of all the tests. For experiments Bd-2, Bd-3, Bd-10 and Bd-6 a ½" thick AA6061-T6 aluminum plate was used that covered a much smaller area of the front bumper beam extension plate than the end plate did in test Bd-7. The idea with this end condition is that the aluminum plate covers the same area of the front bumper beam extension plate that the weld on bumper crush can would. In Figure 82b it is also observed that the end plate extends past the mounting plate towards the vehicle outboard. This extension is built in to try and facilitate the eccentric start to the folding on the enclosure panel that occurs in the SUV model due to the bumper structure (Figure 82d). A wedged end plate is bolted onto the front bumper beam extension plate in test Bd-9. The wedged plate causes the outboard side of the side frame member rail to be loaded initially causing the irregular start of folding, shown in Figure 82d, on the outboard enclosure panel.

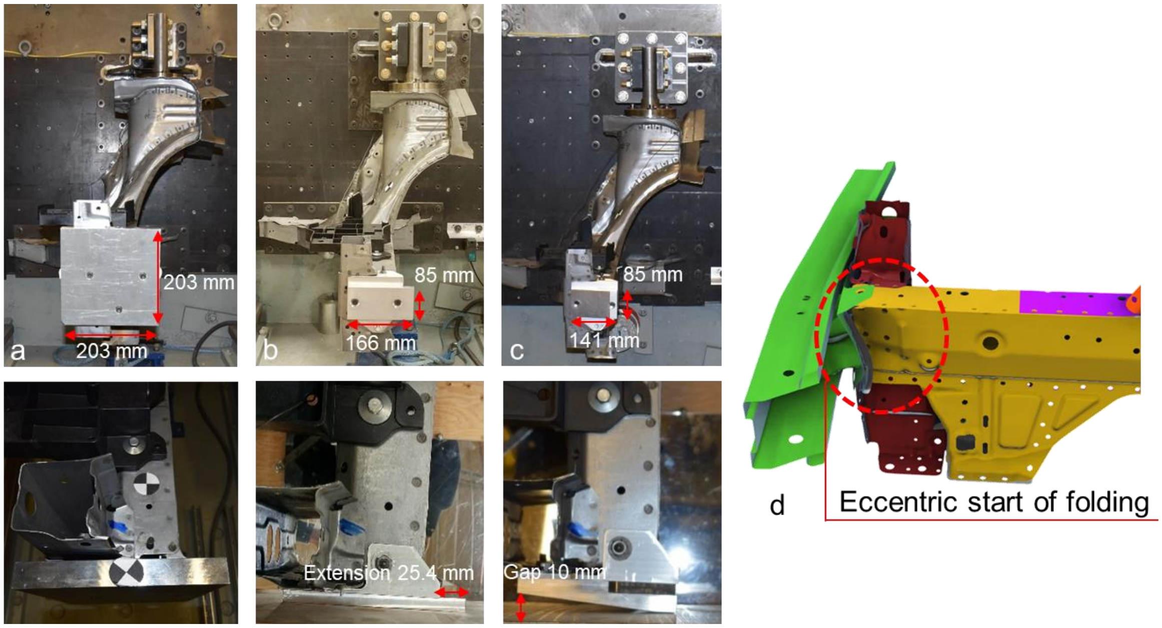

Figure 82. End plate configurations used for test **(a)** Bd-7, **(b)** Bd-2, Bd-3, Bd-10, Bd-6 and **(c)** Bd-9 showing the front view (top) and upper view (bottom) of the baseline front end module. **(d)** The eccentric start of folding shown on the SUV model.

In the ninth baseline front end module test (Bd-6) an additional component was added into the test configuration. The bulkhead brace (Figure 83) connects the side frame member to the lower bulkhead, however in this test the lower bulkhead is not included and therefore the brace is cut 180 mm from the side frame member bolted end.

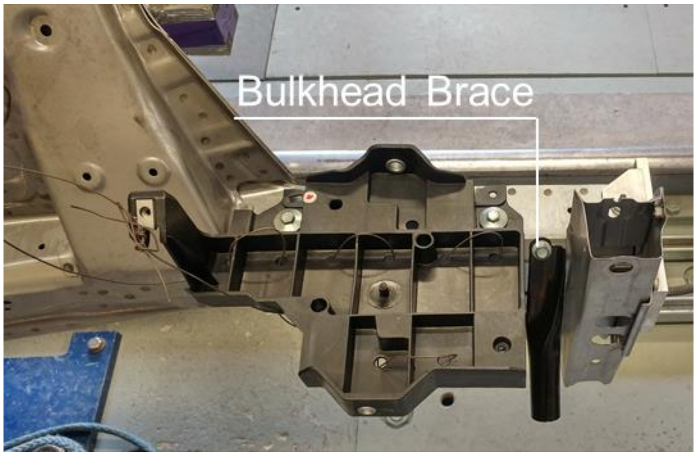

Figure 83. Bulkhead brace component added to baseline front end module Bd-6.

3.3 Baseline Front End Module Frontal Crash Model

The front end module crash model is built from the commercial US-NCAP Full Width Rigid Barrier SUV frontal crash model. Unused modelled subsystems from the SUV frontal crash model were removed until only the necessary components from the front end module remained. Due to the origin of the front end module model the modelling parameters such as element type, element size, contact algorithm and the amount of the through thickness integration points used remain the same as the SUV model presented in Chapter 2 of this thesis.

In the SUV frontal crash model the vehicle is prescribed an initial velocity and impacts a stationary rigid wall. However, because the front end module is tested using a dynamic crash sled the impact boundary conditions change. The front end module is fixed to a rigid wall through upper and lower wall mounts and the crash sled is prescribed an initial velocity, which propels it towards the front end module, as illustrated in Figure 84. Procedural changes were made throughout the baseline front end module crash testing to alter and improve its crash response. A consequence of this iterative testing procedure is that different numerical models were needed for each test to correlate the CAE predictions with the test results.

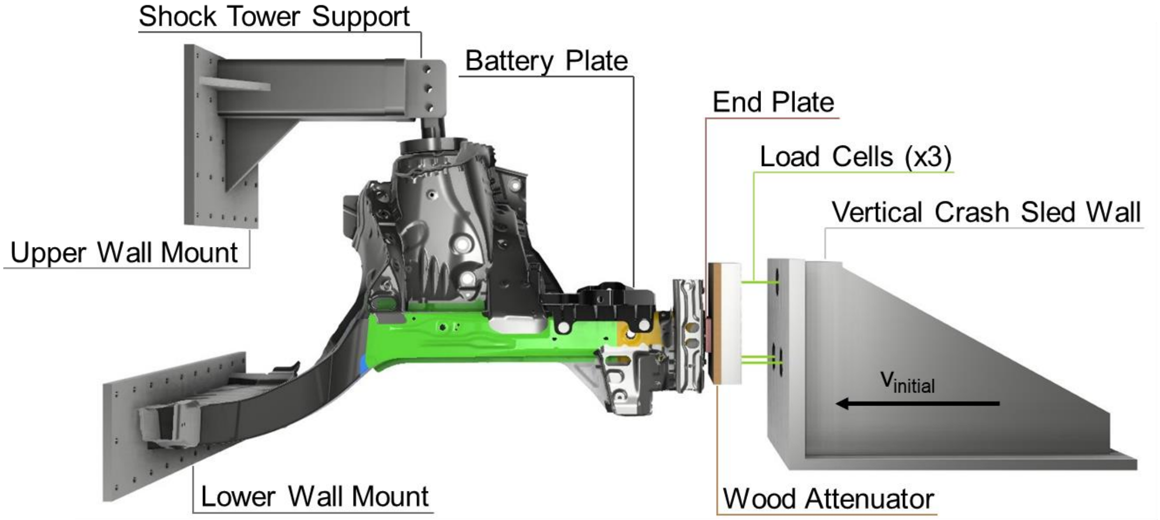

Figure 84. Front end module frontal crash model boundary conditions.

3.3.1 Crash Sled

The crash sled shown in Figure 85 is modelled using a variety of sizes of single integration point solid elements and has been assigned properties of linear elastic steel with the exception of the base plate, which is a rigid body. The gussets and vertical wall of the crash sled are tied together using the contact definition *TIED_SURFACE_TO_SURFACE in LS-Dyna. The load cells are modelled with linear elastic steel spot weld (type 9) beams that are attached to the crash sled and impact face through nodal rigid body constraints.

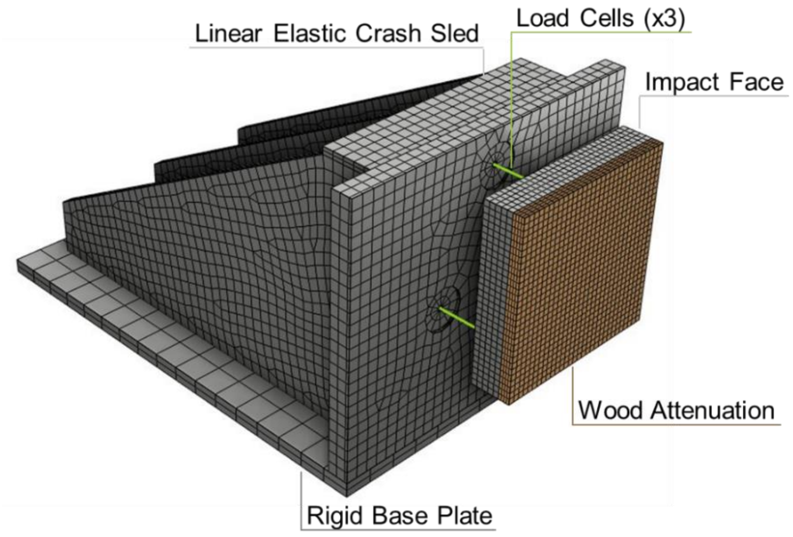

Figure 85. Crash sled modelling method.

To dampen the initial shock load of the impact, the model includes the sheet of wood mounted to the front of the impact face through a surface based, tied contact definition, to represent tests Bd-2, Bd-3, Bd-10, Bd-9 and Bd-6. In the model of experiments Bd-1, Bd-5 and Bd-4, the wood is left free-floating and placed in contact with the aluminum mounting plate on the impacted end of the baseline front end module. A tied contact is not prescribed to the wood attenuator for these tests because of the fact that the glued bond between the mounting plate and wood has very low strength, and was considered negligible. The wood attenuator is modelled with 10 mm single point integration solid elements (type 1). The wood material model used is *MAT_WOOD_PINE, which is a transversely isotropic material, including: hardening rate effects and fracture, with the default properties for Southern Yellow Pine (Table 5). The parallel axis defines the axis along the grain of the wood, which was tested in the z-axis (Figure 85), while the perpendicular axis is oriented against the grain and was tested in the y-axis (Figure 85). Note that in the actual experiments, plywood was used for experiments Bd-1, Bd-5, Bd-4 and Bd-7, while the balance of the experiments used white pine board since Southern Yellow Pine was not readily available. The differences in properties between these grades of pine is not known.

The displacement of the crash sled is monitored from a node on the rigid base plate using the nodal output definition *DATABASE_HISTORY_NODE, which provides nodal displacement, velocity and acceleration over the entire crash event. The crush force exerted by the front end module is monitored using the contact definition *CONTACT_FORCE_TRANSDUCER_PENALTY, which is prescribed a slave surface and forces associated with everything that comes in contact with that surface are recorded. In the numerical models of tests Bd-1, Bd-5 and Bd-4 the force transducer slave surface is the impact face and for the remainder of the modelled tests it is the leading face of the wood attenuator.

Table 5. Southern Pine Wood material properties with moisture content of 30 percent, from Otkur [87].

Stiffness:			**Strength:**		
EL	Parallel Normal Modulus	11.3500 GPa	Xt	Parallel Tensile Strength	0.0400 GPa
ET	Perpendicular Normal Modulus	0.2468 GPa	Xc	Parallel Compressive Strength	0.0133 GPa
GLT	Parallel Shear Modulus	0.7152 GPa	Yt	Perpendicular Tensile Strength	0.0009 GPa
GLR	Perpendicular Shear Modulus	0.0875 GPa	Yc	Perpendicular Compressive Strength	0.0026 GPa
PR	Parallel Major Poisson’s Ratio	0.1568			
Damage:			**Hardening:**		
Gf1	Parallel Fracture Energy in Tension	0.0200 kJ	Npar	Parallel Hardening Initiation	0.5000
Gf2	Parallel Fracture Energy in Shear	0.0415 kJ	Cpar	Parallel Hardening Rate	1008.0000
Bfit	Parallel Softening Parameter	30.0000	Nper	Perpendicular Hardening Initiation	0.4000
Dmax	Parallel Damage Parameter	0.9999	Cper	Perpendicular Hardening Rate	252.0000
Gf1	Perpendicular Fracture Energy in Tension	0.0004 kJ			
Gf2	Perpendicular Fracture Energy in Shear	0.0083 kJ			
Dfit	Perpendicular Softening Parameter	30.0000			
Dmax	Perpendicular Maximum Damage	0.9900			

The entirety of the nodes that make up the crash sled, including the load cells and wood are included in an initial velocity set. The initial velocity prescribed to the crash sled is based on a target sled speed of 51 km/hr for each test except for the first test which had an impact speed of 56 km/hr. In order to match the deceleration rate recorded in each crash test the *LOAD_RIGID_BODY boundary condition card was applied to the rigid base plate on the modelled crash sled to simulate the effect of the honeycomb arrestors. The load curves used to define the honeycomb stacks are calculated based on the cross-sectional area of each block of honeycomb multiplied by the crush strength of the honeycomb. The curves of rigid body load *versus* the displacement of the crash sled used to simulate the honeycomb configuration of each experiment are shown in Figure 86.

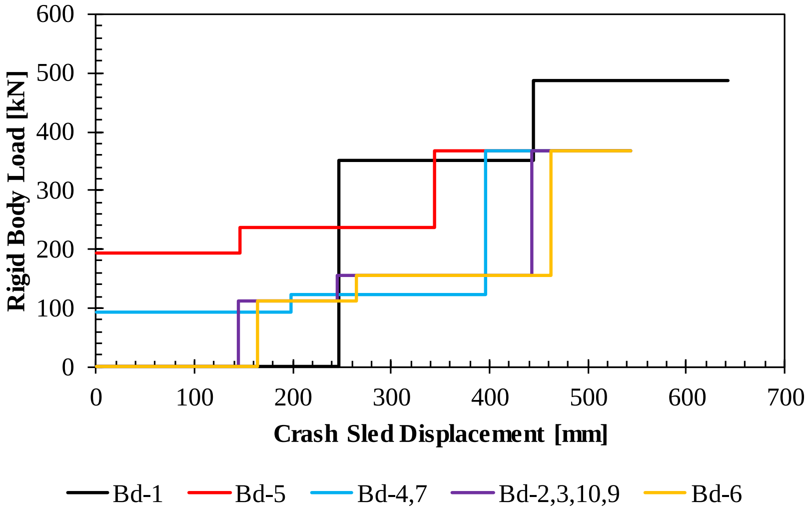

Figure 86. Rigid body load *versus* crash sled displacement curves for each test to simulate the effect of the honeycomb arrestors.

3.3.2 Fixed Barrier Wall

The baseline front end module model must be constrained to the fixed barrier wall, just as it is in the test setup. It is observed in Figure 84 that there are supports connecting the baseline front end module to the fixed barrier wall. The first boundary condition is the shock tower support and the second is the lower wall mount.

The modelled connection between the baseline front end module shock tower and the fixed barrier wall is depicted through the cross-section shown in Figure 87. The shock tower support extends from the fixed barrier wall, which has been modelled by fixing all degrees of freedom of the nodes that lie on the furthest right plane of the shock tower support. The shock tower support is then connected to the bar and upper plate welded component using a tied contact definition. The bar goes through the hole in the shock tower where the shock strut would be mounted and the upper plate then rests on the top face of the shock tower. A lower plate is fit to the underside of the shock tower upper face, where the automatic single surface contact definition maintains a cylindrical joint type boundary condition between the bar and lower plate, as well as contact with the shock tower. All of the solid elements of the shock tower support are modelled with type 1 elements and have been assigned linear elastic steel properties. Bolts are modelled through the three shock tower holes to clamp the shock tower between the lower and upper plates. The bolts are modelled using spot weld beams (type 9) with nodal rigid body connections to each plate. A pre-tension of 50 kN is applied to the bolts through a *INITIAL_AXIAL_FORCE_BEAM boundary condition card.

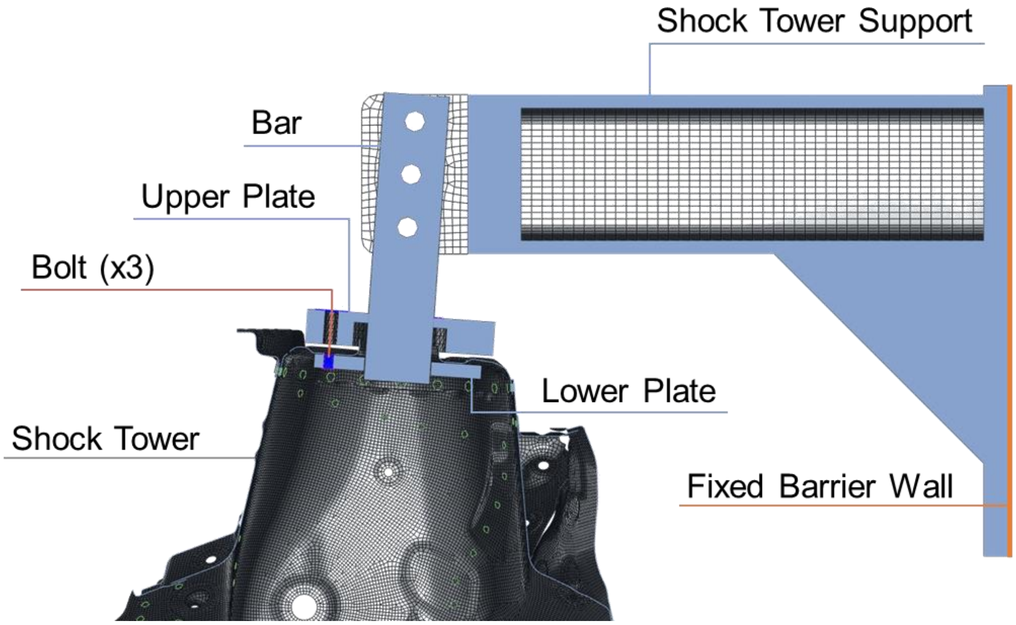

Figure 87. Cross-sectional view of the modelled connection between the baseline front end module shock tower and fixed barrier wall.

The connection between the baseline front end module S-rail and the fixed barrier wall is much simpler than that with the shock tower, as shown in Figure 88. The lower wall mount is fixed on its furthest left face by fixing all degrees of freedom of the nodes that lie on its plane. The baseline front end module is then secured to the lower wall mount through a tied connection that simulates a MIG weld along all the exterior components in contact with the lower wall mount. The lower wall mount is modelled with solid type 1 elements and is assigned the properties of linear elastic steel.

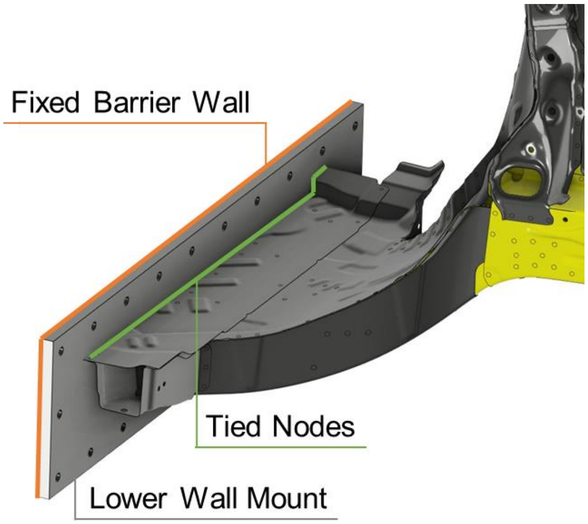

Figure 88. Modelled connection between the baseline front end module and fixed barrier wall.

3.3.3 Modelling Connection of Secondary Components

The secondary components modelled in the baseline front end module include the battery base plate, front bulkhead brace and various end plates. Each of these components bolt onto the baseline front end module in various locations and the bolted connections have been modelled in different ways.

The battery base plate supports the battery in the vehicle and is made from molded fiber reinforced plastic, modelled using tetrahedral solid elements (type 13) and a kinematic hardening material (*MAT3) with a failure strain for element erosion of 0.3. The battery base is connected to the side frame member crush tip using modelled bolts, as shown in Figure 89. Steel bolts, without pretension applied, have been modelled using Hughes-Liu beams (type 1) with cross-section integration and a diameter of 10 mm. The beams are connected to the battery base and side frame member using constrained nodal rigid bodies. To account for failure of the battery base a spot weld beam is placed between two bolt beams using the *CONSTRAINED_SPOTWELD definition. The total normal and shear force for spot weld failure to occur is 9 kN. The normal and shear load exponents are 2 and 3, respectively.

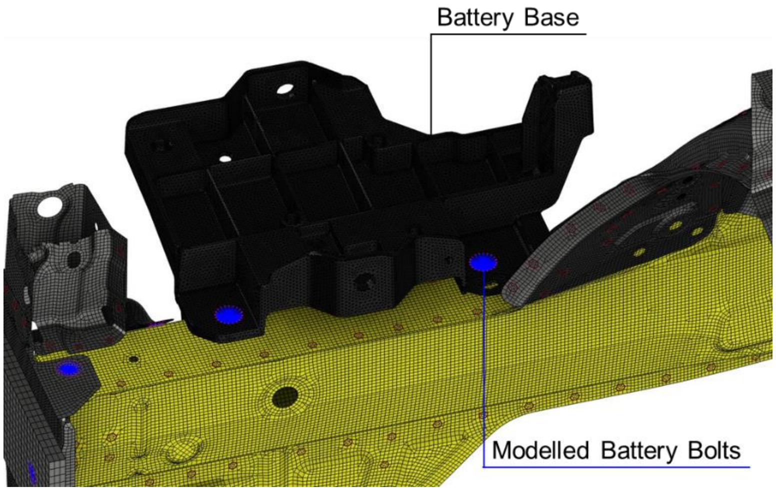

Figure 89. Modelled battery base and its connection to the side frame member.

The front bulkhead brace is trimmed 180 mm from the end that bolts onto the side frame member to remove the unnecessary length of the brace that no longer fixes to the radiator support, as shown in Figure 90. Connection to the side frame member is accomplished through using an 8 mm diameter Hughes-Liu (type 1) beam, which fixes the brace to the side frame member with constrained nodal rigid bodies. It is to be noted that the front bulkhead brace is not incorporated into tests 1 through 8 and therefore their respective models do not include this component.

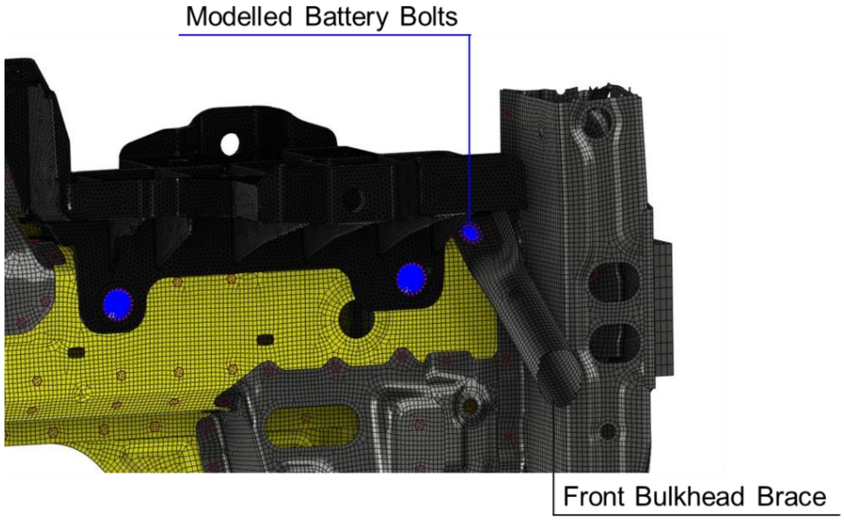

Figure 90. Modelled front bulkhead brace and its connection to the side frame member, as used in Bd-6.

There are four different end plate configurations used in the testing program, as described in section 3.2.2.3. Each of the end plate conditions are modelled using 8 mm single integration point solid elements and are assigned the plastic material properties of 6061-T6 aluminum (material data due to Ambriz and Jaramillo

[88]), as shown in Figure 91. The end plate bolted connection is modelled using spot weld (type 9) beams attached to the end plate and mounting plate with constrained nodal rigid bodies. The spot weld beams are given a typical pretension of an M8 fastener by supplying an initial axial force of 29.2 kN to the beam. Figure 92 shows the different end plate type and connection methods used.

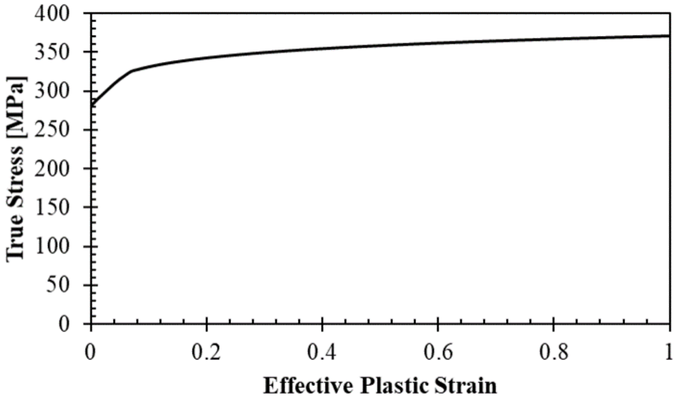

Figure 91. Hardening curve used to define 6061-T6 aluminum end plates. Data due to Ambriz and Jaramillo [88].

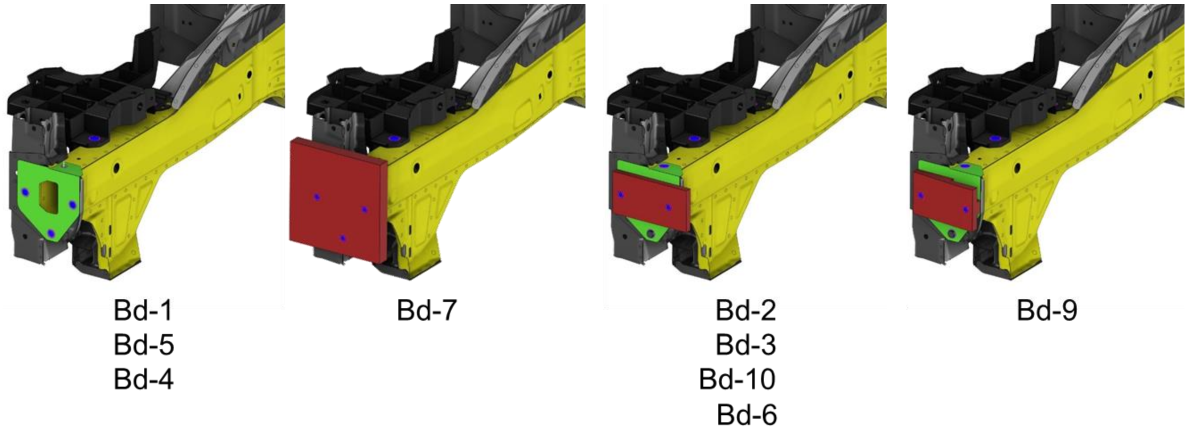

Figure 92. Connection method for each end plate considered in the experimental curriculum.

3.3.4 Sheet Material and Spot Weld Modelling

The sheet material and spot welds are modelled in the same way as described in section 2.2.1, for brevity they will therefore not be explained again for the baseline front end module model.

3.4 Test Results and Numerical Predictions

The baseline front end module test results and their respective numerical model predictions are discussed in this section. Each test or test series (in the case of repeats Bd-2, Bd-3 and Bd-10) is presented in its own sub-section the measured results and numerical predictions for crush modes, sled deceleration, crush force and energy absorption are shown. This section concludes with a summary and discussion of all the baseline front end module testing and numerical modelling.

3.4.1 Test 1: Bd-1

High speed video images from the first baseline front end module (Bd-1) test (conducted by Peister [19]) and its corresponding numerical simulation are shown in Figure 93, Figure 94, Figure 95 and Figure 96 for the outboard side view, outboard isometric view, top view and inboard isometric view, respectively. The fourth frame from the inboard isometric view in Figure 96 has been omitted because the crash sled obscures any useful detail of the specimen's deformation. In the bottom left corner of each frame, the time in milliseconds from the first contact between the crash sled and specimen is shown. The first frame shows the undeformed specimen at first contact of the crash sled. The second frame shows the consolidation of the crush tip, from which point the crush mode changes to a vehicle inboard plastic hinge forming just in front of (to the left of) the forward shock tower support, as illustrated in the third frame. In the fourth frame the specimen has buckled vehicle outboard, with the initiation point being the large fold initiator below the shock tower and just in front of the S-rail section. It is observed in the high speed images that the side frame member rotates to the vehicle outboard due to triggering of the large fold initiator. In the second frame of Figure 95 it is observed that the battery base shears off at approximately 14 ms into the crash event, which is also captured by the model. The deformation modes predicted by the model are nicely capture the deformation modes observed in the experiment.

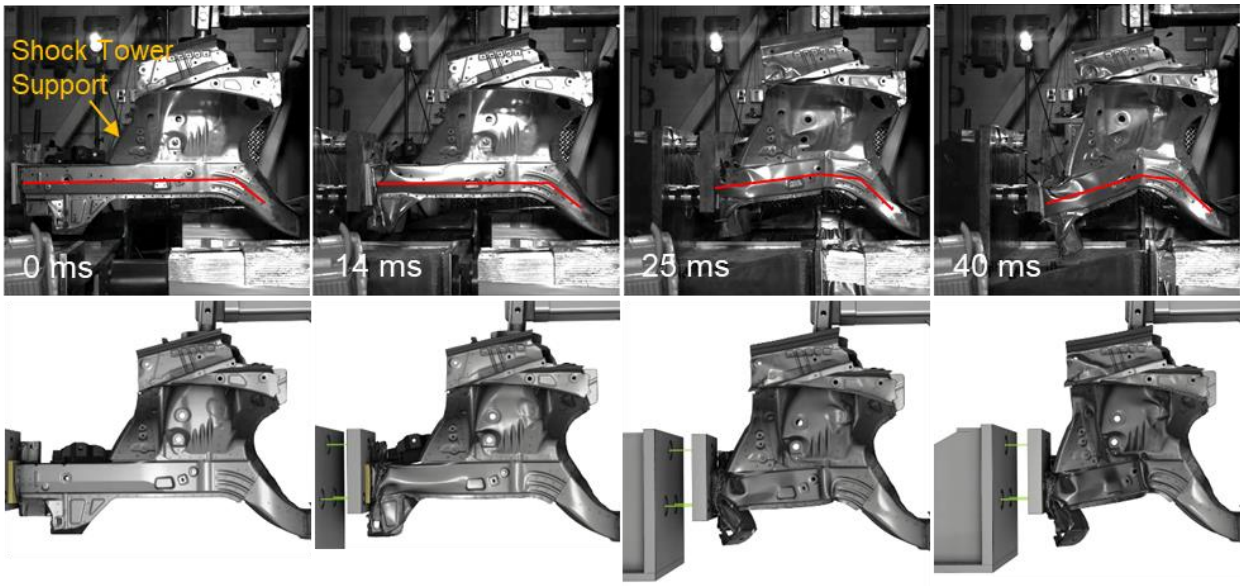

Figure 93. High speed camera images and synchronized model predictions for Bd-1 test showing the deformation modes from the outboard side view.

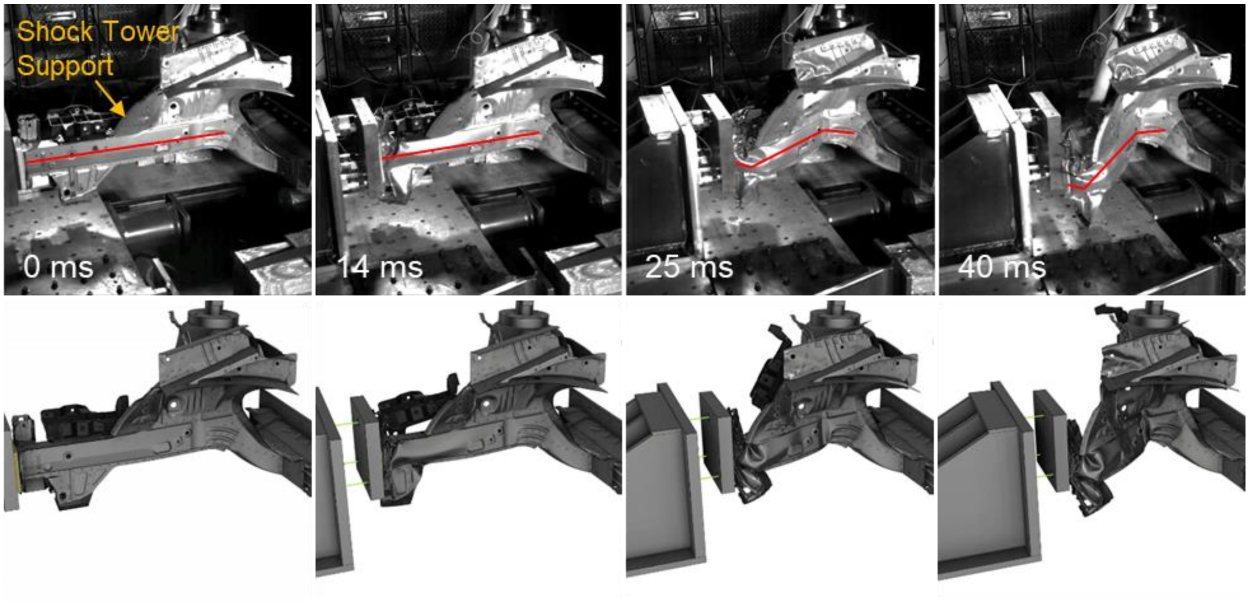

Figure 94. High speed camera images and synchronized model predictions for Bd-1 test showing the deformation modes from the outboard isometric view.

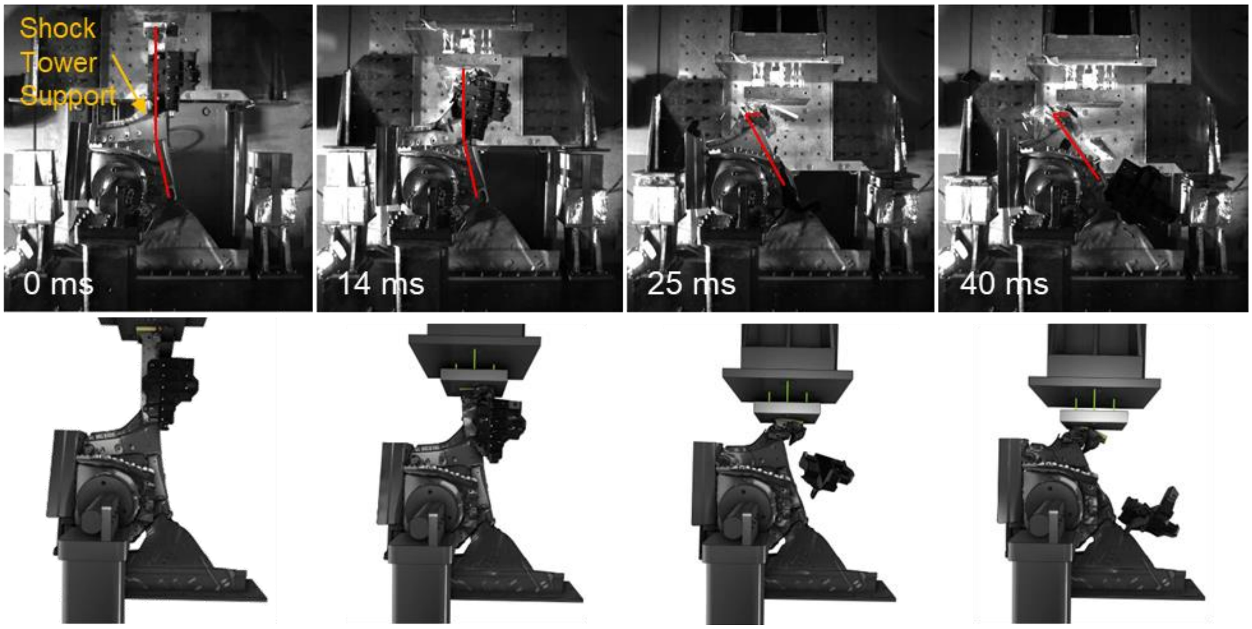

Figure 95. High speed camera images and synchronized model predictions for Bd-1 test showing the deformation modes from the top view. The battery base is noted to shear off at approximately 14 ms.

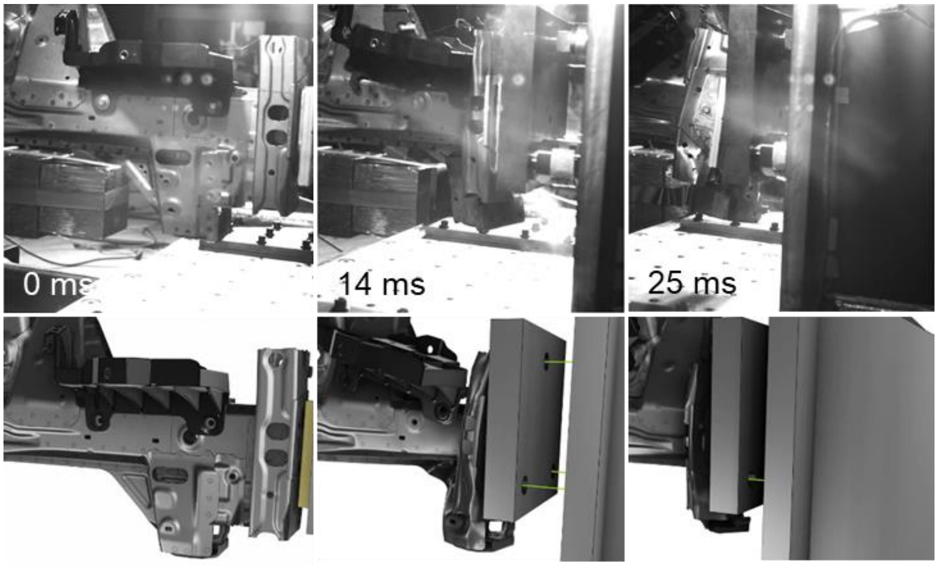

Figure 96. High speed camera images and synchronized model predictions for Bd-1 test showing the deformation modes from the inboard isometric view.

The crash sled deceleration profiles for test Bd-1 and its associated numerical model (Trial 1101) are shown in Figure 97. It is observed from this figure that the measured and predicted crash sled deceleration profiles are almost identical, which is a good indication that the crush behaviour of the model along with the applied rigid body load to simulate the honeycomb are a close match to the test. The final crash sled crush distance is measured to be 409 mm and predicted to be 406 mm.

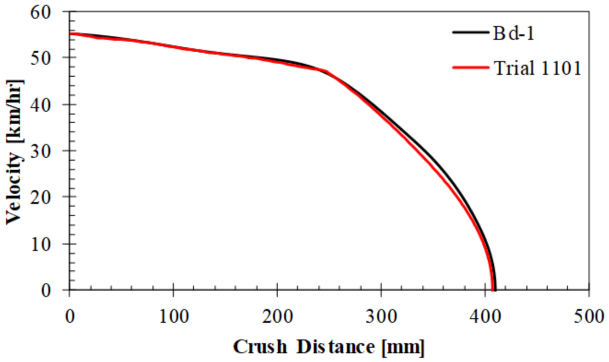

Figure 97. Crash sled deceleration profile for Bd-1 test and its respective numerical model Trial 1101.

The crush force and energy absorption, measured from the load cell pack, are plotted against the crash sled crush distance, as shown in Figure 98. In addition, crush force and energy absorption has been estimated from the accelerometer data (measured in g's) by multiplying it with acceleration due to gravity (9.81 ms^{-2}) and the total mass of the crash sled (803 kg). The estimated crush force from the accelerometer data also includes the force due to the honeycomb and therefore the theoretical honeycomb load was subtracted from the estimated crush force. It is observed that there is a close correlation between the model prediction and test measurement from the load cells. The global trend from the accelerometer estimated crush force coincides very well with the measured load cell data from Bd-1; however, the peak forces do not match those measured from the load cell data, especially after 250 mm of crush distance (coincides with when the honeycomb is activated). Differences in the peak forces between the estimated crush forces from the accelerometer data and the load cell data are attributed to the increased measurement noise associated with accelerometer measurements. The measured peak force from the impact is 166 kN, while the predicted peak force is 141 kN. Over the first 300 mm of crush distance, the measured average force is 104 kN and the predicted average force is 108 kN. The calculated energy absorption from the load cell and accelerometer data is 36 kJ, while the predicted energy absorption is 38 kJ. For brevity, the estimated crush force from the accelerometer data will not be included in each of the test result sections.

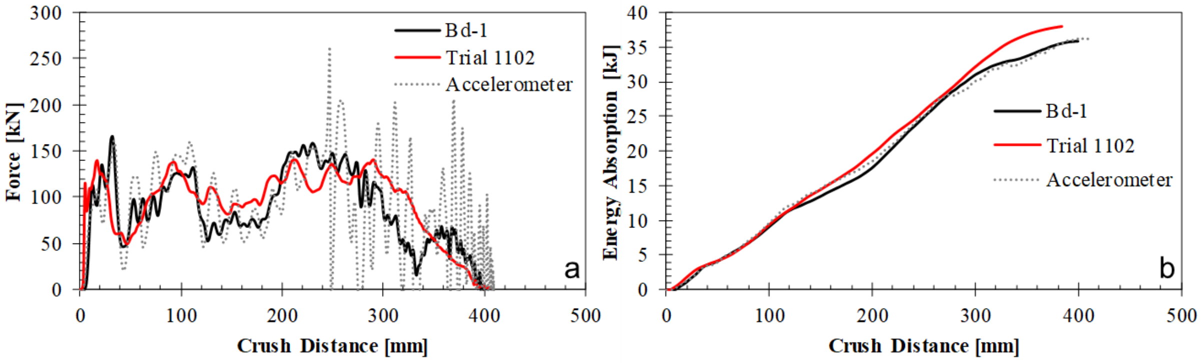

Figure 98. (a) Crush force and **(b)** energy absorption for test Bd-1 and its respective model Trial 1101.

3.4.2 Test 2: Bd-5

In the second baseline front end module (Bd-5) test (conducted by Peister [19]) the free crush distance was reduced to 0 mm, meaning that the honeycomb is activated as soon as the crash sled impacts the specimen. In addition, the impact speed was reduced and the honeycomb sizes increased. The high speed video images and synchronized model results are shown in Figure 99, Figure 100, Figure 101 and Figure 102 for Bd-5 in the outboard side view, outboard isometric view, top view and inboard isometric view, respectively. It is observed from the high speed video images that the combination of reduced free crush distance, reduced impact speed and increased honeycomb sizes caused the crash sled to be arrested too early, not fully crushing the specimen as represented by the fourth frame, which corresponds to the end of the test.

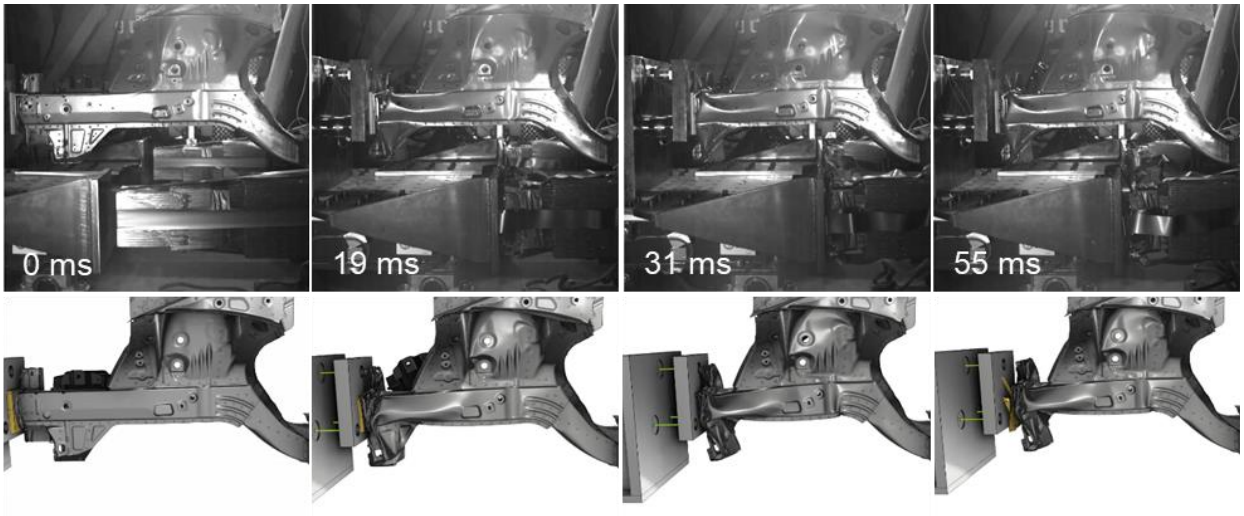

Figure 99. High speed camera images and synchronized model predictions for Bd-5 test showing the deformation modes from the outboard side view.

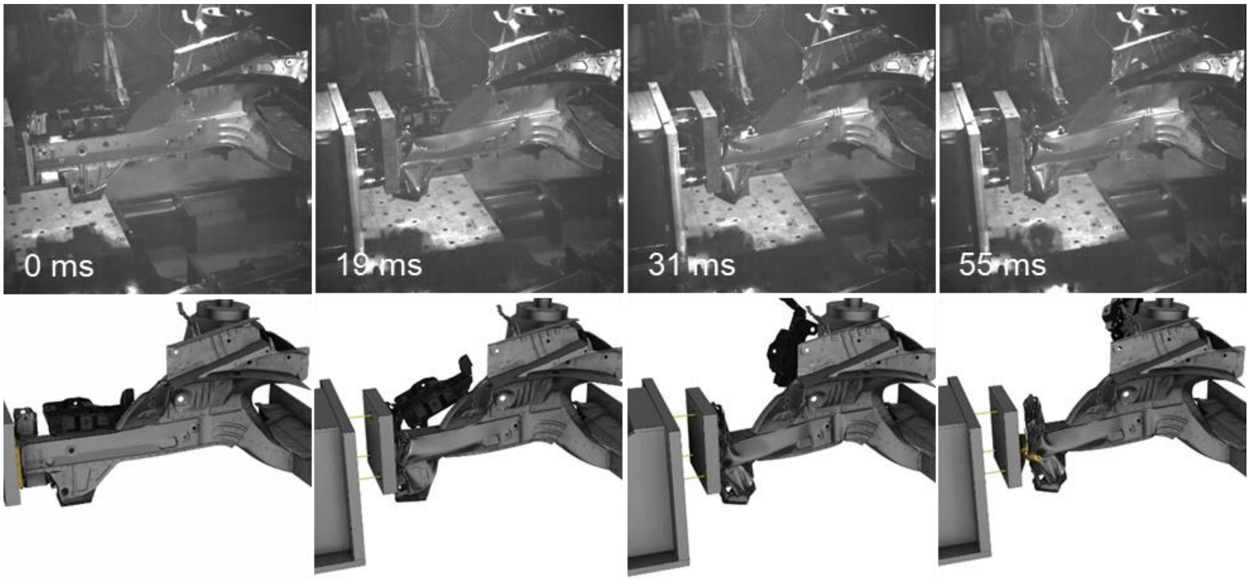

Figure 100. High speed camera images and synchronized model predictions for Bd-5 test showing the deformation modes from the outboard isometric view.

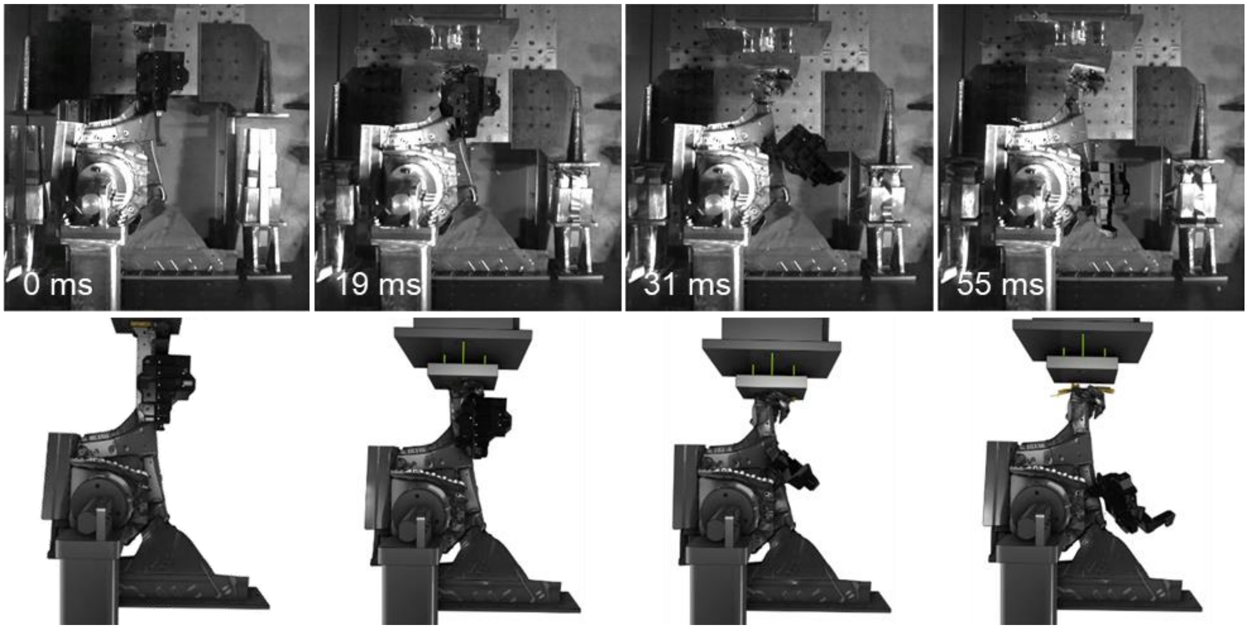

Figure 101. High speed camera images and synchronized model predictions for Bd-5 test showing the deformation modes from the top view.

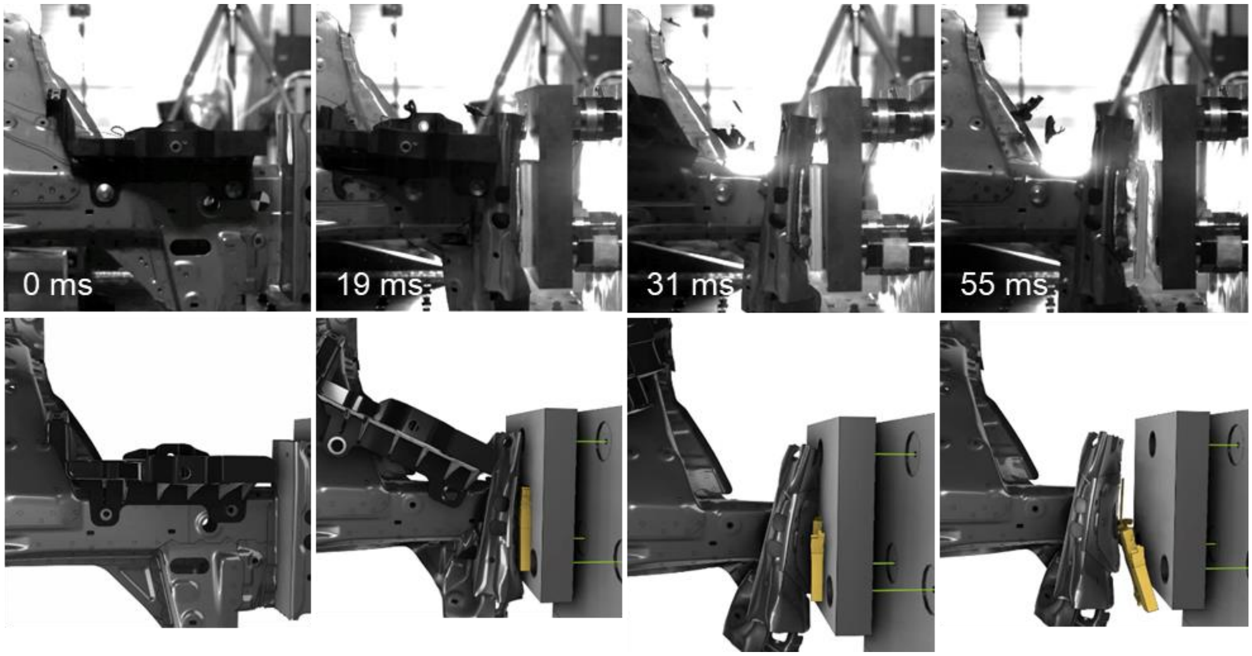

Figure 102. High speed camera images and synchronized model predictions for Bd-5 test showing the deformation modes from the inboard isometric view.

The crash sled deceleration profiles for test Bd-5 and its associated numerical model (Trial 1202) are shown in Figure 103. The measured and predicted crash sled deceleration profiles are almost identical, which is a good indication that the crush behaviour of the model along with the applied rigid body load to simulate the honeycomb are a close match to the test. The final crash sled crush distance is measured to be 246 mm and predicted to be 247 mm.

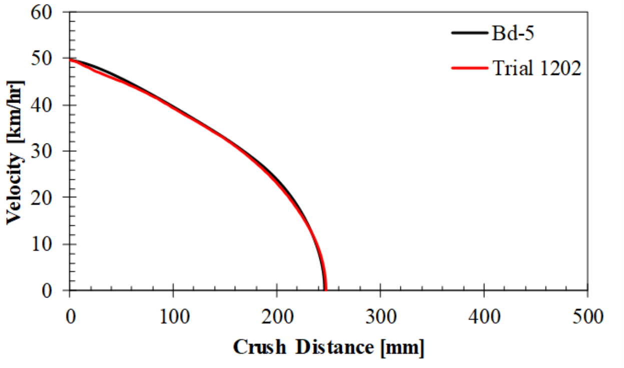

Figure 103. Crash sled deceleration profile for Bd-5 test and its respective numerical model Trial 1202.

The crush force and energy absorption plotted against the crash sled crush distance are shown in Figure 104. It is observed that there is a close correlation between the model prediction and test measurement from the load cells up until approximately 200 mm of displacement, after which the force is under predicted by the model. The measured peak force from the impact is 160 kN, while the predicted peak force is 138 kN. Over the first 200 mm of crush distance the measured average force is 87 kN and the predicted average force is 95 kN. Both the calculated energy absorption from the measured force values and the predicted energy absorption are 24 kJ.

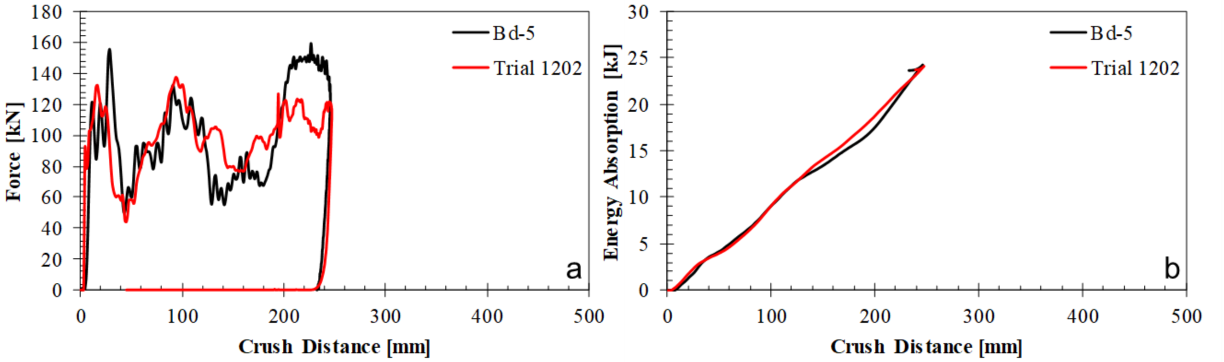

Figure 104. **(a)** Crush force and **(b)** energy absorption for test Bd-5 and its respective model Trial 1202.

3.4.3 Test 3: Bd-4

In the third baseline front end module (Bd-4) test (conducted by Peister [19]) the honeycomb sizes were decreased to increase the crush distance of the sled. High speed camera images and synchronized model deformation predictions are shown in Figure 105, Figure 106 and Figure 107 in the outboard side view, outboard isometric view and inboard side view, respectively. The top view is omitted because of triggering issues during testing. The deformation is very comparable to Bd-1, with the same crush modes being observed. The plywood piece added to the impacted end of the baseline front end module is observed to eject away from the specimen, in both the test and simulation, as shown in Figure 107.

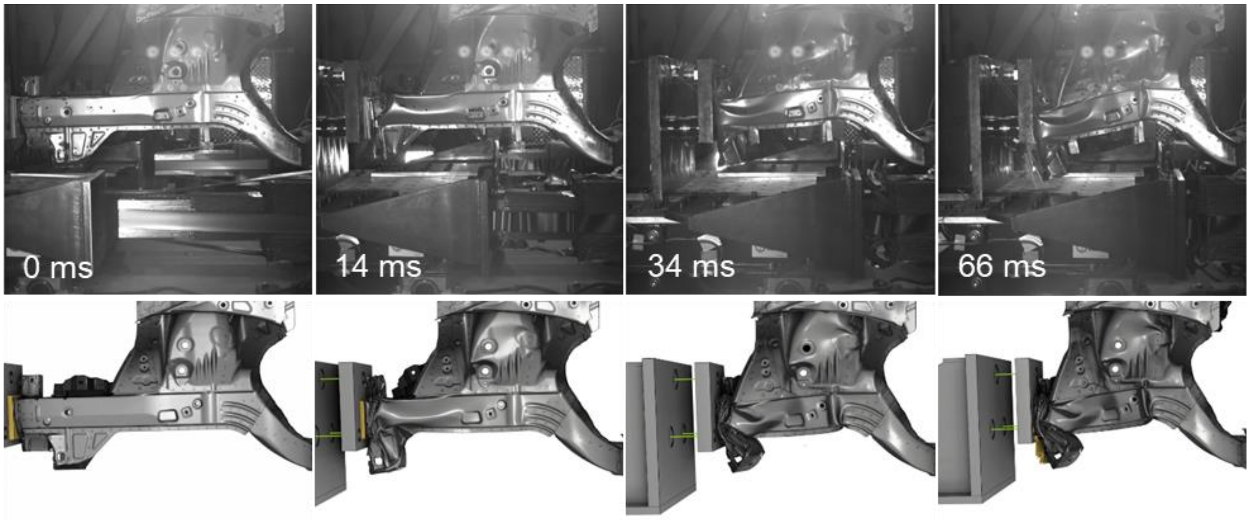

Figure 105. High speed camera images and synchronized model predictions for Bd-4 test showing the deformation modes from the outboard side view.

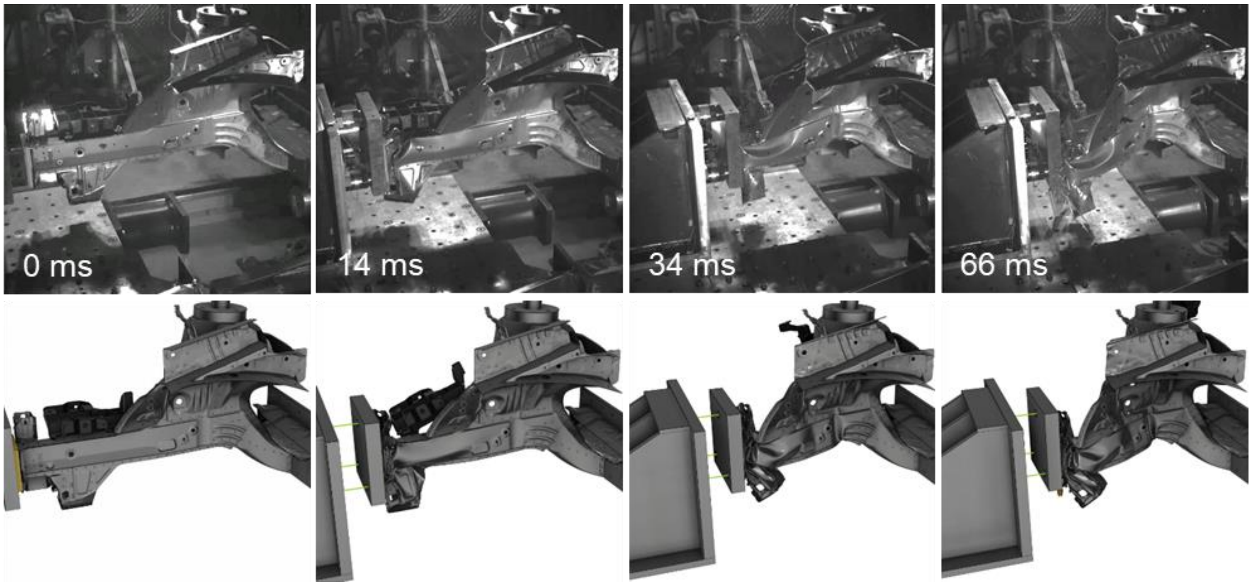

Figure 106. High speed camera images and synchronized model predictions for Bd-4 test showing the deformation modes from the outboard isometric view.

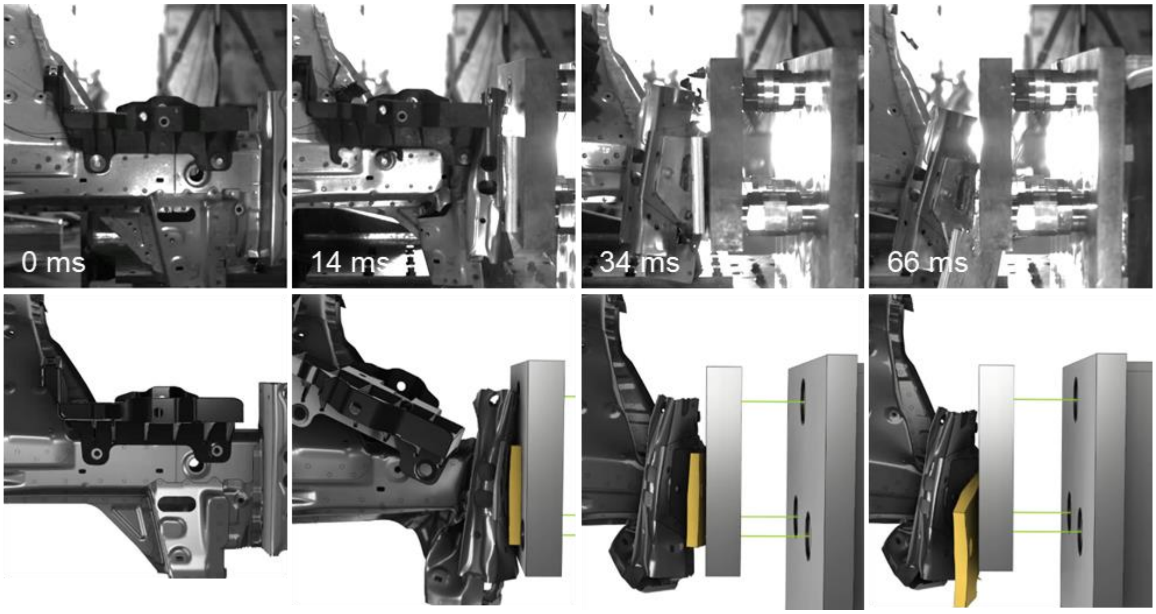

Figure 107. High speed camera images and synchronized model predictions for Bd-4 test showing the deformation modes from the inboard isometric view. Plywood ejected from specimen in both the test and simulation.

The crash sled deceleration profiles for test Bd-4 and its associated numerical model (Trial 1301) are shown in Figure 108. A good correlation between the tested and modelled deceleration profile is observed up until 300 mm of crash sled crush distance, at which point the model under predicts the deceleration of the test specimen. The final crash sled crush distance is measured to be 357 mm and predicted to be 370 mm.

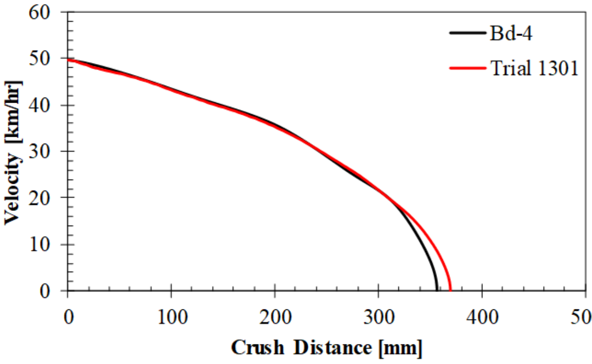

Figure 108. Crash sled deceleration profile for Bd-4 test and its respective numerical model Trial 1301.

The crush force and energy absorption plotted against the crash sled crush distance are shown in Figure 109. It is observed that there is a very close correlation between the model prediction and test measurement from the load cells. The measured peak force from the impact is 163 kN, while the predicted peak force is 138 kN. Over the first 300 mm of crush distance the measured average force is 100 kN and the predicted average force is 105 kN. Both the calculated energy absorption from the measured force values and the predicted energy absorption are 33 kJ.

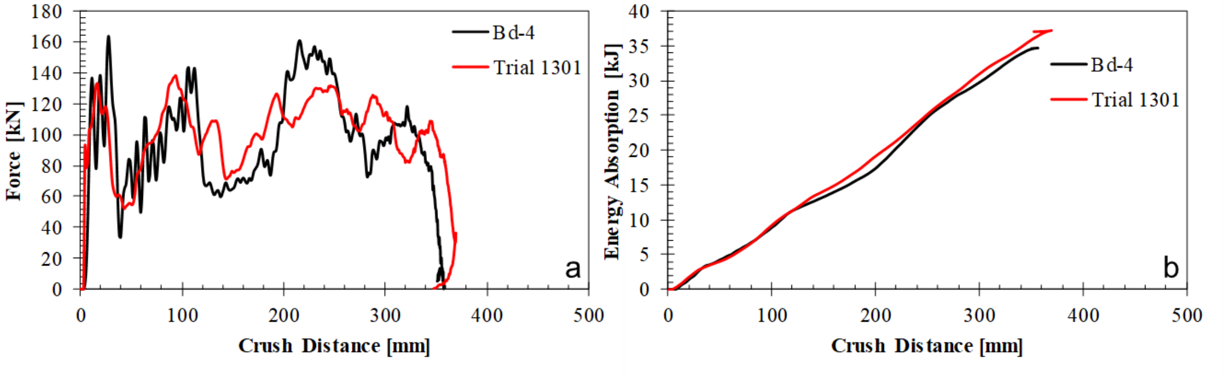

Figure 109. (a) Crush force and **(b)** energy absorption for test Bd-4 and its respective model Trial 1301.

3.4.4 Test 4: Bd-7

In the fourth baseline front end module test (Bd-7) the honeycomb configuration and crash sled impact speed remained the same as Bd-4. The major change in this test was the impacted end boundary condition, in which the plywood is mounted to the front of the crash sled and a large aluminum plate is added to the front of the specimen. The high speed video images and synchronized model results are shown in Figure 110 and Figure 111 for Bd-7 in the outboard isometric view and inboard isometric view, respectively. The top view is not included because insufficient lighting was used to illuminate the part, making it impossible to observe the deformation. In addition, the outboard side view is not included because the camera angle used does not capture the initial crush of the side frame member crush tip. It is observed from the high speed video frames shown that the addition of the large aluminum plate to the impacted end of the specimen causes a catastrophic plastic hinge to form behind the first shock tower support. This premature plastic hinge formation allows only a small portion of the crush tip to consolidate before the crush mode transfers from energy absorption through sequential folding to a global buckle dominant crush mode.

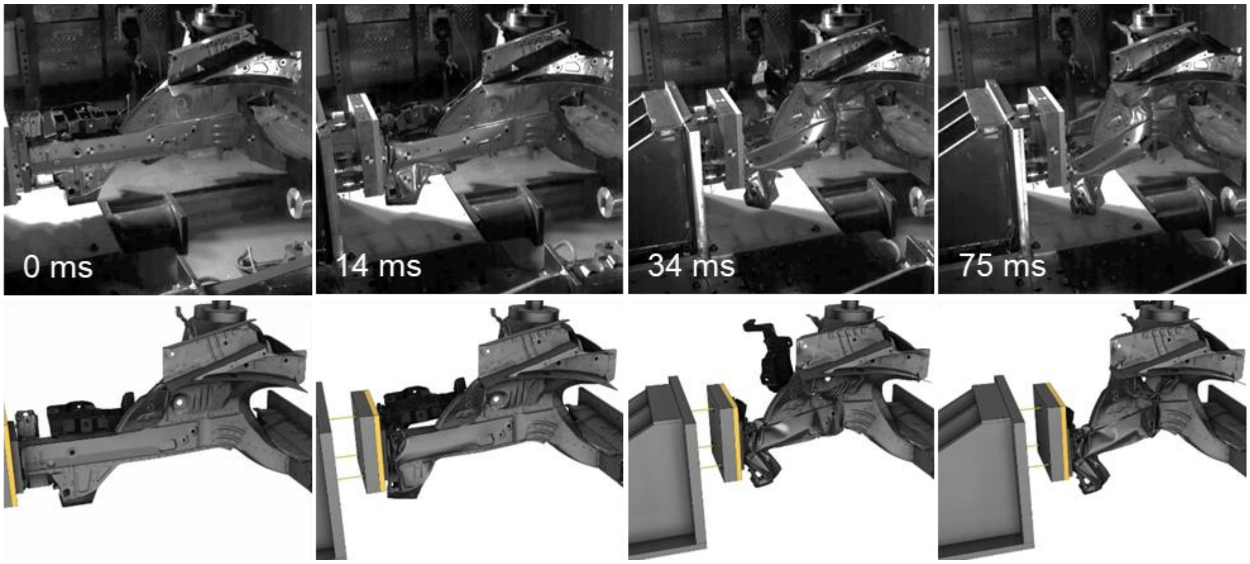

Figure 110. High speed camera images and synchronized model predictions for Bd-7 test showing the deformation modes from the outboard isometric view.

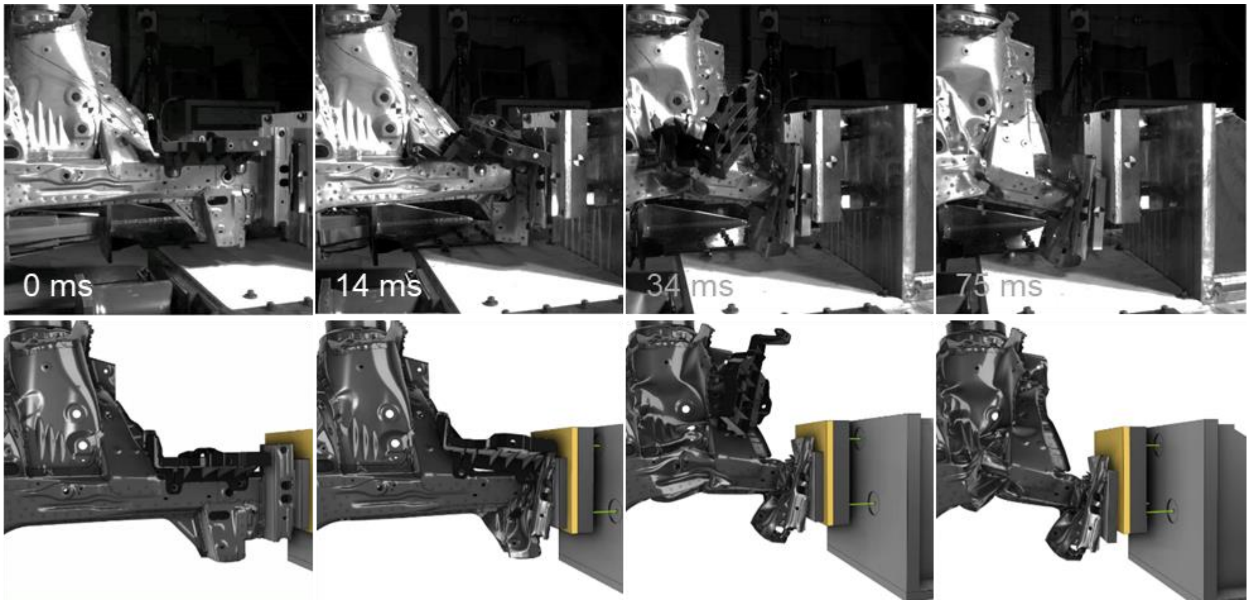

Figure 111. High speed camera images and synchronized model predictions for Bd-7 test showing the deformation modes from the inboard isometric view.

The crash sled deceleration profile for specimen Bd-7 and its corresponding numerical simulation (Trial 1402) are shown in Figure 112. It is quite apparent from the two velocity profiles that there is a significant discrepancy between the measured deceleration profile and that predicted with the model. The reason for the over prediction of crash sled deceleration can be explained by observing the inboard side honeycomb stack behaviour during the initial stages of the crash event, as shown in Figure 113. It is highlighted in this figure that as the crash sled impact progresses the inboard honeycomb stack buckles upward, significantly reducing the energy absorbed by the honeycomb. The reduced energy absorption from the honeycomb explains why the measured crush distance of 439 mm exceeds the predicted distance by 62 mm (377 mm).

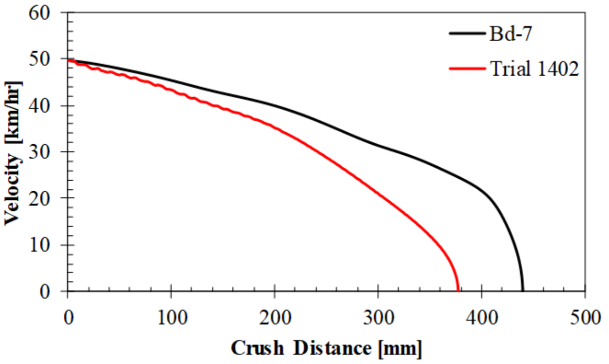

Figure 112. Crash sled deceleration profile for Bd-7 test and its respective numerical model Trial 1402.

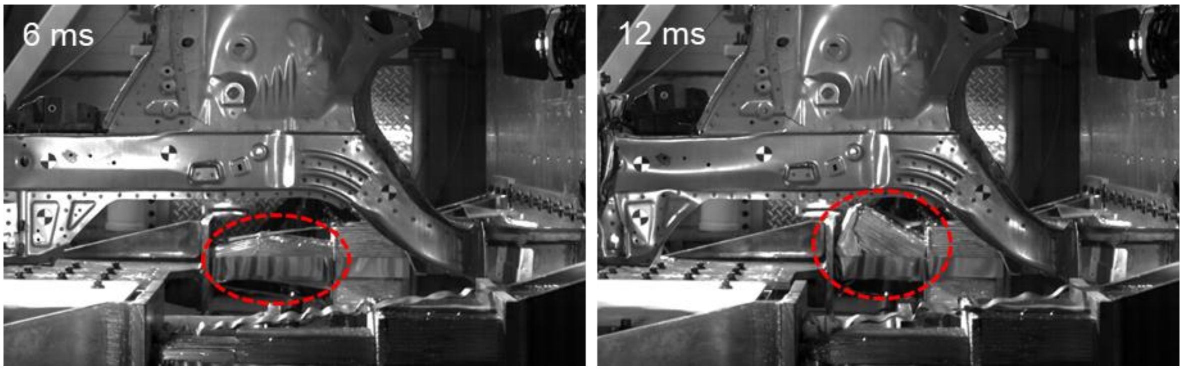

Figure 113. Vehicle inboard honeycomb stack buckles upward very early in the crush of Bd-7.

The crush force and energy absorption plotted against the crash sled crush distance are shown in Figure 114. Contrary to the fact that the measured and simulated deceleration profiles differ so greatly, a very close correlation between the model prediction and test measurement from the load cells is observed. The measured peak force from the impact is 291 kN, while the predicted peak force is 331 kN. Over the first 300 mm of crush distance the measured average force is 99 kN and the predicted average force is 110 kN. Both the calculated energy absorption from the measured force values and the predicted energy absorption are 34 kJ.

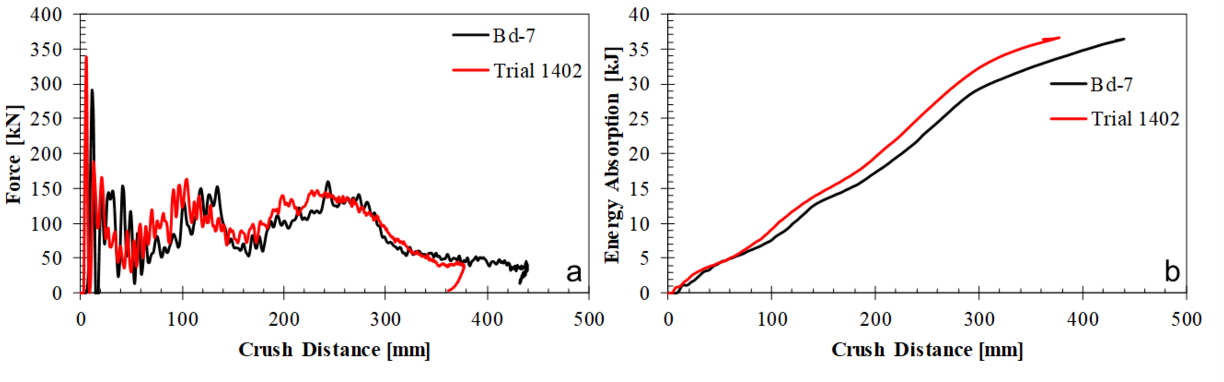

Figure 114. (a) Crush force and **(b)** energy absorption for test Bd-7 and its respective model Trial 1402.

3.4.5 Tests 5, 6 and 7: Bd-2, Bd-3 and Bd-10

The fifth, sixth and seventh baseline front end module tests (Bd-2, Bd-3 and Bd-10) were tested with identical conditions and are therefore reported together in this sub-section. To promote further crash sled crush distance in this series of three tests, a free crush distance of 145 mm is used, as well as smaller honeycomb blocks in the stack. A small aluminum plate is added to the impacted end of each specimen and the pine board is mounted to the front of the crash sled. One numerical model (Trial 1501) was created to represent each of the three test specimens and their associated boundary conditions. High speed video images and synchronized model results for the three tests are shown in Figure 115 and Figure 116 in the outboard isometric view and inboard isometric view, respectively.

It is observed in both Figure 115 and Figure 116 that each of the three tests yield different deformation modes. In specimen Bd-2 full consolidation of the side frame member crush tip occurs (frame 2), followed by a plastic hinge being formed in front of the foremost shock tower support (frame 3) and then slightly later in the crash another plastic hinge behind the shock tower support (frame 4). Specimen Bd-3 also displayed full consolidation of the side frame member crush tip (frame 2) as well as the formation of a plastic hinge in front of the shock tower support (frame 3), however an additional plastic hinge behind the shock tower support was not observed. Similar to the other two tests, full consolidation of the side frame member crush tip is observed in specimen Bd-10, however only a plastic hinge behind the shock tower support is observed in the deformation.

One model was created to correlate with the test results, however of the three tests performed under identical boundary conditions three different deformation modes were observed. It is therefore impossible for the model to correlate to each of the test specimen. In observing the simulated deformation modes it is noticed that the numerical model correlates well to the deformation modes displayed in specimen Bd-10.

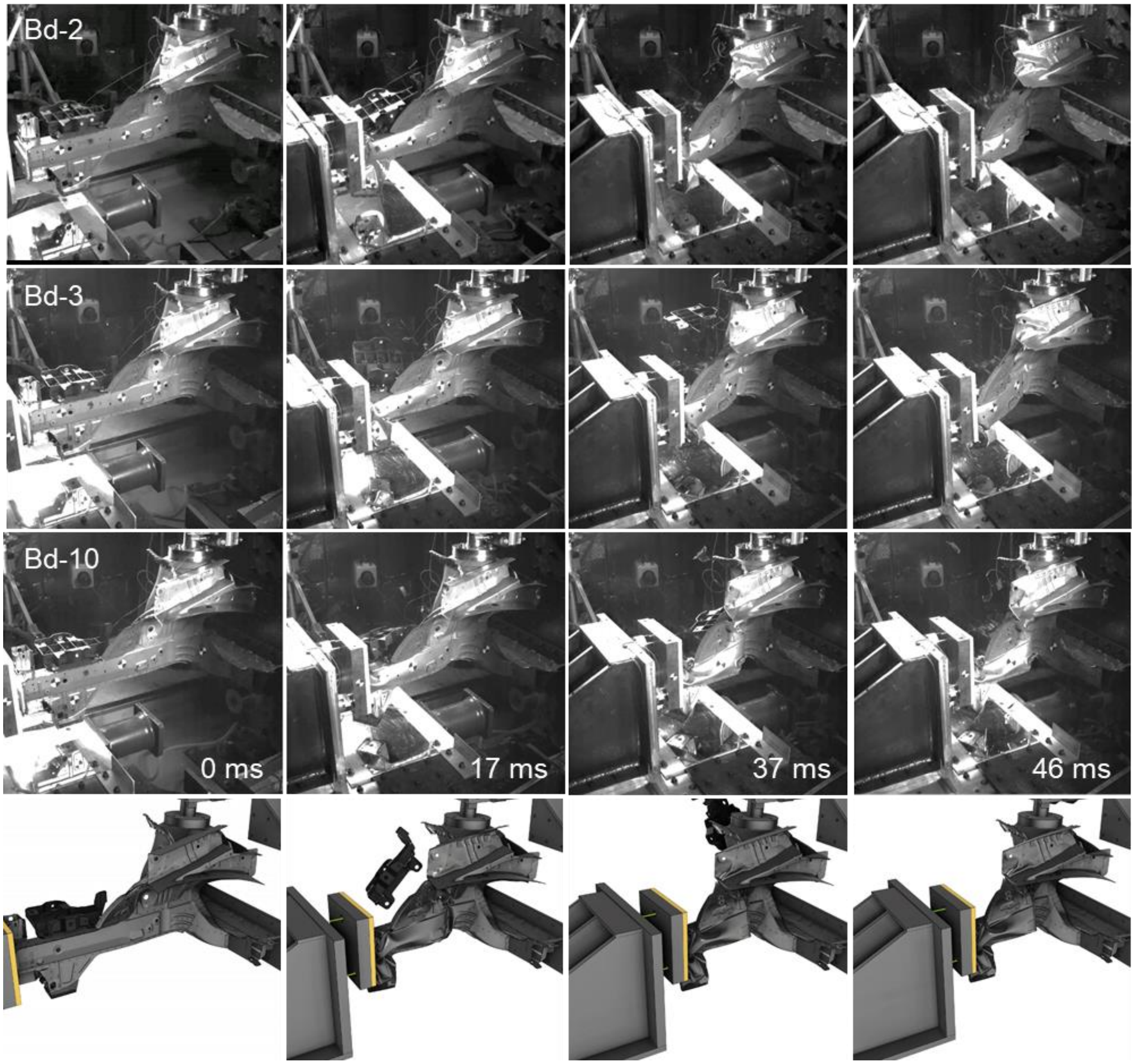

Figure 115. High speed camera images and synchronized model predictions for Bd-2, Bd-3 and Bd-10 tests showing the deformation modes from the outboard isometric view.

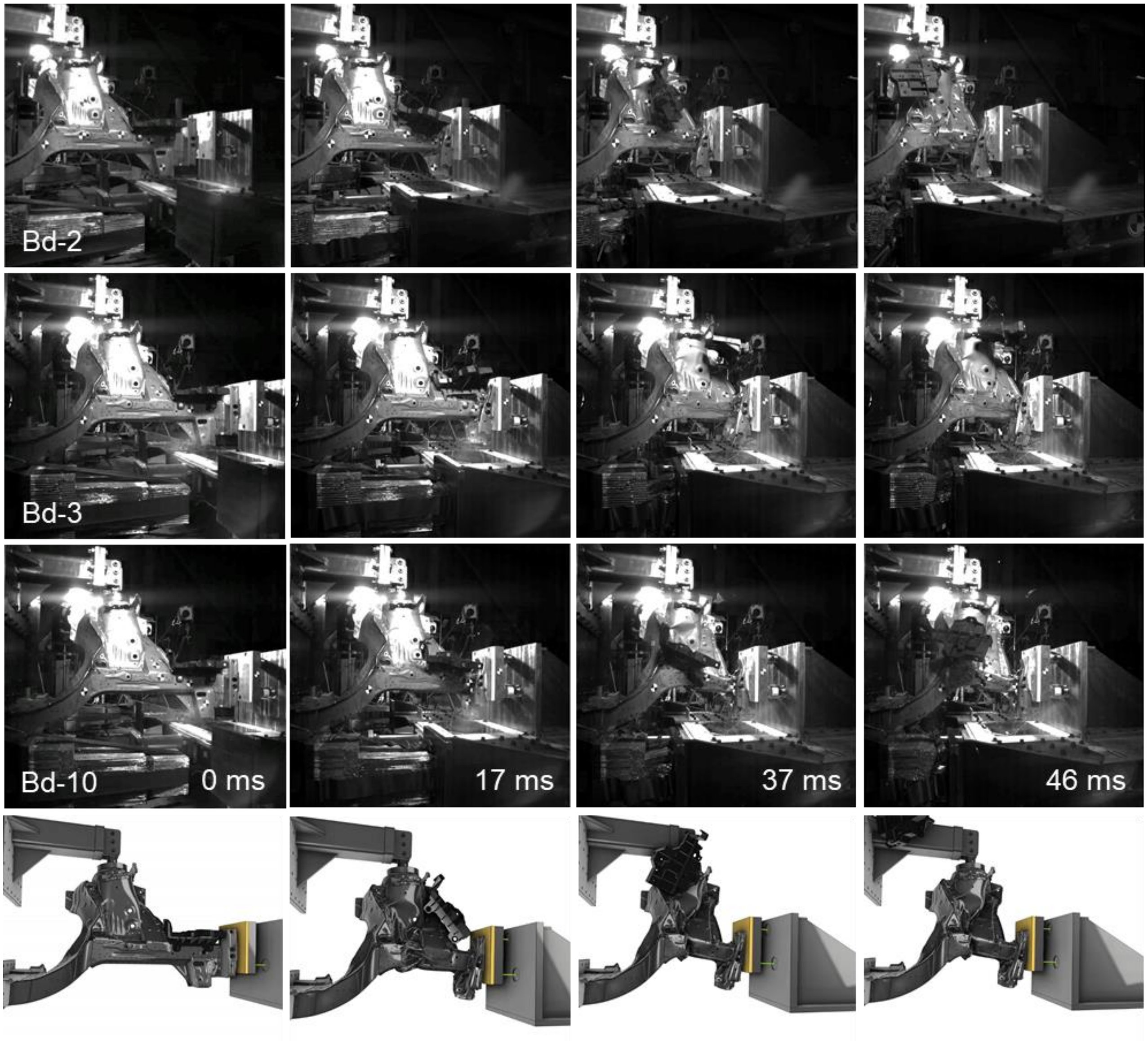

Figure 116. High speed camera images and synchronized model predictions for Bd-2, Bd-3 and Bd-10 tests showing the deformation modes from the inboard isometric view.

The crash sled deceleration profiles for tests Bd-2, Bd-3 and Bd-10 as well as their associated numerical model Trial 1501 are shown in Figure 117. Though the deformation modes of each test were noticeably different, the overall effect on the deceleration profile and sled crush distance is very slight. The previously mentioned correlation between specimen Bd-10 and the numerical model is observed to hold true by comparing the deceleration profiles, which are almost identical. The measured crash sled crush distance for Bd-2, Bd-3 and Bd-10 are 420 mm, 420 mm and 433 mm, respectively. The predicted crash sled crush distance is 443 mm, which still over predicts specimen Bd-10 by 10 mm.

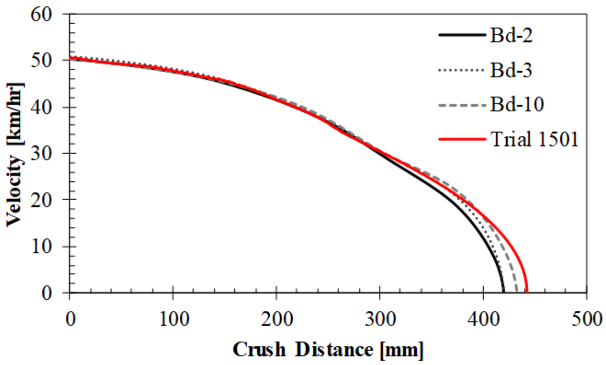

Figure 117. Crash sled deceleration profile for Bd-2, Bd-3 and Bd-10 tests and their respective numerical model Trial 1501.

The crush force and energy absorption plotted against the crash sled crush distance are shown in Figure 118. It is observed that there is a very close correlation between the model prediction and test measurement for specimen Bd-10 from the load cells throughout the duration of the crash event. It is also observed that within the first 240 mm of crush distance that the measured force from each specimen follow a similar profile and have very similar magnitudes. The measured peak force from the impact for specimen Bd-2, Bd-3 and Bd-10 are 155 kN, 176 kN and 164 kN, respectively, while the predicted peak force is 166 kN. Over the first 300 mm of crush distance, the measured average forces for specimen Bd-2, Bd-3 and Bd-10 are 104 kN, 101 kN and 99 kN, respectively, while the predicted average force is 95 kN. The calculated energy absorption from the measured force values are 38 kJ, 36 kJ and 34 kJ for Bd-2, Bd-3 and Bd-10, respectively, and the predicted energy absorption is 34 kJ.

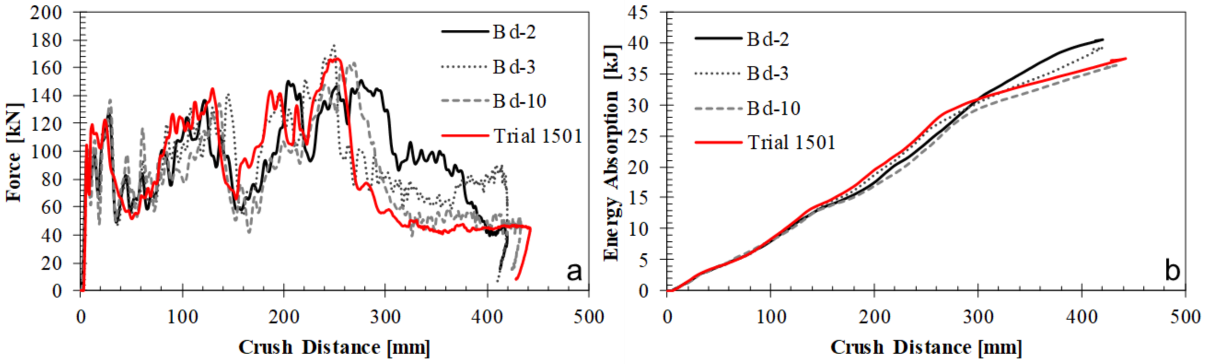

Figure 118. (a) Crush force and **(b)** energy absorption for tests Bd-2, Bd-3, Bd-10 and their respective model Trial 1501.

3.4.6 Test 8: Bd-9

In baseline front end module test number 8 (Bd-9), a wedged block of aluminum is added to the impacted end of the specimen, while all other test conditions remain the same as tests 5, 6 and 7 (Bd-2, Bd-3 and Bd-10, respectively). The high speed video images and synchronized model results are shown in Figure 119 and Figure 120 for Bd-9 in the outboard side view and inboard isometric view, respectively. It is observed from frame 2 that full consolidation of the side frame member's crush tip occurs but is followed by a global buckle aft of the shock tower support (frame 3). The numerical model accurately captures both the consolidation of the crush tip as well as the global buckle aft of the shock tower support. In frame 4 of Figure 120 it is observed that in the test the pine board fractures away, whereas in the simulation the wood remains intact with only small amounts of fracture occurring.

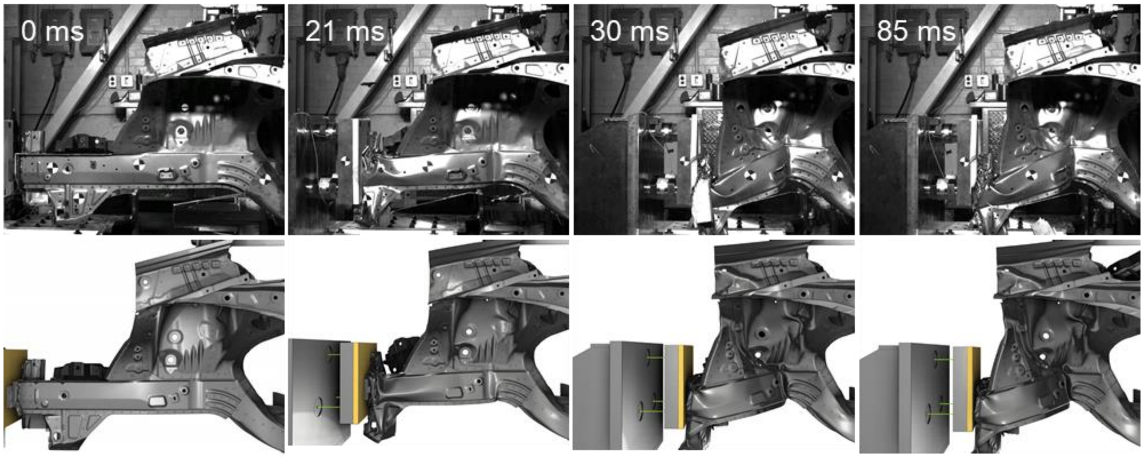

Figure 119. High speed camera images and synchronized model predictions for Bd-9 test showing the deformation modes from the outboard side view.

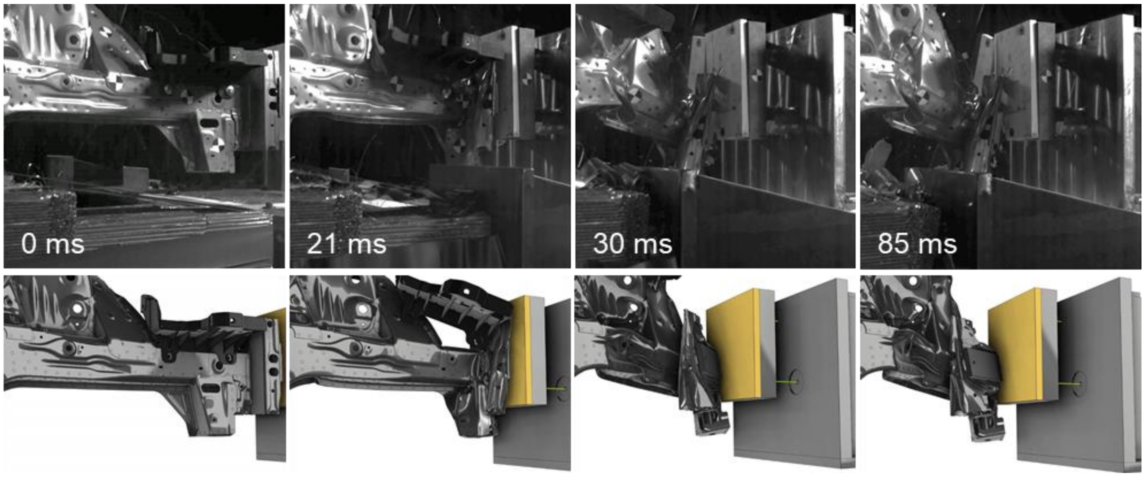

Figure 120. High speed camera images and synchronized model predictions for Bd-9 test showing the deformation modes from the inboard isometric view.

The crash sled deceleration profiles for test Bd-9 and its associated numerical model (Trial 1601) are shown in Figure 121. A good correlation between the tested and modelled deceleration profile is observed up until 200 mm of crash sled crush distance, at which point the model over predicts the deceleration of the crash sled. This over predicted deceleration causes the predicted final crash sled crush distance to be 28 mm less than (437 mm) the measured crush distance of 465 mm.

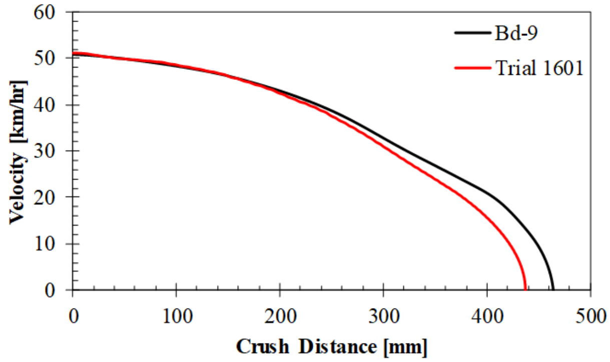

Figure 121. Crash sled deceleration profile for Bd-9 test and its respective numerical model Trial 1601.

The crush force and energy absorption plotted against the crash sled crush distance are shown in Figure 122. Despite there being a discrepancy between the simulated and measured crash sled crush distance it is observed that the simulated and measured crush forces are very similar. The measured peak force from the impact is 145 kN, while the predicted peak force is 151 kN. Over the first 300 mm of crush distance the measured average force is 101 kN and the predicted average force is 106 kN. The calculated energy absorption from the measured force values is 37 kJ and the predicted energy absorption is 36 kJ.

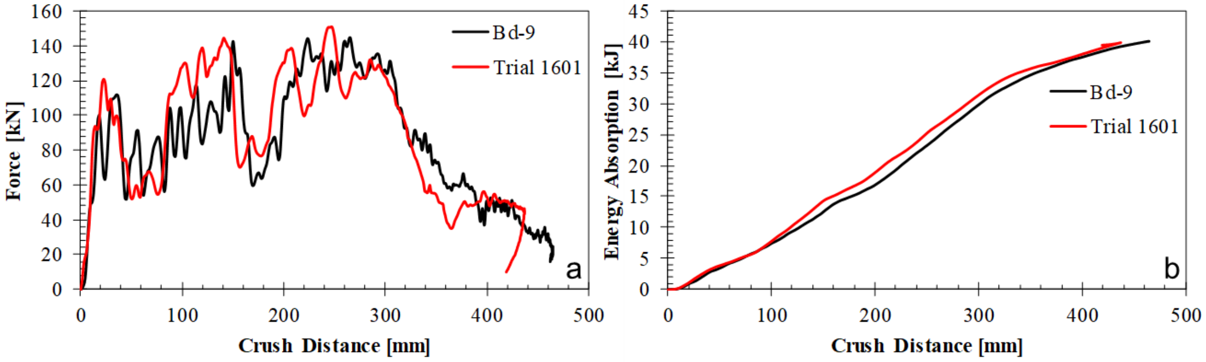

Figure 122. (a) Crush force and **(b)** energy absorption for test Bd-9 and its respective model Trial 1601.

3.4.7 Test 9: Bd-6

In the ninth baseline front end module test (Bd-6) the flat aluminum plate mounted to the impacted end of the specimen, used for tests Bd-2, Bd-3 and Bd-10, is reinstated. The high speed video images and synchronized model results are shown in Figure 123, Figure 124, Figure 125 and Figure 126 in the outboard side view, outboard isometric view, top view and inboard isometric view, respectively. In the second frame it is observed that full consolidation of the crush tip occurs, which is followed by a small plastic hinge forming in front of the shock tower support (frame 3). The small plastic hinge in front of the shock tower support is immediately followed by a large plastic hinge forming behind the shock tower support. In comparing the high speed camera images to the deformations predicted by the model it is quite clear that the model correlates well with the observed deformations from the test.

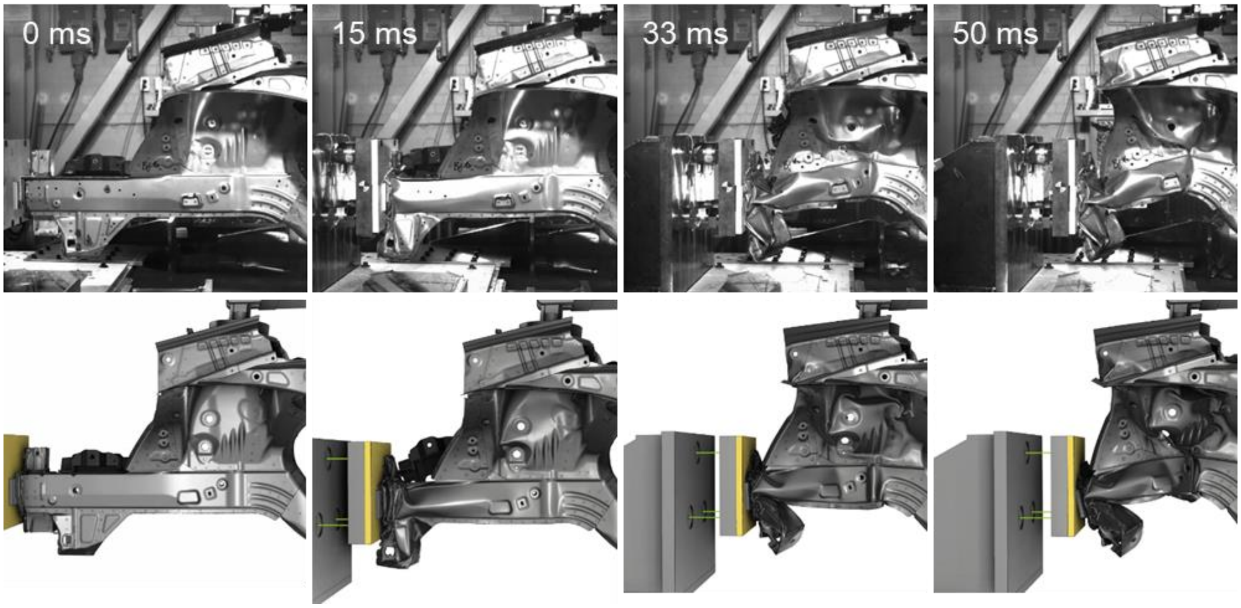

Figure 123. High speed camera images and synchronized model predictions for Bd-6 test showing the deformation modes from the outboard side view.

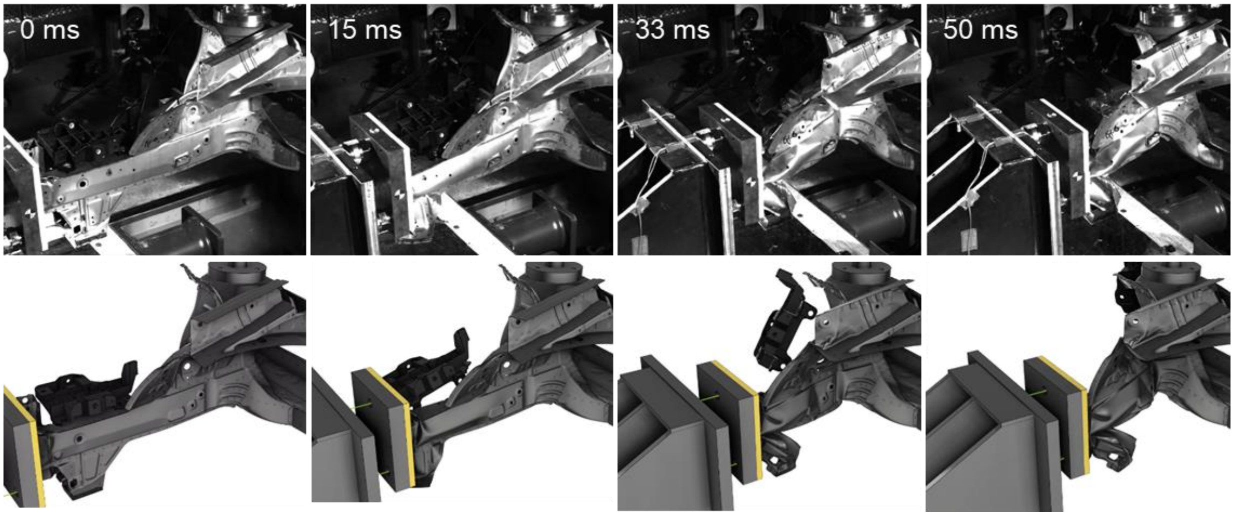

Figure 124. High speed camera images and synchronized model predictions for Bd-6 test showing the deformation modes from the outboard isometric view.

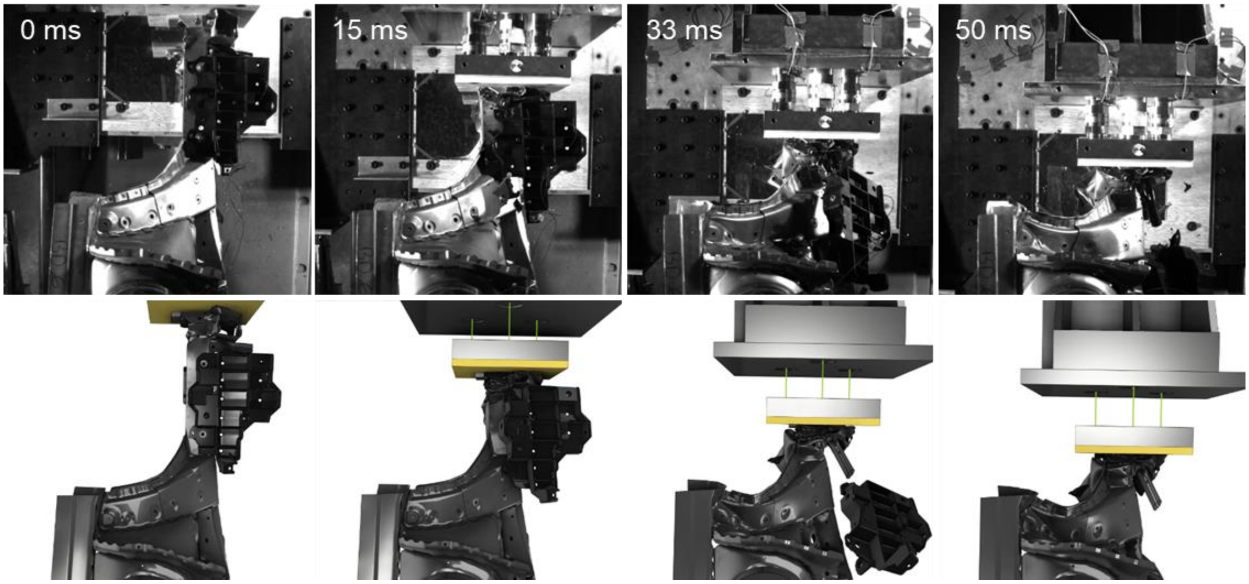

Figure 125. High speed camera images and synchronized model predictions for Bd-6 test showing the deformation modes from the top view.

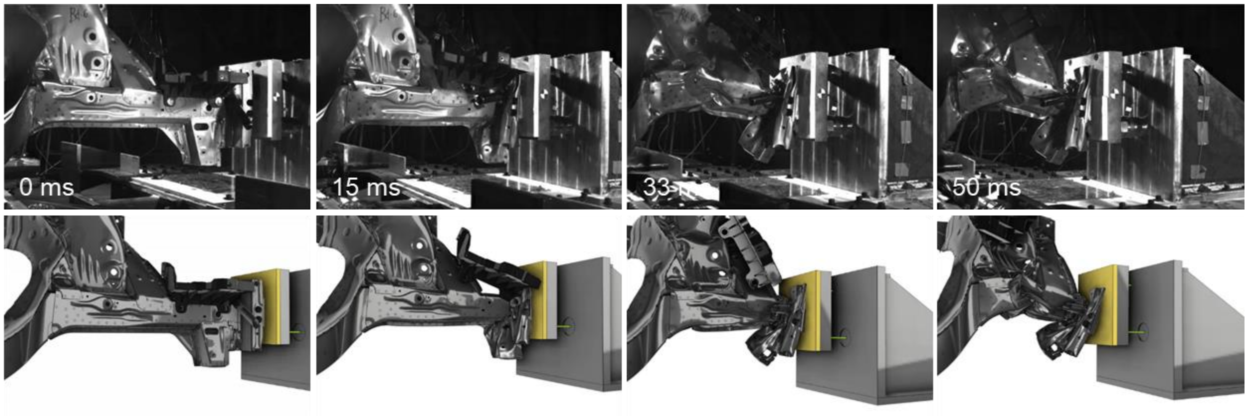

Figure 126. High speed camera images and synchronized model predictions for Bd-6 test showing the deformation modes from the inboard isometric view.

The crash sled deceleration profiles for test Bd-6 and its associated numerical model Trial 1710 are shown in Figure 127. A good correlation between the tested and modelled deceleration profile is observed up until 300 mm of crash sled crush distance, at which point the model over predicts the deceleration of the crash sled. This over predicted crash sled deceleration causes the predicted final crash sled crush distance to be 15 mm less than (426 mm) the measured crush distance of 441 mm.

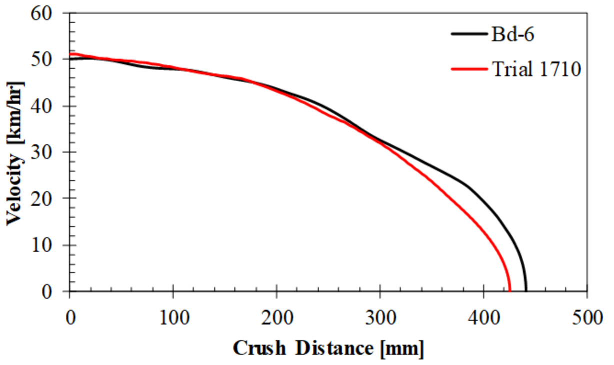

Figure 127. Crash sled deceleration profile for Bd-6 test and its respective numerical model Trial 1710.

Unfortunately one of the three load cells did not record during the crash test of Bd-6 and therefore the crush force could not be measured in the conventional manner using the load cell data. Instead, the measured crush force was estimated from the accelerometer data (measured in g's) by multiplying it with the acceleration due to gravity (9.81 ms^{-2}) and the total mass of the crash sled. The force calculated from the accelerometers includes the force applied due to the honeycomb in addition to the specimen. The force due to the honeycomb was removed from the calculated crush force by subtracting the theoretical honeycomb load curve for this test (Figure 86) from the calculated and predicted crush forces.

The calculated crush force and energy absorption plotted against the crash sled crush distance are shown in Figure 128. It is observed that the crush forces calculated with the accelerometer data is very noisy, however the general trend of the crush force can be seen easily. The predicted crush force using the conventional method of the force transducer (labelled "Force Transducer") is also plotted to show that the trend of the crush force curves are reasonable. Despite the noisy calculated crush force data, the measured and predicted crush forces and energy absorptions are very similar. Peak forces are not highlighted for this specimen because the noisy accelerometer data gives too many artificial peaks. Over the first 300 mm of crush distance the measured average force is 117 kN and the predicted average force is 122 kN. The calculated energy absorption from the measured force values is 49 kJ and the predicted energy absorption is 50 kJ.

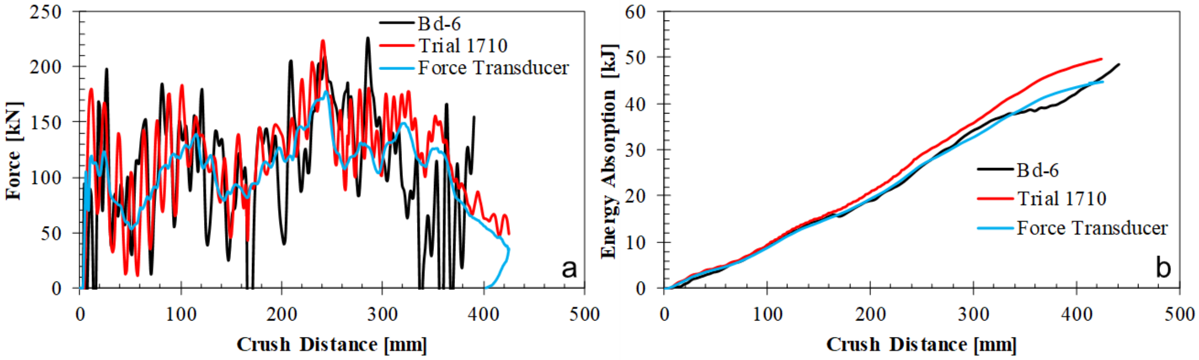

Figure 128. **(a)** Crush force and **(b)** energy absorption for test Bd-6 and its respective model Trial 1710 calculated from the accelerometer data and predictions.

3.5 Baseline Front End Module Crash Test Summary

The foregoing description of the baseline demonstrated structure experiments has detailed the predictions and measurements as well as high speed video images from each of the baseline front end module tests conducted. Here, a compilation and comparison of these predictions and measurements is provided in order to identify trends in the structural response as a function of loading conditions. Of particular interest are: the effect that the displayed crush mode has on the overall crash performance of the front end module, including the crush distance and energy absorption. The interface between the impacted end of the specimen and the crash sled proved to have a significant affect on the displayed crush mode and will therefore be discussed. In addition, the peak force and average force exerted by the front end module are discussed along with the overall correlation of the finite element models to their respective test specimen.

Various crush modes are displayed by the baseline front end modules during crash testing and can be discerned and categorized in terms of their final deformed shape. Figure 129 and Figure 130 are the top down and outboard side views, respectively, of the deformed shape of the baseline front end modules. Figure 129 is centered on the foremost shock tower support. In these figures, it is observed that three distinct crush modes exist in the baseline front end module crash tests.

The first crush mode (highlighted with a green box) is one in which the side frame member crush tip fully consolidates followed by a plastic hinge being initiated in front of the shock tower support. The plastic hinge in front of the shock tower support creates a pivot point from which the consolidated crush tip rotates around. Another defining feature of this crush mode is the downward rotation of the rail once the large rear fold initiator begins collapsing. The test specimens associated with the first crush mode type are Bd-1, Bd-4 and Bd-3. For specimen Bd-5, it is hypothesized that this specimen would have displayed the first crush mode, however, the crash sled was arrested prematurely by the honeycomb, preventing full development of the crush mode.

The second crush mode (highlighted with a purple box) is defined by full or partial consolidation of the side frame member crush tip, followed by the formation of a plastic hinge behind the shock tower support. Once a plastic hinge is initiated behind the shock tower support, all of the load transfer through the side frame member goes into increasing the buckle deformation, which is a relatively low energy absorption mode. The test specimens associated with the second crush mode are Bd-7, Bd-10 and Bd-9. In Bd-10 and Bd-9, full consolidation of the side frame member crush tip is achieved, while in Bd-7 only partial consolidation of the crush tip occurs before the crush mode changes to a global buckle behind the shock tower support.

The third observed crush mode (highlighted with a yellow box) is the most complex of the three and consists of full consolidation of the side frame member crush tip, followed by the formation of a plastic hinge in front of the shock tower support. Once the plastic hinge in front of the shock tower support is developed, load continues to be transmitted through the side frame member causing another buckle to form behind the shock tower support. Recalling the target crush modes from the SUV model (section 2.3) it is clear that the third crush mode is the desired crush mode for the baseline front end module. The test specimens associated with the third crush mode are Bd-2 and Bd-6. In Bd-2 the final deformation with plastic hinges in front and behind the shock tower create a distinct C-shape, with the shock tower support at its center. In Bd-6, plastic hinges in front and behind the shock tower are observed, however the C-shape is much less distinct than in Bd-2.

The end condition used on the impacted end of the specimen that comes in contact with the crash sled has a significant effect on the displayed crush response. Baseline front end module tests 1, 2 and 3 (Bd-1, Bd-5 and Bd-4) did not have end plates mounted to them and have crush responses that are distinguished by a large inboard rotation of the crush tip in front of the shock tower support. It is suspected that without the rigidity of an end plate, the crush tip is able to rotate too freely, leading to over rotation of the crush tip about the plastic hinge in front of the shock tower support. Test 4 (Bd-7) had a large 1” thick AA6061-T6 plate mounted to its impacted end. The large thick end plate suppressed any rotation of the crush tip, which did not allow for a plastic hinge to be formed in front of the shock tower support, thus overloading the side frame member, causing global buckling of the structure to follow. Test 8 (Bd-9) had an AA6061-T6 wedge mounted to its impacted end, which was to initiate the eccentric folding observed in the SUV model (Figure 82d). In practice, however, the wedge applied too much load on a small area of the pine board and caused it to compress deep into the board, destroying the pine board and reducing the effectiveness of the wedge.

Baseline front end module tests 5, 6 and 7 (Bd-2, Bd-3 and Bd-10) shared common test configurations, using a small ½” AA6061-T6 end plate, but each test displayed a different crush response, as shown in Figure 129 and Figure 130. It is observed in Figure 118 that the measured crush forces from each of the three tests are almost identical up to 250 mm of crush distance (marks the formation of the first plastic hinge, in front of the shock tower support), at which point the differences in crush response causes the measured forces to deviate from one another. The fact that the load levels are so close leading up to the formation of the plastic hinge in front of the shock tower support suggests that small differences in fabrication and/or test specimen alignment may be responsible for the spurious differences in crush response between tests. In test 9 (Bd-6) the same end plate as tests 5, 6 and 7 was used, with the addition of the front bulkhead brace.

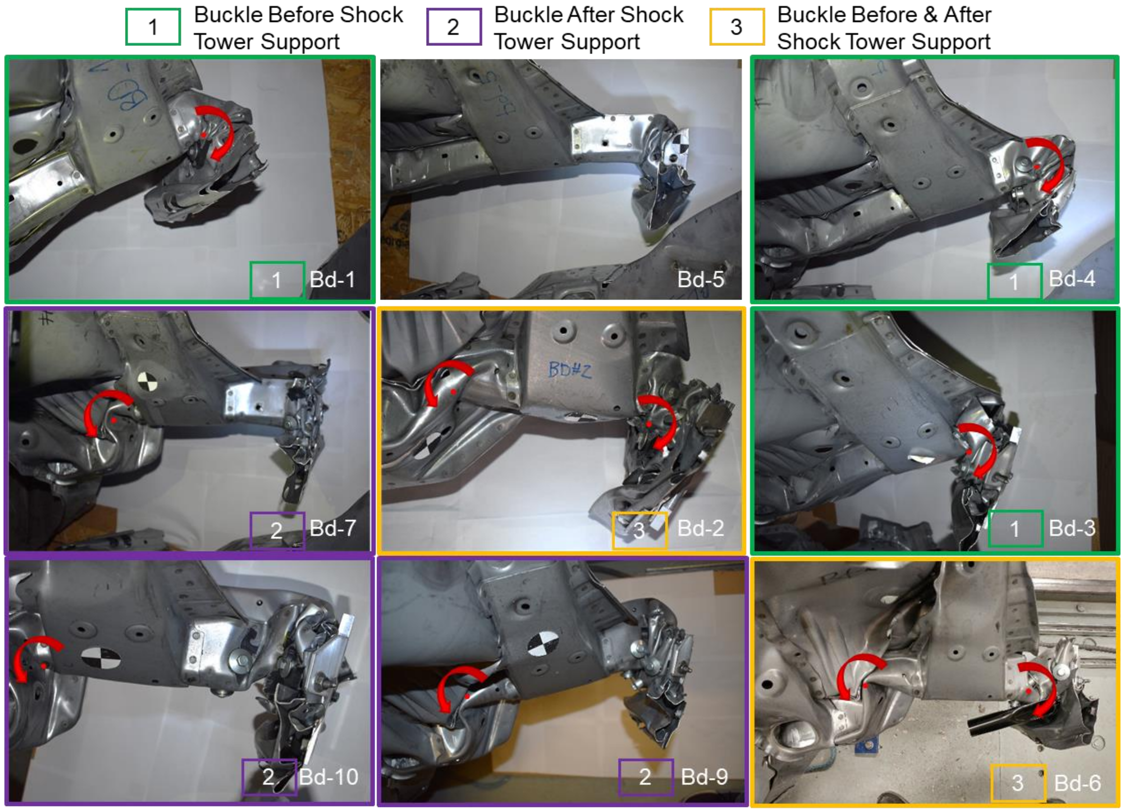

Figure 129. Images of the final deformed shape of each specimen after impact testing to highlight the differences and similarities in crush modes between the nine test specimens. Shown in the top down view,

centered on the foremost shock tower support. No mode is identified for specimen Bd-5 since this test was interrupted prematurely.

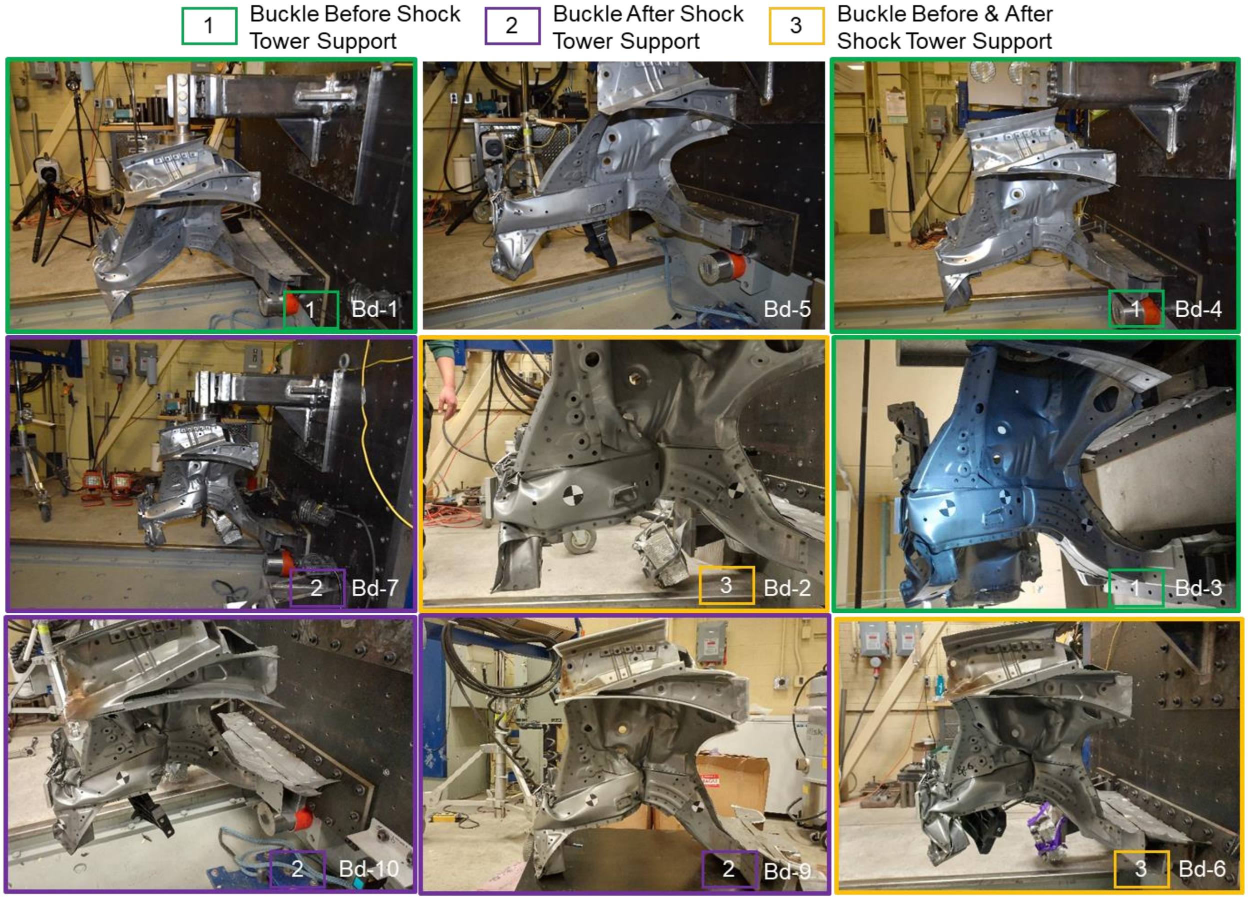

Figure 130. Images of the final deformed shape of each specimen after impact testing shown in the outboard side view. No mode is identified for specimen Bd-5 since this test was interrupted prematurely.

The final crash sled crush distance for each test is plotted in Figure 131 along with the total energy absorbed by the honeycomb. In addition, the crush mode exhibited by each specimen is also indicated so that the effect of crush mode on crash sled crush distance can also be examined. It is important to note that Bd-1 was tested with a higher target speed of 56 km/hr while in the rest of the tests a speed of 51 km/hr was targeted. The most obvious effect of the honeycomb on crush distance is observed between specimen Bd-5 and Bd-4. In Bd-5 the honeycomb absorbs double the amount of the crash sled's energy than in Bd-4, which caused the crash sled to travel 111 mm less distance in test Bd-5. However, in tests Bd-4 and Bd-7 the crash sled energy absorbed by the honeycomb is constant but the crush modes between the two are different. Comparing the effect of the type of crush mode on crush distance without honeycomb as a variable shows that the second crush mode type allows for a higher (82 mm) crash sled penetration distance into the front end module than the first crush mode type does. In comparing tests Bd-2, Bd-3 Bd-10 and Bd-9, which all have the same honeycomb energy absorption a similar trend is observed in which the tests demonstrating the second crush mode (Bd-10 and Bd-9) allow more crash sled travel than the first and second crush modes. In Bd-6 the honeycomb stack is shortened 20 mm and as a result it absorbs 5 kJ less energy than the honeycomb used for specimens Bd-2, Bd-3, Bd-10 and Bd-9. An interesting note is that even with less energy absorbed by the honeycomb the crash sled travels less distance in the third crush mode than it does in the second crush mode.

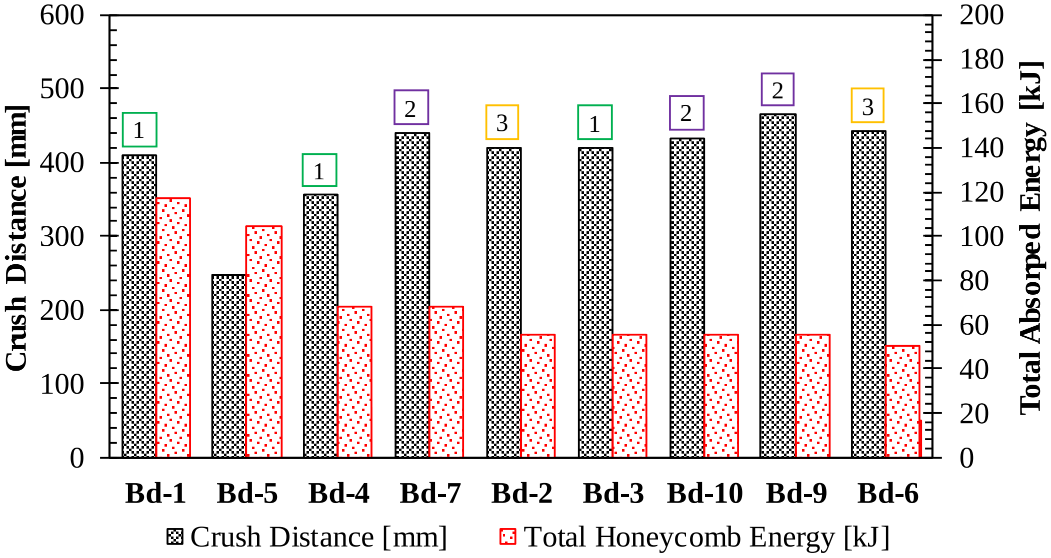

Figure 131. Final crash sled crush distance measured for each test along with the total energy absorbed by the honeycomb stacks during the crash event.

Average energy absorption as a function of the crush mode type and crash sled crush distance is plotted in Figure 132. In this figure the bars represent the average energy absorption for each crush mode type at a particular crash sled crush distance and the error bars represent the maximum and minimum energy absorption for that particular mode. The results from Bd-6 have been omitted from this plot due to the lack of load cell data. In addition, the results from Bd-5 are omitted due to prematurely arresting the crash sled. It is observed from this figure that the first and second crush mode types absorb almost the same amount of energy for each crash sled crush distance. Furthermore, up until 300 mm of crash sled displacement all of the crush mode types absorb an equivalent amount of energy. The fact that the first 300 mm of crash sled crush distance is essentially unaffected by the crush mode type implies that crash performance of the crush tip is independent of the crush mode type, impacted end boundary condition and honeycomb stack configuration, within the range of loading scenarios tested in this work. The energy absorption of the crush tip being equivalent between the three crush mode types up to 300 mm of crush distance provides justification that pursuing the testing of only the tailor-welded hot stamped crush tip is reasonable. Another important observation made from this figure is that the third crush mode absorbs approximately 4 kJ more energy than the first and second modes in the 300 mm to 400 mm of crush distance range.

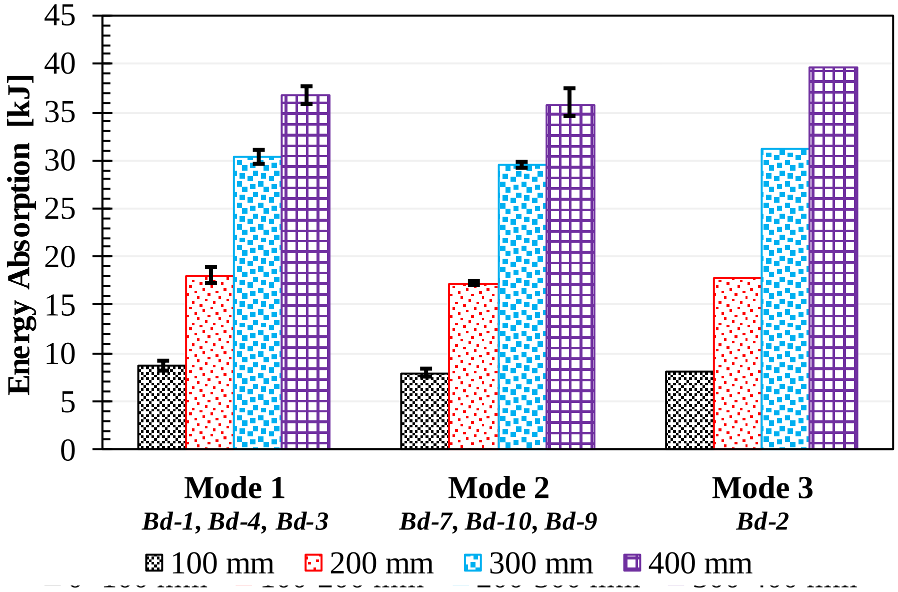

Figure 132. Baseline front end module energy absorption plotted as a function of crush mode and crash sled crush distance.

In reviewing the force-displacement curve from specimen Bd-7 (Figure 114) and comparing it to the force-displacement curves from the rest of the tests, an unusually high peak force is observed within the first 100 mm of crush. The outlier peak force in Bd-7 is 291 kN, which is 131 kN greater than the average peak force (159 kN) of the remaining tests. For this reason, the results from specimen Bd-7 have been excluded from the peak force, average force and energy absorption summary of this section.

A summary of the test quantities of interest (peak force, average force and energy absorption) are shown in Figure 133. The results from Bd-6 have been omitted from this plot due to the lack of load cell data. In this figure each of the quantities of interest are plotted as a function of crush distance in intervals of 100 mm (0 to 100 mm, 100 to 200 mm, 200 to 300 mm and 300 to 400 mm). The bar represents the average value of all the tests (excluding Bd-7), while the error bars represent the maximum and minimum value from all the tests. In cases where the test's crush distance did not reach 400 mm (Bd-5 and Bd-4) no result from that particular test was included in the calculated average.

Despite the differing test conditions used for each specimen, it is illustrated in Figure 133 that the quantities of interest (peak force, average force and energy absorption) are quite close for all the tests. This is especially true for the initial 200 mm of crush, where the error bars for peak force, average force and energy absorption are relatively small in comparison to the values after 200 mm of crush. Peak force has a relatively large discrepancy between tests in the first 100 mm of crush because the change in impacted end boundary condition has the greatest effect on the first few millimetres of crush. Much larger discrepancies are observed after 200 mm of crush due to variation in crush modes between the test specimens. Ultimately, what this data shows is that the sequential folding crush response of the side frame member crush tip is much less effected by the test conditions than the later portions of the crush response that are more buckle dominant.

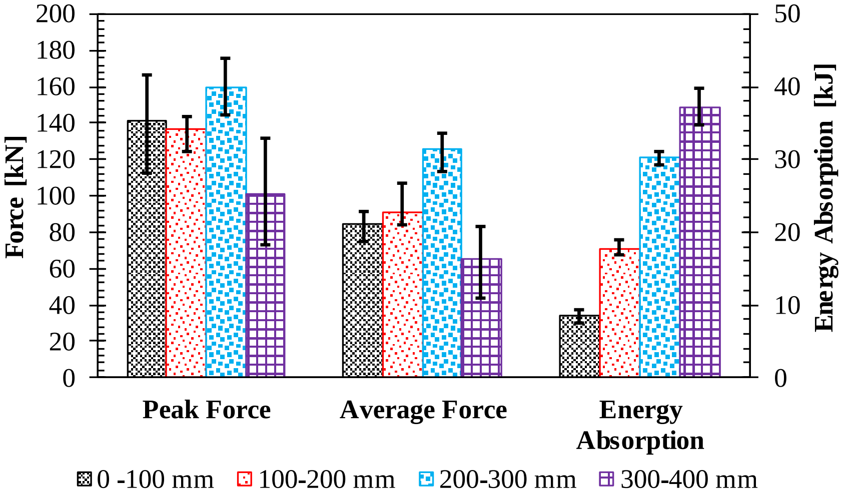

Figure 133. Summary of the average measured peak force, average force and energy absorption for each test specimen as a function crush distance. Data is averaged for all test specimens except for Bd-7 (1" thick end plate) which is omitted due to outlier peak force and Bd-6 for which there was a load cell data acquisition failure. Error bars show maximum and minimum forces and energy.

The degree of correlation between the measured results for each test specimen and their respective model predictions is shown in Figure 134. The results and predictions from Bd-6 have been omitted from this plot due to the lack of load cell data. The quantities of interest are the initial peak force measured in the first 100 mm of crush distance, the total crash sled crush distance and the total energy absorbed by the specimen. In this figure, the bars represent the measured values from the test and the error bar tails represents the model predicted values. The largest error between measured results and predictions are observed for the test specimen whose models did not capture the crush modes observed in the test, such as the model for tests Bd-2 and Bd-3. In addition, a large amount of error is observed for test Bd-7 and its model, which is explained by the malfunction of the honeycomb stack shown in Figure 113.

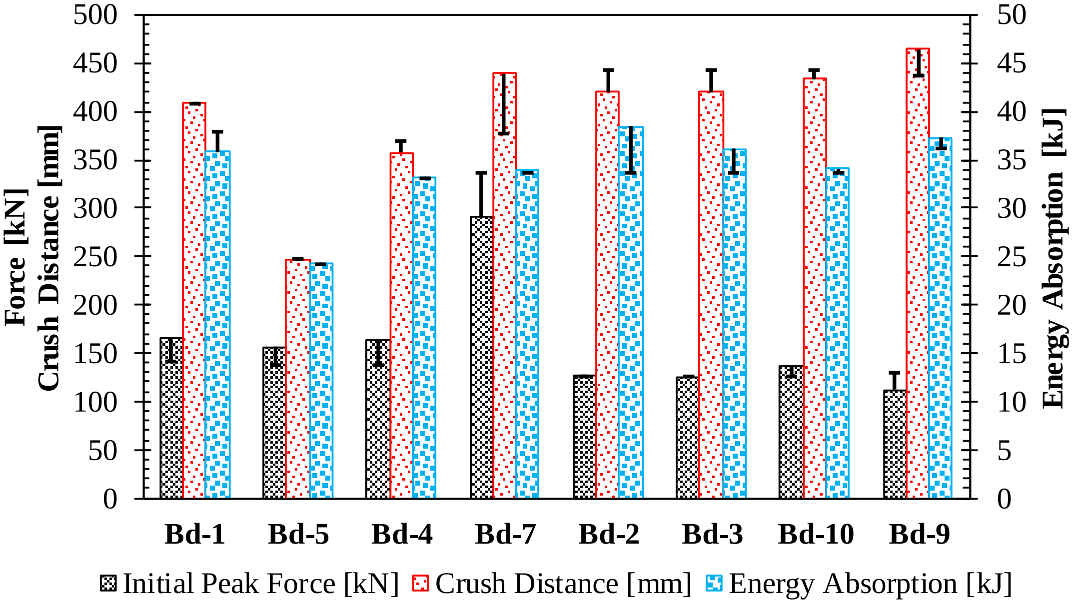

Figure 134. Correlation of numerically modelled predictions to the measured test results for initial peak force, crash sled crush distance and energy absorption. The bars represent the measured results while the error bar tails represent the modelled prediction.

3.6 Evaluation of the Baseline Front End Module

This section presents an evaluation of the baseline front end module, through comparison with the response of the side frame member within the full SUV model, and through assessment in terms of the evaluation criteria prescribed in Table 3. Here, the baseline front end module will be both qualitatively and quantitatively compared to the SUV model to ensure a good match to the side frame member crush response, crush forces, passenger compartment intrusion and extent of spot weld failure. In order to simplify the comparison of the baseline front end module tests and simulations with the SUV model, representative tests for each particular crush mode type are selected.

The Mode 1 type deformation (exhibited by Bd-1, Bd-4 and Bd-3) is selected to be represented by specimen Bd-4 and its associated model Trial 1301. The initial velocity of the crash sled in test 1 (Bd-1) was 56 km/hr, which is 5 km/hr faster than all of the other tests, therefore Bd-1 was not selected. Specimen Bd-3 was one of the three front end modules (Bd-2, Bd-3 and Bd-10) tested with the exact same conditions, but displayed different crush modes. Due to the variability in crush response between like test conditions in this series of experiments, the model (Trial 1501) could not be correlated to each test and did not correlate with the response displayed by specimen Bd-3, therefore Bd-3 was not selected for the evaluation.

The Mode 2 type deformation (exhibited by Bd-7, Bd-10 and Bd-9) is selected to be represented by specimen Bd-10 and its associated model Trial 1501. Specimen Bd-7 was not selected to represent Mode 2 type deformation due to the buckling of the honeycomb that occurred during testing (Figure 113), causing the crash sled to travel much further than predicted. The deformation exhibited by specimen Bd-10 corresponded more closely to Mode 2-type deformation than the deformation observed in specimen Bd-9, which was very close to Mode 3 type deformation, but did not have enough inboard rotation in front of the shock tower support. In order to provide the clearest example of Mode 2 type deformation Bd-10 was selected over Bd-9.

The Mode 3 type deformation (exhibited by Bd-2 and Bd-6) is selected to be represented by specimen Bd-6 and its respective simulation Trial 1710. Specimen Bd-2 was one of the three front end modules (Bd-2, Bd-3 and Bd-10) tested with the exact same conditions, but displayed different crush modes. The model associated with specimen Bd-2 (Trial 1501) predicted Mode 2 type deformation, which did not correlate with the crush response observed in the test, therefore Bd-2 was not selected to represent Mode 3 type deformation in this evaluation.

3.6.1 Crush Response Comparison

The outboard side view, shown in Figure 135, compares the predicted deformation modes from the full vehicle model to the deformation modes observed in test specimen Bd-4 and Bd-6 which correspond to Modes 1 and 3, respectively. High speed camera images were not recorded in the outboard side view for specimen Bd-10, and it has therefore been omitted from the figure. It should be noted that the front end module is isolated from the full vehicle model within the post-processor for better visualization of the crush response. Through the outboard side view it is observed that within the first 140 mm of crush, both the Mode 1 and Mode 3 representative experiments correlate well with the crush response in observed in the full vehicle model. It is only after 317 mm of crush distance that a difference in crush response is noticed between the Mode 1 experiment and the full vehicle model, whereas the Mode 3 experiment maintains good correlation to the full vehicle model.

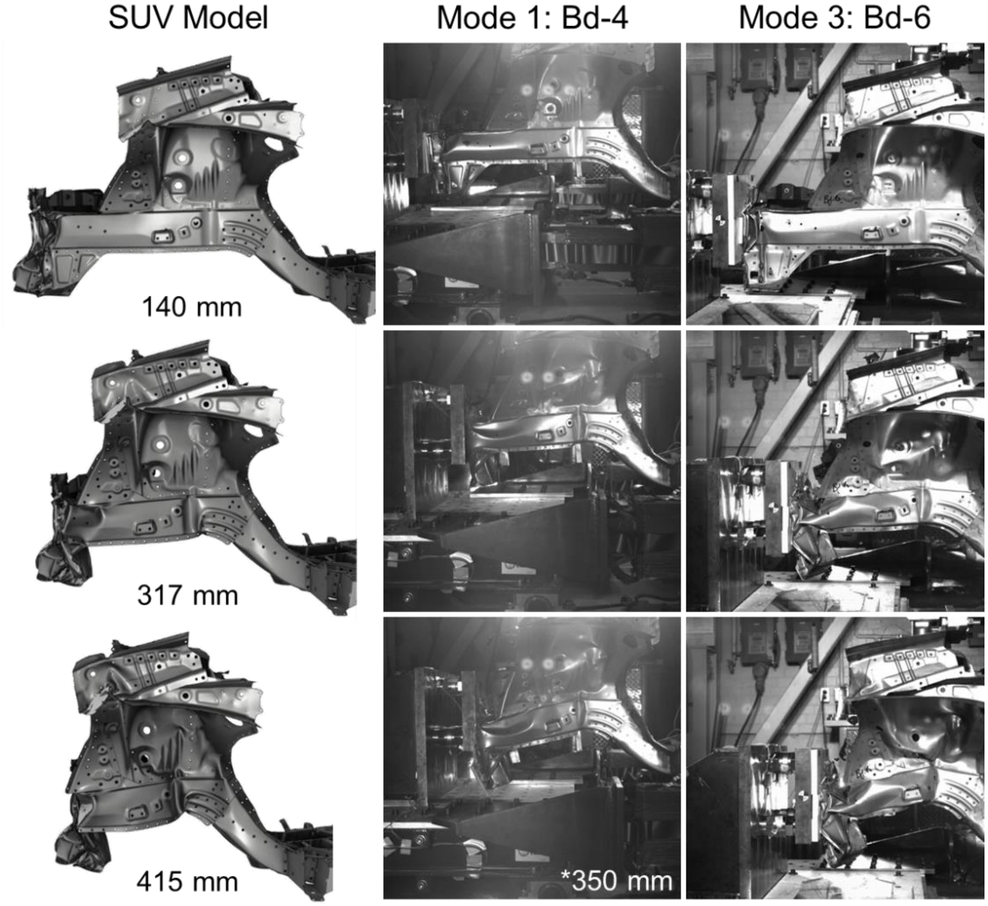

Figure 135. Comparison of predicted deformation from the full vehicle model to the high speed camera images from Bd-4 and Bd-6 in the outboard side view. Specimen Bd-10 did not have an outboard side view, and is therefore omitted from this figure. Note that the front end module is isolated from the full vehicle model for visualization purposes.

The outboard isometric view, shown in Figure 136, compares the predicted deformation modes from the full vehicle model to the deformation modes observed in test specimen Bd-4, Bd-10 and Bd-6 (Modes 1-3, respectively). In the outboard isometric view it is again observed that up to 140 mm of crush distance, the responses of all the crush mode types compare very similarly to the full vehicle model. With progression of the crush distance past 317 mm, differences in crush response are observed between all of the crush mode types. In the Mode 1 deformation type it is observed that at 350 mm of crush distance the side frame member crush tip is buckled in front of the shock tower support. However, without a buckle behind the shock tower support, the middle section of the side frame member remains straight, causing the side frame member to rotate outboard about the shock tower axis. In the Mode 2 deformation type, a premature buckle behind the shock tower support prior to 317 mm of crush distance causes a transition from crush tip consolidation to global buckling, well before it occurs in the full vehicle model. The Mode 3 deformation type is observed to correlate well with the full vehicle model crush response because full consolidation of the crush tip section is observed, followed by a plastic hinge forming in front of the shock tower support, as well as aft the shock tower support as the crash progresses even further.

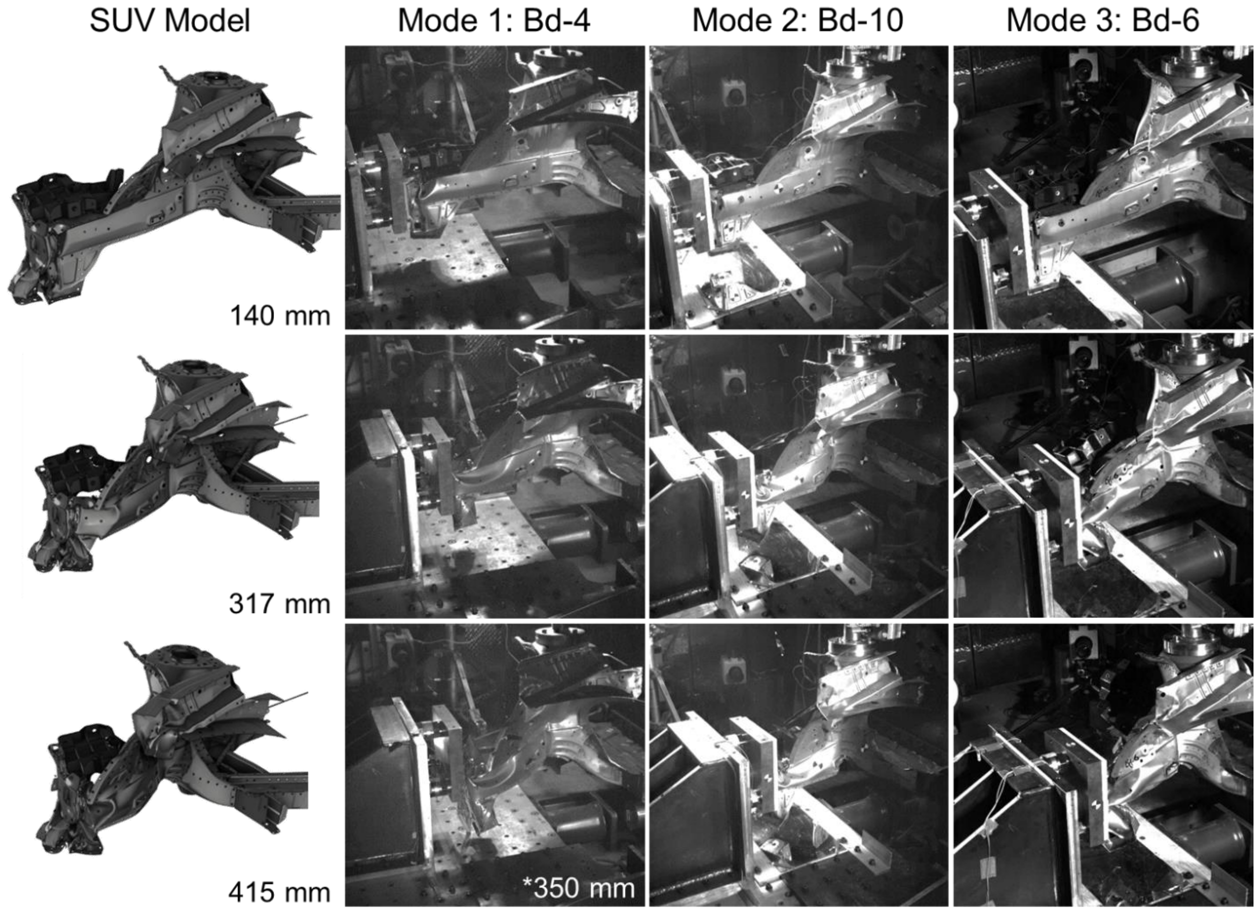

Figure 136. Comparison of predicted deformation from the full vehicle model to the high speed camera images from Bd-4, Bd-10 and Bd-6 in the outboard isometric view. Note that the front end module is isolated from the full vehicle model for visualization purposes.

The inboard isometric view, shown in Figure 137, compares the predicted deformation modes from the full vehicle model to the deformation modes observed in test specimen Bd-4, Bd-10 and Bd-6. An image is not included for Bd-4 at 415 mm of crush distance because the crash sled obscures the view entirely for the camera angle adopted in that test. At 317 mm of crush distance, it is observed that a large amount of inboard rotation occurs in the crush tip of the Mode 1 (Bd-4) deformation type (highlighted with a red arrow), which is exemplified by the loss of contact between the impact face and specimen on the inboard side. In both the Mode 2 and Mode 3 deformation types the specimen remains in contact with the impact face throughout the crash event, however the premature plastic hinge formation (highlighted with a blue arrow) behind the shock tower support in Mode 2 yields a different crush response than the full vehicle model. The Mode 3 crush response, with both buckles in front and behind the shock tower support correlates well with the full vehicle model.

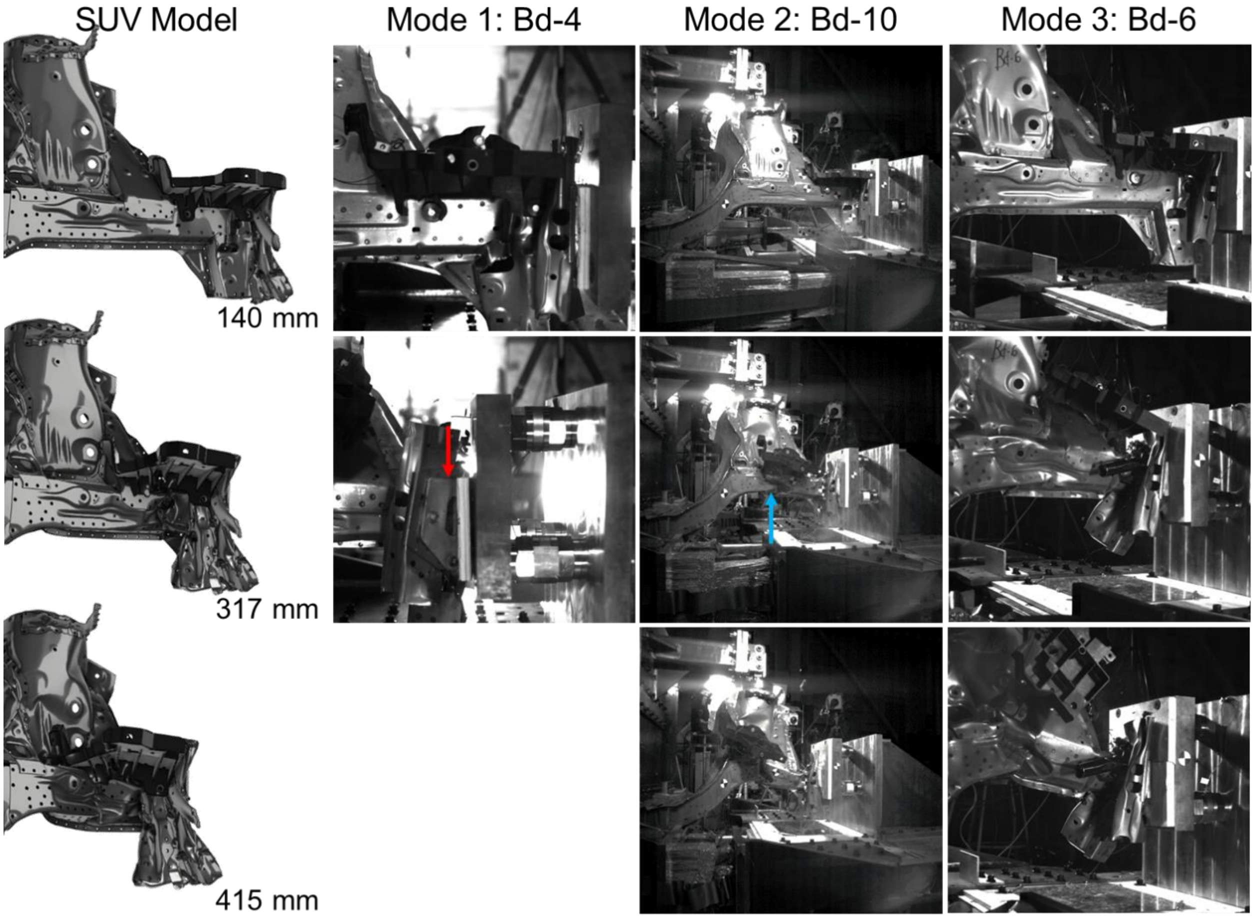

Figure 137. Comparison of predicted deformation from the SUV model to the high speed camera images from Bd-4, Bd-10 and Bd-6 in the inboard isometric view. Note that the front end module is isolated from the SUV model for visualization purposes.

Top views of the final predicted shape after impact for the SUV model and photographs of test specimens after testing for each deformation type are shown in Figure 138. It is observed that the Mode 1 and Mode 2 deformation types do not display a crush response that is similar to the side frame member within the SUV model. The Mode 3 (Bd-6) deformation type however, does display a similar crush response to the SUV model. An additional baseline front end module (Bd-2) that exhibited the Mode 3 deformation type is also shown in Figure 138 to highlight the C-shape (red dashed line) created by the buckles in front and behind the shock tower support (recall that the load data was lost for Bd-2, but that the crush response was clearly Mode 3). The final deformed shapes in this figure clearly show that the Mode 3 deformation type demonstrates: full consolidation of the crush tip, a buckle in front of the shock tower support and a buckle behind the shock tower support.

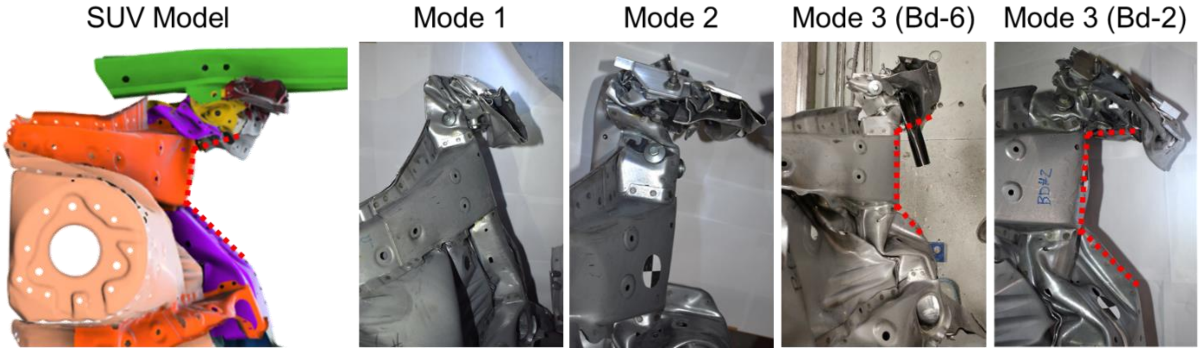

Figure 138. Final deformed shape of each crush mode along with the predicted deformed shape from the SUV model. Specimen Bd-2 has been included in Mode 3 to highlight the C-shape buckled structure.

3.6.2 Vehicle Deceleration

The predicted velocity history for the SUV model compared to the measured velocity histories from Bd-4 (Mode 1), Bd-10 (Mode 2) and Bd-6 (Mode 3) are shown in Figure 139. In the representative Mode 1 deformation type test (Bd-4), the crash sled did not crush the specimen fully, due to an erroneous honeycomb stack configuration. To better represent the Mode 1 deformation type the velocity history of specimen Bd-3, which also displayed Mode 1 deformation, has also been included in Figure 139.

The predicted final crush distance of the side frame member in the SUV model is 422 mm, while the final crush distance for Mode 1 (using Bd-3 velocity history), Mode 2 is 433 mm and for Mode 3 is 442 mm; all of which are within the ± 30 mm final crush distance tolerance. It is observed that the measured velocity history from Mode 1 (using Bd-3 velocity history), Mode 2 and Mode 3 are within the SUV model velocity history 10% error bounds. It is hypothesised that if the honeycomb stack had been fine tuned for specimen Bd-4, it too would have matched the velocity history of the SUV model.

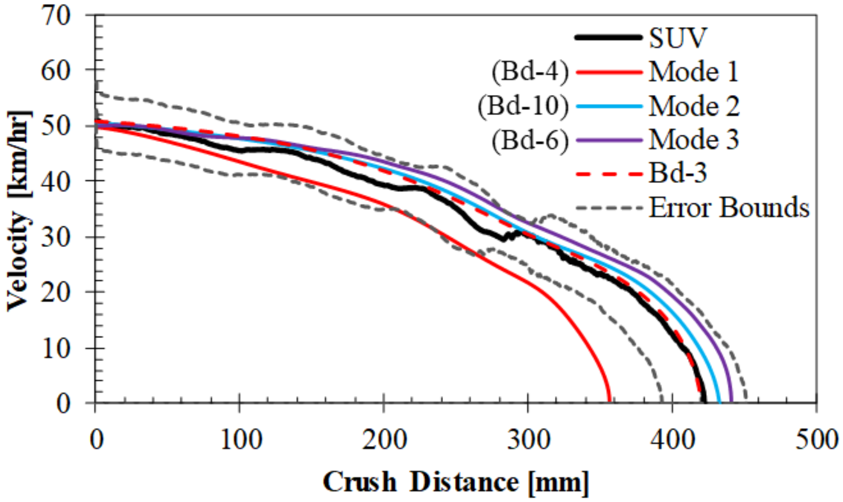

Figure 139. Predicted velocity history of the SUV model compared to the measured velocity histories for representative tests of the Mode 1 (Bd-4 and Bd-3), Mode 2 (Bd-10) and Mode 3 (Bd-6) deformation types.

3.6.3 Crush Forces

The predicted cross-sectional forces along the length of the side frame member are plotted against the crush distance for each crush mode type, as well as the SUV model, shown in Figure 140. Only predicted force values have been plotted since internal forces cannot be measured during the baseline front end module testing. Comparing the predicted crush loads predicted for each crush mode at each cross-section, it is observed that the general trend of the response of the SUV model is matched by each of the deformation mode types. The largest differences are noticed after 250 mm of crush distance at which point the differences in deformation mode types become evident. In the Mode 2 response a large difference in crush force is observed in force planes 5, 6, 7 and 8 after 250 mm, at which point the crush force significantly drops due to the premature buckle formed behind the shock tower support. The general trend of the predicted cross-sectional crush forces are captured by the Mode 1 and Mode 3 deformation types.

The predicted crush force from the force planes should be considered as a means to evaluate the trends in the side frame member, however it should not be regarded as absolute. The reason for this hesitation in relying on the sectional force planes is that if two side frame members fold slightly differently at the force plane, different folds can come in contact with each other through the plane, causing load sharing to occur between folds, which can skew the force prediction.

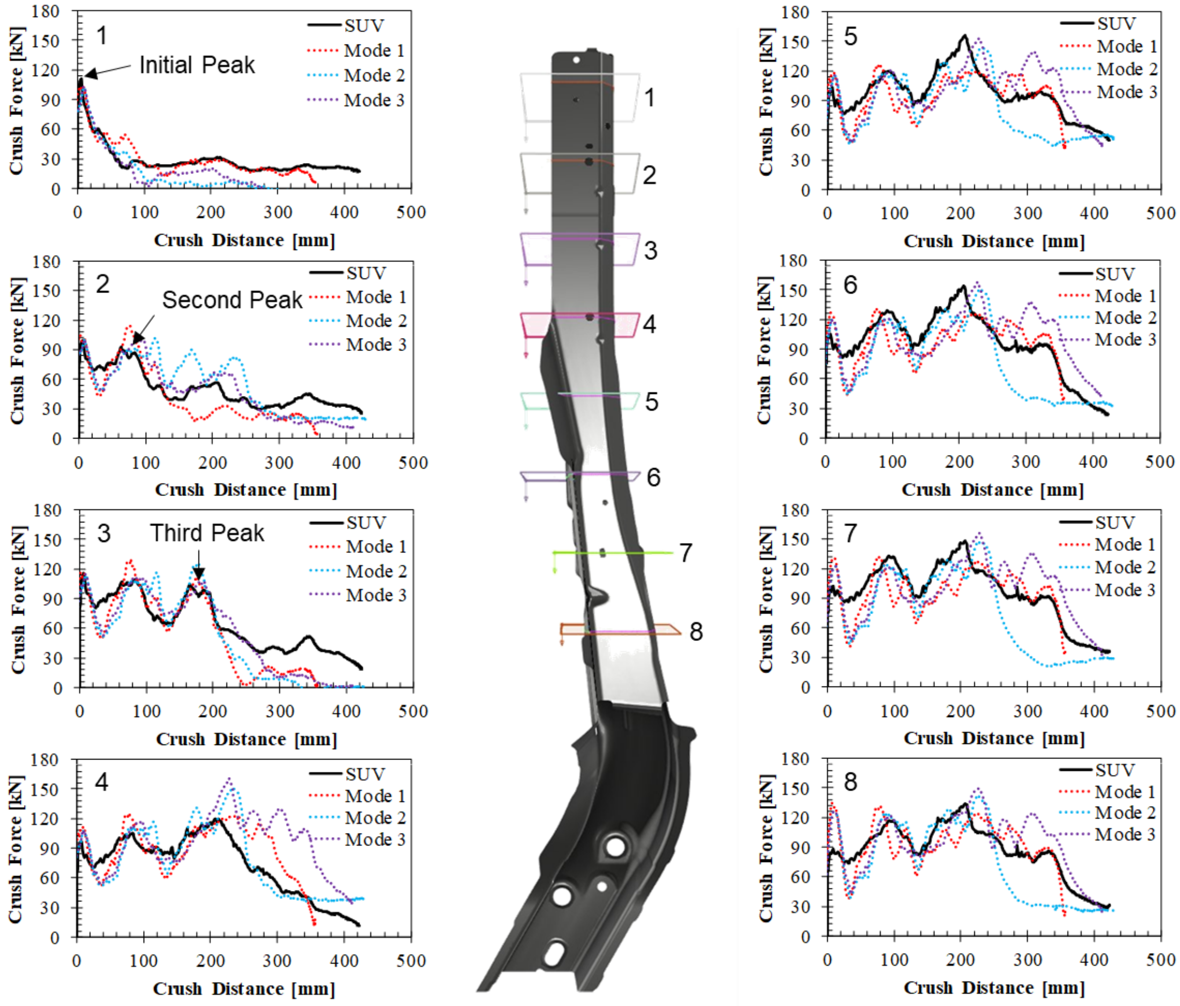

Figure 140. Predicted cross-sectional forces from the SUV model and representative models for the Mode 1 (Trial 1301), Mode 2 (Trial 1501) and Mode 3 (Trial 1710) deformation types.

In Figure 141 the predicted peak forces from the first three force planes are shown for the SUV model and each of the deformation mode types. The location of each of the three peak forces are highlighted in Figure 140. It is observed in Figure 141 that the peak forces are very similar at the first two peaks, but a large difference is observed for the Mode 2 deformation type in the third peak. The much higher third peak in the Mode 2 deformation type can be a cause of the premature buckle after the fold initiator; since, a higher load early on in the crash event is transmitted through the side frame member, potentially overloading the rail and causing a buckle to form. The percent difference between the SUV model predicted peak force and each respective deformation mode peak force is shown above each of the bars. From these percent difference values, it is observed that all of the peak force values are acceptable, except for the third peak in the Mode 2 deformation type.

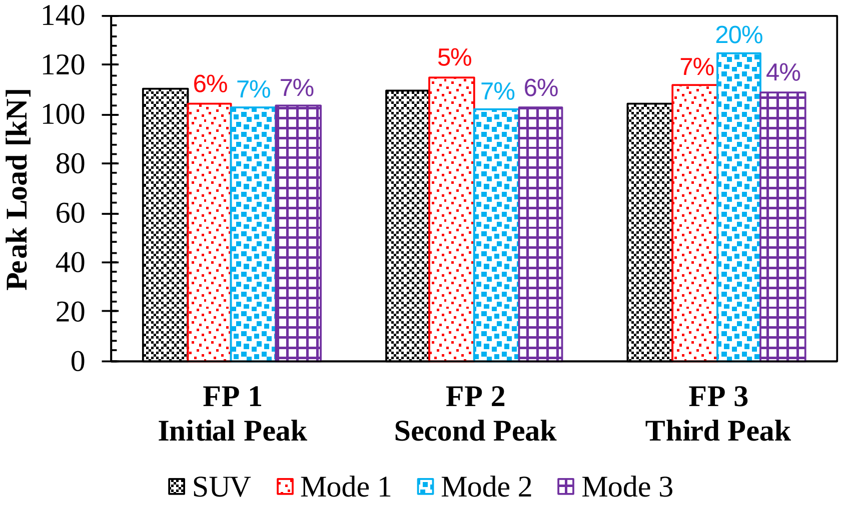

Figure 141. Predicted peak forces calculated from the first three cross-sectional force planes (FP) for the SUV model and representative models of the Mode 1 (Trial 1301), Mode 2 (Trial 1501) and Mode 3 (Trial 1710) deformation types at the initial, second and third peaks.

3.6.4 Occupant Compartment Intrusion

The occupant compartment intrusion was characterized by measuring the predicted displacement of the top of the side frame member S-rail section, in the same location as is shown in Figure 52. The summarized x-coordinate (into the passenger compartment) and z-coordinate (upwards) displacements are shown in Table 6. It is observed from these numbers that the each of the baseline front end module deformation modes have more displacement in at least one coordinate when compared to the SUV model. It should be noted that Mode 1 had the least amount of crash sled crush distance (370 mm), while the others have cash sled crush distances well over 400 mm. The Mode 3 deformation type predicts the most intrusion into the passenger compartment, with 19.2 mm and 31.2 mm more displacement in the x-coordinate and z-coordinate, respectively. At first glance this seems like too large an increase in side frame member intrusion; however, 2 cm inwards and 3 cm upwards are relatively insignificant amounts of intrusion considering a rigid wall frontal impact at 56 km/hr. Comparing the intrusion displacements to the tolerable upper bound, it is observed that all of the crush modes predict occupant compartment intrusion resistance within the acceptable limits.

Table 6. Predicted displacement of the side frame member S-rail section at peak impact.

Coordinate	SUV Model	Upper Bound	Mode 1	Mode 2	Mode 3
x	25.9 mm	55.9 mm	16.5 mm	28.0 mm	45.1 mm
z	3.0 mm	43.0 mm	8.7 mm	14.2 mm	34.3 mm

3.6.5 Extent of Spot Weld Failure

The high speed thermal imaging only allows for a relatively small length of the crush tip to be captured for a given test and it is not always easy to distinguish the occurrence of spot weld failures. Specimen Bd-3 was one of the only high speed thermal videos that distinctly demonstrated spot weld failure, as shown in Figure 142a, which is accompanied by the high speed optical camera footage at the same instant in the crash event (Figure 142b). Note that the temperatures indicated by the scale are inflated by the heat from the large mercury lights for the tests and therefore only the temperature difference should be considered. In Figure 142a two distinct rings of high heat are observed around two spot welds on the upper flange (white arrows), signifying high levels of plastic work generating heat in these areas. The failure of these spot welds are confirmed in the optical high speed image (Figure 142b), in which the flange is observed to pull apart (red arrow).

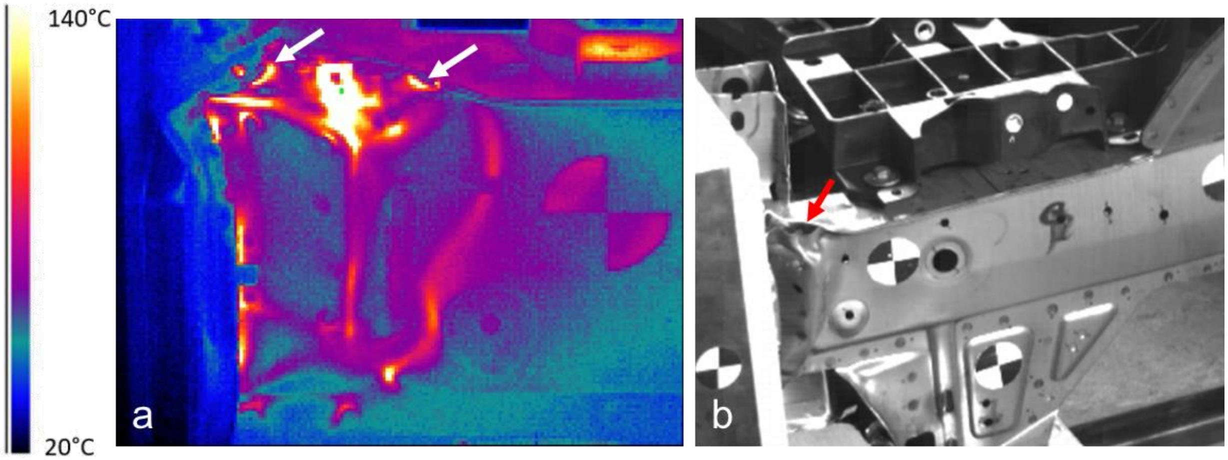

Figure 142. Failure of two spot welds on the upper flange of test Bd-3 shown by the **(a)** infrared red high speed camera image and **(b)** optical high speed camera.

The quantity and location of spot weld failures in the side frame member crush tip for the SUV model and the models of each of the representative deformation types are shown in Figure 143. Spot weld failure is monitored numerically through the failure parameter calculated within the spot weld model (section 2.2.2). A failure parameter equal to unity denotes the initiation of damage accumulation within a spot weld assembly (and signifies a spot weld failure for the purpose of this thesis), and is represented by a check mark in Figure 143. It is observed from this figure that both the Mode 1 and Mode 2 deformation types experience fewer weld failures than the SUV model within the side frame member crush tip, which may be due to the lesser extent of crush tip consolidation occurring in these crush modes. The locations of the spot weld failures are notably similar, with a few exceptions, for all of the deformation modes and the SUV model, especially in the top flange of the crush tip. Moreover, the Mode 3 deformation type displays a similar extent of spot weld failure as the SUV model does. In the crush tip bottom flange, some variability in location of spot weld failure is noticed between the SUV model and the Mode 3 deformation type, however these are only subtle differences in location.

Ultimately, the extent of the predicted spot weld failures and spot weld failure locations in the side frame member crush tip are acceptable for each of the deformation mode types. In addition, no catastrophic spot weld separations occurred in any of the crush response modes or the SUV model.

	Weld	SUV Model	Mode 1	Mode 2	Mode 3
Top Flange	1				
	2				
	3	✓	✓	✓	✓
	4	✓		✓	✓
	5				
	6				
	7	✓	✓		
Bottom Flange	8				
	9			✓	✓
	10	✓		✓	
	11				✓
	12				✓
	13	✓			
	Total	5	2	4	5

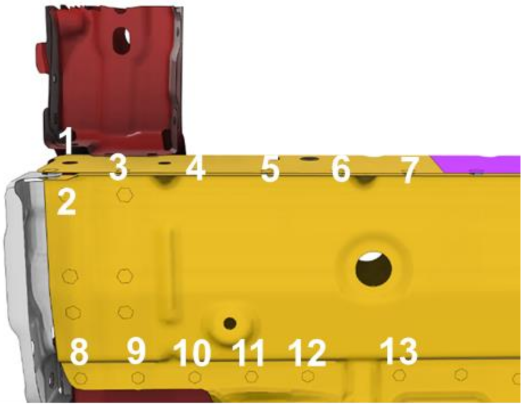

Figure 143. Side frame member crush tip spot weld failure (monitored from the failure parameter) quantity and locations from the SUV model, as well as the Mode 1 (Trial 1301), Mode 2 (Trial 1501) and Mode 3 (Trial 1710) deformation types.

3.6.6 Evaluation Summary

The selection of the proposed baseline front end module configuration (and crush Mode) that best mimics the response exhibited by the side frame member in the SUV model is determined based on the design specifications displayed in Table 3. The assessment is applied to each representative deformation Mode and the adherence of the representative baseline front end module for each Mode to the design specifications is summarized in Table 7, in which a check mark signifies a met target. It is observed that the Mode 3 deformation type meets each of the design specifications, while both the Mode 1 and Mode 2 deformation types do not display the same crush response as the side frame member from the SUV model. In addition, the Mode 2 deformation type does not meet the acceptable limits for crush force response or peak force when compared to the SUV model.

Table 7. Evaluation of the proposed baseline front end module against the design specifications.

	Qualitative	**Target**	**Upper**	**Lower**	**Baseline Front End Module**		
	Quantitative		**Bound**	**Bound**	**Mode 1**	**Mode 2**	**Mode 3**
Crush Response							
Consolidation of crush tip (Fig. 56)	Qualitative	Match	-	-	✓	✓	✓
Buckle in front of shock tower support (Fig. 56)	Qualitative	Match	-	-	✓		✓
Buckle behind shock tower support (Fig. 56)	Qualitative	Match	-	-		✓	✓
Vehicle Decleration							
Velocity history	Quantitative	Match	+ 10%	- 10%	✓	✓	✓
Final crush distance	Quantitative	422 mm	+ 30 mm	- 30 mm	✓	✓	✓
Crush Forces							
Sectional force plane (SFP) - global trend	Qualitative	Match	-	-	✓		✓
SFP - peak forces (1st, 2nd, 3rd)	Quantitative	Match	+ 10%	- 10%	✓		✓
Occupant Compartment Intrusion							
x-coordinate displacement	Quantitative	25.9 mm	+ 30 mm	-	✓	✓	✓
z-coordinate displacement	Quantitative	3.0 mm	+ 40 mm	-	✓	✓	✓
Spot Weld Failure							
Weld locations	Quantitative	Match	-	-	✓	✓	✓
Quantity	Quantitative	Match	-	-	✓	✓	✓

Through examination of Table 7, it is concluded that the baseline front end module, Mode 3 deformation type accurately represents the crash performance of the side frame member, predicted by the SUV model. The baseline front end module specimens that represent this deformation type are Bd-2 and Bd-6, which both had a ½" aluminum plate affixed to their impacted end, and in the case of Bd-6, had the front bulkhead brace bolted onto the crush tip. Moving forward, the tailor-welded hot stamped side frame member will be designed and evaluated using the boundary conditions imposed on specimen Bd-6.

Chapter 4 – Development of a Tailor-Welded Hot Stamped Side Frame Member

A key objective of this thesis is to evaluate the suitability of using hot stamped Ductibor® 1000-AS as a replacement for JAC590R in frontal crash energy management structures and to investigate the potential weight savings achieved through sheet material down-gauging. The side frame member (driver's side) from the SUV will be redesigned such that it can accommodate a hot stamped TWB, comprising various thicknesses of Ductibor® 1000-AS and Usibor® 1500-AS, which is referred to as the tailor-welded hot stamped side frame member. In this tailor-welded hot stamped side frame member it is intended that the current production JAC590R material in the crush tip and middle section be replaced with Ductibor® 1000-AS, while the thicker production JAC590R material in the S-rail section be replaced with Usibor® 1500-AS, as illustrated in Figure 144. Ductibor® 1000-AS is believed to be a suitable replacement for thinner gauge material in crash energy absorption zones (crush tip and middle section), due to its high strength and relatively high ductility. The replacement of thicker gauge material in occupant compartment intrusion resistant zones (S-rail) with Usibor® 1500-AS is suitable due to its demonstrated ultra-high strength, although its ductility is relative low.

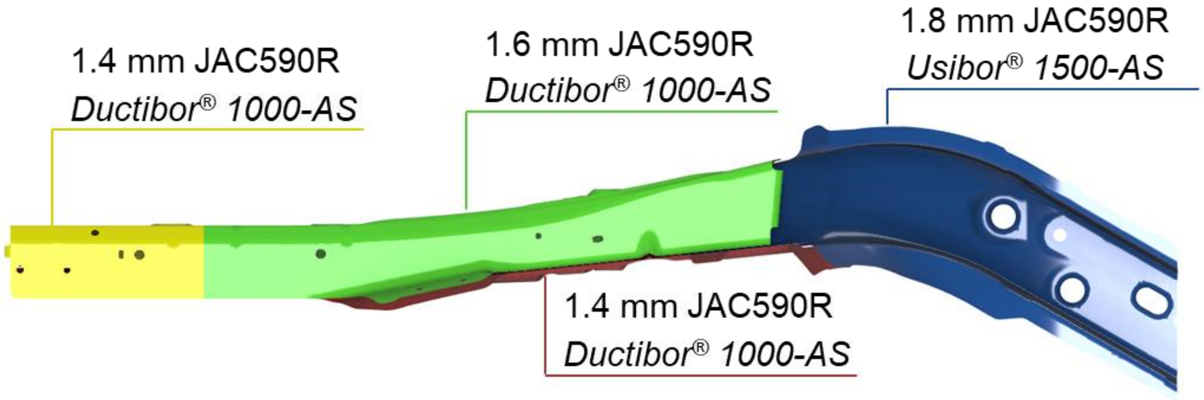

Figure 144. Side frame member showing the production material and thickness along with the ideal hot stamping material replacement, shown in italics.

This chapter details the design decisions and methods used to develop a tailor-welded hot stamped side frame member, which is numerically evaluated against the baseline front end module. The chapter opens with discussion of the initial design decisions that could be made without the need for simulation-based iteration. The numerical model used to simulate the tailor-welded hot stamped side frame member behaviour under the front end module test conditions is then described. Simulation-based design decisions are documented, which is concluded by presenting a finalized tailor-welded hot stamped side frame member and evaluating its crash performance against the baseline front end module. Further validation is conducted by inserting the tailor-welded hot stamped side frame member into the SUV model, in place of the production JAC590R side frame member.

4.1 Initial Design Decisions

The purpose of the side frame member is to safely manage the kinetic energy of the vehicle, while preventing structural component intrusion into the occupant seating envelope in the event of a full-frontal crash. In accordance with this purpose, the design of the tailor-welded hot stamped side frame member must meet the design specifications laid out in Table 3; these include, matching the overall crush response, the crush forces, the resistance to passenger compartment intrusion and the quantity as well as severity of spot weld failures that occur. In addition to meeting crash performance requirements, the tailor-welded hot stamped side frame member must also be reliably formable in a lab-scale hot stamping process. Furthermore, the tailor-welded hot stamped side frame member design must seamlessly interface with the BIW of the SUV such that it could be swapped into the vehicle in place of the production JAC590R side frame member. In order, for the design to be deemed successful, all of the aforementioned requirements must be met, while also ensuring a significant weight savings is associated with implementing the hot stamped materials (greater than 15%); otherwise it is unlikely that the capital cost associated with the hot stamping process would be justified.

4.1.1 Two Component Design

The production JAC590R side frame member is comprised of three separate conventionally formed components, as shown in Figure 145a. In order to minimize the expenditure associated with fabricating the hot stamping tooling the tailor-welded hot stamped side frame member is designed as two components, thus requiring that only two separate tools be made, instead of the three required by the production design. Coincidentally, consolidation of components is actually a positive aspect for automotive manufacturers because it means fewer tools are required to be fabricated, as well assembly times are reduced due to less components.

In the hot stamped design (Figure 145b), the two components are referred to as the main rail and enclosure panel. The main rail is a C-channel cross-section along the length of the crush tip and middle sections, however in the S-rail section, where the rail opens up to accommodate the dashboard and floor panels, the cross-section becomes an L-shape. The enclosure panel is a relatively straight cross-section that closes off the crush tip and middle sections, however in the S-rail section it only provides one sidewall for the main rail and leaves the top open for the dashboard and floor panel to close off the rail. Paying particularly close attention to the S-rail section of the main rail and enclosure panel, it is observed that a flange is added along the bottom of the rail (dashed red line) to make it possible for the enclosure panel to interface with the main rail in this section. This added flange is a direct continuation of the lower flange that already exists on the production main rail and enclosure panel.

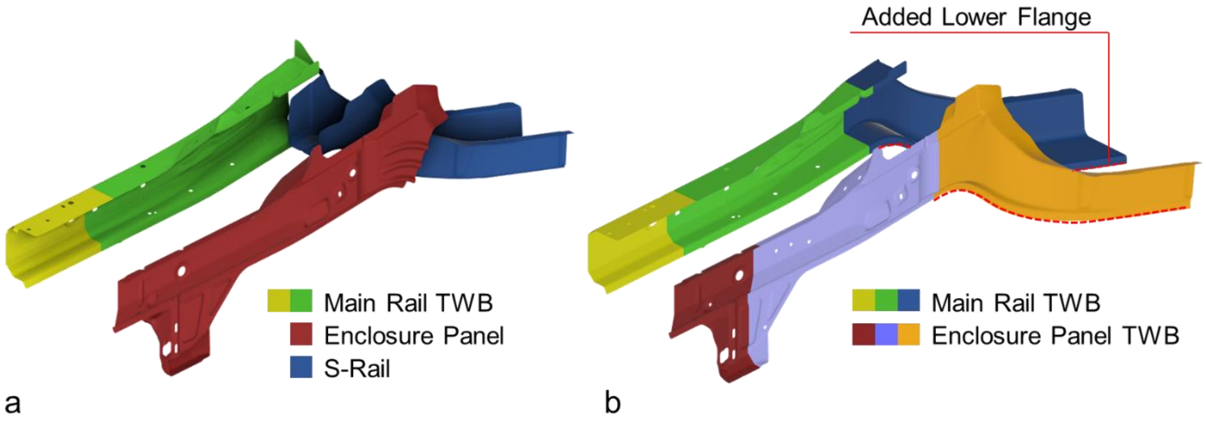

Figure 145. Exploded view of the (a) three component production JAC590R side frame member and (b) two component Ductibor® 1000-AS/Usibor® 1500-AS tailor-welded hot stamped side frame member.

4.1.2 Tailor-Welded Blank Laser Weld Line Locations

The laser weld line locations on the TWBs that separate each of the different zones (crush tip, middle section and S-rail) along the side frame member are determined from the production side frame member. In the main rail part, the weld line separating the two different gauges of Ductibor® 1000-AS is directly determined from the location of the weld line between the 1.4 mm and 1.6 mm JAC590R material in the production side frame member (weld line 1 in Figure 146). In the production side frame member, the 1.8 mm JAC590R S-rail section inserts 105 mm into the 1.6 mm JAC590R middle section for assembly, creating a material overlap and thus an area of high strength in this region. The weld line for separating Ductibor® 1000-AS in the middle section from Usibor® 1500-AS in the S-rail (weld line 2 in Figure 146) is located at the end of the 105 mm component overlap, ensuring that the higher strength Usibor® 1500-AS is located in this area. To simplify the blank design and fabrication, the same locations of the laser weld lines from main rail part were used on the enclosure panel part.

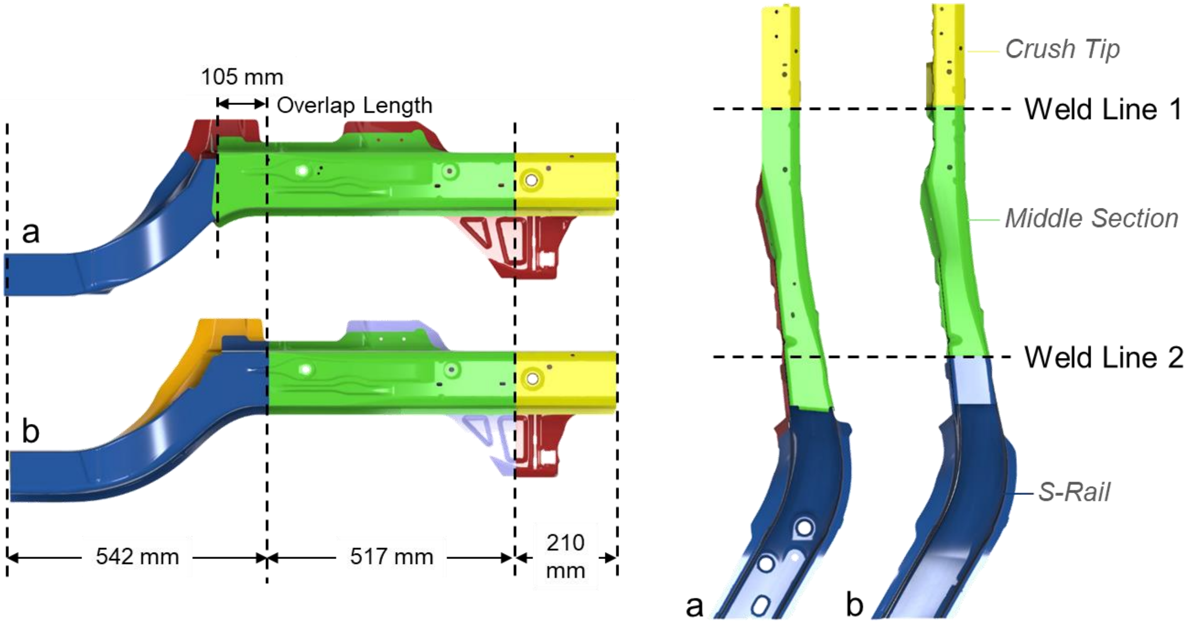

Figure 146. Location of TWB weld lines and the length of each crush zone in the **(a)** production side frame member and **(b)** tailor-welded hot stamped side frame member.

4.1.3 Sheet Material Thickness Selection

The thicknesses of the TWB sheet material in each section of the side frame member are selected from a list of currently available sheet thicknesses of Ductibor® 1000-AS and Usibor® 1500-AS, as provided by Soldaat [89]. By selecting currently available sheet thicknesses, the fabrication of the tailor-welded hot stamped side frame member TWBs becomes much more feasible, for this lab-scale project. The alternative to selecting from available gauges is to perform an optimization with the goal of minimizing sheet thickness, while maintaining frontal crash performance; however, this sort of optimization was considered outside of the scope of this thesis.

Determining the sheet thickness in the axial collapse sections (crush tip and middle sections) of the side frame member is accomplished using the strength to thickness ratio relationship based on the axial crush relation developed by White *et al.* [43] given by Equation (6). In this equation, the ultimate tensile strengths of JAC590R (635 MPa) and Ductibor® 1000-AS (1067 MPa) are used in conjunction with the thicknesses of each zone from the production side frame member, to determine what the equivalent thickness would be for the hot stamped sheet material. The calculated thicknesses of the hot stamped material in the crush tip and middle sections are shown in Table 8. Using the strength to thickness ratio it is observed that the calculated thickness of the Ductibor® 1000-AS crush tip and middle section are non-standard gauges (1.02 mm and 1.17 mm, respectively). To determine the nominal gauge of Ductibor® 1000-AS in the crush tip and middle section, the non-standard calculated thicknesses are rounded to the nearest available thickness. The calculated 1.02 mm

Ductibor® 1000-AS crush tip becomes 1.0 mm and the calculated 1.17 mm Ductibor® 1000-AS middle section becomes 1.2 mm. The nominal thicknesses of the Ductibor® 1000-AS crush tip and middle section are shown in Figure 147 alongside the production JAC590R side frame member. The determination of the sheet thickness of the Usibor® 1500-AS s-rail section were determined using an iterative approach based on model predictions, as described in section 4.3.1.

Table 8. Calculated thickness of the Ductibor® 1000-AS crush tip and middle section.

Crush Section	Production Thickness	Calculated Thickness
Crush Tip	(JAC590R) 1.4 mm	(Ductibor® 1000-AS) 1.02 mm
Middle Section	(JAC590R) 1.6 mm	(Ductibor® 1000-AS) 1.17 mm

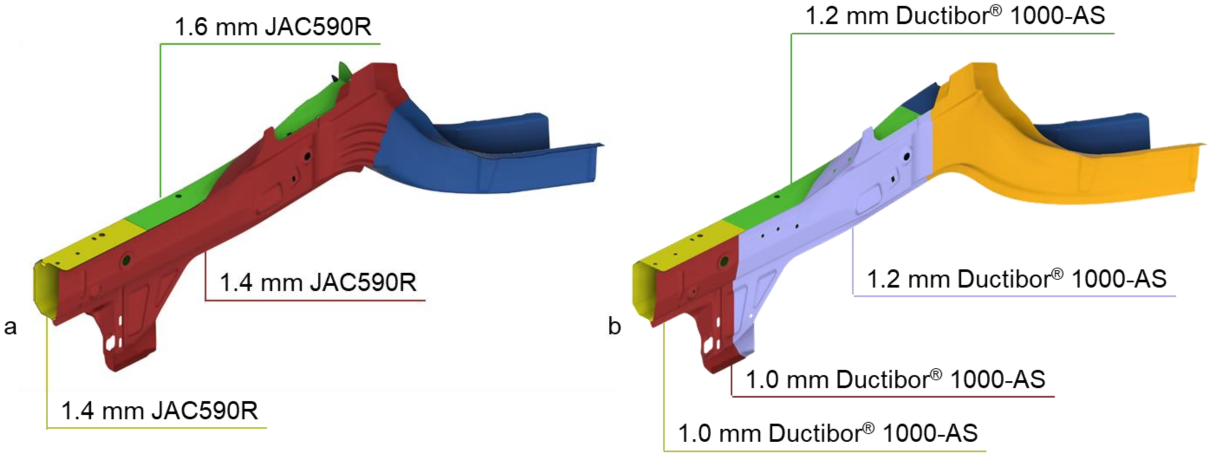

Figure 147. Thickness and sheet material used in the crush tip and middle section of the **(a)** production side frame member and **(b)** tailor-welded hot stamped side frame member.

4.2 Numerical Model

The tailor-welded hot stamped side frame member is directly interchanged with the current production JAC590R side frame member, within the baseline front end module, as illustrated in Figure 148. This new front end module structure will henceforth be referred to as the tailor-welded hot stamped front end module. Due to the interchangeability of the side frame members, the crash sled and wall mounting boundary conditions, as well as the location and joining method for the weld-on and secondary bolt-on production components remain largely the same as for the baseline front end module model, discussed in section 3.3. Differences in the models of the front end module configurations (tailor-welded hot stamped and baseline) are related to the differences in side frame members, including: minor topological changes, material model, sheet metal thickness and spot weld model. It is important to note that the hot stamped sheet material thicknesses in this section are given as a nominal thickness. The actual thickness of the hot stamped sheet material used in the simulations are 50 μm (0.05 mm) less than the nominal thickness, due to subtraction of the non-load bearing Al-Si coating thickness (as explained in section 1.1.3) on both sides of the part.

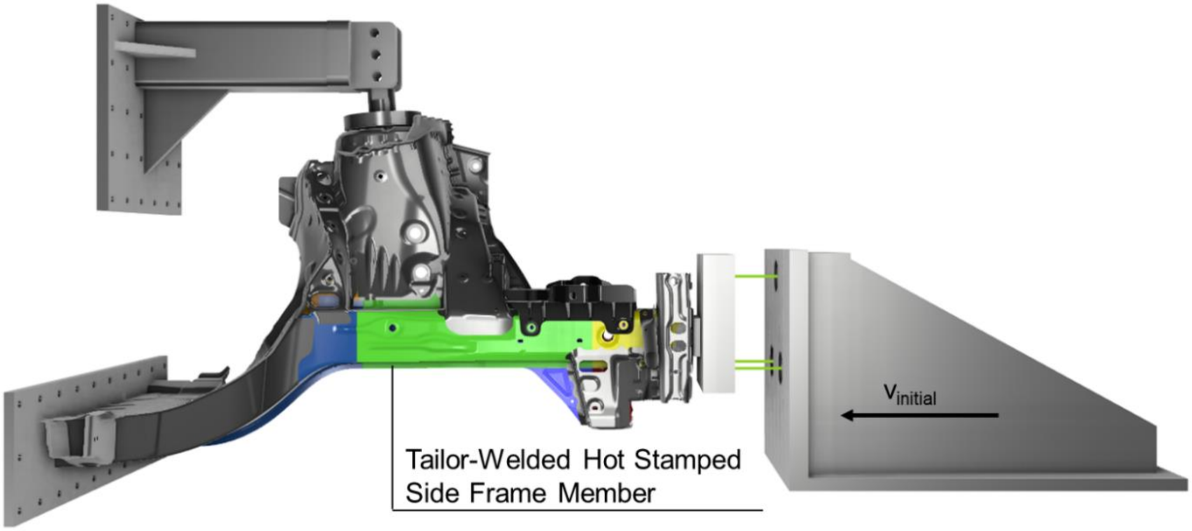

Figure 148. Numerical model of the tailor-welded hot stamped front end module.

4.2.1 Hot Stamped Steel Material Model

The two hot stamped steels considered in the tailor-welded hot stamped side frame member are Usibor® 1500-AS and Ductibor® 1000-AS. Both materials are used in their fully-quenched state, which are associated with a Vickers hardness number of 490 HV [19] and 380 HV [90] for Usibor® 1500-AS and Ductibor® 1000-AS, respectively. The stress-strain response and strain-rate sensitivity for Usibor® 1500-AS is predicted from the eTCM constitutive model (section 1.5.4) [56], for a fully-martensitic microstructure (490 HV). The stress-strain response and strain-rate sensitivity for Ductibor® 1000-AS is determined from the combined experimental work of Abedini and Samadian [91]. The flow stress curves at different strain-rates (0.001 s^{-1}, 0.01 s^{-1}, 0.1 s^{-1}, 1 s^{-1}, 10 s^{-1}, 100 s^{-1} and 1000 s^{-1}) for both of these hot stamped materials are shown in Figure 149. The hardening behaviour of both materials has been modelled in LS-Dyna using the *MAT_PIECEWISE_LINEAR_PLASTICITY material card.

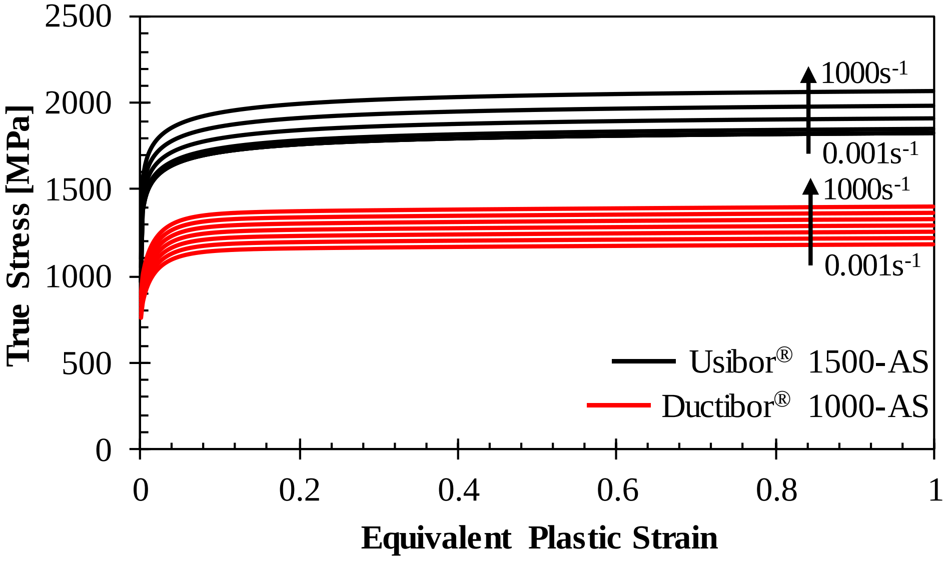

Figure 149. Modelled, strain rate sensitive, constitutive behaviour of Usibor® 1500-AS (from Omer *et al.* [56]) and Ductibor® 1000-AS (from Abedini and Samadian [91]).

Both Usibor® 1500-AS and Ductibor® 1000-AS are ultra-high strength materials with different degrees of ductility. It is therefore crucial to the accuracy of the modelling effort that failure be incorporated into these material models. The failure model used is the GISSMO formulation [80], which is based on the fracture *loci* for Usibor® 1500-AS (developed by ten Kortenaar [13]) and Ductibor® 1000-AS (developed by Samadian and Lee [92]), as illustrated in Figure 150. Both fracture curves have been calibrated from fracture test data using the 6-parameter model due to Bai and Wiezbicki [81]. It is observed that the fracture strain at each triaxiality is higher for Ductibor® 1000-AS, which is an indication that Ductibor® 1000-AS has superior fracture resistance, relative to Usibor® 1500-AS. In order for an element deletion to be triggered, the damage parameter must accumulate to unity in at least 70% of the elemental integration points. To account for the variation in mesh size in the tailor-welded hot stamped side frame member, a mesh regularization curve (Figure 151) is input to scale each fracture *locus* (Usibor® 1500-AS and Ductibor® 1000-AS) with respect to mesh element size. The regularization curve for Usibor® 1500-AS has been developed by ten Kortenaar [13], while the curve for Ductibor® 1000-AS is constant at 0.4 for all mesh sizes and was developed as combined effort by Samadian *et al.* [93].

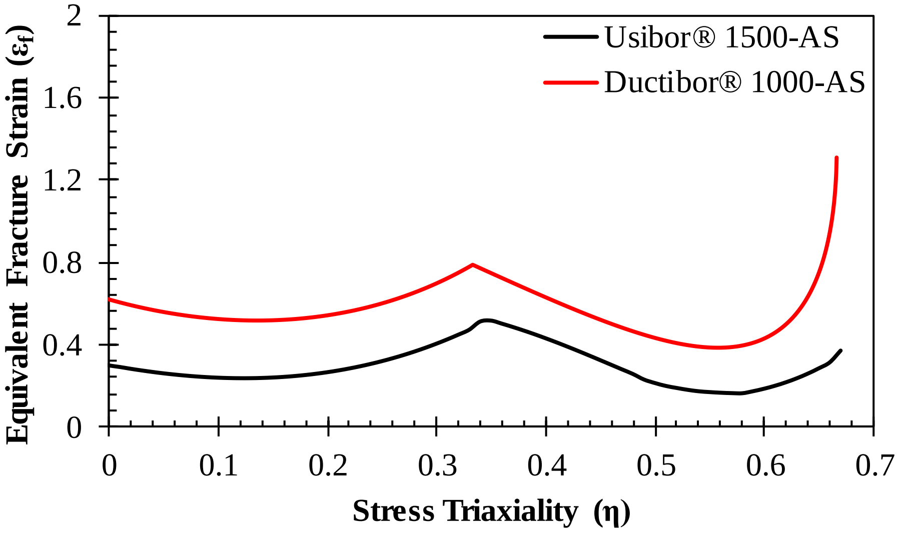

Figure 150. Fracture *loci* of Usibor® 1500-AS (from ten Kortenaar [13]) and Ductibor® 1000-AS (from Samadian and Lee [92]).

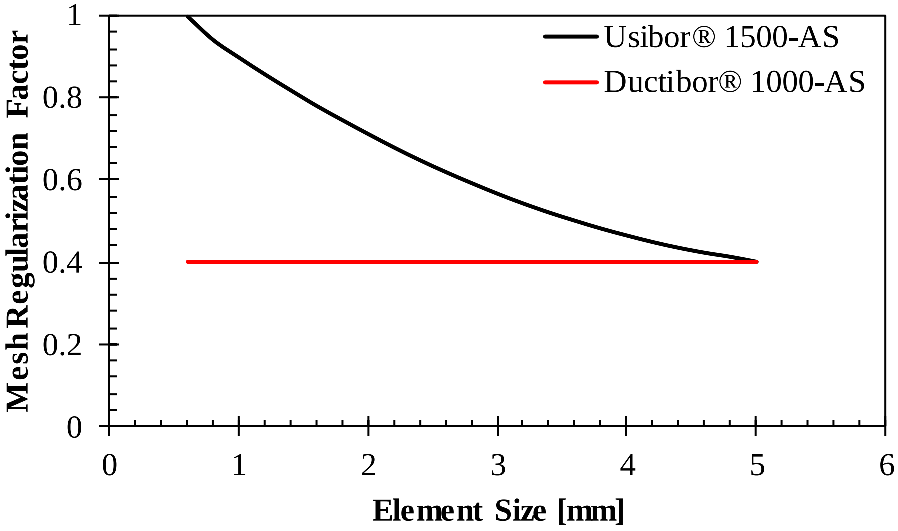

Figure 151. Mesh regularization curves used to scale the equivalent fracture strain of Usibor® 1500-AS (from ten Kortenaar [13]) and Ductibor® 1000-AS (developed by Samadian *et al.* [93]) with respect to mesh size.

4.2.2 Hot Stamped Steel Spot Weld Model

The modelling method for spot welds, in terms of material and failure model type, remains the same as in the baseline front end module and SUV model (described in section 2.2.2). Failure strengths for the hot stamped material spot welds differ from the JAC590R spot welds, however the numerical values used in the simulations cannot be published, since the data is proprietary. Table 9 shows representative axial and shear failure loads for Ductibor® 1000-AS and Usibor® 1500-AS spot welds in both 1.0 mm and 1.2 mm thicknesses.

Table 9. Spot weld axial and shear failure loads for 1.2 mm and 1.6 mm Ductibor® 1000-AS from Tolton [94] and Usibor® 1500-AS from O'Keeffe [65].

Material	Thickness	Axial Failure Load	Shear Failure Load
Ductibor® 1000-AS	1.2 mm	6.6 kN	16.8 kN
	1.6 mm	12.3 kN	20.9 kN
Usibor® 1500-AS	1.2 mm	4.0 kN	6.6 kN
	1.6 mm	5.5 kN	19.0 kN

4.3 Simulation-Based Design Process

The design of an automotive component for crash safety, such as a side frame member, is complex and often requires an iterative, simulation-based design process to be implemented. In the current work, the aspects of the side frame design that require an iterative process include: (i) the selection of the sheet material thickness for the S-rail section, as well as topological additions such as (ii) fold initiators and (iii) changes to the side frame member flange geometry.

4.3.1 Selection of Sheet Thickness for the S-Rail

The sheet thickness of the Ductibor® 1000-AS crush tip and middle sections were calculated using the strength to thickness ratio relation (Equation (6)), as described in section 4.1. The same ratio could not be used to calculate the thickness of the intrusion resistant S-rail section, since this relation is derived for cross-sections experiencing the axial collapse deformation mode. The S-rail section does not undergo axial collapse, rather its purpose is to maintain rigidity and prevent intrusion into the passenger compartment. In order to determine the sheet material thickness for the S-rail section a numerical parametric study is conducted.

In the numerical parametric study, the thickness of the Usibor® 1500-AS S-rail section is varied from 1.0 mm to 1.6 mm, in increments of 0.2 mm. The thicknesses of the Ductibor® 1000-AS crush tip and middle sections remain constant at 1.0 mm and 1.2 mm, respectively. The predicted deformation of the S-rail (red), for each thickness, at a crash sled displacement of 350 mm is shown in Figure 152. It is observed from this figure that both the 1.0 mm and 1.2 mm thick S-rail sections buckle under the crush load, while the 1.4 mm and 1.6 mm thick S-rail sections remain composed. Furthermore, the deformation observed between the 1.4 mm and 1.6 mm thick S-rail sections are almost identical in appearance, implying that the S-rail thickness study converges at 1.4 mm thick Usibor® 1500-AS. An S-rail thickness of 1.4 mm is selected from the numerical parametric study and will be used throughout the duration of the tailor-welded hot stamped side frame member design.

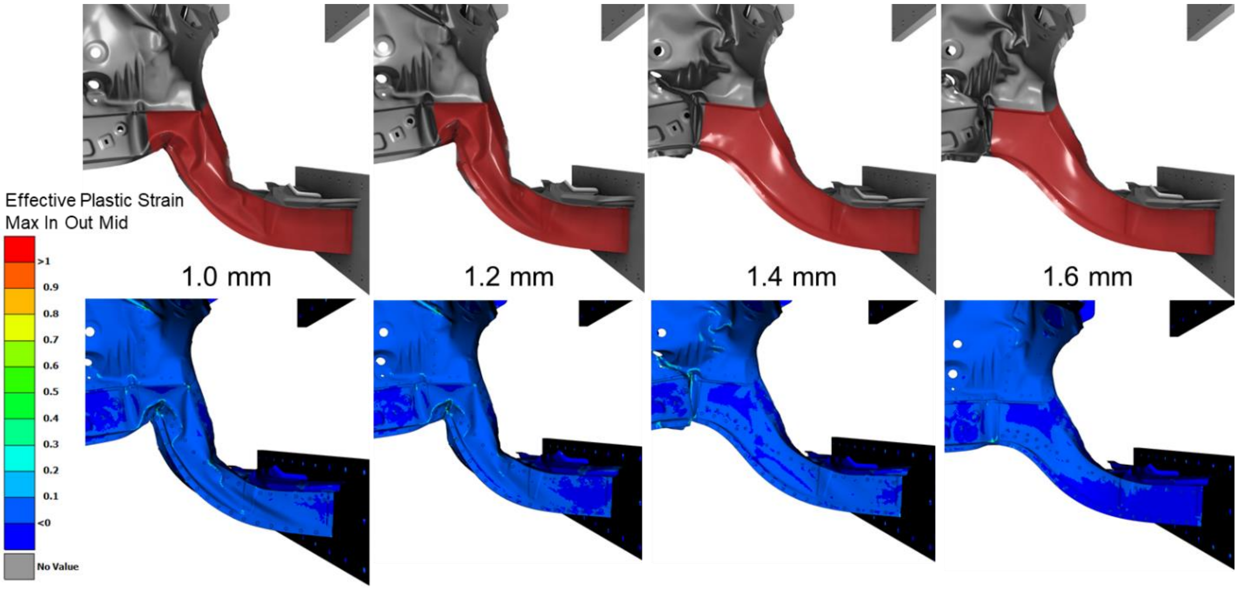

Figure 152. Numerical parametric study of the Usibor® 1500-AS S-rail thickness (red) at 1.0 mm (Trial 3801), 1.2 mm (Trial 3802), 1.4 mm (Trial 3800) and 1.6 mm (Trial 3803) showing the predicted deformation (top) and effective plastic strain (bottom) at a crash sled crush distance of 350 mm.

4.3.2 Fold Initiator Development

With the sheet material thickness for each section of the tailor-welded hot stamped side frame member fully defined, effort can be transitioned to tuning the crush response of the tailor-welded hot stamped side frame member. An initial model was developed in which the hot stamped materials were inserted into the two component tailor-welded hot stamped side frame member design (Figure 145b), while keeping all other topological features the same. The predicted crush response of that tailor-welded hot stamped side frame member is shown in Figure 153. It is observed from this figure that early into the consolidation of the crush tip (170 mm) a significant number of spot weld failures occur along the top and bottom flanges, causing the enclosure panel crush tip to “unzip” from the main rail. (Close-up images of the predicted flange unzipping response can also be seen in Figure 153c.) In addition, the crush response does not match that of the accepted baseline front end module, since no buckle is formed in front of the shock tower support after the consolidation of the crush tip (1). There is however a buckle that forms after the shock tower support (2). Ultimately, this figure shows that a simple material substitution (Ductibor® 1000-AS and Usibor® 1500-AS replacing JAC590R) will not be sufficient to reproduce the crush behaviour displayed by the baseline side frame member because of the much higher strengths of the hot stamped materials and their associated lower ductility and fracture resistance.

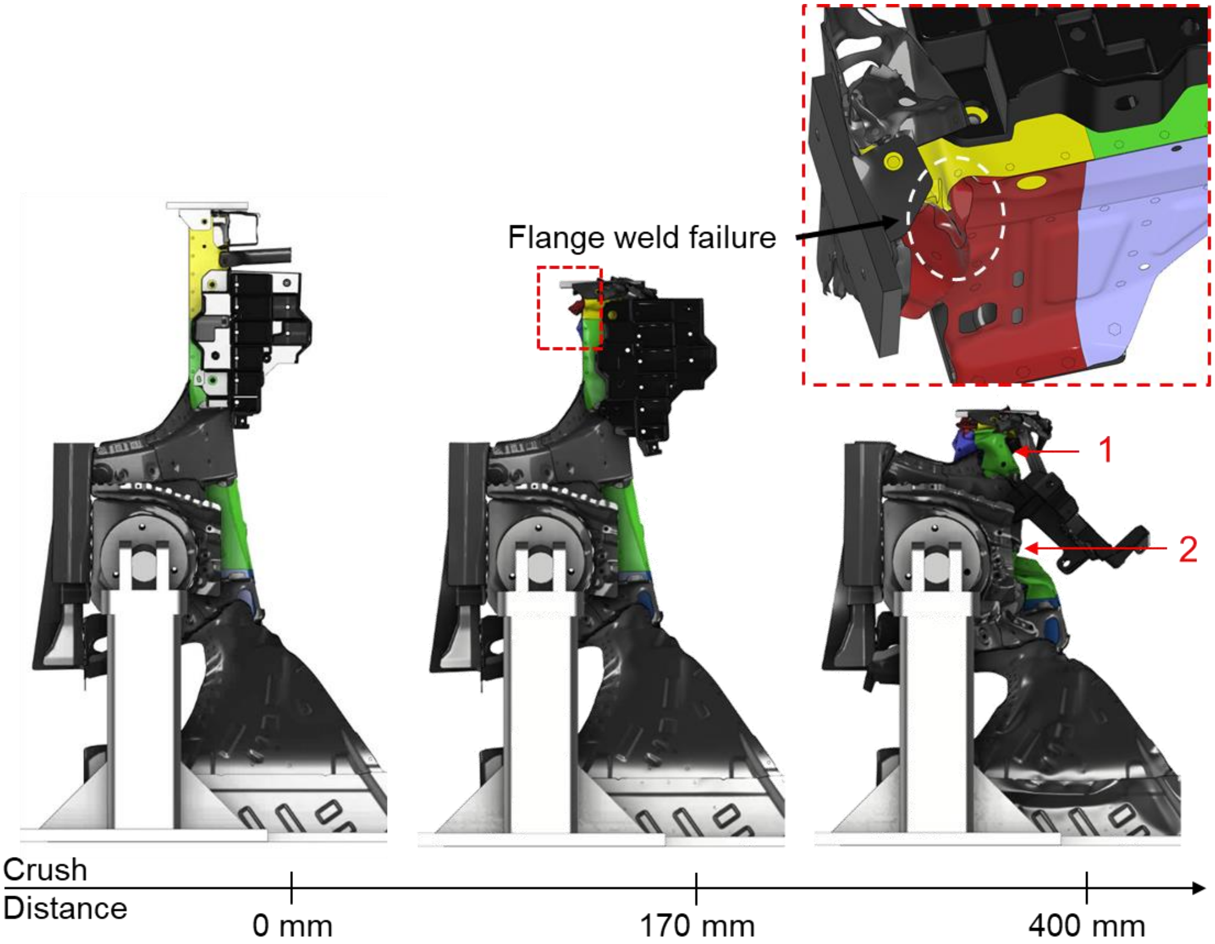

Figure 153. Crush response of the two component tailor-welded hot stamped side frame member (Trial 3800), highlighting the crush tip flange spot weld failure, crush tip consolidation without buckle in front of the shock tower support (1) and buckle after the shock tower support (2).

It is apparent from Figure 153 that simply replacing the production JAC590R sheet material with Ductibor® 1000-AS and Usibor® 1500-AS will not yield adequate crush response predictions. Rather, in order to obtain a desirable crush response, topological features must be added to the tailor-welded hot stamped side frame member. The first topological feature additions considered the introduction of new fold initiators, designed to improve the folding behaviour of the side frame member. The fold initiators added to the outboard side of the tailor-welded hot stamped side frame member are displayed in Figure 154b, while those added to the inboard side are shown in Figure 155b. The deformation of the production topology tailor-welded hot stamped side frame member, at specific crush distances, is also shown in Figure 154c and Figure 155c to highlight the undesirable folding behaviour the new fold initiators are intended to eliminate.

In Figure 154 the outboard fold initiators have been numbered 1 through 8 and their intended contribution to the crush response will be described in this paragraph. Fold initiator number 1 is comprised of two indents oriented into the rail section and located at the impacted end. Their purpose is to initiate an inward fold prior to large outward fold, highlighted at 42 mm of crush distance (white arrow), which would cause less shear force to be placed on the top flange spot welds. Fold initiators 2, 3 and 4 are located on the lower flange and have orientation out, out and in, respectively. The purpose of these initiators are to suppress the spot weld unzipping along the lower flange at 42 mm of crush distance (lower dashed white circle). Fold initiator number 5 is the large inward oriented initiator, located in the middle of the crush tip. It is intended that this fold initiator acts as a pivot for the large outward fold at 42 mm crush distance (white arrow), that will suppress its outward motion and put less shear and peel loading on the top flange spot welds. Fold initiators 6, 7 and 8 have orientations down, up and down, respectively, along the top flange. The purpose of these initiators are to encourage sequential folding along the top flange and reduce the severity of the tight radius folds of the main rail flange forming inside of shallow radius folds of the enclosure panel flange (white arrow at 100 mm crush distance), which put harsh shear and peel loads on the adjacent spot welds.

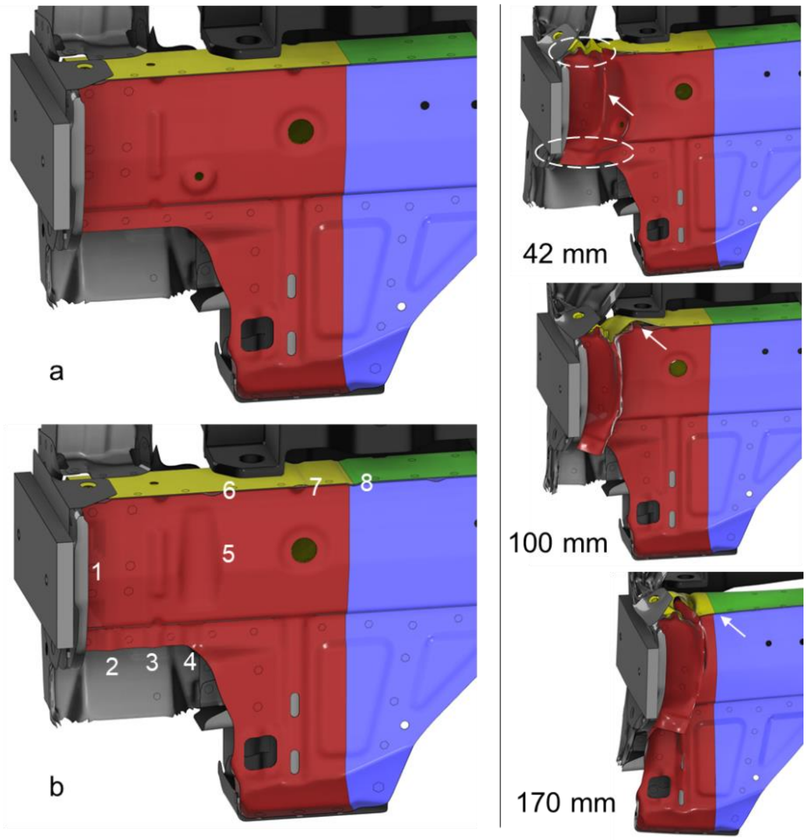

Figure 154. Outboard side of the tailor-welded hot stamped side frame member with **(a)** topology of side frame member identical to production, **(b)** addition of fold initiators. The deformed side frame member (topology identical to production) is shown on the right to highlight certain aspects of the deformation.

In Figure 155 the fold initiators on the inboard of the side frame member are located on the middle section (green) of the rail and have been numbered 9 and 10. Fold initiator number 9 is oriented inward and is located on the chamfered surface between the main rail sidewall and C-channel bottom surface. The purpose of this fold initiator is to create an inward buckle at 264 mm of crush distance, instead of the rail remaining straight, as it does in the tailor-welded hot stamped side frame member with baseline topology (white arrow at crush distance of 264 mm). The inward buckle produced by fold initiator number 9 is intended to promote sequential folding in the middle section, in front of the shock tower support. Fold initiator number 10 is a large inward indent running from the top of the sidewall to the bottom of the sidewall, directly in front of the shock tower support. The purpose this tenth fold initiator is to help create a buckle in front of the shock tower support, that will rotate the crush tip inboard. In the baseline topology tailor-welded hot stamped side frame member, the crush tip rotates to the vehicle outboard and a fold is not created in front of the shock tower support on the inboard side (white arrow at 335 mm of crush distance).

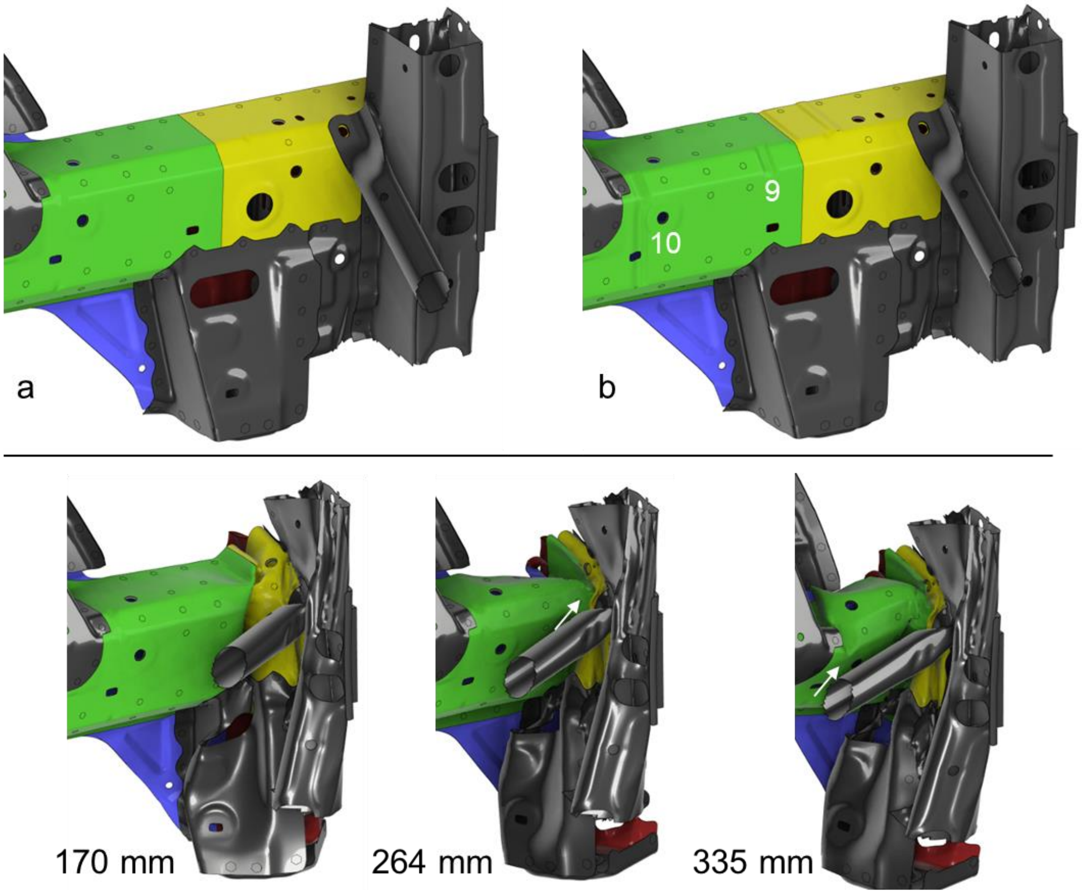

Figure 155. Inboard side of the tailor-welded hot stamped side frame member with **(a)** topology of side frame member identical to production (Trial 3800), **(b)** the addition of fold initiators (Trial 3809) and **(c)** the predicted deformation of the crush tip section using the baseline topology (Trial 3800).

The crush response of the tailor-welded hot stamped side frame is compared with (Figure 156b) and without (Figure 156a) the addition of fold initiators, from the top view. It is observed from the top view that the crush response of the tailor-welded hot stamped side frame member is significantly improved with the addition of the new fold initiators. With the new fold initiators (Figure 156b), full consolidation of the crush tip is observed (200 mm of crush distance), followed by a buckle created in front of the shock tower support (red arrow at 330 mm of crush distance) and then a buckle behind the shock tower support (second red arrow at 400 mm of crush distance). Without the addition of the new fold initiators (Figure 156a), a buckle is only created behind the shock tower support, after the consolidation of the crush tip.

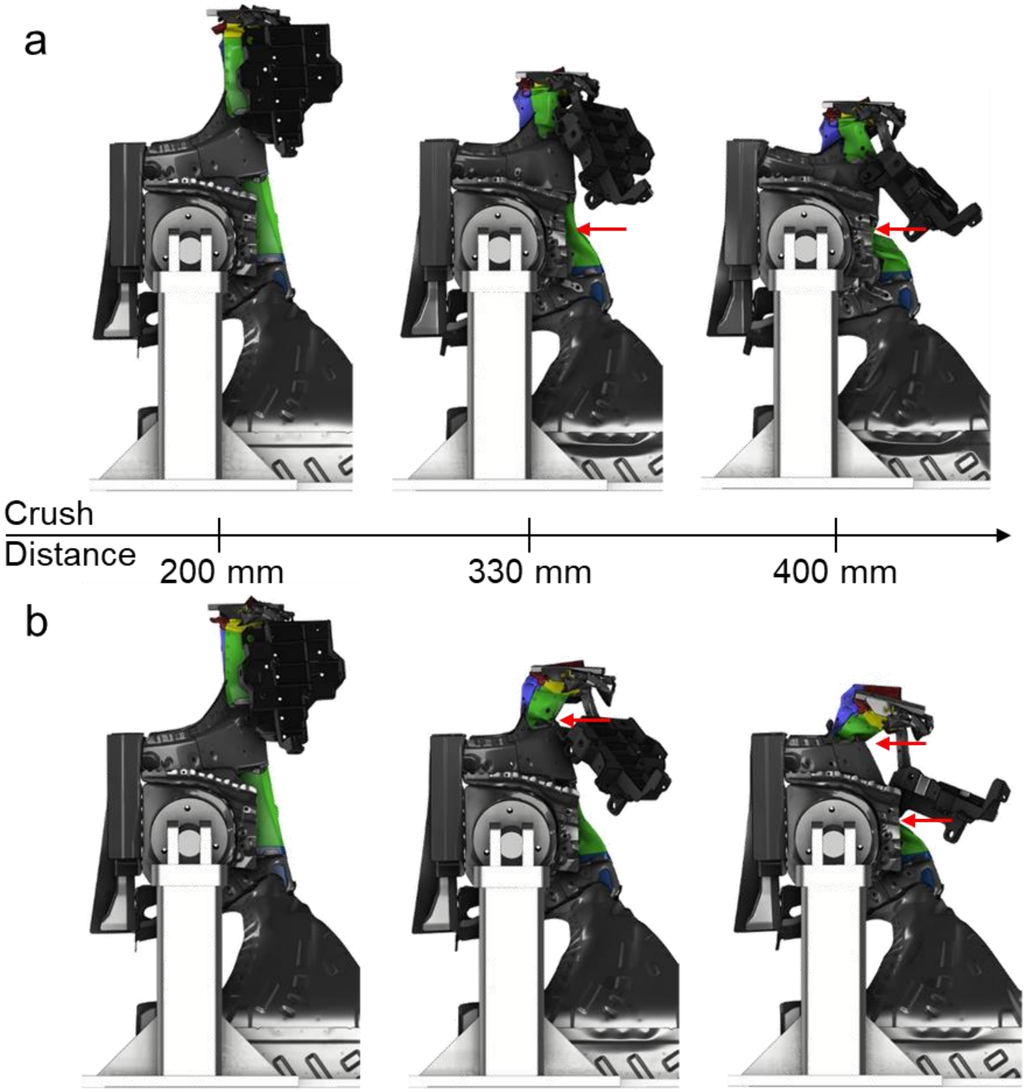

Figure 156. Top view comparison of the tailor-welded hot stamped side frame member crush response **(a)** before (Trial 3800) and **(b)** after the addition of fold initiators (Trial 3809).

The predicted extent of spot weld failure occurring in the crush tip of the tailor-welded hot stamped side frame members is analyzed from the outboard isometric view, as shown in Figure 157. Comparing both the tailor-welded hot stamped side frame member with (Figure 157b) and without (Figure 157a) fold initiators, it is observed that the extent of spot weld failure occurring in the crush tip is not significantly improved with the addition of fold initiators. The flange spot weld failures (white dashed circles) are observed to occur in the same locations, with the same level of severity, for both fold initiator configurations. A difference in spot weld failure is noticed at 40 mm of crush, in which spot weld failure is delayed in the lower flange of the side frame member with added fold initiators. In addition, desirable sequential folding in the middle section (green) is observed in the side frame member, with the addition of fold initiators, as highlighted by the white arrow at 240 mm of crush.

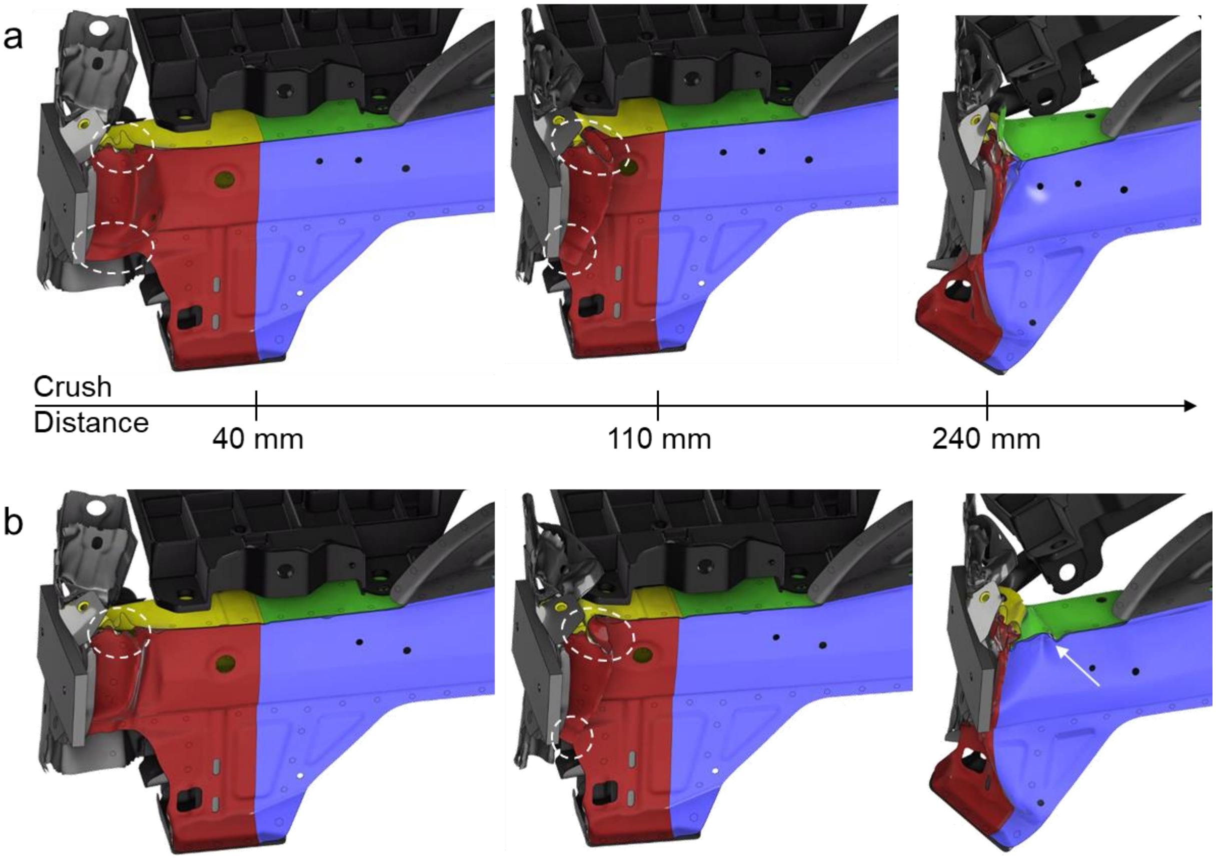

Figure 157. Outboard isometric comparison of the tailor-welded hot stamped side frame member crush response and crush tip spot weld failure **(a)** before (Trial 3800) and **(b)** after the addition of fold initiators (Trial 3809).

The predicted crush forces for the tailor-welded hot stamped side frame member with and without fold initiators are compared to the baseline front end module, as shown in Figure 158. It is observed from this figure that in either configuration of the tailor-welded hot stamped side frame member, the final force peak starting at 320 mm of crash sled crush distance is not captured. The predicted average force for the tailor-welded hot stamped side frame member with and without fold initiators are 71 kN and 67 kN, respectively, which are much lower than the baseline front end module average force of 91 kN. The relatively large discrepancy in crush forces between the hot stamped configurations and the baseline are due to difference in the observed crush modes. In the tailor-welded hot stamped side frame member without fold initiators a plastic hinge is formed behind the shock tower support after consolidation of the crush tip section at approximately 300 mm of crush distance, as shown in Figure 153. In the hot stamped configuration with fold initiators the plastic hinge formed in front of the shock tower is much larger than that formed in the baseline front end module, as shown in Figure 156.

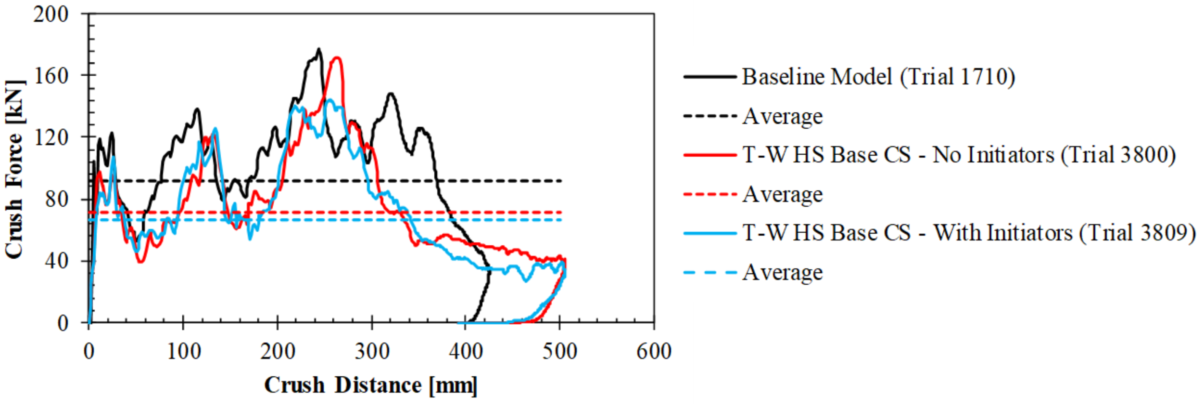

Figure 158. Crush force and average crush force for the baseline cross-section tailor-welded hot stamped side frame member with (Trial 3809) and without (Trial 3800) the addition of fold initiators compared to the baseline front end module model (Trial 1710).

It is concluded from this initial study that the introduction of the higher strength hot stamping materials (Ductibor® 1000-AS and Usibor® 1500-AS) requires topological changes to the side frame member to achieve a similar crush response to the baseline. The addition of the new fold initiators to the tailor-welded hot stamped side frame member did serve to improve the overall folding and crush response of the structure when compared to the side frame member without fold initiators. Unfortunately, the extent of spot weld failure and flange unzipping persisted in the models, even after the introduction of the new fold initiators.

4.3.3 Cross-Section Development

In order to reduce the extent of spot weld failure occurring in the tailor-welded hot stamped side frame member, additional topological changes are investigated, focused on the cross-sectional and flange geometry. The current cross-section of the tailor-welded hot stamped side frame member (Figure 159a) is comprised of a main rail (cyan), with a horizontally oriented flange on the top and vertically oriented flange on the bottom, as well as an enclosure panel (orange), with mating flange orientations. It is observed from the current cross-section that the enclosure panel has three radii (r_1, r_2 and r_3), in which radii r_2 and r_3 create a double hat channel-type geometry. The additional radii associated with a double hat channel section provide extra stiffness to the structure, when compared with a single hat channel section. A stiffer structure is associated with higher crush forces and more energy absorption; however, due to the increased strength of Ductibor® 1000-AS and Usibor® 1500-AS, compared to JAC590R, the additional stiffness provided by the two radii (r_2 and r_3) results in additional load on the spot welds along the bottom flange. Therefore, to reduce the amount of weld failure on the bottom flange and to improve the overall crush response of the tailor-welded hot stamped side frame member the two radii (r_2 and r_3) are removed, as shown in proposed vertical flange cross-section (Figure 159b). In addition, a 3 degree draft angle was added to the sidewall of the vertical flange geometry main rail to improve the formability of the channel section.

Peel moment was determined to be the dominant contributing loading condition to spot weld failure, as discussed in section 2.7. To mitigate weld failure due to peeling, a geometric change is also introduced into the top flange to change its crush behaviour and reduce the high loads on the spot welds. The geometric change made to the top flange is to orient it vertically (Figure 159b). A subtle consequence of the vertical top flange orientation and removal of the two radii is that the vertex separating the vertical wall face from the angled wall face must be moved upwards, as highlighted by the dashed circle.

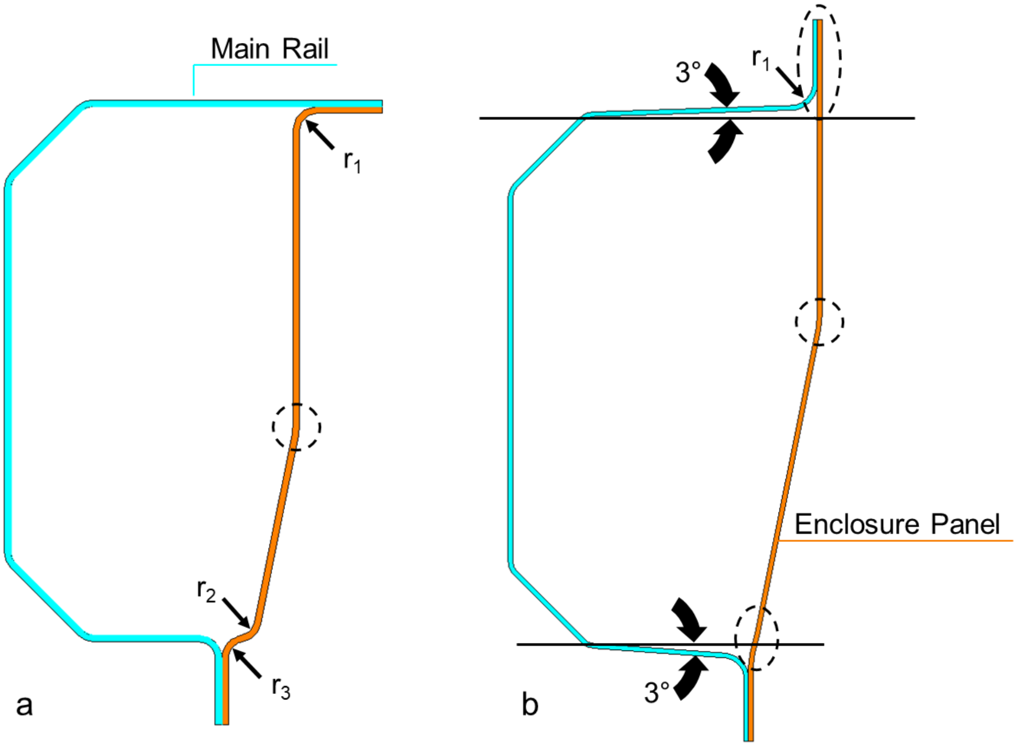

Figure 159. (a) Current cross-section and **(b)** proposed vertical flange cross-section of the tailor-welded hot stamped side frame member.

The proposed vertical flange tailor-welded hot stamped side frame member is shown adjacent to the original geometry in Figure 160. The S-rail section and the rearward middle section remain unchanged by the vertical flange geometry change, since these sections already have vertical flanges. The location changed by the proposed vertical flange geometry is the crush tip section. The change on the upper flange, from a horizontally oriented flange to a vertically oriented flange, is highlighted with a black dashed ellipse. A particularly interesting addition is the blended surface connecting the crush tip vertical flange to the pre-existing vertical flange, where the shock tower support is welded to the side frame (arrow). The change to the lower flange, in which the double radii is eliminated in the vertical flange design, is also highlighted by a black arrow. It is also noted that a few of the datum holes in the crush tip have been removed to further simplify the tailor-welded hot stamped side frame member geometry for simulation purposes. Finally, it is important to note that the geometry shown in Figure 158 utilizes the fold initiator configurations from the baseline geometry in order to isolate the effects of the enhanced initiators shown in the previous section *versus* the effect of the changes to the cross-section.

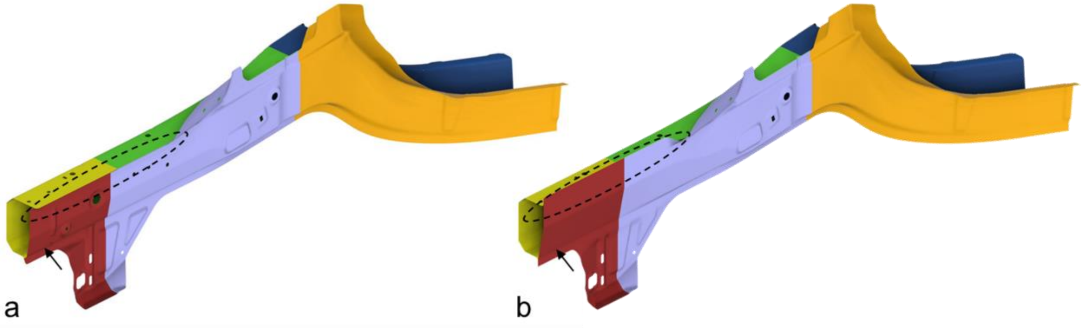

Figure 160. (a) Original side tailor-welded hot stamped side frame member geometry compared to the **(b)** proposed vertical flange tailor-welded hot stamped side frame member.

The crush response of the vertical flange tailor-welded hot stamped side frame member is shown in Figure 161 (top view). Consolidation of the crush tip is observed at 100 mm of crash sled crush distance, which continues to progress through to 300 mm of crush distance. This full consolidation is quickly followed by the formation of a buckle behind the shock tower support (red arrow at 300 mm of crush distance), which transitions the crush mode from a progressive folding mode to a buckle dominant mode, as observed at 400 mm of crush distance. A buckle in front of the shock tower support is not observed in the vertical flange tailor-welded hot stamped side frame member.

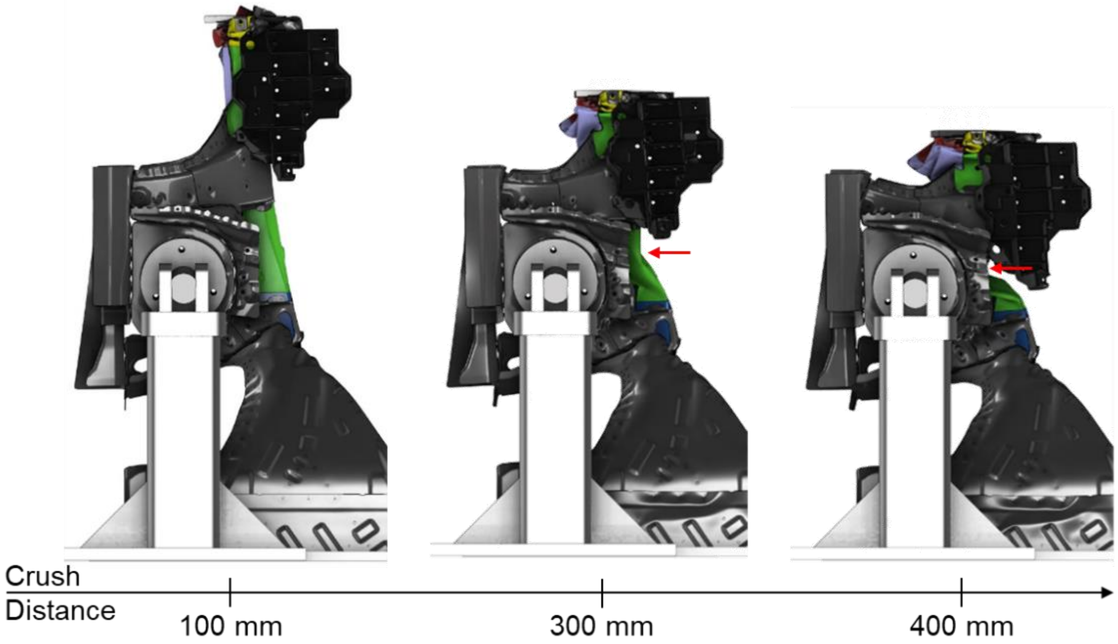

Figure 161. Top view of the vertical flange tailor-welded hot stamped side frame member (Trial 3900) showing the crush response of the structure.

The crush tip deformation and extent of spot weld failure in the vertical flange tailor-welded hot stamped side frame member is shown in Figure 162. In this figure it is clearly observed that spot weld failure (white dashed circles) still occurs in the vertical flange tailor-welded hot stamped side frame member; however, it is much less severe than that which occurs in the original flange geometry tailor-welded hot stamped side frame member (Figure 157).

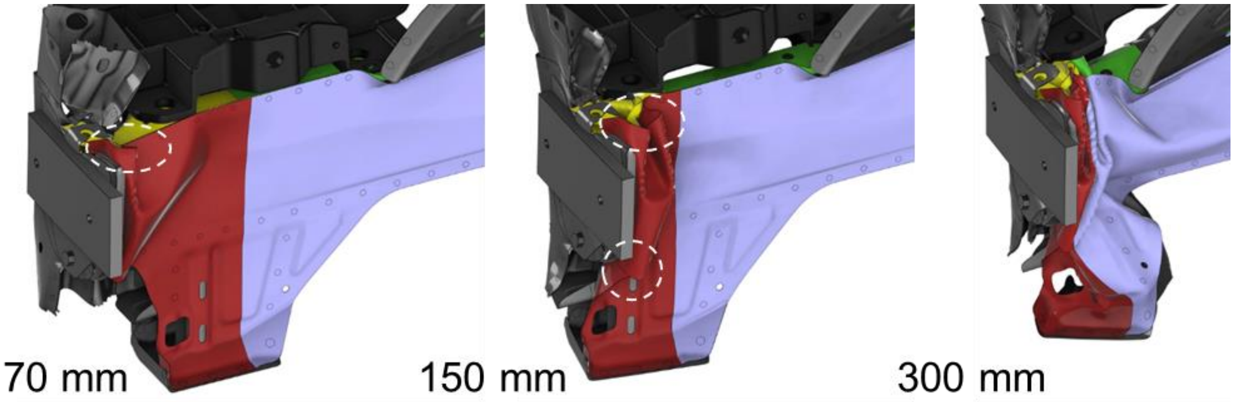

Figure 162. Deformation of the vertical flange geometry tailor-welded hot stamped side frame member (Trial 3900), highlighting the crush behaviour and spot weld failure (white dashed circle).

In order to mitigate the predicted spot weld failures and capture the required deformation modes in the vertical flange tailor-welded hot stamped side frame member, the addition of fold initiators is investigated. The crush tip of the vertical flange tailor-welded hot stamped side frame member is shown with and without the addition of fold initiators in Figure 163. It can be seen that the fold initiators are uniformly spaced along the length of the crush tip. The initiators are situated between adjacent spot welds, following an alternating inward-outward pattern. The purpose of this inward-outward fold initiator pattern, from fold initiator number 1 through to 8, is to create accordion-style sequential folding between spot welds, which is intended to improve the consolidation crush response of the crush tip, as well as reduce spot weld failure.

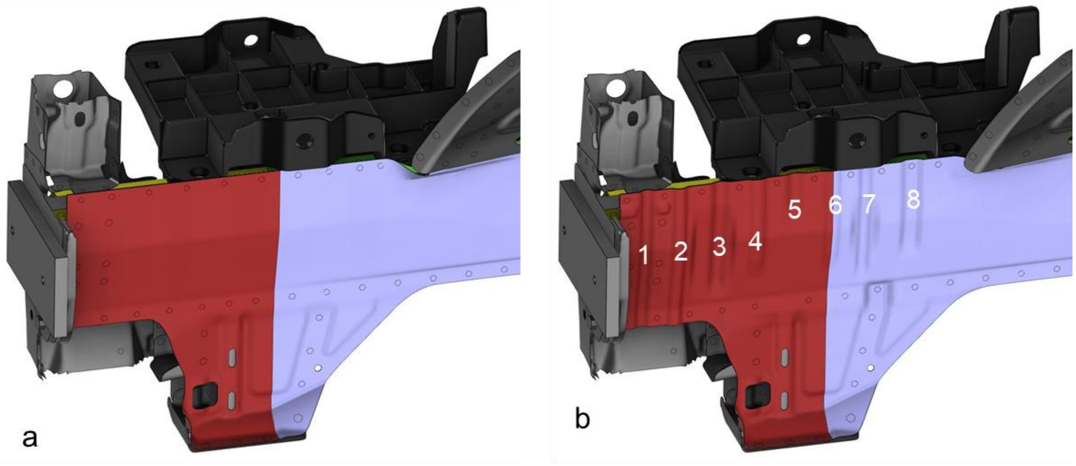

Figure 163. Outboard view of the vertical flange tailor-welded hot stamped side frame member **(a)** without the addition of fold initiators (Trial 3900) and **(b)** with the addition of fold initiators (Trial 3920).

To capture the correct crush response, fold initiators are added to the inboard side of the vertical flange tailor-welded hot stamped side frame member, as shown in Figure 164. The fold initiators on the inboard of the side frame member are numbered 9 to 16. To promote sequential folding in the main rail crush tip an inward oriented fold initiator (number 9), located at the base of the main rail C-channel, is added. Inward oriented fold initiators 10, 11 and 13 are added to the upper chamfered surface of the main rail, between the side wall and C-channel base, which assist in controlling the folding response along the length of the crush tip. Fold initiators 12, 15 and 16 have been added to the base of the main rail C-channel to promote the formation of a buckle in front of the shock tower support. The vertical flange geometry tailor-welded hot stamped side frame member, with the addition of fold initiators, was adopted as the final design solution and will be evaluated against the production side frame member in the following sections.

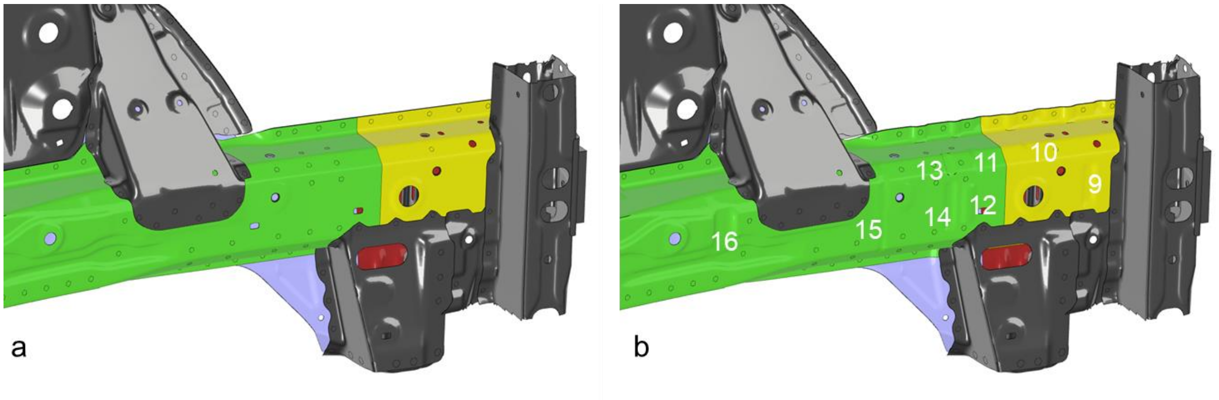

Figure 164. Inboard view of the vertical flange tailor-welded hot stamped side frame member **(a)** without the addition of fold initiators (Trial 3900) and **(b)** with the addition of fold initiators (Trial 3920).

4.4 Evaluation of the Tailor-Welded Hot Stamped Side Frame Member

The crash performance of the tailor-welded hot stamped side frame member, within the front end module, is numerically evaluated against the accepted baseline front end module (Bd-6 and Trial 1710). The evaluation seeks to assess whether a Ductibor® 1000-AS and Usibor® 1500-AS side frame member is a suitable replacement for the production JAC590R side frame member in frontal crash applications. In this section, the characteristics, crush response, crush forces, passenger compartment intrusion resistance and spot weld failure of the tailor-welded hot stamped side frame member are compared to the baseline front end module to determine whether the design specifications listed in Table 3 are met.

The characteristics of the proposed tailor-welded hot stamped side frame member are shown in Table 10. The proposed tailor-welded hot stamped side frame member is comprised of two components, a main rail and an enclosure panel. Each of these components is stamped from a three zone TWB consisting of a 1.0 mm Ductibor® 1000-AS crush tip (was 1.4 mm JAC590R), a 1.2 mm Ductibor® 1000-AS middle section (was 1.6 mm and 1.4 mm JAC590R) and a 1.4 mm Usibor® 1500-AS S-rail section (was 1.8 mm JAC590R), as demonstrated in Figure 165. Due to this significant down-gauging, a mass savings of 2.1 kg is obtained by introducing the 5.5 kg tailor-welded hot stamped side frame member, which corresponds to a 27.6% reduction in mass compared to the 7.6 kg production JAC590R side frame member. In addition, the tailor-welded hot stamped side frame member requires only two major hot stamped components, instead of the three major stamped components in the production side frame member. There is an additional minor reduction in the number of spot welds required for assembly by 6 (from 245 spot welds to 239 spot welds).

Table 10. Characteristics of the proposed tailor-welded hot stamped side frame member compared to the baseline production side frame member, including: number of components, total mass and total number of spot welds.

Side Frame Member Configuration	Number of Components	Total Mass (kg)	Number of Spot Welds
Production	3	7.6	245
Tailor-Welded Hot Stamped	2	5.5	239

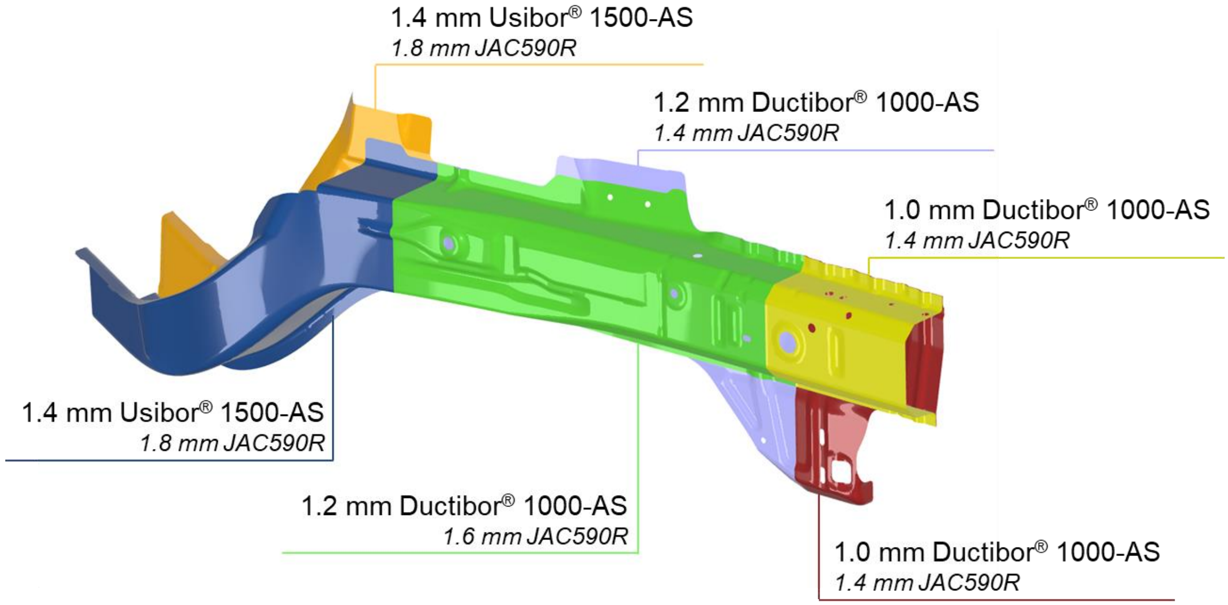

Figure 165. Schematic of the finalized tailor-welded hot stamped side frame member showing the adopted alloys and thicknesses, with the corresponding production JAC590R material thicknesses shown in italics.

4.4.1 Crush Response

The predicted crush response of the tailor-welded hot stamped side frame member, within the front end module, is shown in Figure 166, along with the predicted crush response of the accepted baseline front end module. It is observed that within the first 200 mm of crash sled crush distance, the crush tip of the side frame member in both configurations is fully consolidated, as highlighted with the red dashed box. In both configurations at 330 mm of crash sled crush distance, a buckle is formed on the inboard side of the vehicle (red arrow), in front of the shock tower support. With progression of the crash sled to 425 mm of crush distance, a buckle is initiated behind the shock tower support for both the production and tailor-welded hot stamped side frame member configurations. The predicted deformation of the tailor-welded hot stamped side frame member, within the front end module, clearly shows that the crush response matches the design specifications (Table 3).

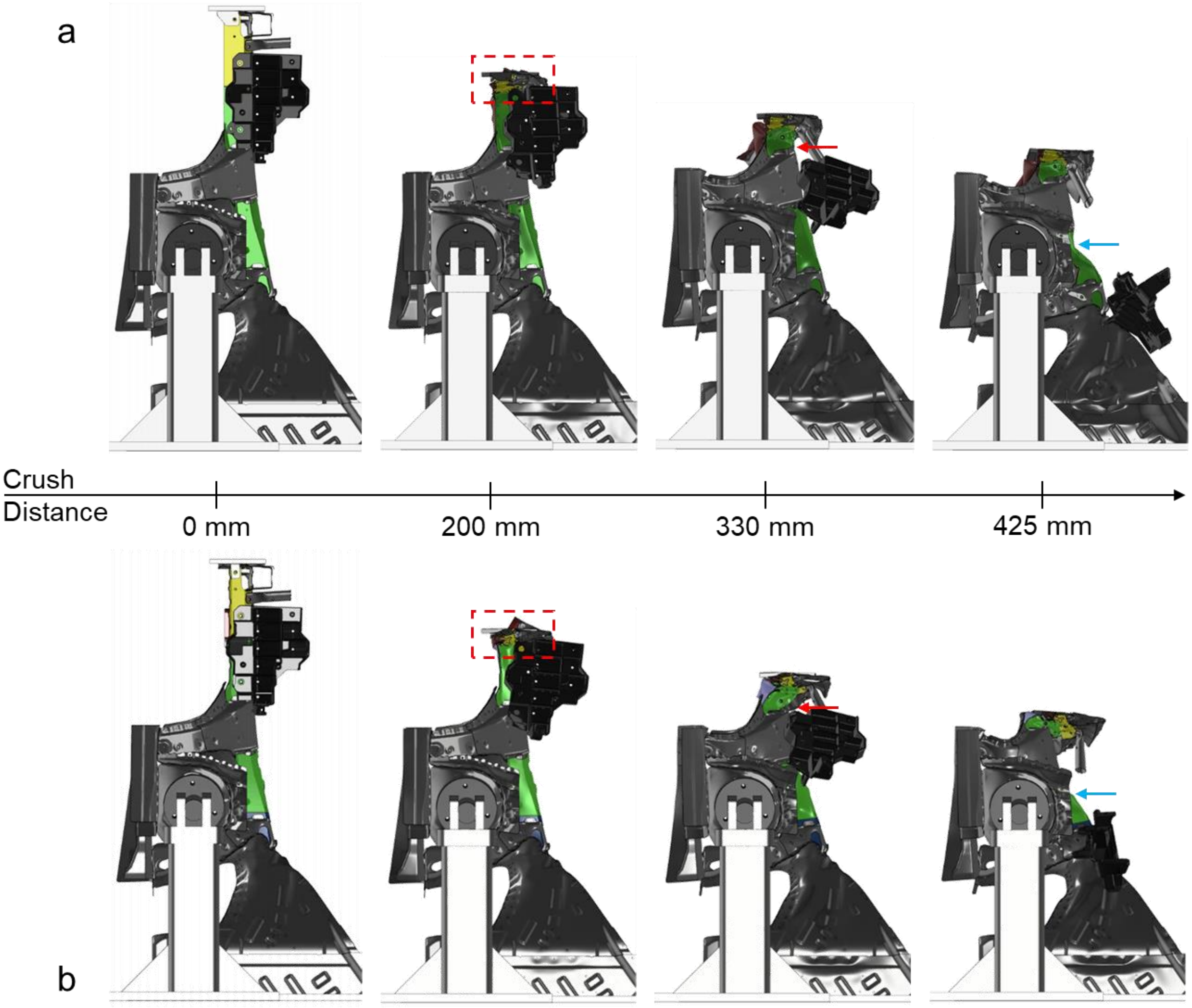

Figure 166. Predicted crush response of the **(a)** baseline front end module model (Trial 1710) and **(b)** the front end module model with finalized tailor-welded hot stamped side frame member (Trial 3920).

Parent metal fracture in the Ductibor® 1000-AS crush tip of the tailor-welded hot stamped side frame member is most easily visualized through contouring the damage parameter. In Figure 167, contours of the maximum through-thickness damage parameter are plotted for the tailor-welded hot stamped side frame member. In this figure, it is observed that the locations where the damage parameter is greater than 1 (red) are located on the tight radius bends that occur during folding. These locations, are where fracture in the parent material is most likely to occur. It should be noted that at least 70% of the through thickness integration points must reach a damage parameter value of unity for an element to be deleted; therefore, locations of red contours do not necessarily mean fracture occurs. Ultimately, this figure demonstrates that fracture in the Ductibor®

1000-AS crush tip only occurs locally in the tight radius folds and no catastrophic fracture propagation is observed, which would compromise the integrity of the structure.

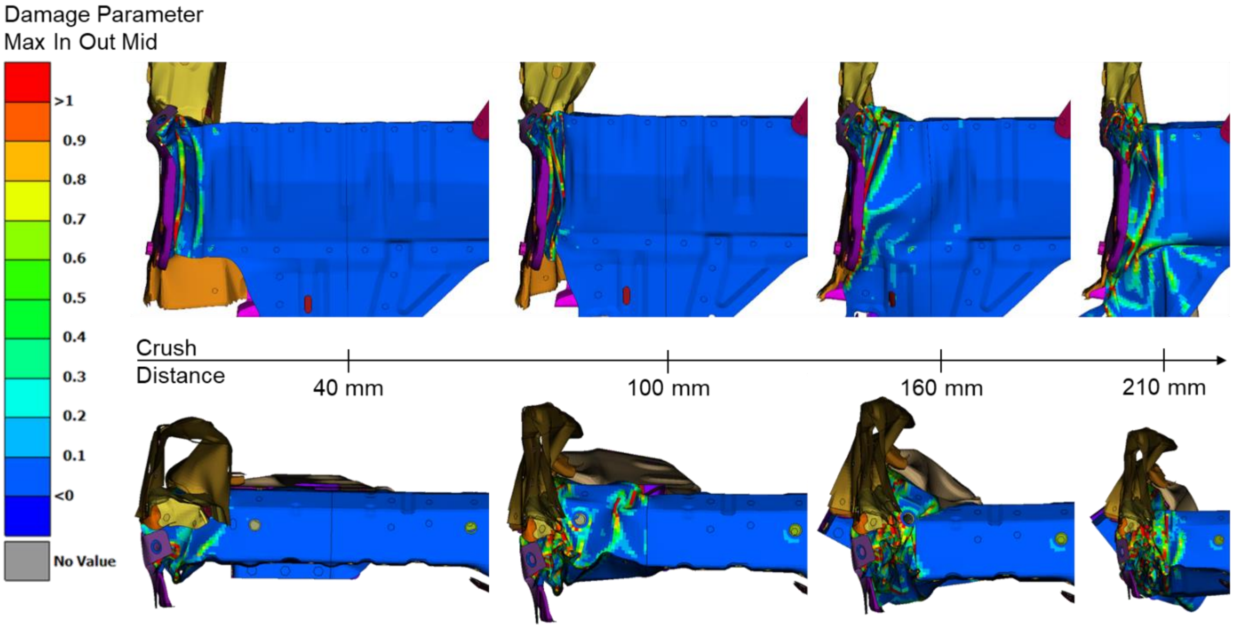

Figure 167. Contours of maximum damage parameter for the tailor-welded hot stamped side frame member crush tip (Trial 3920), shown from the outboard side view (top) and top view (bottom).

4.4.2 Crash Sled Deceleration

In Figure 168 the predicted velocity history of the tailor-welded hot stamped side frame member, within the front end module, is compared with the baseline front end module test results and simulation predictions. It is observed in this figure that the velocity history of the tailor-welded hot stamped side frame member is well within the ± 10% velocity profile and ± 30 mm crush distance error tolerance (dashed-dot error bounds) from the design specifications (Table 3). Furthermore, it is observed that the velocity history of the tailor-welded hot stamped side frame member is almost exactly the same as that of the baseline front end module test result (Bd-6). The final crash sled crush distance measured in the baseline front end module test (Bd-6) and predicted from its simulation (Trial 1710) are 442 mm and 426 mm, while the tailor-welded hot stamped side frame member simulation predicts a final crush distance of 442 mm. It is clear from Figure 168 that the tailor-welded hot stamped side frame member meets both the velocity history and final crash sled crush distance design specifications.

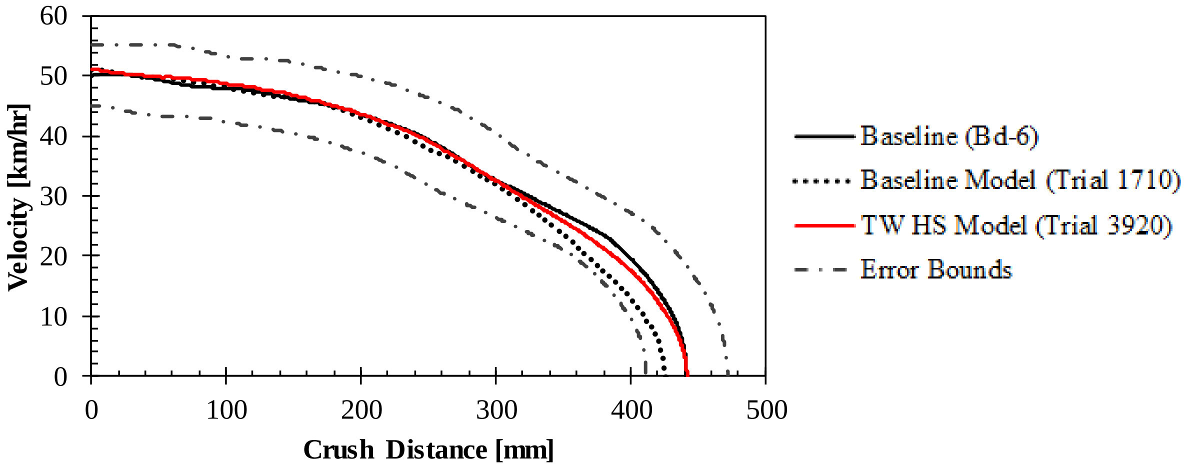

Figure 168. Predicted velocity history of the tailor-welded hot stamped side frame member (Trial 3920), within the front end module, compared to the baseline front end module test results (Bd-6) and numerical predictions (Trial 1710).

4.4.3 Crush Forces

The predicted crush force versus crush distance histories for the baseline and tailor-welded hot stamped front end modules are shown in Figure 169. It is observed from this figure that the crush force trends are very similar between both front end module configurations. In the tailor-welded hot stamped front end module, the location and magnitude of crush force peaks and troughs are relatively consistent with those from the baseline front end module. The average crush force is also shown in Figure 169 for both of the front end module configurations. The predicted average forces for the baseline and tailor-welded hot stamped front end modules are 91 kN and 82 kN, respectively, corresponding to a 10% decrease in average force for the tailor-welded hot stamped front end module. The decrease in average force of 10% for the tailor-welded hot stamped front end module compared to the baseline front end module is within the design specification (Table 3) tolerance of ± 20%.

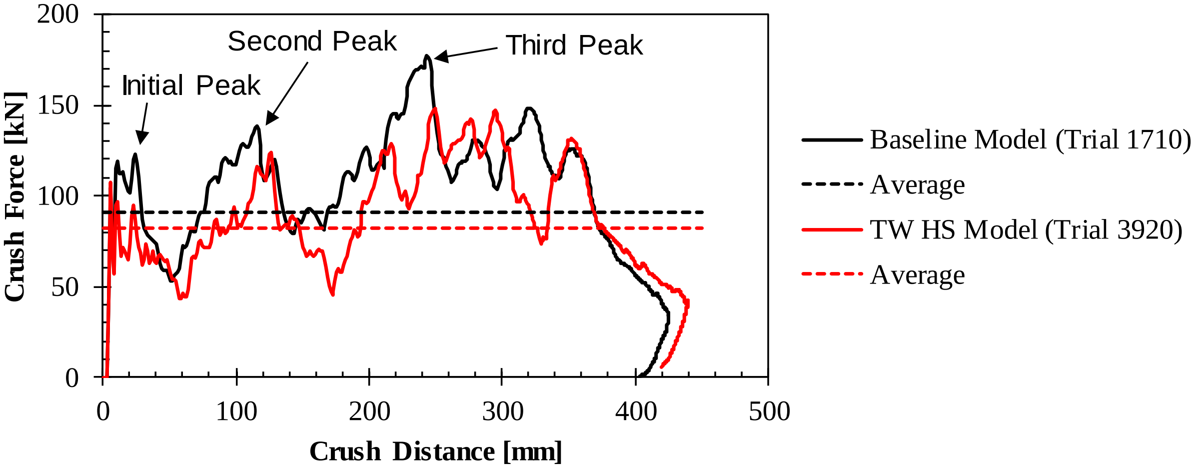

Figure 169. Predicted total force and average total force from the baseline front end module model (Trial 1710) and the tailor-welded hot stamped front end module model (Trial 3920).

The peak crush forces for each of the three peaks highlighted in Figure 169, in addition to a comparison the percent difference in predicted peak force are listed in Table 11. It is observed that the peak forces from the tailor-welded hot stamped front end module are consistently lower than those from the baseline front end module; however, the percent decrease remains within the tolerance of ± 15% specified in the design specifications (Table 3). The initial peak force, which occurs in the first 20 mm of crush, has the largest difference (13%) compared to the second and third peaks. This larger difference can be attributed to the complex system of fold initiators that were added to the crush tip in the tailor-welded hot stamped side frame member design. Though the addition of fold initiators improves the crush behaviour, it also decreases the required force to crush the structure, and hence leads to a decrease in the peak force. Note that it should be possible to slightly increase the thickness of the current tailor-welded hot stamped side frame member to better match the crush force history of the baseline front end module; however, this was judged beyond the resources of this current project. Furthermore, matching the crush forces exactly would have likely required use of sheet thickness values falling between commonly available sheet thicknesses.

Table 11. Predicted peak forces and associated percent error from the baseline front end module model (Trial 1710) and the tailor-welded hot stamped front end module model (Trial 3920).

	Initial Peak	**Second Peak**	**Third Peak**
Baseline Model (Trial 1710)	123 MPa	139 MPa	177 MPa
TW HS Model (Trial 3920)	107 MPa	127 MPa	158 MPa
Percent Decrease	13%	9%	11%

4.4.4 Occupant Compartment Intrusion Resistance

The predicted occupant compartment intrusion and associated displacements, measured from the top of the S-rail, are shown in Figure 170 for the baseline and tailor-welded hot stamped front end modules. It is observed from this figure that the displacement into the occupant compartment is less in both coordinate directions (13.2 mm and 18.9 mm less in the x and z directions, respectively) for the tailor-welded hot stamped front end module. The occupant compartment intrusion for the baseline front end module was already verified to have met the design specification (Table 3) and clearly the tailor-welded hot stamped front end module configuration also meets the design specification.

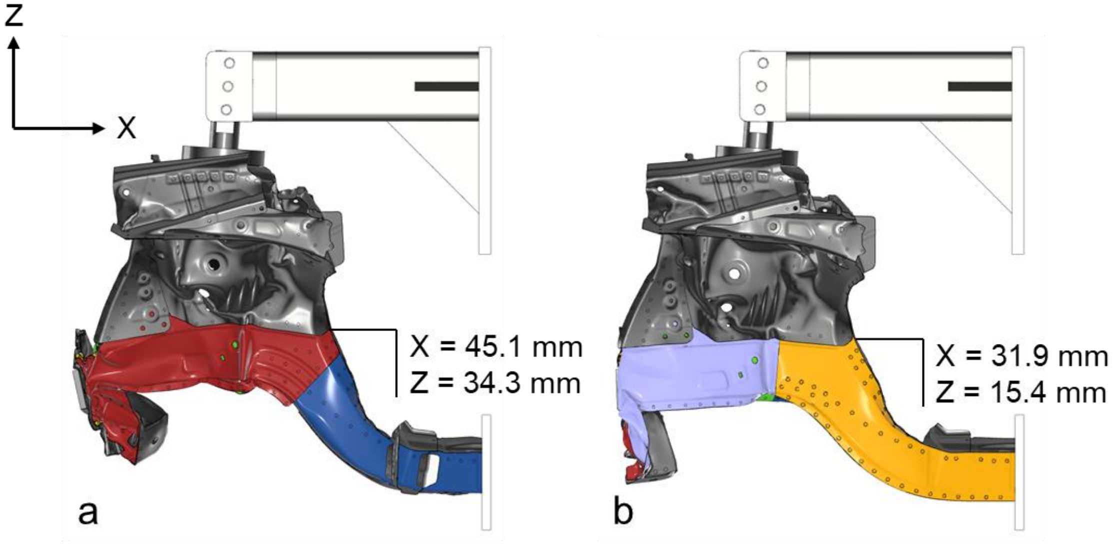

Figure 170. Predicted occupant compartment intrusion for the **(a)** baseline front end module (Trial 1710) and **(b)** tailor-welded hot stamped front end module (Trial 3920).

4.4.5 Extent of Spot Weld Failure

The quantity and location of spot weld failure, in the top and bottom flanges of the baseline and tailor-welded hot stamped front end module configurations are shown in Figure 171. Through monitoring the failure parameter (demonstrates failure initiation of spot welds), in both configurations, it is observed that several more (4) spot welds exceed the failure criterion in the tailor-welded hot stamped side frame member than in the production side frame member. Though complete deletion of spot welds occurs along the crush section flanges, the spot weld failures occur in the midst of sequential folding and do not result in uncontrolled spot weld failure or flange unzipping, as observed in Figure 172.

The severity of spot weld failure is determined based on the type of deformation that follows the failure, as well as when during the deformation the failure occurs. If, for example, after the failure of a spot weld, the flanges open up ("unzips"), the spot weld failure is considered severe because the deformation that follows will be uncontrolled. Alternatively, if the spot weld failure occurs in an already formed, tight fold during sequential folding, the failure is considered less severe. In the case of the tailor-welded hot stamped side frame member, controlled sequential folding is observed (Figure 172), without "unzipping" of the flanges. In addition, spot weld failure only occurs after tight folds are formed along the flanges. Therefore, the severity of the spot weld failures occurring in the tailor-welded hot stamped side frame member crush tip region was judged to be relatively low.

	Weld	Baseline	TW Hot Stamped
Top Flange	1		
	2	✓	✓
	3	✓	✓
	4		✓
	5		✓
	6		✓
Bottom Flange	7		
	8	✓	✓
	9		✓
	10	✓	
	11	✓	✓
	12		✓
	Total	5	9

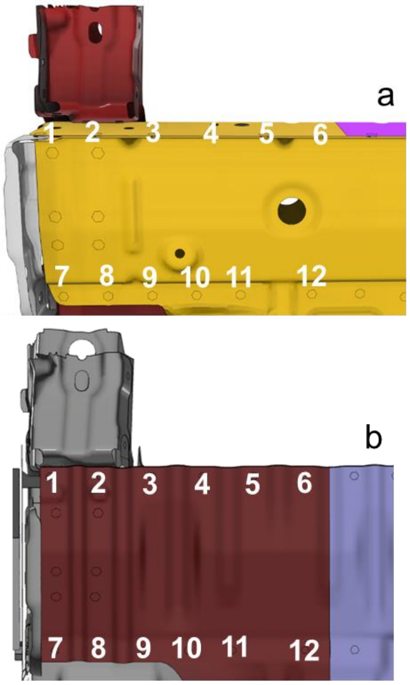

Figure 171. Spot weld failure location (based on the predicted failure parameter, or damage initiation) in the **(a)** baseline (Trial 1710) and **(b)** tailor-welded hot stamped front end module (Trial 3920) configurations.

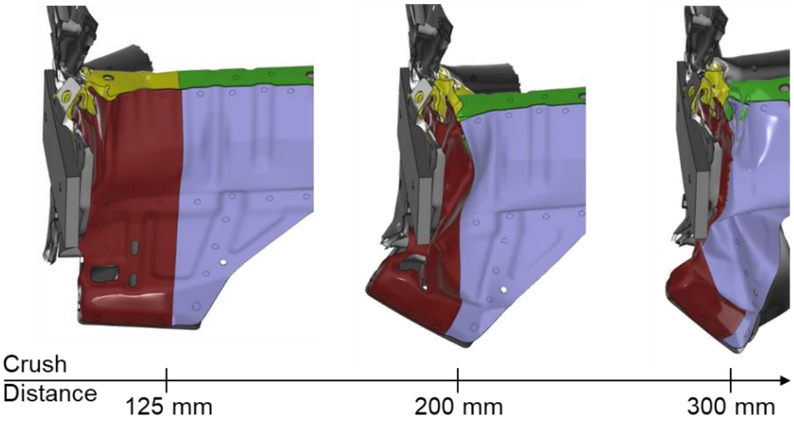

Figure 172. Tailor-welded hot stamped front end module demonstrating the controlled folding behaviour of the crush tip region and low severity of spot weld failures.

4.5 SUV Crash Model Comparison

For further design validation, the driver's side production JAC590R side frame member is replaced with the proposed vertical flange tailor-welded hot stamped side frame member (red dashed box), within the SUV model (Figure 173). The passenger's side frame member remains constant (production JAC590R) for both SUV simulations. All of the bolt-on and spot weld connections between adjacent BIW components were made to connect to the tailor-welded hot stamped side frame member, just as in the case of the production JAC590R side frame member.

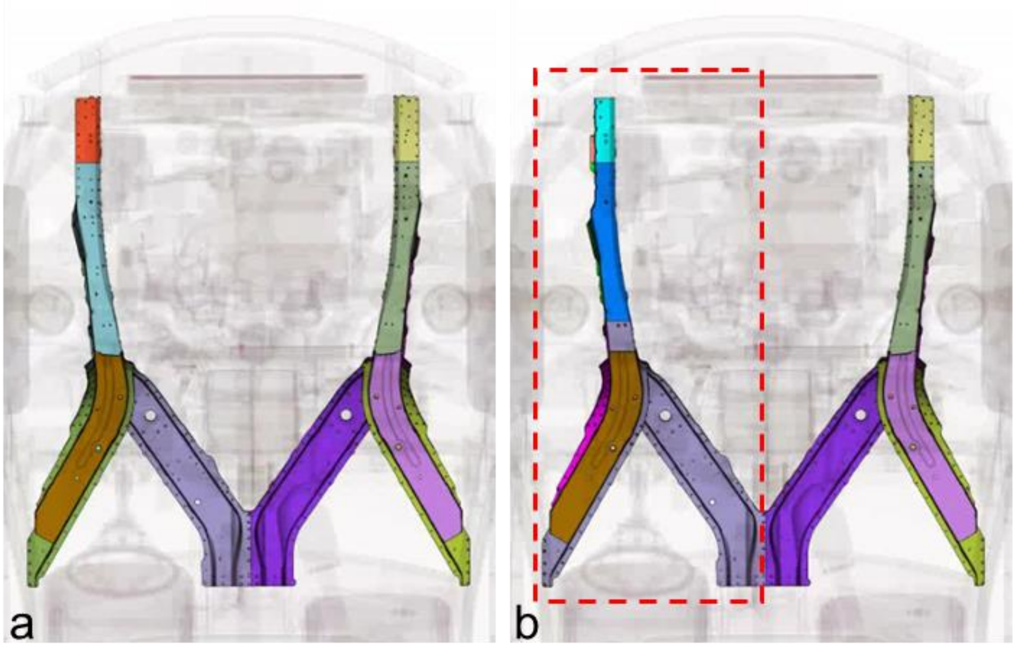

Figure 173. US-NCAP Full Width Rigid Barrier SUV frontal crash model with **(a)** the production JAC590R side frame member and **(b)** the replacement of the driver's side rail with the proposed tailor-welded hot stamped side frame member (red dashed box).

4.5.1 Crush Response

The crush response of the production JAC590R and tailor-welded hot stamped side frame members, within the SUV model (transparent), are shown in Figure 174. It is observed that the deformation of the driver's (left) side frame member for both the production and tailor-welded hot stamped conditions are very similar. At 0.2 seconds into the crash event the crush tip is fully consolidated in both conditions, followed by a buckle occurring in front of the shock tower support at 0.5 seconds. A buckle behind the shock tower support is seen in both conditions at 0.7 seconds into the crash event. Some differences in the crush behaviour of the passenger side frame member between the two models can be observed; however, that is viewed as out of the scope of the current work.

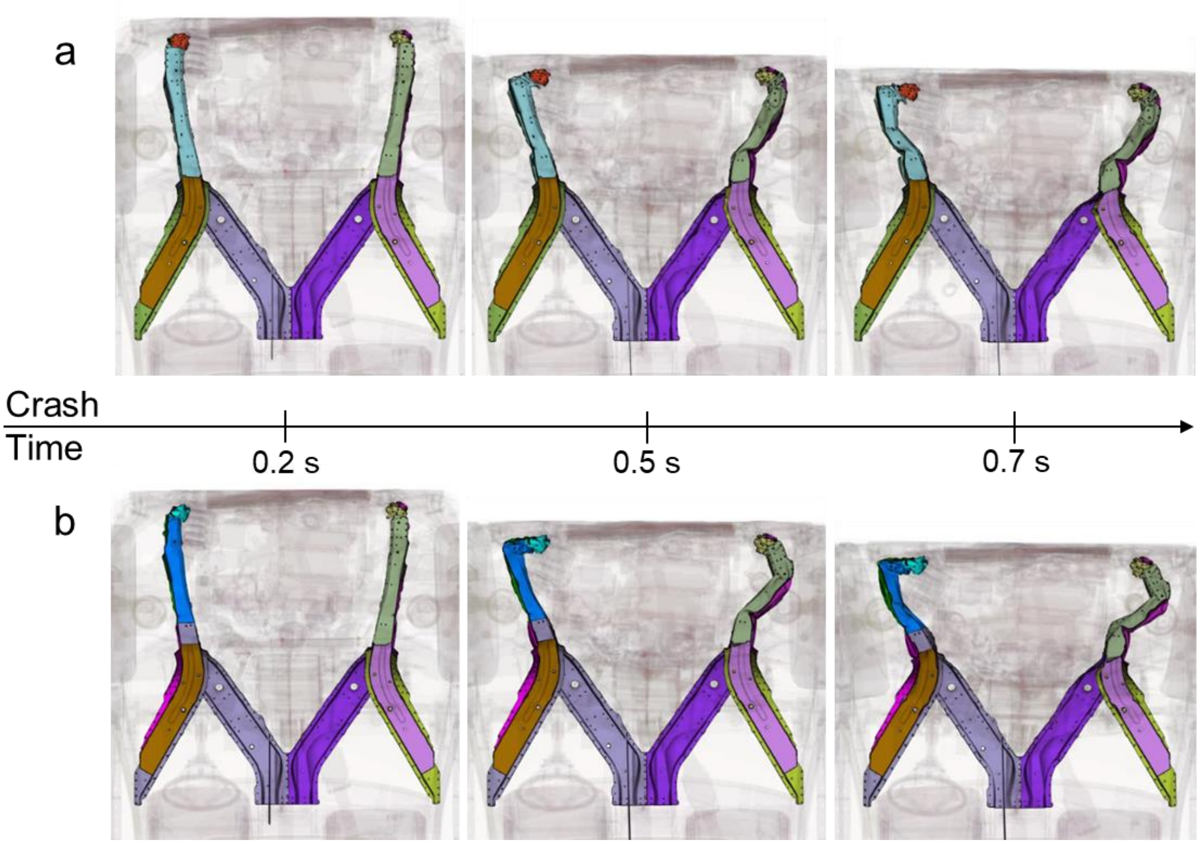

Figure 174. Crush response of the **(a)** production JAC590R side frame member and **(b)** tailor-welded hot stamped side frame member in the SUV frontal crash model. Note that the driver's side frame member is the left rail.

The maximum through-thickness damage parameter is used to evaluate the extent of parent metal fracture within the crush section of the tailor-welded hot stamped side frame member, in the SUV model (Figure 175). It is observed that locations where the damage parameter exceeds unity (red), representing material failure, are very sparse throughout the crush section of the tailor-welded hot stamped side frame member. The severity of the parent metal fracture in the Ductibor® 1000-AS crush section is deemed to be very low because no catastrophic fracture propagation occurs.

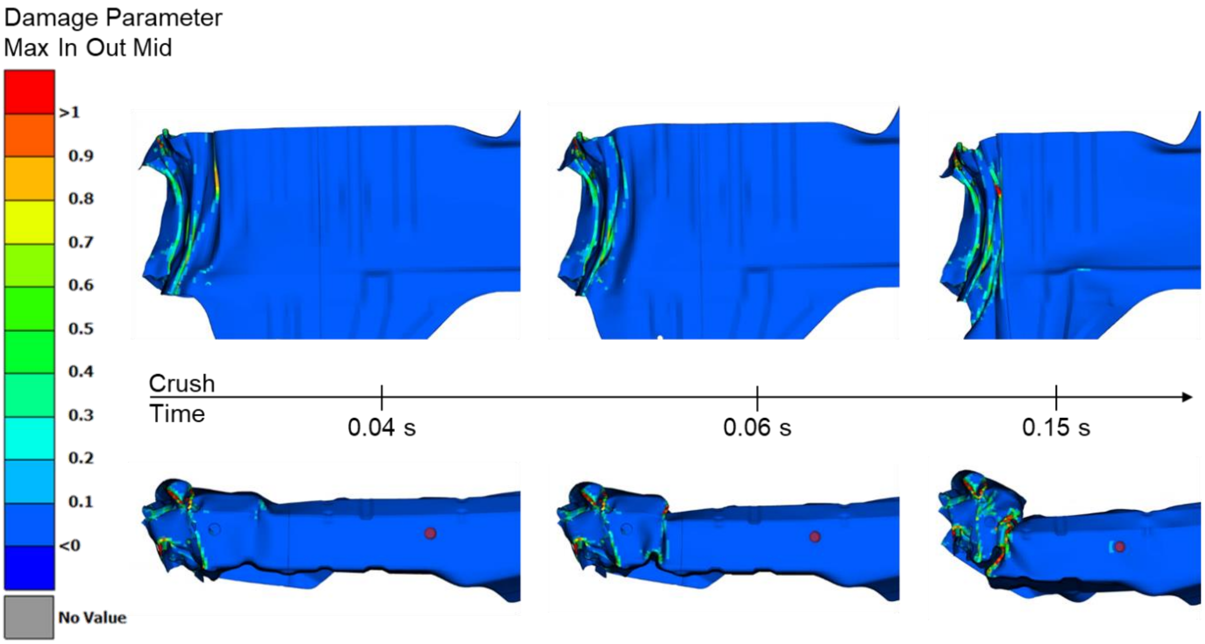

Figure 175. Maximum damage parameter contoured on the crush section of the tailor-welded hot stamped side frame member, within the SUV model, shown from the outboard side view (top) and top view (bottom).

4.5.2 Vehicle Deceleration

The predicted velocity histories and deceleration profiles for the SUV model are shown in Figure 176 for the production JAC590R and tailor-welded hot stamped side frame member configurations. From these plots it is observed that the deceleration of the vehicle is very similar for both of the side frame member configurations. A discrepancy is observed in peak deceleration pulse at 0.05 seconds into the crash event, in which the peak deceleration in the production side frame member configuration is 50 g's and the peak deceleration in the tailor-welded hot stamped side frame member configuration is 36 g's. The fact that the tailor-welded hot stamped side frame member deceleration pulse at 0.5 seconds is 14 g's less than the production configuration is not concerning because it means less severe deceleration would be felt by the occupants. In addition, the deceleration pulse after 0.5 seconds is similar in both configurations, meaning the deceleration peak is not just shifted later on in the crash event for the tailor-welded hot stamped side frame member. The velocity history and deceleration profile are both within the design specifications (Table 3).

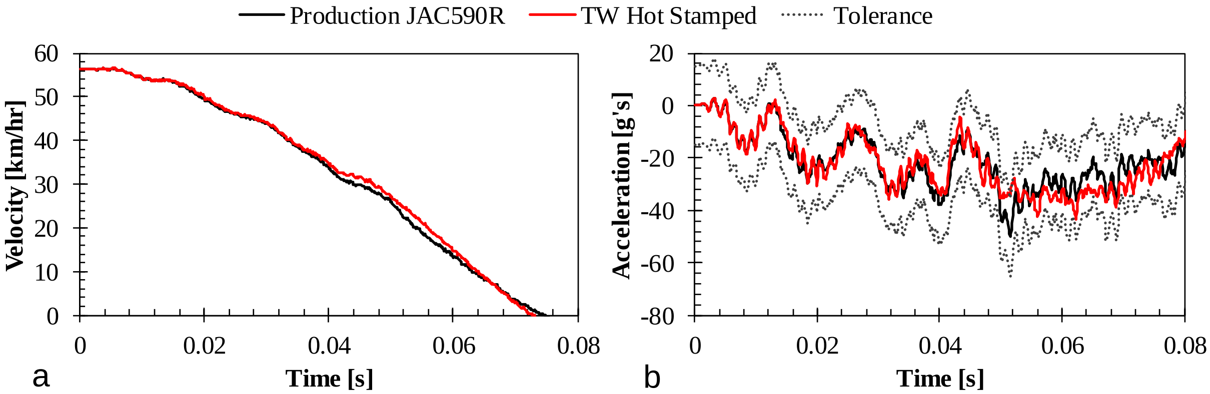

Figure 176. (a) Velocity history and **(b)** deceleration profile predictions for the SUV model with production JAC590R and tailor-welded hot stamped side frame member configurations.

4.5.3 Crush Forces

The crush forces, predicted from eight cross-sectional force planes along the length of the side frame member, are shown in Figure 177 for the SUV model with production and tailor-welded hot stamped side frame member configurations. It is observed from the first cross-sectional force plane that the initial peak force predicted by the tailor-welded hot stamped side frame member is much less (57 kN less) than the production configuration. This large reduction in peak force is thought to be due to the fact that many fold initiators have been included in the crush tip section of the tailor-welded hot stamped side frame member, which is known to reduce peak forces, as discussed in section 1.2.3. The second and third peak forces from the tailor-welded hot stamped side frame member however are very similar to the production configuration. Furthermore, with the exception of the first cross-sectional force plane, the global trend, as well as peak forces from the tailor-welded hot stamped side frame member are very comparable to the in both configurations, which implies that the crush forces and energy absorption are not compromised by using the tailor-welded hot stamped side frame member.

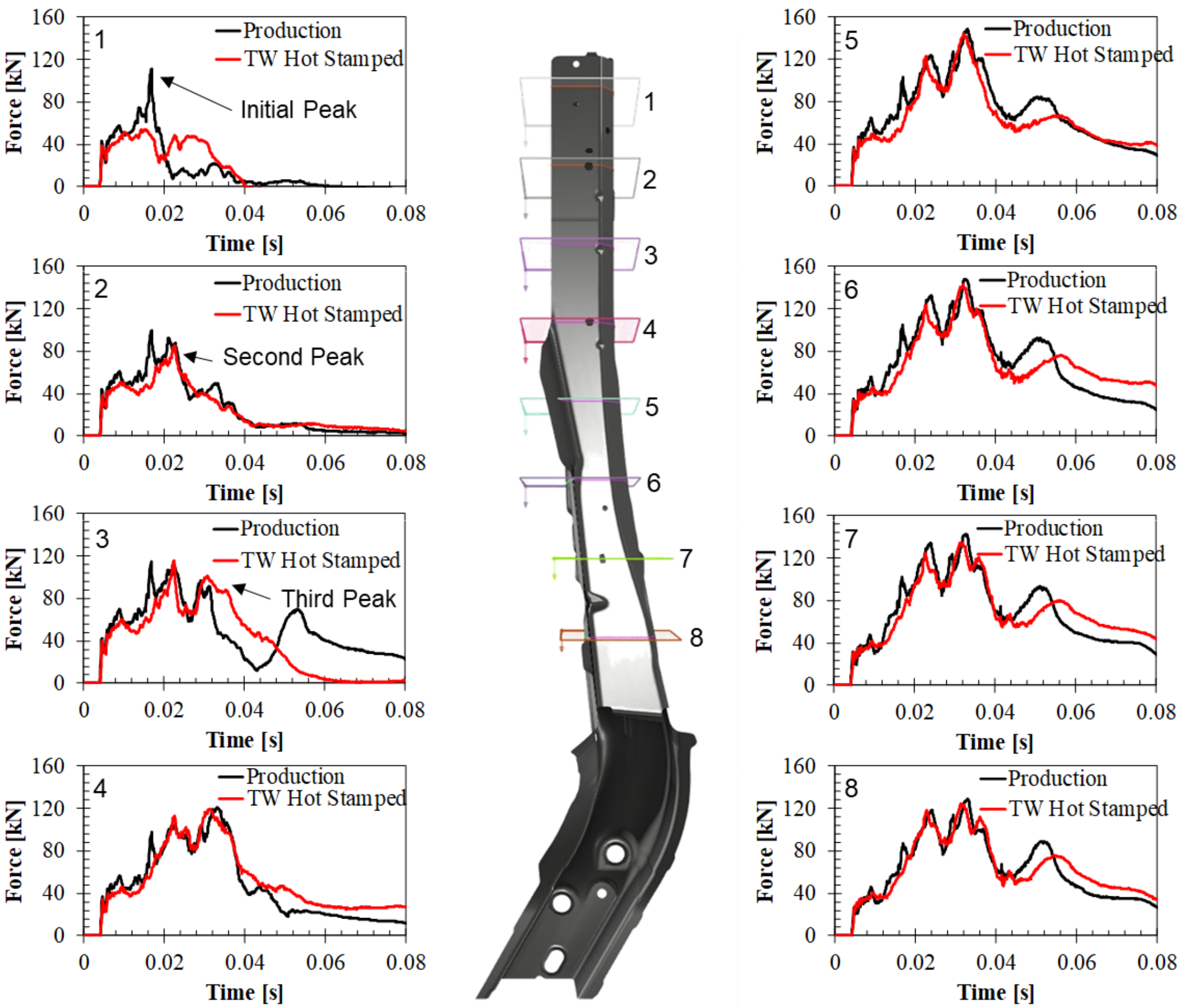

Figure 177. Cross-sectional crush forces predicted along the length of the driver's side production JAC590R and tailor-welded (TW) hot stamped side frame member configurations, within the SUV model.

4.5.4 Occupant Compartment Intrusion

The deformation of the production and tailor-welded hot stamped side frame member S-rail sections, in the fully impacted state, are shown in Figure 178. More collapse of the S-rail section is observed in the tailor-welded hot stamped side frame member than in the production configuration; however, the amount of intrusion 35.2 mm in the x-coordinate and 21.7 mm in z-coordinate are within the tolerances specified in the design specifications (Table 3). The tailor-welded hot stamped side frame member therefore meets the occupant compartment intrusion resistance criteria.

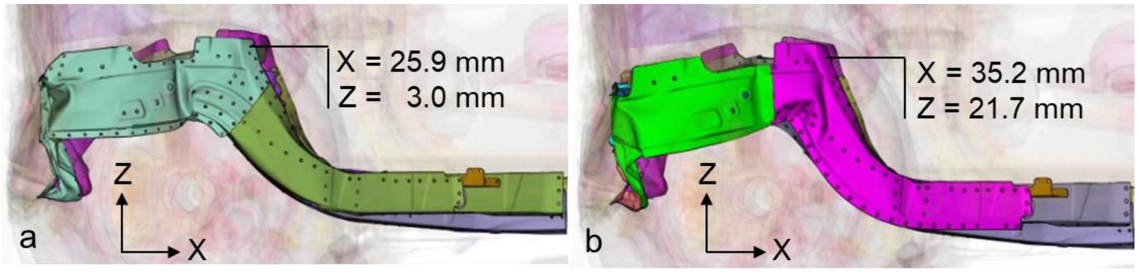

Figure 178. S-rail displacement into the passenger compartment, measured from the top flange, for the **(a)** production JAC590R and **(b)** tailor-welded hot stamped side frame member configurations.

4.5.5 Extent of Spot Weld Failure

A comparison of the crush tip spot weld failure occurring in the production JAC590R side frame member to that which is occurring in the tailor-welded hot stamped side frame member, SUV model configuration, is shown in Figure 179. From the table it is clear that more (3 more) spot weld failure occurs in the tailor-welded hot stamped configuration than in the production configuration.

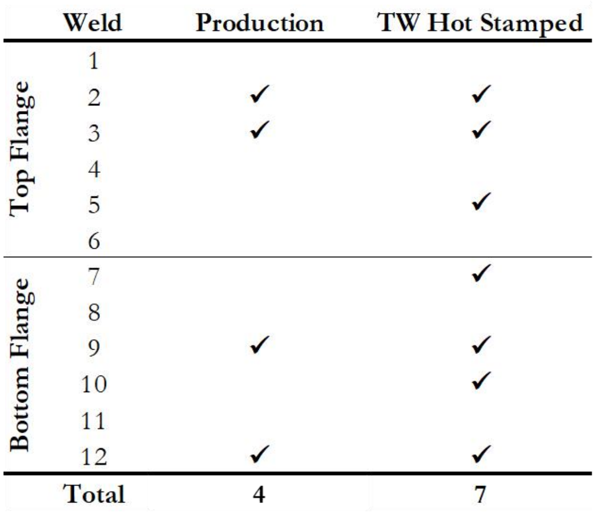

	Weld	Production	TW Hot Stamped
Top Flange	1		
	2	✓	✓
	3	✓	✓
	4		
	5		✓
	6		
Bottom Flange	7		✓
	8		
	9	✓	✓
	10		✓
	11		
	12	✓	✓
	Total	4	7

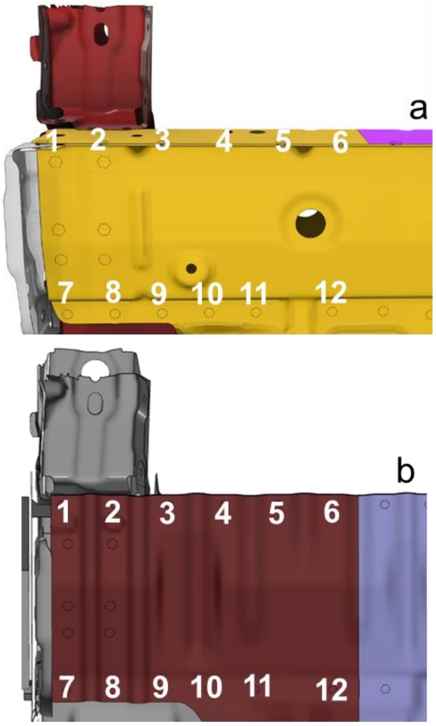

Figure 179. Side frame member crush tip spot weld failure (monitored from the failure parameter) quantity and locations from the SUV model with **(a)** production JAC590R side frame member and **(b)** vertical flange tailor-welded hot stamped side frame member.

Though more spot weld failure occurs in the tailor-welded hot stamped side frame member than in the production side frame member, it is shown in Figure 180 that the severity of the spot weld failure is relatively low. It is observed in this figure that even though spot weld failures are occurring along the length of the crush section flanges, no flange "unzipping" occurs, rather controlled sequential folding is obtained.

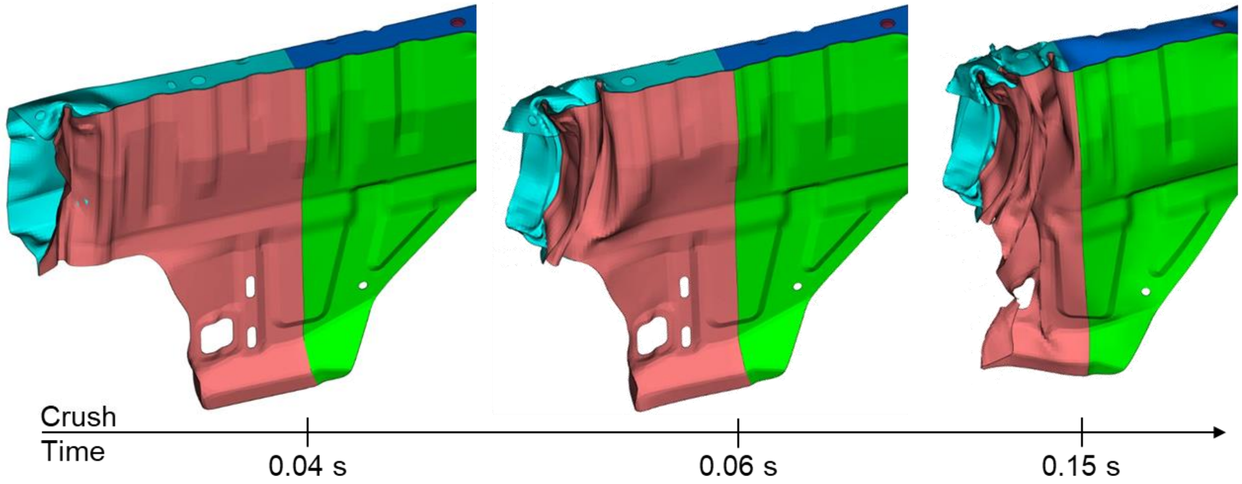

Figure 180. Spot weld failure demonstrates low severity due to sequential folding that occurs in the tailor-welded hot stamped side frame member, within the SUV model.

4.6 Crush Performance Summary

The crush performance of the proposed tailor-welded hot stamped side frame member, within the front end module and SUV models, are compared to accepted baseline front end module and production SUV models, respectively, as shown in Table 12. It is observed that the tailor-welded hot stamped side frame member meets each of the design criteria, except for the spot weld failure locations and total number of spot welds occurring in the crush tip section flanges. In both cases, however, the severity of the spot weld failure is considered to be low and spot weld flange "unzipping" is not observed.

Through using UHSS in crash applications it is difficult to avoid spot weld failure completely due to the heightened strength of the materials, thus subjecting the spot welds to greater loads. It is therefore deemed that a more important metric for spot weld failure is the effect a spot weld failure has on the structural integrity of the welded assembly. If for example, controlled sequential folding is observed after a spot weld failure then the structural integrity of the welded assembly is not compromised and the weld failure severity is considered low. Since the weld failures that occurred in the tailor-welded hot stamped side frame member had a low impact on the structural integrity of the welded assembly, it is considered to meet the spot weld failure criteria.

Table 12. Evaluation of the proposed tailor-welded hot stamped side frame member, within the front end module (T-W HS Model) and SUV model (T-W HS SUV), using the design specifications.

	Qualitative Quantitative	**Target**	**Upper Bound**	**Lower Bound**	**T-W HS Model**	**T-W HS SUV**
Crush Response						
Consolidation of crush tip (Fig. 56)	Qualitative	Match	-	-	✓	✓
Buckle front of shock tower support (Fig. 56)	Qualitative	Match	-	-	✓	✓
Buckle behind shock tower support (Fig. 56)	Qualitative	Match	-	-	✓	✓
Parent material fracture severity	Qualitative	Minimize	-	-	✓	✓
Vehicle Decleration						
Velocity history	Quantitative	Match	+ 10%	- 10%	✓	✓
Final crush distance	Quantitative	422 mm	+ 30 mm	- 30 mm	✓	✓
Crush Forces						
Sectional force plane (SFP) - global trend	Qualitative	Match	-	-	N/A	✓
SFP - peak forces (1st, 2nd, 3rd)	Quantitative	Match	+ 15%	- 15%	N/A	✓
Total Force (TF) - global trend	Qualitative	Match	-	-	✓	N/A
TF - peak forces (1st, 2nd, 3rd)	Quantitative	Match	+ 15%	- 15%	✓	N/A
TF - average force	Quantitative	Match	+ 20%	- 20%	✓	N/A
Occupant Compartment Intrusion						
x-coordinate displacement	Quantitative	25.9 mm	+ 30 mm	-	✓	✓
z-coordinate displacement	Quantitative	3.0 mm	+ 40 mm	-	✓	✓
Spot Weld Failure						
Weld locations	Quantitative	Match	-	-		
Quantity	Quantitative	Match	-	-		
Severity	Qualitative	Minimize	-	-	✓	✓
Side Frame Member Characteristics						
Mass	Quantitative	< 7.6 kg	- 15%	-	✓	N/A
Total number of spot welds	Quantitative	≤ 245	-	-	✓	N/A
Total number of components	Quantitative	≤ 3	-	-	✓	N/A

Chapter 5 – Tailor-Welded Hot Stamped Crush Tip – Formability Assessment and Fabrication Strategy

The crash performance assessment of the tailor-welded hot stamped side frame member, presented in the previous chapter, has served to demonstrate (numerically) that the current concept meets all of the design specifications. This chapter presents research undertaken to assess the feasibility of fabricating a hot stamped tailor-welded hot stamped side frame member, focusing on the formability and assembly aspects of fabrication. Initial numerical simulation of the forming process and die development efforts led to a realization that a large, near-production complexity tool would be required to form these 1640 mm long side frame member components, with an expected tooling cost in excess of $500,000, which far exceeds the available funds for this aspect of the current project. Consequently, it was elected to focus on the formability, assembly and crash testing of a reduced section of the tailor-welded side frame member, referred to as the "crush tip" and depicted in Figure 181. This simplification reduced the tooling cost to about $50,000 while still capturing the complexity of the crush tip fold initiators and extensive folding that occurs in the side frame member during crash. This chapter introduces the tailor-welded hot stamped crush tip, the formability process simulations and formability experiments. The chapter closes with a plan for assembly (integration) of the crush tip for crash testing. Simulation of the crash tip crush response and comparison with the full side frame model is presented in Chapter 6 of this thesis.

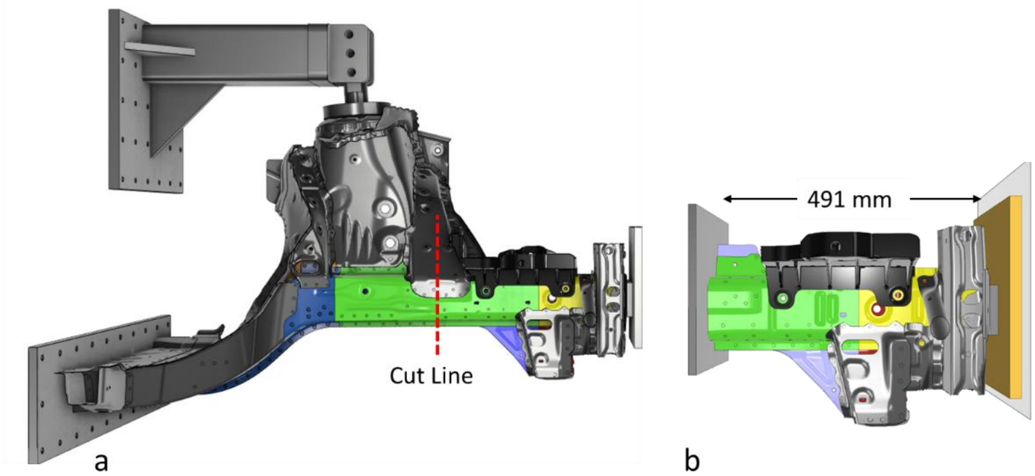

Figure 181. (a) Full-length tailor-welded hot stamped side frame member in the front end module showing the cut line for **(b)** the tailor-welded hot stamped crush tip.

5.1 Reduced Crush Tip Structure

The ability to evaluate whether Ductibor® 1000-AS is a suitable candidate for frontal crash applications is not hindered by the isolation of the side frame member crush tip. Results from the baseline front end module crash testing (discussed in section 3.5) and predictions from the tailor-welded hot stamped side frame member simulations (discussed in section 4.4) have shown that the area of interest, in terms of crashworthiness, is the crush tip section of the side frame member prior to the foremost shock tower support. Within the crush tip section, tight radius sequential folding occurs to absorb the kinetic energy of the vehicle. These tight radius bends from folding provide the favourable conditions for fracture to occur in the parent material, due to approaching the plane-strain stress state. In addition, tight radius folds subject spot welds to high separation loads, making spot weld failures more likely. Therefore, the crush tip consolidation response, the potential for fracture of the material during folding, potential for spot weld failure along the flanges and the crush forces present during axial collapse can still be assessed using the tailor-welded hot stamped crush tip.

A similar testing approach was undertaken by Peister [19] who crash-tested the production JAC590R crush tips from the baseline (JAC950R) side frame. In that study, the crush tip length was only 340 mm, which included the entire crush tip section, along with 120 mm of the middle section; however, at this length only the first 200 mm of crush can be observed before consolidation between the crash sled and mounting plate skew the results. The length of the tailor-welded hot stamped crush tips studied in this thesis is 491 mm long (Figure 181b). At this length, the full length of crush tip is included along with 268 mm of the middle section, which allows for more crush distance to be observed without consolidation effects.

The major components of the tailor-welded hot stamped crush tip comprise the hot stamped main rail and enclosure panel section, as shown in Figure 182. The main rail is a flanged C-channel section, while the enclosure panel is a flat section with mating flanges to the main rail. Due to the differences in their geometry, forming these components requires the use of two separate hot stamping tools.

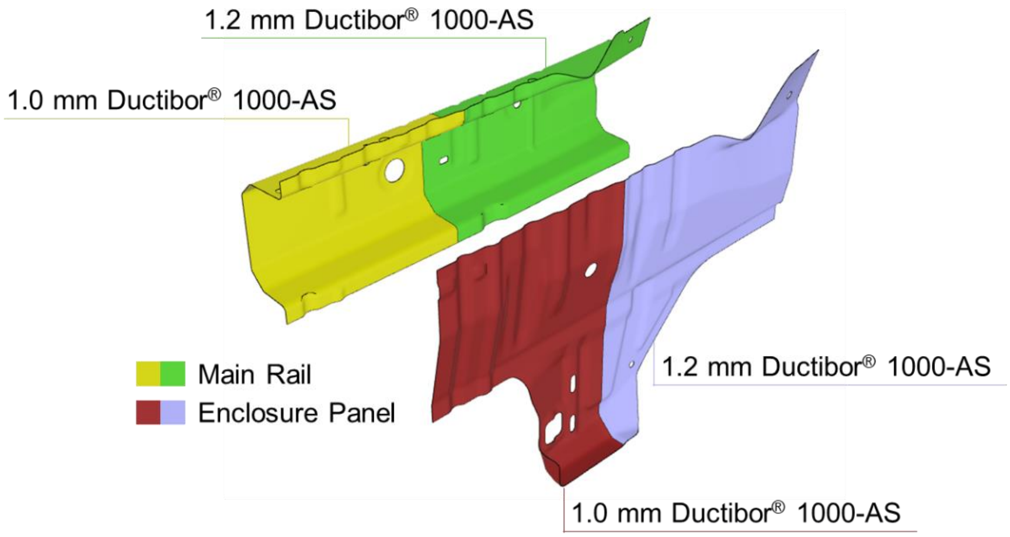

Figure 182. Exploded view of the tailor-welded hot stamped crush tip, showing the main rail and enclosure panel sections and their respective material and thickness composition.

5.2 Hot Stamping Process Design

The hot stamping process is modelled using the commercial sheet metal forming software AutoForm Forming R8. AutoForm uses an implicit solution scheme, which is different than the explicit finite element solver approach taken by George [25] and Omer [16] in LS-Dyna to model the IDH tailored hot stamping process for Usibor® 1500-AS. The modelled hot stamping process (Figure 183) consists of five stages: heating and blank transportation, gravity sag, blank forming and quench, air cooling and trimming.

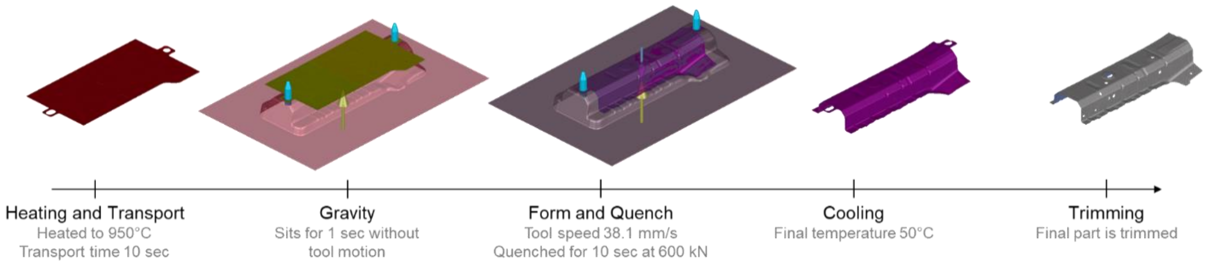

Figure 183. Hot forming process as modelled in AutoForm. Shown for the main rail channel section.

The heating process consists of the blank temperature being increased from 20 °C until it is uniformly 950 °C. The thermal expansion of the blank is calculated during this step according to its thermal expansion coefficient. After the heating is complete the blank is air cooled for 10 seconds to simulate the blank transfer process. The air cooling process considers convection and radiation of the blank as a lumped heat transfer coefficient (HTC) that is temperature dependent, as shown in Table 13. The heat transfer coefficient is notably larger at higher temperatures because of the fact that thermal radiation becomes the dominant form of heat transfer at elevated temperatures, but is almost insignificant at relatively low temperatures [24].

Table 13. Air cooling heat transfer coefficient versus the blank temperature.

Temperature [°C]	HTC [mW/mm^{2}K]
20	0.020
950	0.075

After the air cooling transfer process is complete the blank is aligned onto the punch of the tooling by the pilot pins. The blank is subject to gravity (9.81 m/s^2) which applies a small amount of contact pressure between the punch and blank, initiating heat transfer by conduction. The blank rests on the punch for 1 second without tooling motion to simulate the delay of ram motion.

During the forming stage the die displaces towards the punch and blank at 38.1 mm/s, which is the maximum speed of the press under forming tonnage. With contact and friction enforced between the tooling and blank, the part's geometry is pressed into the blank. During the forming process, the heat transfer coefficient between the blank and tool is a function of the contact pressure, as observed in Table 14. Once the part geometry has been formed, a clamping force of 60 tons is applied to the blank for 10 seconds to rapidly cool the still hot part and transform the austenite to martensite.

Table 14. Heat transfer coefficient as a function of contact pressure between the tooling and blank.

Pressure [MPa]	HTC [mW/mm^{2}K]
0	1.05
1	2.45
2	2.80
3	3.15
20	3.50

The formed and quenched part is removed from the tooling and cooled in air, with convection as the dominant heat transfer method. The heat transfer coefficients used are the same as those in Table 13. A final part temperature of 50 °C is prescribed at which point all microstructural transformations will be complete and the simulation terminates. Once the part is cooled the laser trimming operation is simulated by removing excess material along the part boundary.

5.2.1 Hot Stamping Material Model

The material model used is the AutoForm provided 22MnB5 steel with temperature dependent forming limit curve. 22MnB5 is not the exact same chemical composition as Ductibor® 1000-AS, however, the two materials are similar enough under hot stamping conditions that the tooling and hot forming process can be developed through its use. This approach is necessary since Autoform does not have a calibrated material model for Ductibor® 1000-AS, a relatively new commercial alloy. The shortfall of using the 22MnB5 steel material model is that hardness levels predicted using this model will not correlate to those measured in the formed parts. The basic properties of the material such as Poisson's Ratio, specific weight and temperature-dependent Young's Modulus are shown in Table 15. If the temperature lies between the upper and lower bound, linear interpolation is used to find the Young's Modulus. The hot stamping material model includes phase-dependent thermal dilatation, meaning that depending on the steel's current phase fractions, the thermal expansion coefficient and latent heat change.

Table 15. Basic properties of 22MnB5 hot stamping steel material.

Poisson's Ratio	Specific Weight [MPa/mm]	Young's Modulus [MPa]
0.3	$7.68E^{-5}$	210,000 at 20 °C 45,000 at 950 °C

The hardening response of the material is temperature, phase and strain rate dependent as illustrated in Figure 184a. In this figure it is quite clear that the hardening response is bounded at the upper end by the martensitic phase and the response is bounded at the lower end by the austenitic phase. A yield surface is defined using the Hill-1948 model with r-values of unity. The forming limit curve (Figure 184b) is temperature dependent. Intuitively, it is observed from this forming limit curve that as the temperature increases the formability of the material improves.

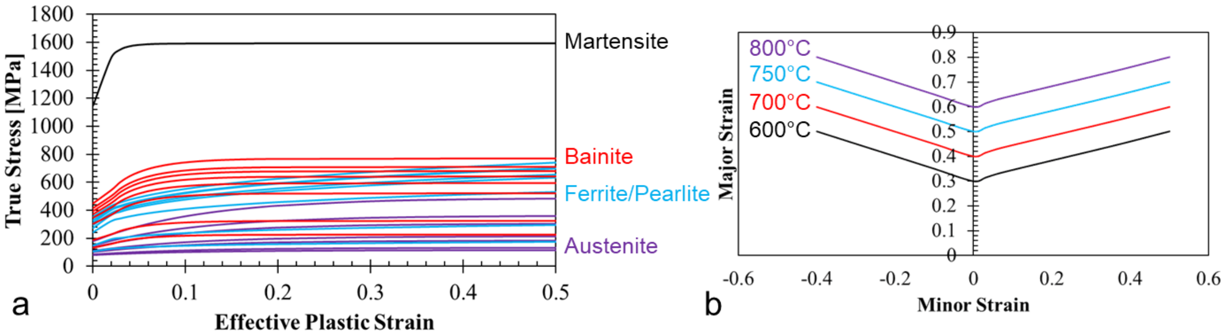

Figure 184. (a) Hardening response of 22MnB5 hot forming material model. **(b)** Forming limit curves for 22MnB5 hot forming material model.

5.2.2 Blank Design and Meshing

The blank shape for both the main rail and enclosure panel sections have been determined through a combination of the AutoForm blank optimizer and a trial-and-error method. The AutoForm blank optimizer was used to come up with an initial estimate of an appropriate shape of the blanks for these two parts. Following this initial estimate, a trial-and-error approach was used to determine a final blank geometry that minimized wrinkling potential, prevented tearing or other unacceptable failures, and most importantly captured all of the part geometry.

Tabs have been included on each end of both blanks (Figure 185c), that incorporate a circular through hole on one side and a slot on the other side. The hole and slot tabs are used to locate the blanks on pilot pins in the tooling during the transfer of the blanks from the furnace to the tool. The circular hole acts as a four-way locator, which constrains the blank from both positive and negative longitudinal and lateral translations. The slot acts as a two-way locator, which constrains the blank from positive and negative translation in only the lateral direction. The slot allows the blank to be located easily onto the pilot pins even after thermal expansion from the austenitization process has occurred and allows contraction once cooling commences. The slot also permits displacement of the blank in the longitudinal direction during the forming process.

The blanks for both the main rail and enclosure panel (Figure 185b and Figure 185c) are laser cut from TWBs supplied by ArcelorMittal. The TWB (Figure 185a) is comprised of a sheet of 1.0 mm Ductibor® 1000-AS, with dimensions 274.5 mm by 700 mm, laser welded to a sheet of 1.2 mm Ductibor® 1000-AS, with dimensions 517.5 mm by 700 mm. The overall dimensions of the TWB are 792 mm by 700 mm, which leaves a few millimeters per side for calibrating the positioning of the laser weld line during the actual forming of these parts.

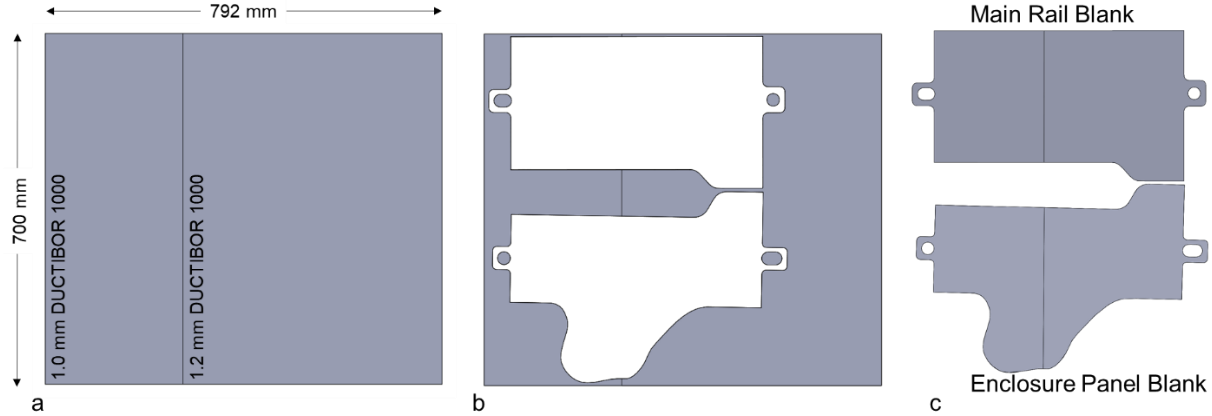

Figure 185. (a) Tailor-welded blank dimensions. **(b)** Tailor-welded blank showing the nesting of both the main rail and enclosure panel blank. **(c)** Final blank shape for both the main rail and enclosure panel.

The blanks are meshed with triangular elasto-plastic shell elements, whose nodes have five degrees of freedom: three translations and two rotations. The elasto-plastic shell element used has eleven thickness layers (EPS-11) or through-thickness integration points. The initial mesh of the blanks shown in Figure 186 are quite coarse with some refinement present at the laser weld line and at the pilot pin alignment tabs on the blank. In the original mesh the large elements in non critical locations are 20 mm in length and in the refined locations the elements are 4 mm in length.

An adaptive meshing scheme is implemented during the forming process to more accurately model the deformation of the blank during the forming process. The strategy for mesh refinement in AutoForm is to use the *h*-method adaptive procedure studied by Belytschko and Tabbara [95]. This adaptive meshing scheme splits elements into finer refinement levels when significant deformation due to bending is undergone. In Figure 186 the automatic re-meshing of both the main rail and enclosure panel are observed during the forming process. Adaptive meshing is preferred over starting with a sufficiently fine mesh because of the fact that refinement is only made when it is needed in the model, which significantly decreases computation times.

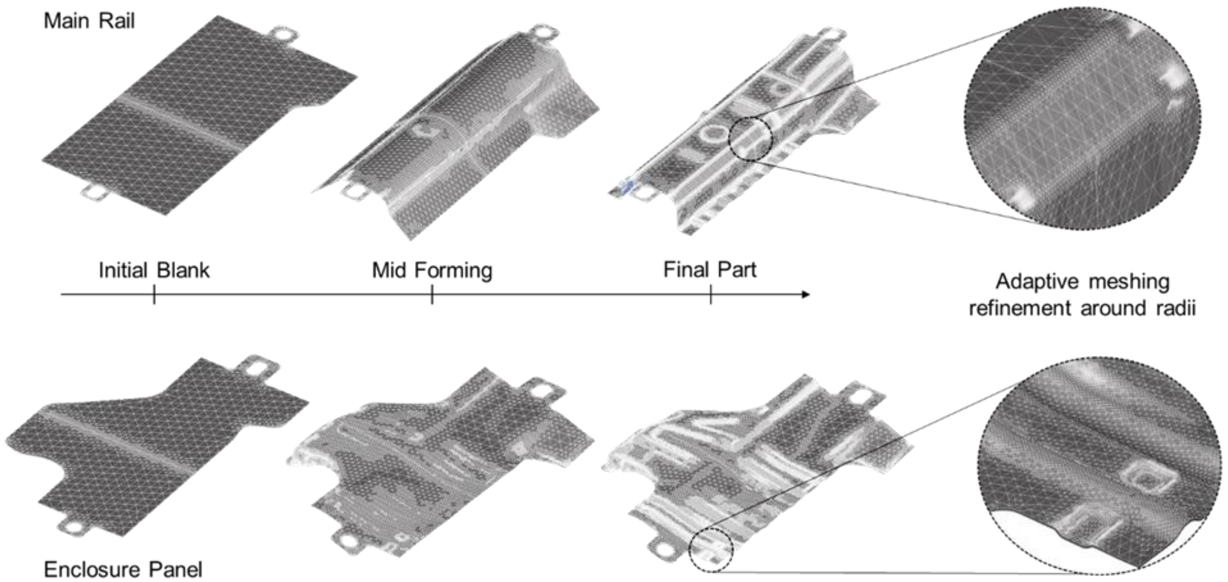

Figure 186. Adaptive mesh refinement showing the evolution of both the main rail and enclosure panel blank meshes from the original to final part mesh.

5.2.3 Tooling

Both the main rail and enclosure panel tools are developed using the crash forming process, which does not include a binder to stretch (decrease wrinkling potential) the blank during the drawing process. Pilot pins have been included into the tooling for alignment of the blank. The tooling (both punch and die shown in Figure 187) is assumed to be comprised of non-deformable surfaces described by discrete triangular facets.

During the hot forming process, a constant tool temperature of 20 °C is enforced, which removes the need for solid modelling and heat transfer within the tooling. Contact between the tool and sheet is enforced using a penetration search algorithm that looks for sheet nodes that are within the Max Penetration and Distance Error tolerance to enforce contact. Friction between the tool and blank is modelled using Coulomb's law where a constant coefficient of friction of 0.45 is enforced, which is in line with the hot stamping material friction experiments conducted by Yanagida and Azushima [96]. A 0.2 mm negative offset is included on one side of the tooling surface that will come in contact with the 1.2 mm thick section of the multi-gauge Ductibor® 1000-AS blank. The offset ensures that the tool surface can come into complete contact with the 1.0 mm thick section of the Ductibor® 1000-AS blank.

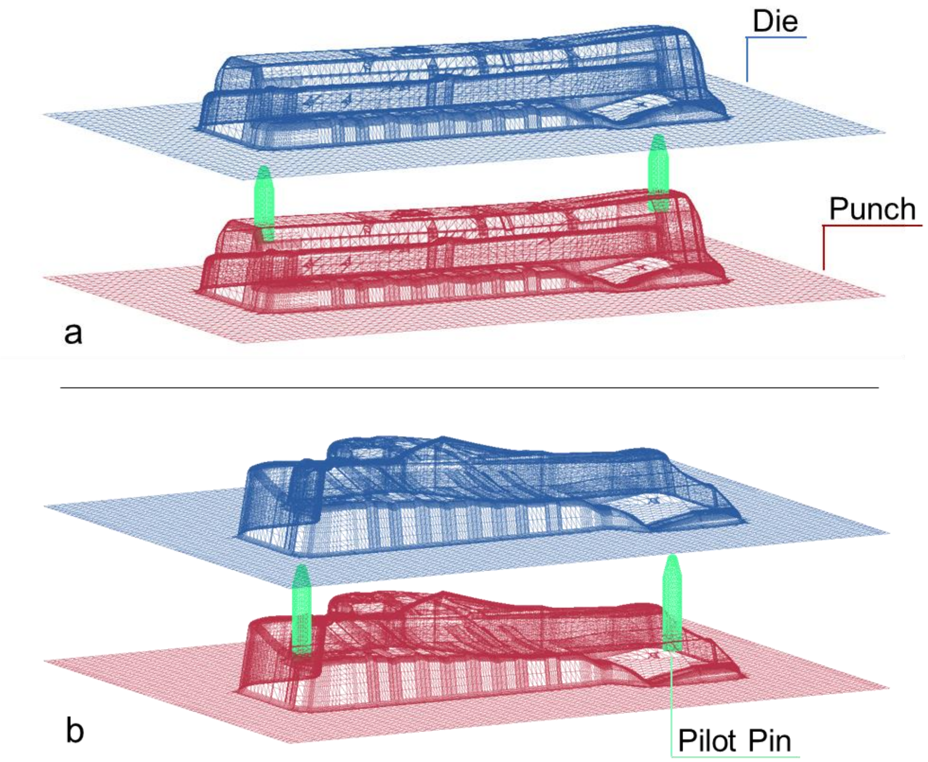

Figure 187. Crash form tooling for both the main rail **(a)** and the enclosure panel **(b)** showing the discretization of the rigid tooling into triangular facets.

5.3 Mapping Forming to Crash Simulations

The inclusion of forming histories into crash models is demonstrated to have significant effects on the predicted crash performance of various specimen, as discussed in section 1.2.4. The forming history of the main rail and enclosure panel to be tracked from the hot stamping model and incorporated into the crush tip crash model. The forming parameter of interest in this thesis is the sheet thickness at each element. Implications to crash performance predictions will be discussed in section 6.2.

The hot stamping model uses the nominal sheet thickness during the forming simulation. To account for the much lower strength of the Al-Si coating in crash simulations, 50 μm must be subtracted from the nominal sheet thickness. Therefore, after the forming simulation 50 μm is subtracted from each predicted integration point thickness.

The mesh used in the hot stamping model, simulated with AutoForm, consists of non-uniformly sized triangular shell elements, as shown in Figure 188a. Ideally, for crash simulations, uniformly sized square shell elements are used (Figure 188b). The difference in mesh sizes and shape means that the thickness at each integration point, from each of the triangular forming mesh elements, must be mapped to the integration points of the crash model mesh.

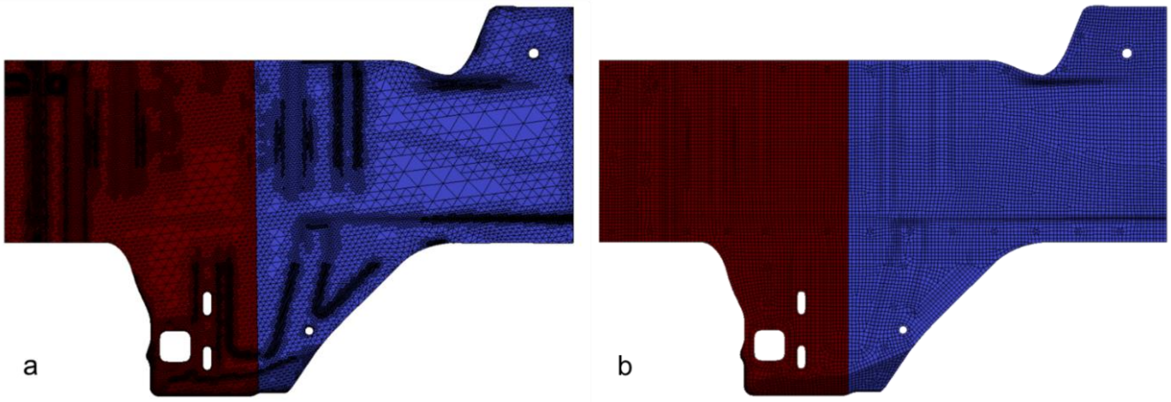

Figure 188. Difference in meshes used between **(a)** the hot stamping model (AutoForm) and **(b)** the crash model (LS-Dyna), demonstrated with the enclosure panel component.

The mapping of integration point thickness from the forming mesh to the crash mesh was accomplished using a history variable mapping algorithm within LS-PrePost, which assigns values based on the closest parametric coordinate for the through-thickness integration point. The forming history-mapped integration point thickness is shown in a contour plot for the main rail and enclosure panel in Figure 189. Contours of shell element thickness, on both the main rail and enclosure panel parts, shows that thinning only really occurs around fold initiators, which intuitively makes sense because the parts are crash formed and very little stretching occurs.

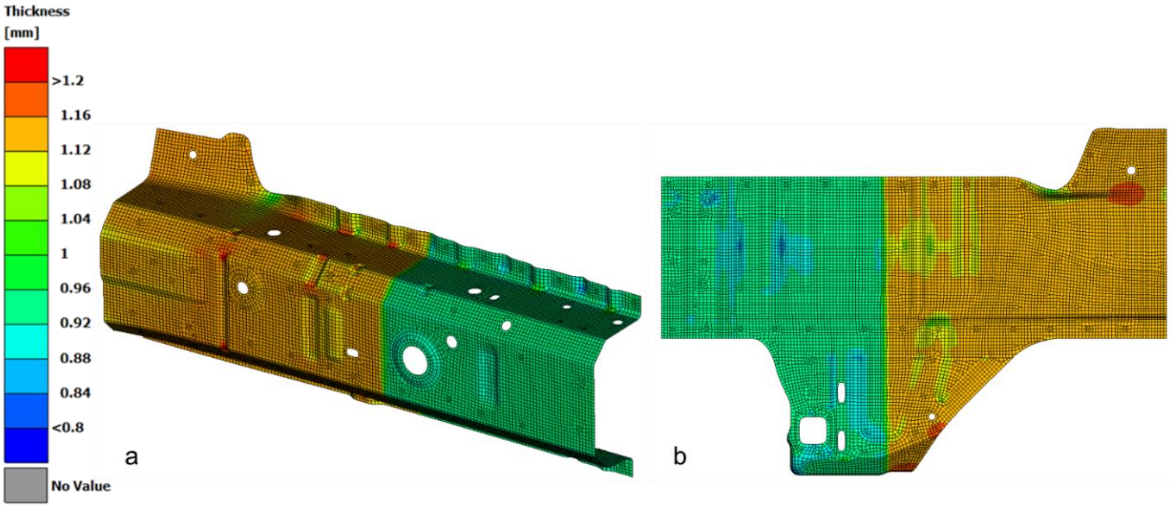

Figure 189. Forming history thickness mapping for the tailor-welded hot stamped crush tip **(a)** main rail and **(b)** enclosure panel.

5.4 Description of Forming Tooling

Preliminary versions of the main rail (Figure 187a) and enclosure panel (Figure 187b) tools were designed by the author of this thesis using AutoForm, as described in section 5.2. The preliminary tool design was then handed off to Cosma Die Technology (CDT) for further hot stamping process verification and then to Promatek Research Centre for the final die design and fabrication.

In both of the tools, forming assist devices, such as pilot pins (blue arrows Figure 190) and flipper gauges (red arrows Figure 190), have been incorporated into the tool designs to improve the formability and repeatability of the hot stamping process. The purpose of the pilot pins is to assist in locating the blank during the transfer from the furnace to tool by providing a location for the blank tabs (described in section 5.2.2) to be placed. The pilot pins ensure that the blank is stamped from the same location every hit. The purpose of the flipper gauges is to hold the blank above the tool until the ram comes down to form the part. This ensures that heat transfer by tool contact prior to forming is minimized, resulting in higher temperatures during forming and better quenched mechanical properties. The flipper gauges are spring loaded so once force is applied from the ram, the gauge retracts allowing the blank to drop onto the tool and form freely.

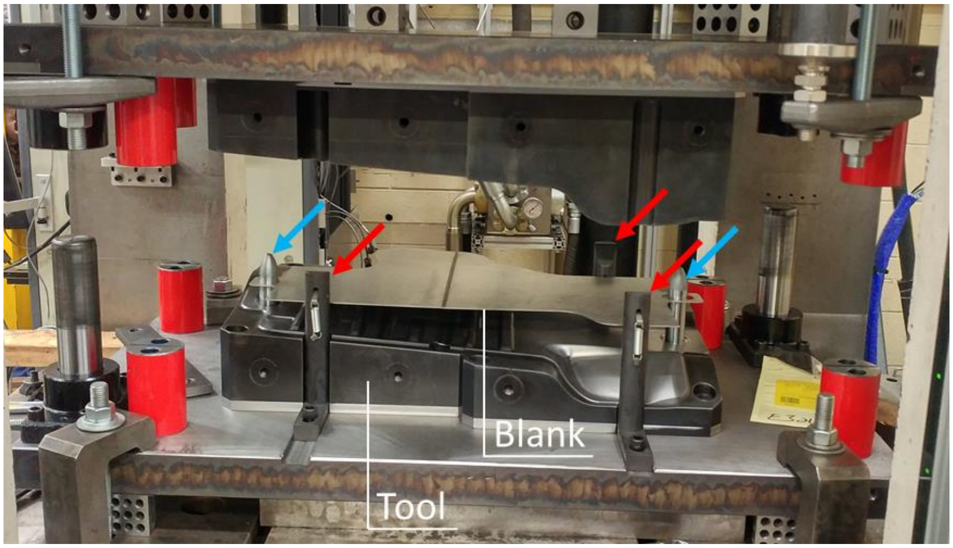

Figure 190. Common features to both die sets such as flipper gauges (red arrows) and pilot pins (blue arrows).

A single "die shoe" is fabricated and is designed to accommodate inserts for both parts (Figure 191). This approach requires changing inserts to switch between parts, but reduces the overall cost of the hot stamped tooling. Inserts have been numbered in each of the tools and the cooling water inlets and outlets have been highlighted.

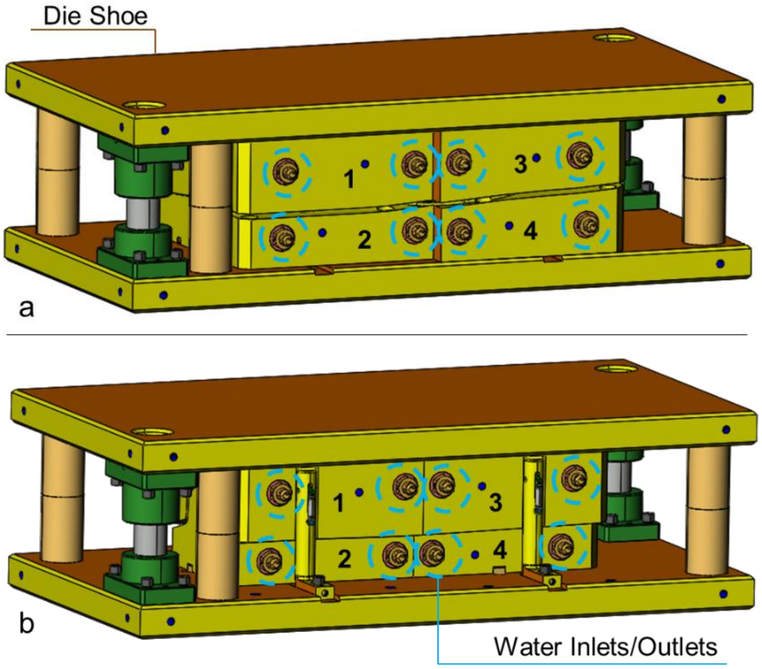

Figure 191. The single die shoe shown with the interchangeable die inserts from the **(a)** main rail and **(b)** enclosure panel.

5.4.1 Enclosure Panel Tool

The enclosure panel is formed using a crash forming tool comprised of four die inserts, as labelled in Figure 192, the die is comprised of sections 1 and 2, while sections 3 and 4 make up the punch. Each of the four sections have a chilled water inlet and outlet, which allows 7 °C water to flow through two channel sections. The exterior temperature of the tool was measured with a thermocouple probe to be between 12 and 15 °C. A pilot pin is located on both sides of the tool, in addition to three flipper gauges. The fourth locator for the blank is the high point of the punch (green dashed circle), which the blank rests on prior to forming.

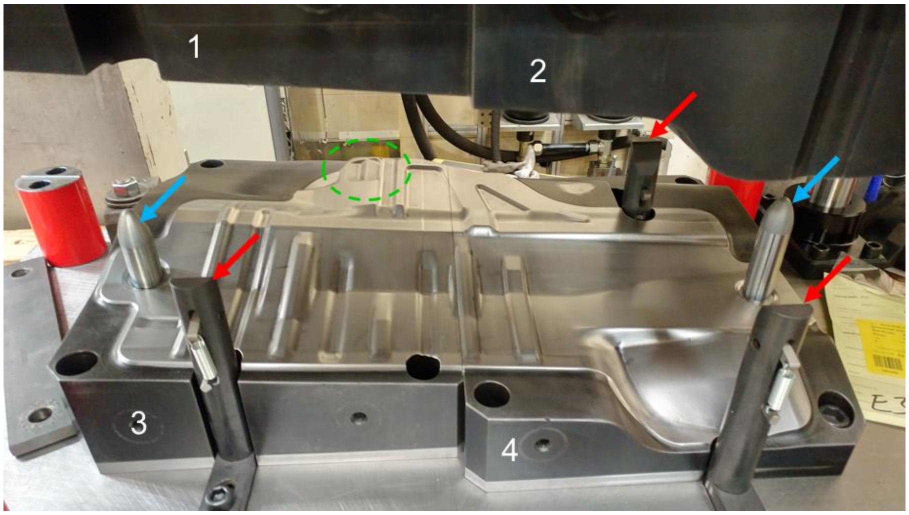

Figure 192. Enclosure panel crash form tooling identification of the four sections of the tool, the flipper gauges (red arrows) and pilot pins (blue arrows)

5.4.2 Main Rail Tool

The main rail is formed using a crash forming tool comprised of four sections, as labelled in Figure 193, in which sections 1 and 2 make up the die, while sections 3 and 4 make up the punch. Each of the four sections have a chilled water inlet and outlet, which allows 7 °C water to flow through a single channel section, travelling down the center of each tool section. The exterior temperature of the tool was measured with a thermocouple probe to be between 12 and 15 °C. A pilot pin is located on both sides of the tool, in addition to four flipper gauges in each corner of the tool.

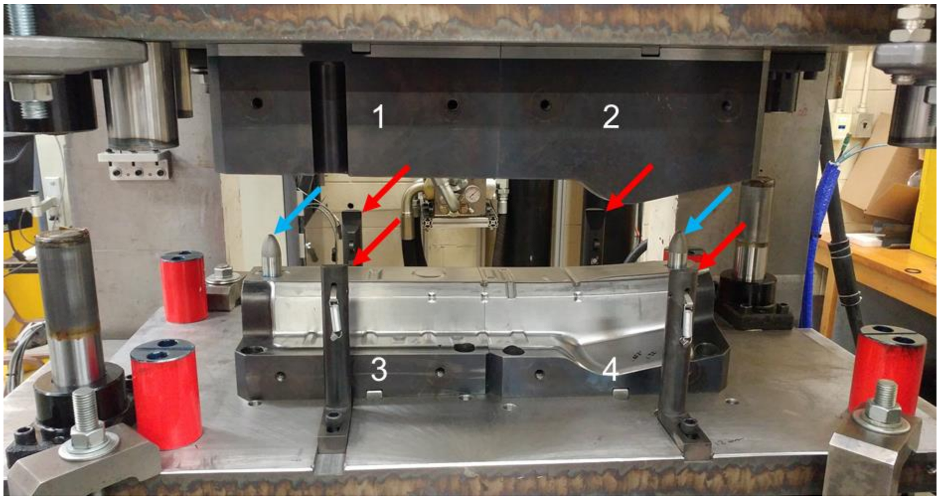

Figure 193. Main rail crash form tooling with identification of the four sections of the tool, the flipper gauges (red arrows) and pilot pins (blue arrows).

An offset of 0.5 mm is cut into the main rail tool, only on the fold initiators, as shown in Figure 194. The purpose of the offset is to allow for a better fit between the main rail and enclosure panel flanges upon assembly of tailor-welded hot stamped crush tips. The fold initiators (green in Figure 194a) have been offset in the positive y-direction, which is the direction opposite the inside of the c-channel section.

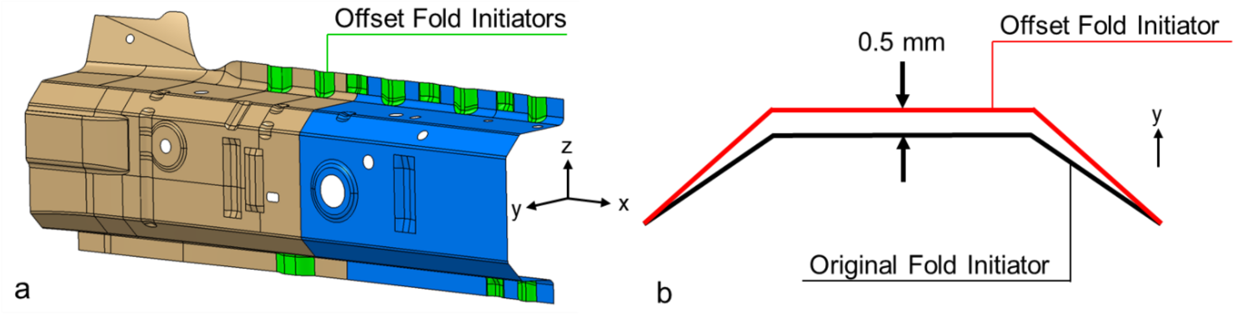

Figure 194. (a) Locations of the offset added to the fold initiators on the main rail part and **(b)** schematic of how the offset is oriented.

5.5 Press and Furnace

The main rail and enclosure panel tools are installed into a 120 ton hydraulic press manufactured by Macrodyne Technologies Inc., as shown in Figure 196. The press has a bed size of 762 mm by 1372 mm that accommodates the tool in both part configurations. The press has a daylight of 711.2 mm (28”) and a shut height of 457.2 mm (18”). Both of the tools, including the die shoes, have a shut height of 301.5 mm (~12”), which means that spacers have to be used to make up the 6” difference in shut height. On the top of the tool

2-4-6 blocks oriented in the 6” dimension have been used, while on the bottom of the tool 1-2-3 blocks oriented in the 1” dimension are used, as shown in Figure 195. A single 120 ton actuator utilizes a 100 GPM servo valve and two 15 gallon accumulators to achieve a maximum displacement speed of 250 mm/s. A custom LabView program runs the press in displacement control. The program works by waiting for a button push signal, at which point the press travels to the pre-defined displacement, in an amount of time defined by the user. The press is held in the closed position, applying full tonnage, for a user-defined quenching time.

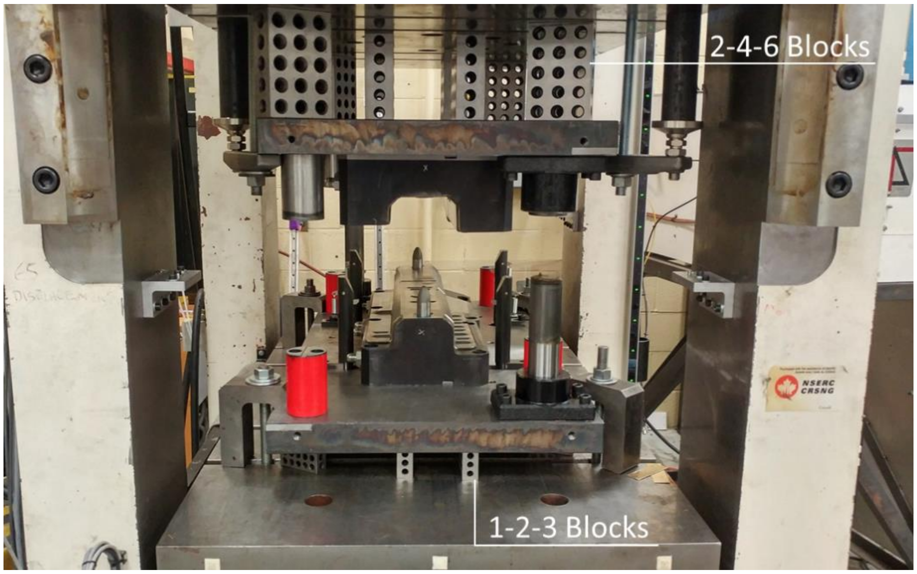

Figure 195. The 120 ton hydraulic press with main rail tool setup showing the use of 2-4-6 blocks and 1-2-3 blocks to make up the difference in shut height.

The furnace used to austentize the main rail and enclosure panel blanks is built by Deltech Inc. and is located adjacent to the press (Figure 196). The internal dimensions of the furnace are 610 mm wide by 203 mm tall, with a depth of 915 mm. Six electric heating elements, arranged in three control zones: front, middle and back of the furnace, provide an 18 kW heating capacity. Blanks lie on two pieces of stainless steel angle sections, running the length of the furnace and can easily be slid along these rails during the transfer of the blank in and out of the furnace.

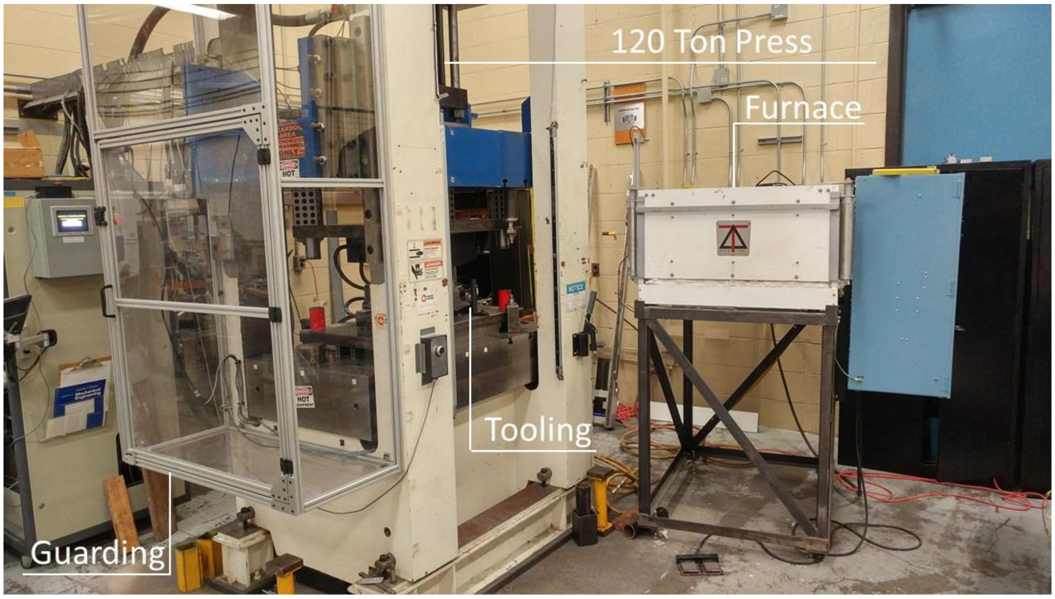

Figure 196. 120 ton Macrodyne hydraulic press with Deltech furnace.

5.6 Hot Stamping Process

The hot stamping process can be broken down into the following four steps: austenitization, transfer, forming and quenching. To begin the austenitization phase, a blank is manually loaded onto the stainless steel rails in the 950°C pre-heated furnace and left to soak in the furnace for 6 minutes, ensuring that full austenitization occurs. After the soaking time is complete, the blank is manually removed from the oven using a pair of long pliers and transferred to the chilled die set, where it is located using the flipper gauges and pilot pins (Figure 190). Timing during the transfer process showed that the manual operation took about 4 seconds on average, from oven to tool. Once the blank is placed onto the locators and the pliers are clear of the press, a button is pushed, displacing the tool from fully-open position to fully closed position in 2 seconds and thus forming the part. At the bottom of the stroke, 110 tons of pressing force is applied for 10 seconds, rapidly quenching the part. Parts removed from the press were only warm to the touch and therefore controlled air cooling procedures were not required.

5.6.1 Blank Temperature Verification

The temperature-time history of the austenitization and transfer stages were verified by mounting high temperature thermocouples to the main rail blank in three locations, as shown in Figure 197. In this image the thermocouple locations are referred to as "Front", "Mid" and "Back", which correspond to their locations in the furnace. The thermocouples were mechanically mounted to the blank by drilling two holes for the thermocouple wires and then crimping them to the blank. It is to be noted that the "Front" thermocouple is affixed to the 1.0 mm Ductibor® 1000-AS section, while the "Mid" and "Back" thermocouples are affixed to the 1.2 mm Ductibor® 1000-AS section.

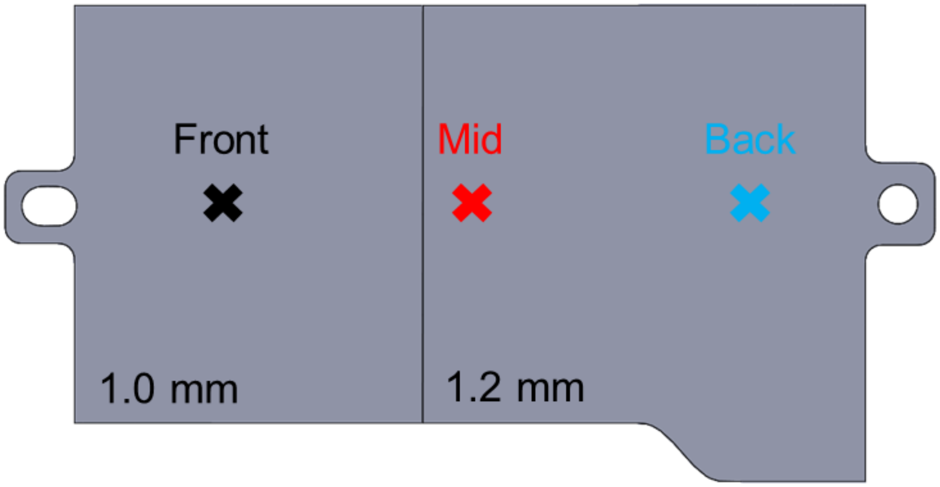

Figure 197. Thermocouple locations on 1.0 mm to 1.2 mm Ductibor® 1000-AS main rail blank.

In Figure 198 the temperature-time history measured by the thermocouple mounted blank is shown. It is observed from this plot that the blank enters the oven at 15 seconds into the recording, which is noted by the rapid increase in temperature. After 4 minutes of being in the 950 °C furnace, the blank temperature in each zone has reached the desired temperature of 950 °C. At 6.5 minutes, just slightly over the desired blank soaking time of 6 minutes, the furnace is opened and the blank is removed for transfer to the chilled die set. Transfer from furnace to locating pins and flipper gauges on the die set takes approximately 4 seconds. From the plot, it is determined that the temperature of the blank is approximately 880 °C at the point in which the forming step would commence. The hot stamping model predicts that the temperature of the 1.0 mm section is 834 °C and the 1.2 mm section is 848 °C after 4 seconds of transfer time. Note that the blank is not formed in the temperature validation experiments since the thermocouples would be crushed in the tooling; rather, the blank is left on the die set to air cool and at 440 seconds the bainite transformation is noted by increase in temperature (release of energy) caused by the change in state. The thermocouple located in the "Front" (1.0 mm Ductibor® 1000-AS) is observed to rise in temperature and cool the fastest up to 440 seconds, which is expected due to the thinner gauge material.

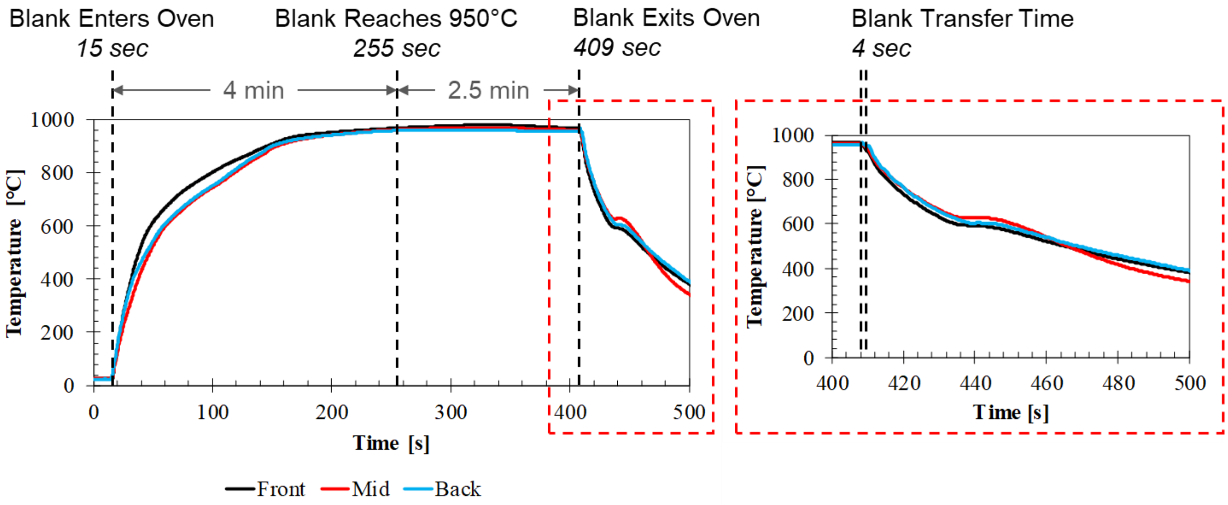

Figure 198. Temperature-time history measured by the thermocouple equipped main rail blank.

5.7 Hot Stamping Results and Numerical Predictions

To-date, thirty of each part (main rail and enclosure panel) were hot stamped using the process parameters described in the previous sections. Examples of both formed parts are shown in Figure 199. Note that the enclosure panel shown in this image had one of its tabs ground off and has been dyed blue for the die contact checks.

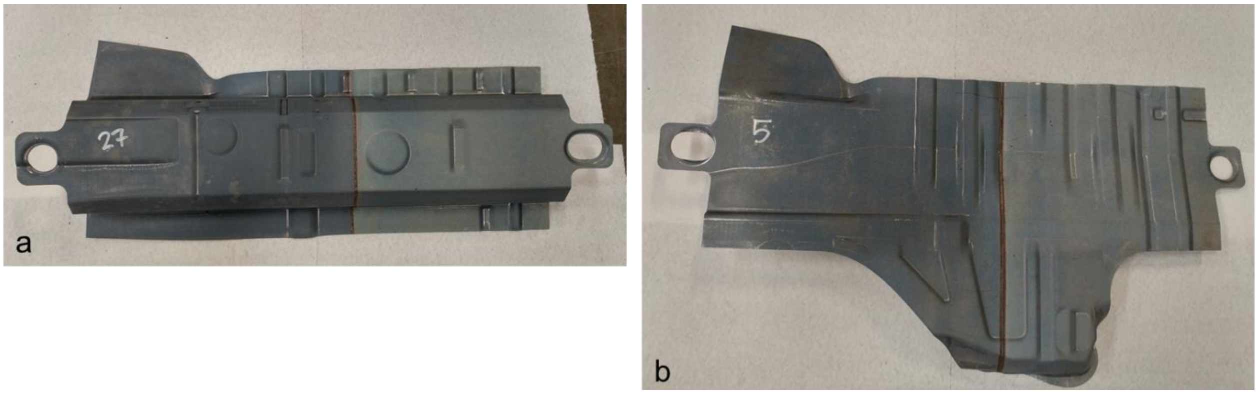

Figure 199. Hot stamped **(a)** main rail and **(b)** enclosure panel parts.

To assess whether splitting or material fold over will occur, regions of high thinning or thickening, identified in the forming simulation, were examined closely in the as-formed parts. In the forming process development, failure criteria were employed based on recommendations from Cosma Die Technology [97] in which the criteria for splitting and material fold over were based on of the percent thinning/thickening in the part. A percent thinning of 17% or greater denotes areas where the material forming is in danger of splitting, whereas a percent thickening of 10% percent or greater signifies areas where material fold over is likely to occur.

The predicted deformation and formed main rail part are shown in Figure 200 and Figure 201, for the upper flange and lower flange, respectively. Contours of percent thinning has been plotted to show the locations where the percent thinning is the highest. All of the thinning hot spots in the main rail are below the splitting criteria of 17%; however, these spots will be regarded as locations suspect of splitting and will therefore be monitored in the formed parts. It is observed in both the upper and lower flange of the main rail that the identified thinning hot spots from the hot stamping simulation form without any splitting or excess thinning.

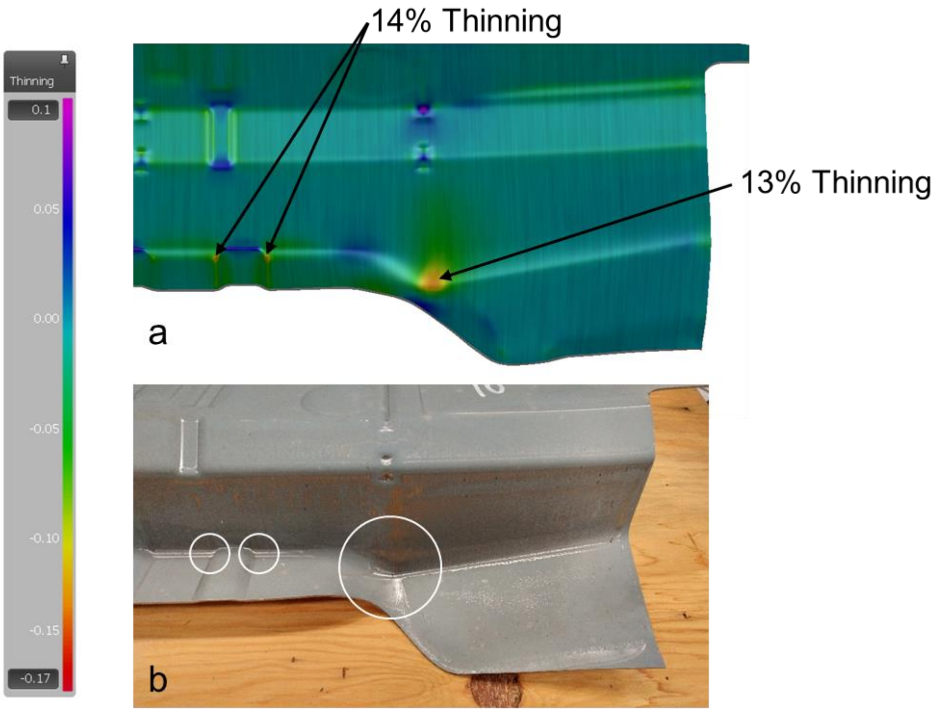

Figure 200. Main rail part upper flange **(a)** forming simulation showing 13% and 14% thinning and **(b)** formed part demonstrating that no splitting has occurred.

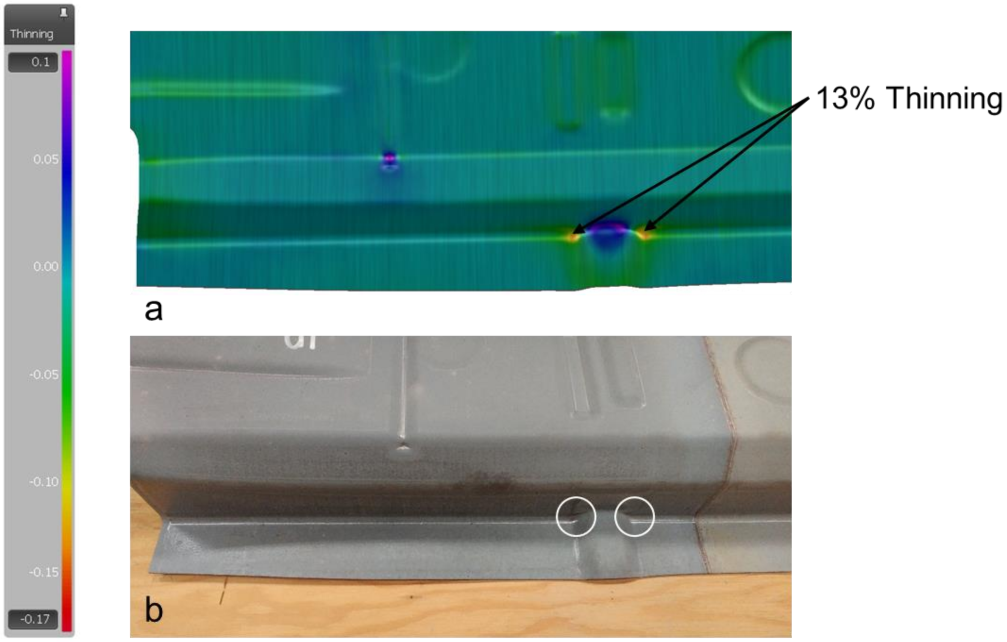

Figure 201. Main rail part lower flange **(a)** forming simulation showing 13% thinning and **(b)** formed part demonstrating that no splitting has occurred.

The predicted deformation from the lower flange of the enclosure panel part and its corresponding location on the formed part are shown in Figure 202. Contours of the percent thinning/thickening have been plotted to show the locations where the percent thickening is the highest. It is observed that around the corner radius of the lower flange the percent thickening is very high, at 22% thickening, which is well above the material fold over criteria of 10% thickening. During forming the corner radius is monitored closely due to the high risk of material fold over. It is however observed that even with the high amount of material compression, no material fold over occurs in the formed parts.

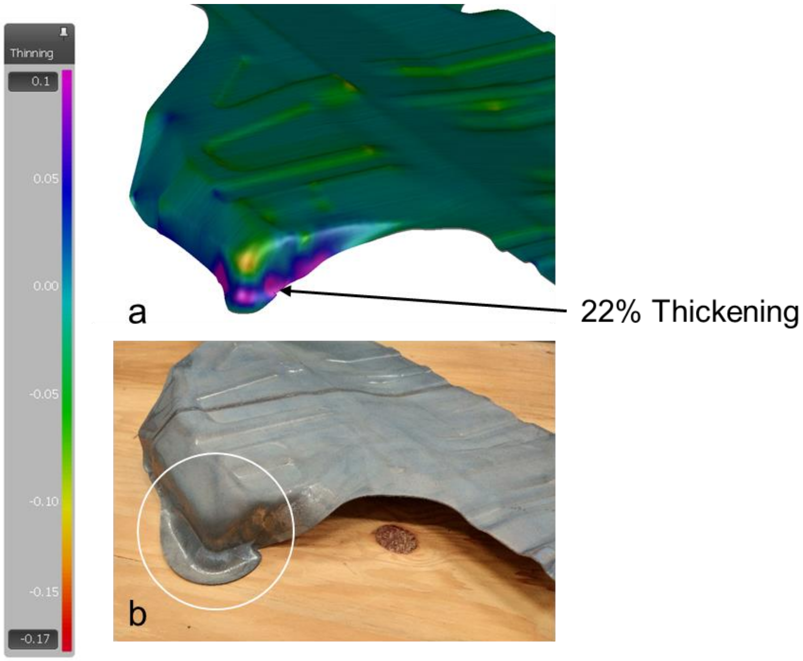

Figure 202. Enclosure panel part lower flange **(a)** forming simulation showing 22% thickening and **(b)** formed part demonstrating that no material fold over has occurred.

5.7.1 Hardness Measurements

After forming the main rail and enclosure panel sections, hardness measurements were taken at various locations on one of each part using the Rockwell C hardness standard. The main purpose of using the Rockwell C hardness test is to confirm the hardness achieved on the parts after quenching.

In Figure 203 the locations where samples have been removed for hardness testing are shown (red circled numbers) for the main rail and enclosure panel parts. Hardness samples were removed from the parts using an angle grinder equipped with an abrasive cutting wheel. The Rockwell C scale hardness measurements for each location are also shown in Figure 203. In the main rail part the average hardness levels measured are 34 HRC (327 HV, 1027 MPa) and 31 HRC (304 HV, 962 HV), for the 1.2 mm and 1.0 mm thick Ductibor® 1000-AS sections, respectively. In the enclosure panel part the average hardness levels measured are 33.5 HRC (323 HV, 1014 MPa) and 32.5 HRC (315 HV, 989 HV), for the 1.2 mm and 1.0 mm thick Ductibor® 1000-AS sections, respectively. Note that the Rockwell C hardness scale has been converted to an estimated Vickers hardness level and UTS using ISO 18265 [98]. It is observed the hardness is lower in the 1.0 mm Ductibor® 1000-AS section than it is in the 1.2 mm Ductibor® 1000-AS section, which may be due to higher contact pressures obtained in the 1.2 mm section.

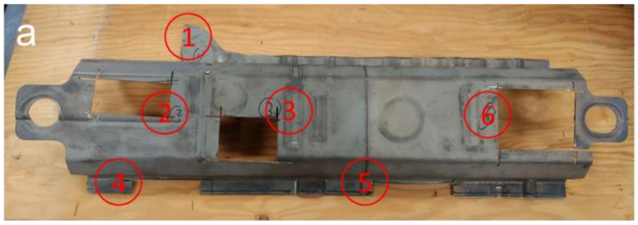

Sheet Thickness	Location	Hardness [HRC]	Average [HRC]
1.2 mm	1	34	34
	2	34	
	3	34	
	4	35	
1.0 mm	5	31	31
	6	31	

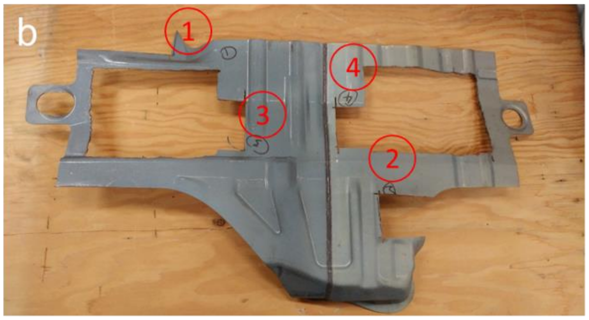

Sheet Thickness	Location	Hardness [HRC]	Average [HRC]
1.2 mm	1	35	33.5
	3	32	
1.0 mm	2	34	32.5
	4	31	

Figure 203. Hardness sample location and Rockwell C hardness value for the **(a)** main rail and **(b)** enclosure panel parts.

In addition to Rockwell C hardness measurements, the hardness of each of the parts were also measured by Yau [99] using a Vickers hardness tester. The locations that hardness samples were laser cut from the parts are shown in Figure 204 along with the corresponding Vickers hardness measurement. In the main rail part, the average measured hardness levels are 401.2 HV and 368.5 HV, for the 1.2 mm and 1.0 mm thick Ductibor® 1000-AS sections, respectively. It is noted that the hardness in the sidewall region is 299.3 HV which likely indicates lower contact pressure in that vicinity. In the enclosure panel part, the average hardness levels measured are 392.8 HV and 412.8 HV, for the 1.2 mm and 1.0 mm thick Ductibor® 1000-AS sections, respectively. The measured hardness range of 299.3 to 419.3 HV corresponds to an Ultimate Tensile Strength (UTS) of 965 to 1320 MPa. This range is somewhat higher than that based on the Rockwell C hardness measurements (31 to 35 HRC), which corresponds to a UTS in the range of 995 to 1110 MPa

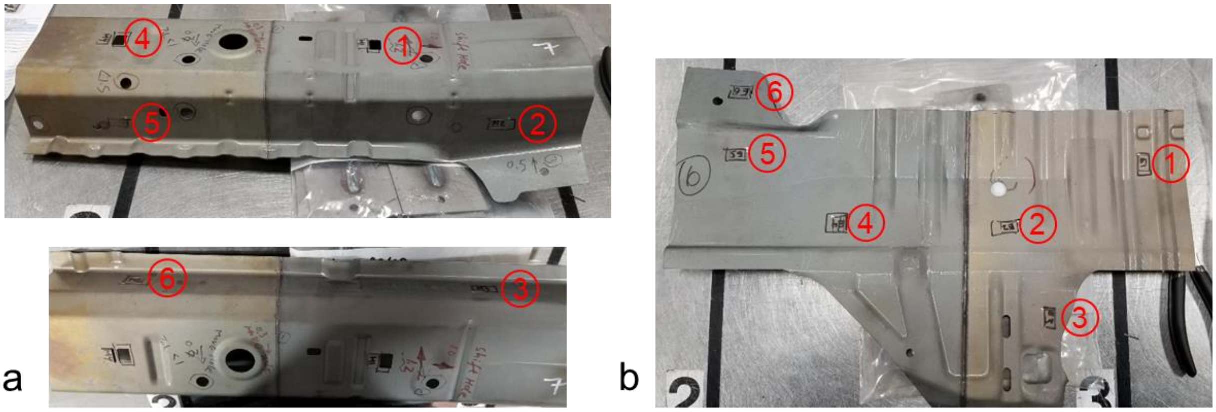

Sheet Thickness	Location	Hardness [HV]	Average [HV]
1.2 mm	1	395.7	401.2
	2	393.7	
	3	414.3	
1.0 mm	4	399.3	368.5
	5	299.3	
	6	407.0	

Sheet Thickness	Location	Hardness [HV]	Average [HV]
1.0 mm	1	410.3	412.8
	2	419.3	
	3	408.7	
1.2 mm	4	398.7	392.8
	5	384.3	
	6	395.4	

Figure 204. Hardness sample locations and values for the Vickers Hardness measurements conducted by Yau [99] on the **(a)** main rail and **(b)** enclosure panel parts.

5.8 Assembly Plan for the Crush Tip Crash Test Specimens

The tailor-welded hot stamped crush tip specimens are composed of a hot stamped multi-gauge Ductibor® 1000-AS main rail (C-channel) section and the enclosure panel section. In addition to these hot stamped components, the tailor-welded hot stamped crush tip also comprises several production components from the front bulkhead, bumper and side frame member assemblies, as shown in Figure 205. The spot welded crush tip assembly is also MIG welded onto a ½" steel plate that can be mounted to the crash sled rigid wall.

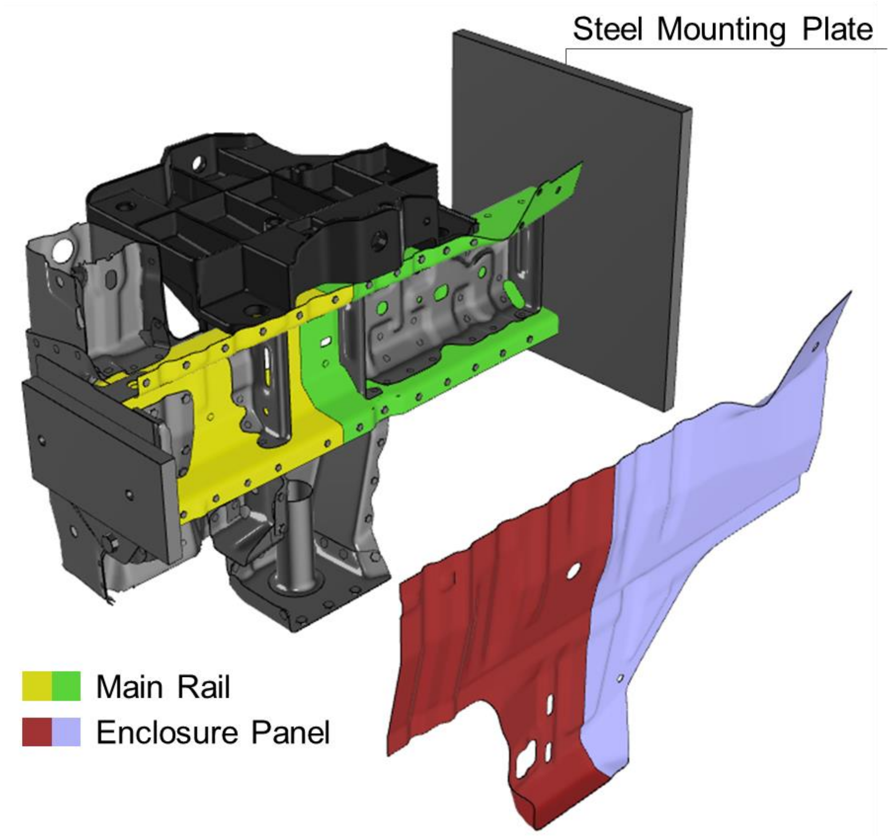

Figure 205. Tailor-welded hot stamped crush tip assembly, highlighting the production components required for its assembly.

The main rail and enclosure panel sections must be laser trimmed following post hot forming, to remove the locating tabs used in the forming process, cut holes for bolt-on locations and provide spot weld fixture datum points, as well as to remove excess material from the developed blank around the flanges (Figure 206). The laser trimming is performed by Promatek Research Centre.

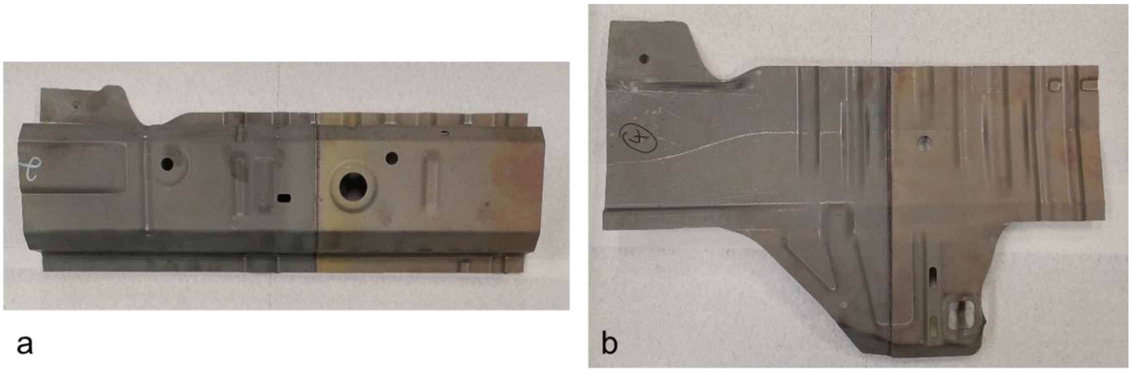

Figure 206. Laser trimmed **(a)** main rail and **(b)** enclosure panel parts.

The laser trimmed main rail and enclosure panel sections will be shipped to Honda R&D Americas to be integrated with the production components and spot welded into the tailor-welded hot stamped crush tip configuration. In total, enough sections to produce 30 crush tips will be shipped to Honda R&D Americas for assembly.

Several modifications to the production components shown in Figure 205 were required to account for the changes in the flange orientation and section profile of the enclosure panel (Figure 159). In addition, the main rail section required the introduction of a sidewall draft angle of 3 degrees that was not present in the cold stamped production main rail. Consequently, all of the production components that are welded to the interior of the main rail section required slight modifications. To accomplish these modifications, the production parts were all subjected to minor reshaping operations utilizing simple tooling sets manufactured for this purpose. The following details the changes made to these production components.

5.8.1 Part Modifications to Accommodate Vertical Flange Design

A consequence of redesigning the hot stamped crush tip to have vertical flanges instead of the horizontal flanges in the production component (explained in section 4.3.3 and illustrated in Figure 159) is that the front weld-on bracket no longer interfaces with the enclosure panel, as shown in Figure 207. It is also observed that interference exists between the front bracket and enclosure panel where the fold initiator is located, as well as on the top flange of the front bracket. The top flange is welded to the enclosure panel flange in the production component's horizontal flange design, however in the new vertical flange design it is not required. A relatively large gap between the enclosure panel and front bracket will also cause problems during spot welding of the two components.

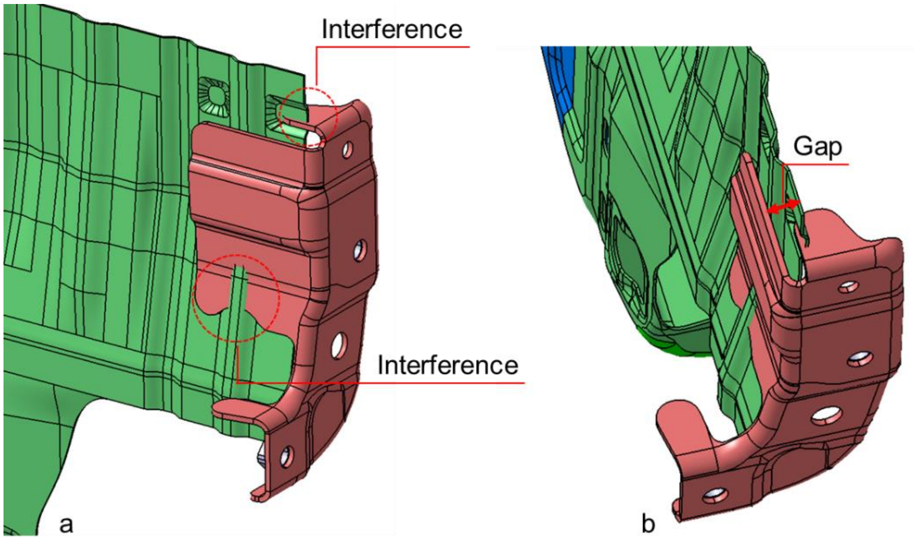

Figure 207. Production front bracket does not interface with the vertical flange design for the hot stamped enclosure panel. **(a)** Highlighting interference and **(b)** gap between front bracket and enclosure panel.

A counter measure to facilitate the interface between the front bracket and enclosure panel is to redesign the front bracket such that it can accommodate the new geometry of the enclosure panel. The redesigned front bracket is shown in Figure 208, from which it was determined that the changes made are minor enough that the existing bracket can be modified to meet the new geometry. In the redesigned front bracket, the flat portion that interfaces with the enclosure panel has been reshaped in order to conform to the inner face of the enclosure panel. The top flange that previously interfered with the enclosure panel has been removed. In addition a fold initiator matching the profile and location of the one on the enclosure panel has been designed into the front bracket so that the two parts can seamlessly interface.

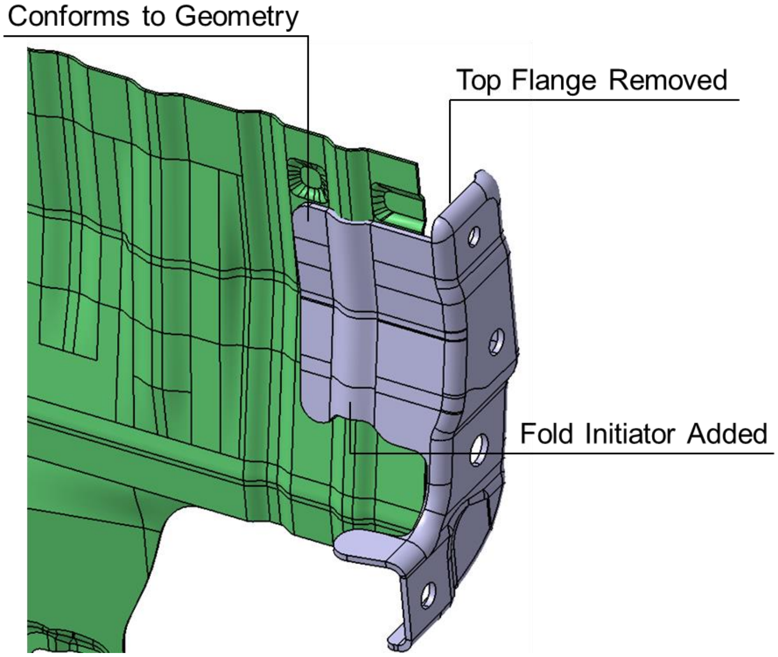

Figure 208. Redesigned front bracket that eliminates interference and gaps.

The re-forming process is designed to accomplish the manufacturing of the redesigned front bracket component, as illustrated in Figure 209. Production front brackets are purchased and serve as the starting point of the re-forming process. The top flange of the front bracket is trimmed off and ground away so that it does not interfere with the enclosure panel. The part is then secured into the stage 1 tooling shown in Figure 210 using two M10 bolts through pre-existing holes in the production bracket. In the stage 1 tooling, the large flat face of the bracket is pressed to the geometry of the inner surface of the enclosure panel using 220,000 lbf supplied by the 120 ton hydraulic Macrodyne Technologies Inc. press. After the stage 1 forming operation is complete the bracket is bolted into the stage 2 tooling, where the fold initiator is pressed into the part using the same tonnage as in stage 1.

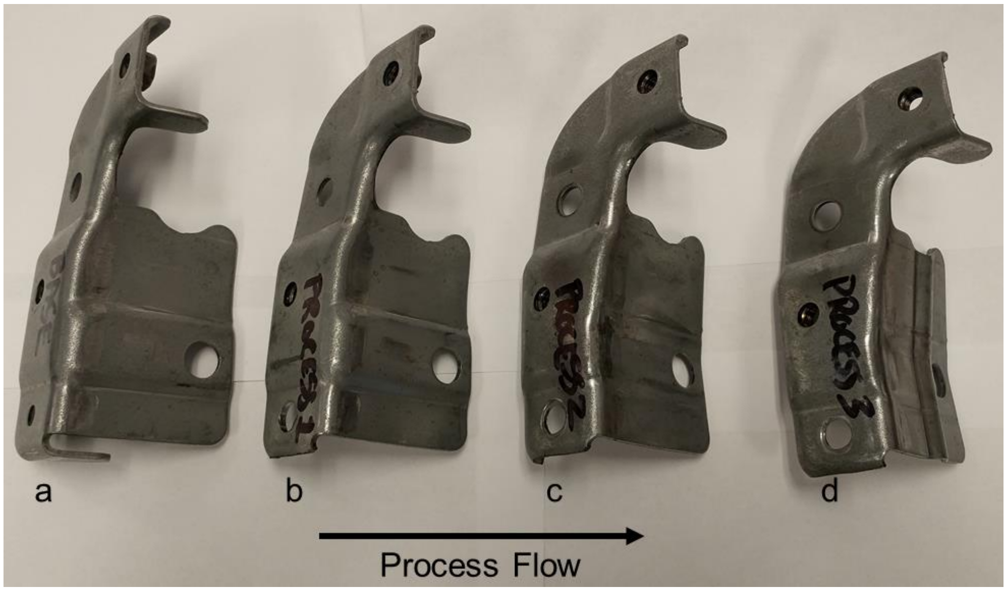

Figure 209. Steps required for the front bracket re-forming: **(a)** starting with a production front bracket, **(b)** the top flange is trimmed off, **(c)** then the large flat face is pressed to the shape of the enclosure panel's inner face and **(d)** a fold initiator is formed into the reshaped face.

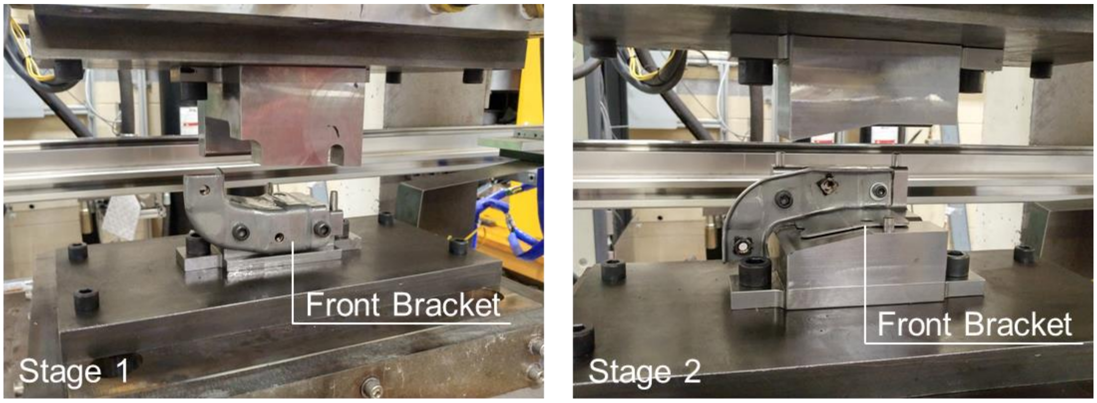

Figure 210. Reforming of the production front bracket broken down into two stages: Stage 1 (left) the bracket face is reformed to match the enclosure panels inner face, Stage 2 (right) fold initiator is formed into the bracket.

An additional consequence of the vertical flange geometry is that the front bumper beam extension plate interferes with the flanges, as illustrated in Figure 211a. To mitigate this interference problem, while continuing to use the production component, the front bumper beam extension plate is trimmed to remove 42 mm of the plate using a band saw, as demonstrated in Figure 211b.

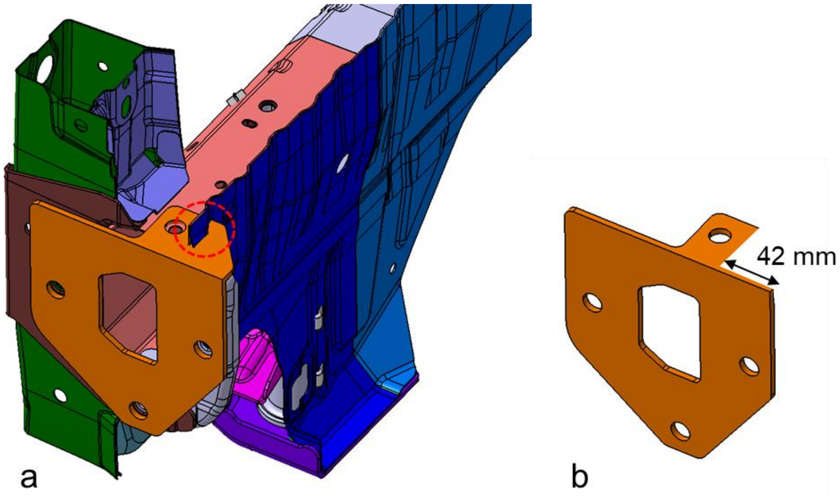

Figure 211. **(a)** Interference between the front bumper beam extension plate and the vertical flange geometry. **(b)** Trimmed front bumper beam extension plate to accommodate new flange geometry.

5.8.2 Part Modifications to Accommodate Side Wall Draft Angle Addition

The addition of a draft angle to the main rail component, to assist in the forming process, is discussed in section 4.3.3. The consequence of adding in this draft angle to the tailor-welded hot stamped main rail component is that the internal and external components that weld onto the sidewall of the main rail no longer interface properly. The components effected by the change in draft angle are shown in Figure 212. To mitigate this problem a series of templates are machined for each part so that the weld flanges can be re-shaped to match the new draft angle of the main rail.

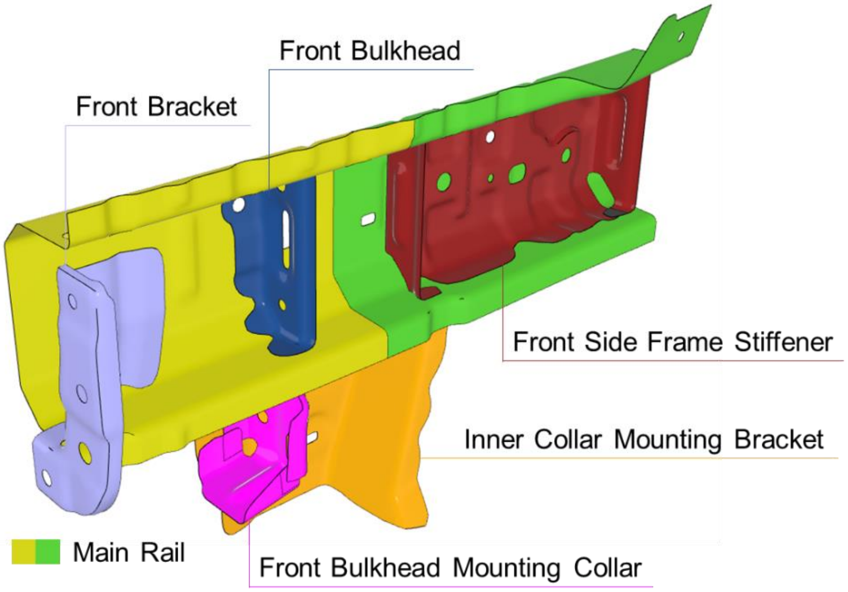

Figure 212. Internal and external components effected by the change in forming draft angle on the main rail.

5.8.2.1 Front Bulkhead Mounting Collar

The template used to re-shape the front bulkhead mounting collar is illustrated in Figure 213, in which the spot weld flange needed to be re-shaped is circled with a red dashed line. The template consists of an upper and a lower section, which are located to the part through two dowel pin holes that share location and diameter of two holes on the front bulkhead mounting collar. The upper template fits inside of the front bulkhead mounting collar and is tapered to the main rail draft angle at the location of the spot weld flange. The upper and lower template assembly are clamped tightly in a vice-grip and the spot-weld flange is re-shaped manually with a steel hammer.

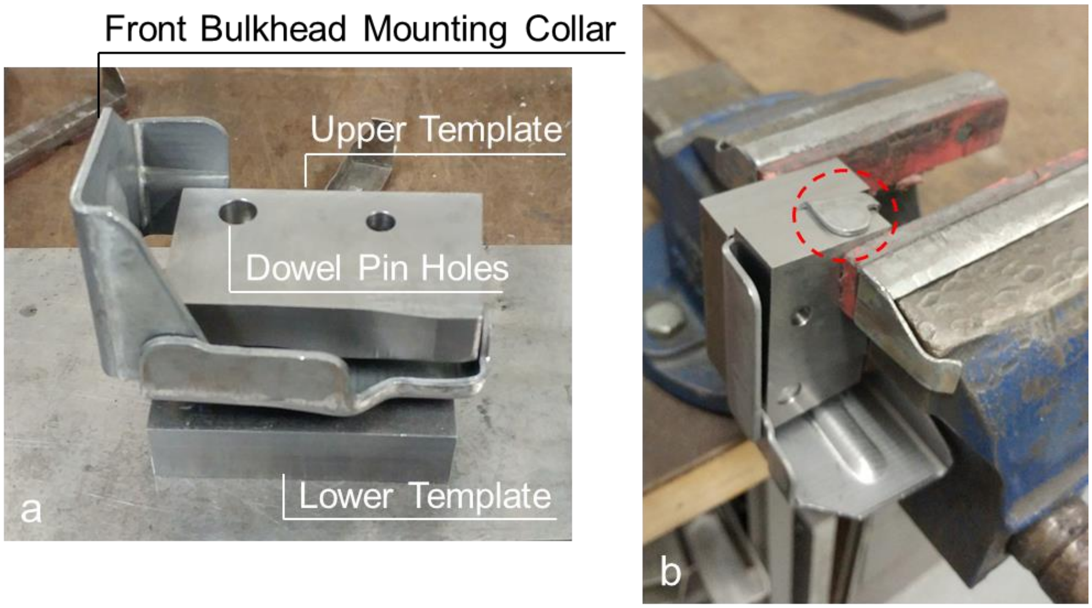

Figure 213. Front bulkhead mounting collar **(a)** template assembly and **(b)** template assembly in vice-grip, highlighting spot weld flange to be re-shaped (red).

5.8.2.2 Front Side Frame Stiffener

The front side frame stiffener is re-shaped by bending the stiffener flanges (red dashed outlines) outwards in a vice-grip, as shown in Figure 214. Once the flanges have been adjusted in the vice-grip, the front side frame stiffener is placed in a template (Figure 214b) to check whether the flanges accommodate the new main rail draft angle. The manual flange adjustment process is continued until the flanges match the template.

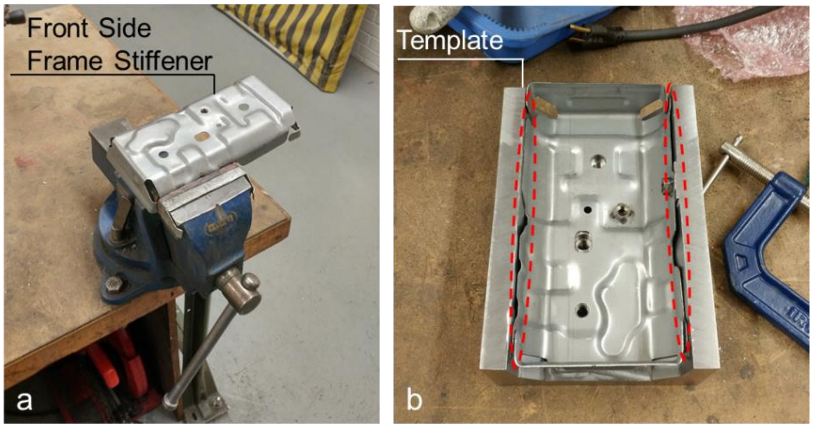

Figure 214. Front side frame stiffener **(a)** flanges (red) being re-shaped in vice-grip and **(b)** then checked for correct fit using the template.

5.8.2.3 Inner Collar Mounting Bracket

The template used to re-shape the inner collar mounting bracket and the location of the spot weld flange to be re-shaped (red dashed circle) are shown in Figure 215. The template fits the outer face of the inner collar mounting bracket and contains the main rail draft angle in the location of spot weld flange. First, a C-clamp is used to align the template to the inner collar mounting bracket. This assembly is then clamped in a vice to secure both the part and template so that the spot weld flange can be manually re-shaped with a steel hammer.

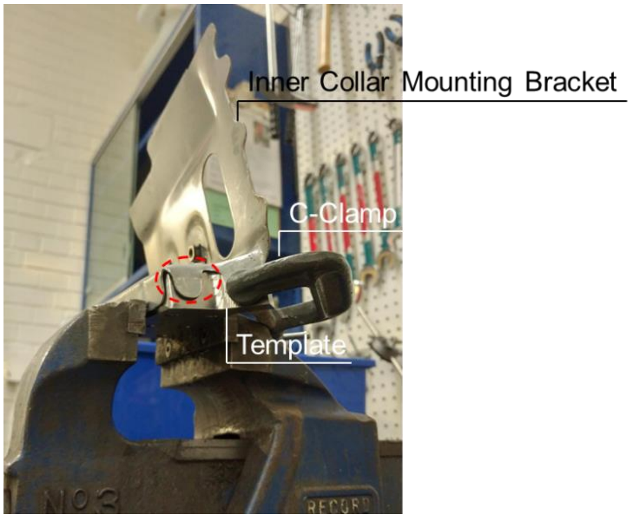

Figure 215. Inner collar mounting bracket template in vice-grip, with the spot weld flange to be re-shaped highlighted (red).

5.8.2.4 Front Bracket

The template used to re-shape the front bracket spot weld flange (red dashed circle) is shown in Figure 216. This template assembly takes advantage of the already machined stage 2 re-forming die, used to re-form the front bracket to the shape of the vertical flange enclosure panel geometry (section 5.8.1). The stage 2 re-forming die secures the front bracket in place so that the spot weld flange can be re-shaped. An angled wedge and template, shaped to the main rail draft angle, are utilized along with a steel hammer to re-work the spot weld flange to match the main rail draft angle.

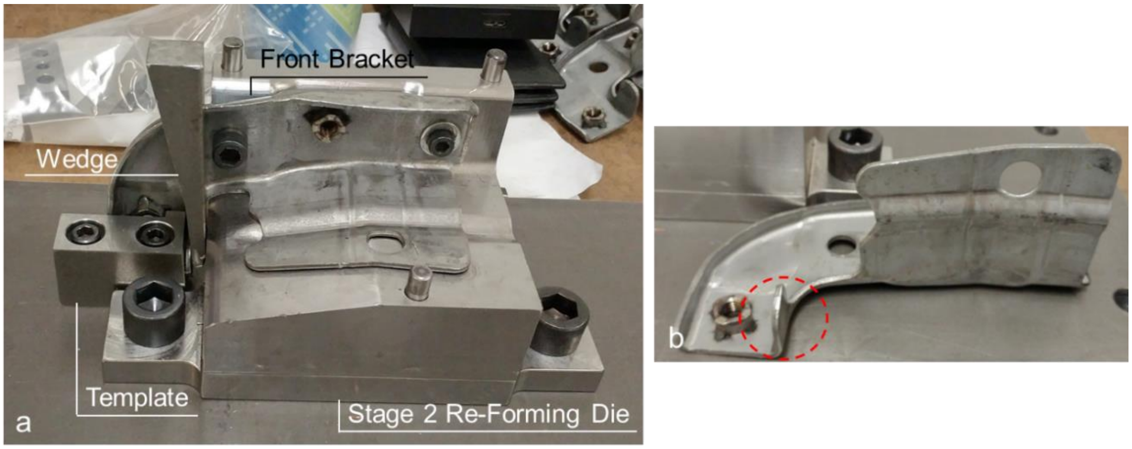

Figure 216. **(a)** Front bracket re-shaping template assembly and **(b)** the location of the spot weld flange to be re-shaped (red).

5.8.2.5 Front Bulkhead

The front bulkhead, positioned in its respective template, is shown in Figure 217, with the spot weld flange location that must be re-shaped highlighted with a red dashed circle. Two C-clamps are used to secure and align the front bulk head in the template and the entire template assembly (front bulkhead, clamps and template) is placed into a vice grip, so that the part can be worked on. A third C-clamp is positioned on the spot weld flange location (red), which is then tightened to deform the spot weld flange to the main rail draft angle.

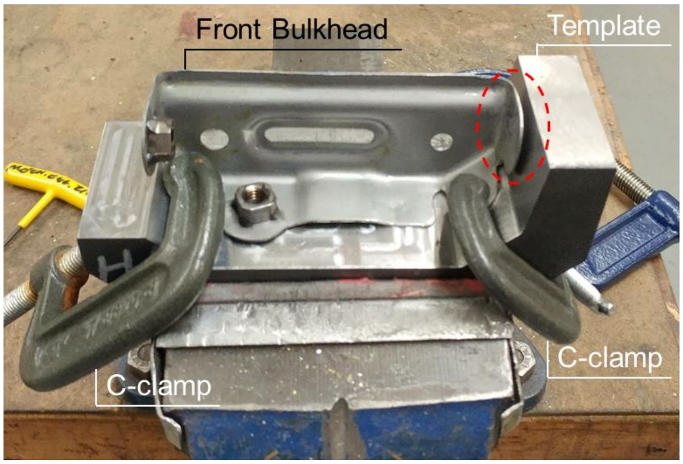

Figure 217. Front bulkhead template in vice-grip, with the spot weld flange to be re-shaped highlighted (red).

Chapter 6 – Tailor-Welded Hot Stamped Crush Tip – Predicted Crash Performance

The previous section detailed the numerical and experimental forming process for the tailor-welded hot stamped crush tip main rail and enclosure panel sections, as well as their assembly procedure. In this chapter the crash performance of the tailor-welded hot stamped crush tip is numerically evaluated. The chapter opens by discussing the plan for dynamically crash testing the tailor-welded hot stamped crush tips and the associated numerical model that represents the test boundary conditions. The numerical predictions from the tailor-welded hot stamped crush tip simulations are presented with and without the inclusions of the hot stamping forming history. Finally, this chapter concludes with an evaluation of the crash performance of the tailor-welded hot stamped crush tip against the design specifications (Table 3), from section 2.8. A discussion regarding the validity of using the crush tip in place of the entire side frame member to evaluate crash performance is also provided.

6.1 Hot Stamped Crush Tip Numerical Model

The 491 mm long tailor-welded hot stamped crush tip is comprised of a multi-gauge hot stamped 1.0 mm/1.2 mm Ductibor® 1000-AS main rail and enclosure panel, as well as several production components (Figure 205), some of which were re-worked as outlined in section 5.8. To mount the crush tips for testing, the non-impacted end of the mail rail and enclosure panel are MIG welded to a ½" thick steel plate. With the crush tip assembly mounted to this steel plate, a crash test setup can be designed such that the crash performance of the crush tip can be evaluated.

A schematic of the tailor-welded hot stamped crush tip setup plan is shown in Figure 218. In this test setup, the standard Seattle Safety crash sled vertical wall [85] is used, which has a sled assembly mass of 855 kg. The standard crash sled vertical wall is used over the vertical wall discussed in section 3.2.1 because there is not a risk of the specimen buckling and coming in contact with the honeycomb stacks during this test. A target sled speed of 51 km/hr is used to closely represent the baseline front end module test speed, discussed in section 0. A ¾" thick pine board is mounted to the front of the crash sled vertical wall to dampen measurement noise in the load cell data due to ringing. The tailor-welded hot stamped crush tip assembly is bolted to a load cell pack (3 load cells), located on the rigid wall, using four M12 bolts in each of its four corners. Honeycomb stacks are mounted to honeycomb standoffs, on either side of the crush tip assembly, to dissipate the excess kinetic energy of the crash sled that the test article does not absorb.

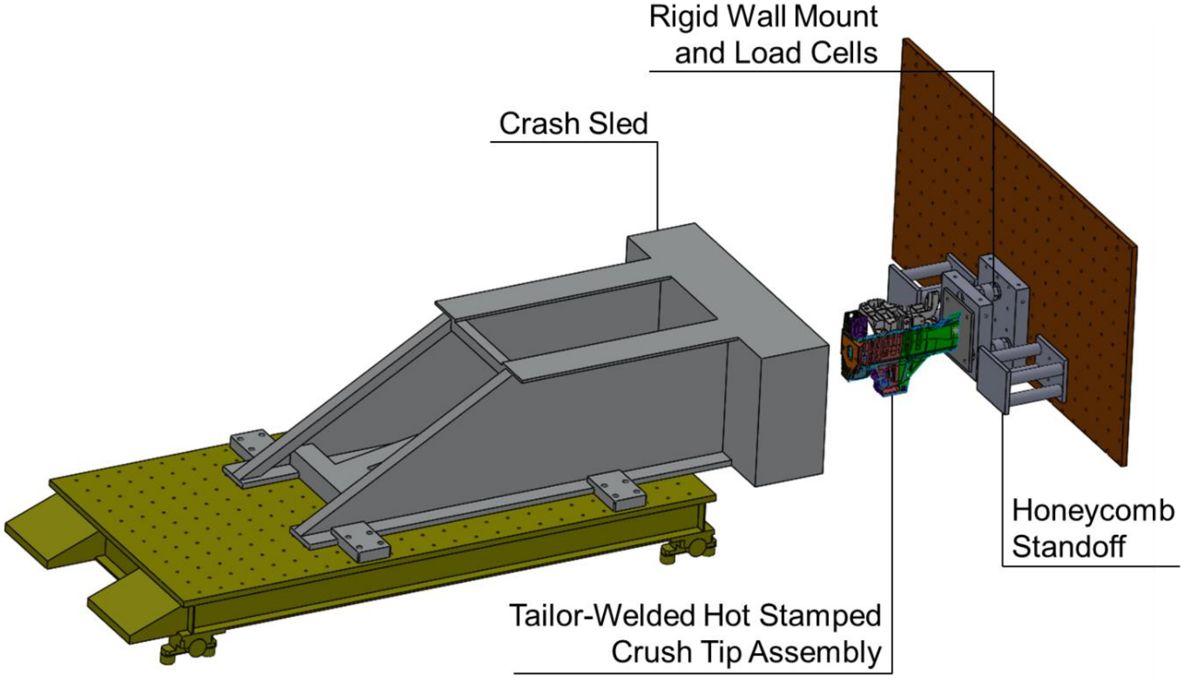

Figure 218. Schematic of the tailor-welded hot stamped crush tip crash test setup.

The test setup is numerically modelled to encompass all of the physical boundary conditions imposed on the tailor-welded hot stamped crush tip, as illustrated in Figure 219. Many of the modelled conditions, including the material properties, weld properties, as well as weld-on and bolt-on connections, remain the same as for the baseline and tailor-welded hot stamped front end module numerical models, described in sections 3.3 and 4.2, respectively. Therefore, only the modelling conditions that differ from the baseline and tailor-welded hot stamped front end module models will be discussed in this section.

The tailor-welded hot stamped crush tip only includes the first 491 mm, from the impacted end of the side frame member; therefore, the rigid reaction wall boundary condition (non-impacted end) must be changed. The MIG weld line between the non-impacted end of the tailor-welded hot stamped crush tip and the ½" thick steel mounting plate (modelled as linear elastic steel with solid elements) is modelled with the *TIED_NODES_TO _SURFACE_OFFSET contact definition. The selected tied nodes, representing the MIG weld line, around the perimeter of the main rail and enclosure panel at the non-impacted end, are highlighted with an orange line. The steel mounting plate is fixed, in all degrees of freedom, using the single point constraint (SPC) boundary condition on the side opposite the part, simulating a rigid wall. Crush force is measured from these constrained nodes, since this is where the load cell pack would be measuring force from in the crash test.

It is observed in Figure 219 that the last 65 mm of the battery base has been removed (red arrow) from the crush tip model. Removing this portion of the battery base does not affect the structural integrity of the component since the bolt-on locations remain unaffected by the trim line. This change to the battery base is however important because the battery base will be more likely to become wedged between the steel mounting plate and the crash sled, if it were full length.

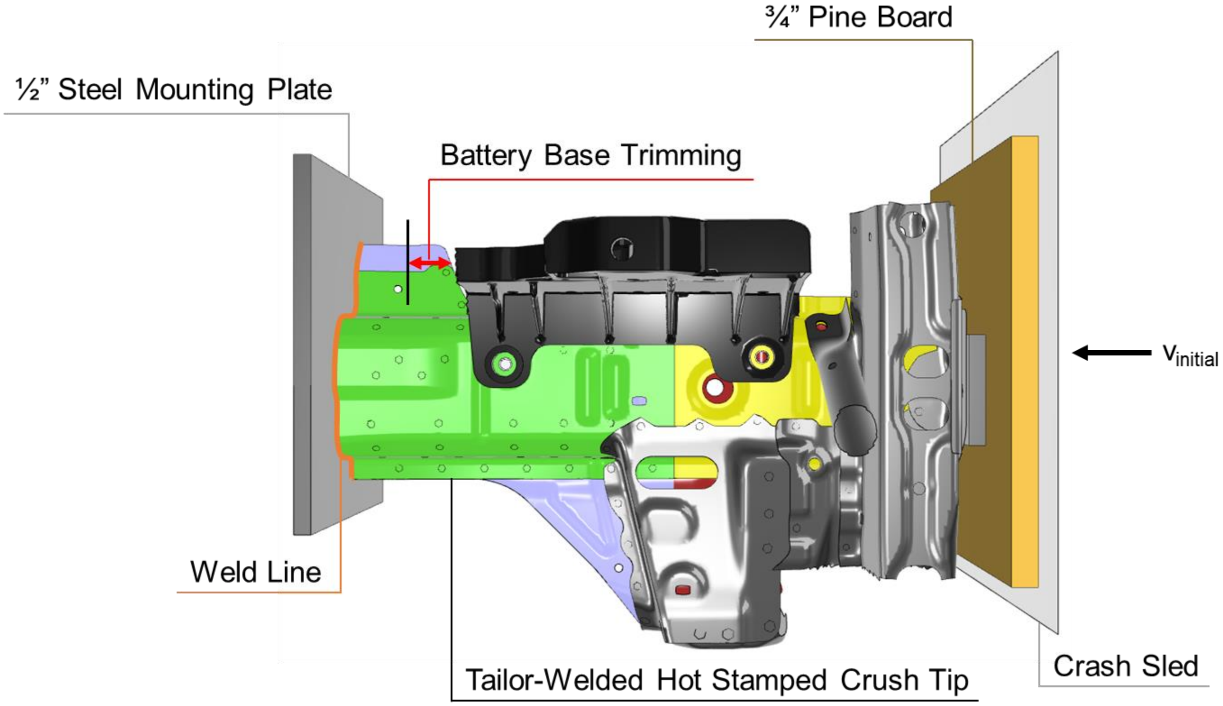

Figure 219. Numerical model setup for the tailor-welded hot stamped crush tips, shown from the inboard side view.

The crash sled is modelled as a rigid plate, comprised of type 2 shell elements, with a prescribed mass of 855 kg and an initial velocity of 51 km/hr. A ¾" pine board is modelled using *MAT_WOOD_PINE, as described in section 3.3.1, and is tied to the rigid crash sled plate using the *TIED_SURFACE_TO_SURFACE _OFFSET contact definition. In order to match the deceleration of the crash sled, honeycomb attenuation has been modelled with the *LOAD_RIGID_BODY load definition, as shown by the loads acting on the crash sled in Figure 220. The modelled honeycomb loads correspond to two stacked blocks, on both sides of the crush tip, one measuring 110 mm by 110 mm with a length of 100 mm, and the other measuring 220 mm by 220 mm with a length of 100 mm. A free crush distance of 145 mm is achieved with the modelled honeycomb configuration.

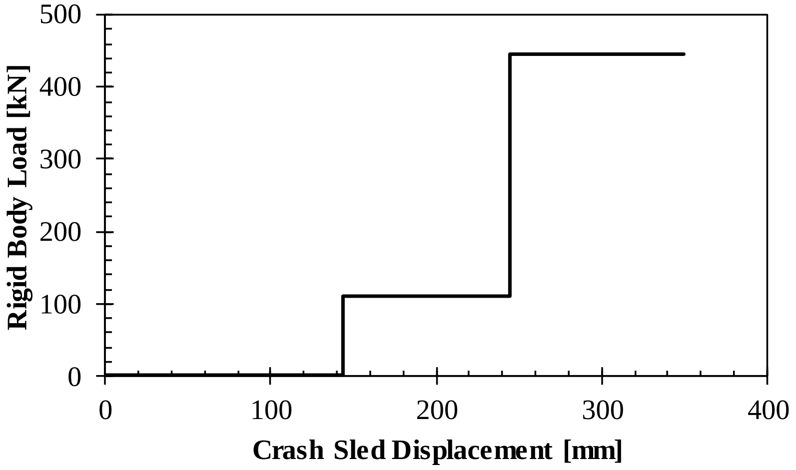

Figure 220. Rigid body load representing the load on the crash sled due to the honeycomb.

6.2 Effects of Forming History

The forming history of the main rail and enclosure panel parts was tracked during the hot stamping simulations (section 5.3), so that the effect that thinning has on the crash performance of the tailor-welded hot stamped crush tip could be evaluated. In this section the crash performance of the tailor-welded hot stamped crush tip, with and without the inclusion of hot stamping thinning predictions, are compared based on crush response and crush forces.

The crush response of the tailor-welded hot stamped crush tip, with and without the hot stamping simulation thinning predictions, are shown in Figure 221. In both of the configurations, the beginning of sequential folding is observed at 83 mm of crush distance, which is apparent from the out-in profile the deformed flange creates. With progression of the crush to 150 mm, the sequential folding continues and no flange unzipping is observed in either configuration. At 250 mm of crush distance, the crush tip section (yellow and red) is fully consolidated and the middle section (green and purple) begins to crush. Even with the crush tip section fully consolidated, desirable accordion type sequential folding is observed. Deformation is not shown past 250 mm of crush distance because the 491 mm long tailor-welded hot stamped crush tip begins to consolidate against the steel mounting plate past this crush distance, which skews the deformation and crush force predictions. Ultimately, it is observed from this figure that the inclusion of the thinning predictions does not have a significant impact on the crush response of the tailor-welded hot stamped crush tip. A small difference is observed at 250 mm of crush distance, in which the simulation with thinning predictions included has more folding occurring in the middle section (green and purple). The additional folding in the middle section is attributed to higher thinning observed in the fold initiators on the 1.2 mm Ductibor® 1000-AS enclosure panel middle section, as seen in section 5.7.

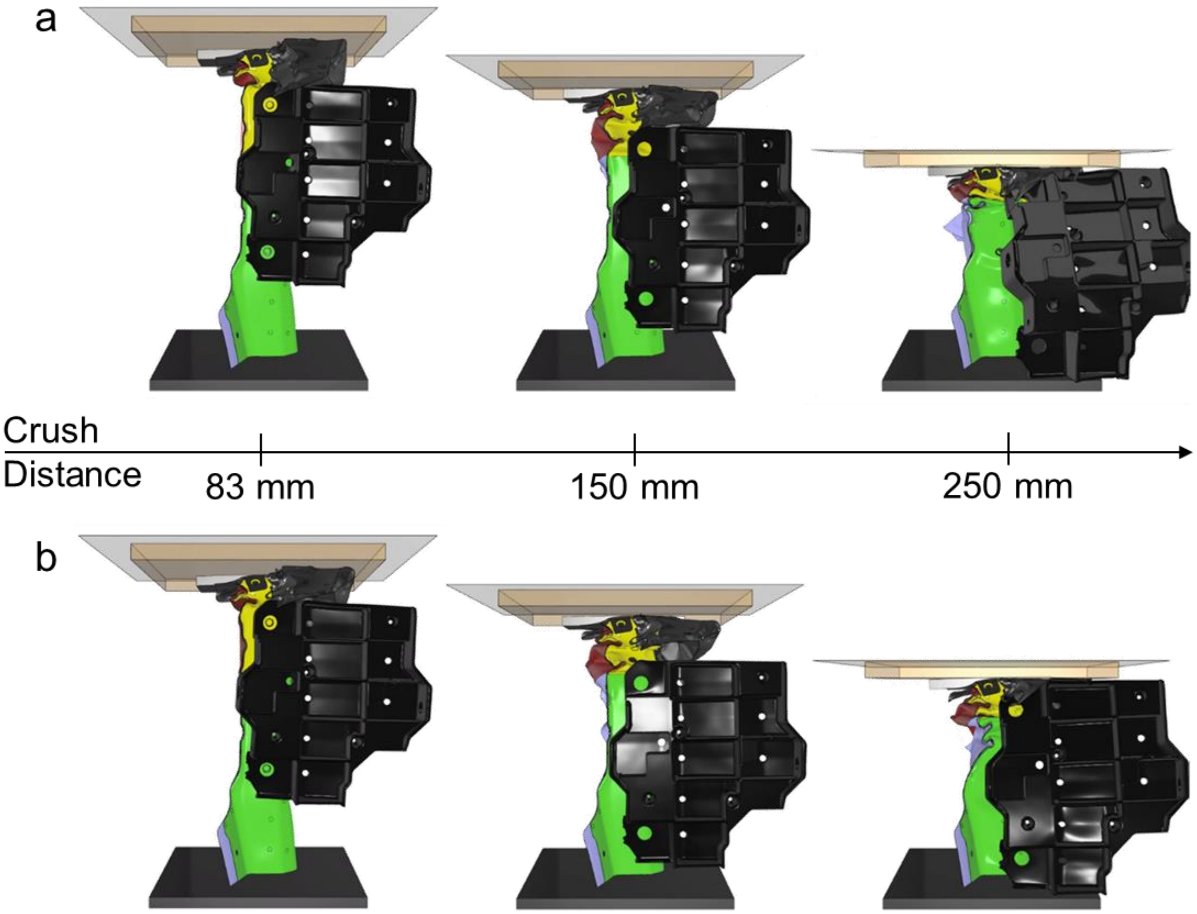

Figure 221. Predicted crush response, shown from the top view, of the tailor-welded hot stamped crush tip **(a)** without the inclusion of thinning predictions (Trial 4019) and **(b)** with the inclusion of thinning predictions (Trial 4103).

In order to better observe the folding behaviour of the tailor-welded hot stamped crush tip, with and without thinning predictions included, the predicted deformation is also shown from the outboard isometric view (Figure 222). It is again observed that the initiation of sequential folding occurs at 83 mm of crush distance, which continues to progress to accordion style sequential folding at 150 mm and 250 mm of crash sled crush distance for both crush tip configurations. In observing this view of the crush tip it is important to note that no catastrophic spot weld flange unzipping occurs during the sequential folding of the crush tip section in either of the configurations.

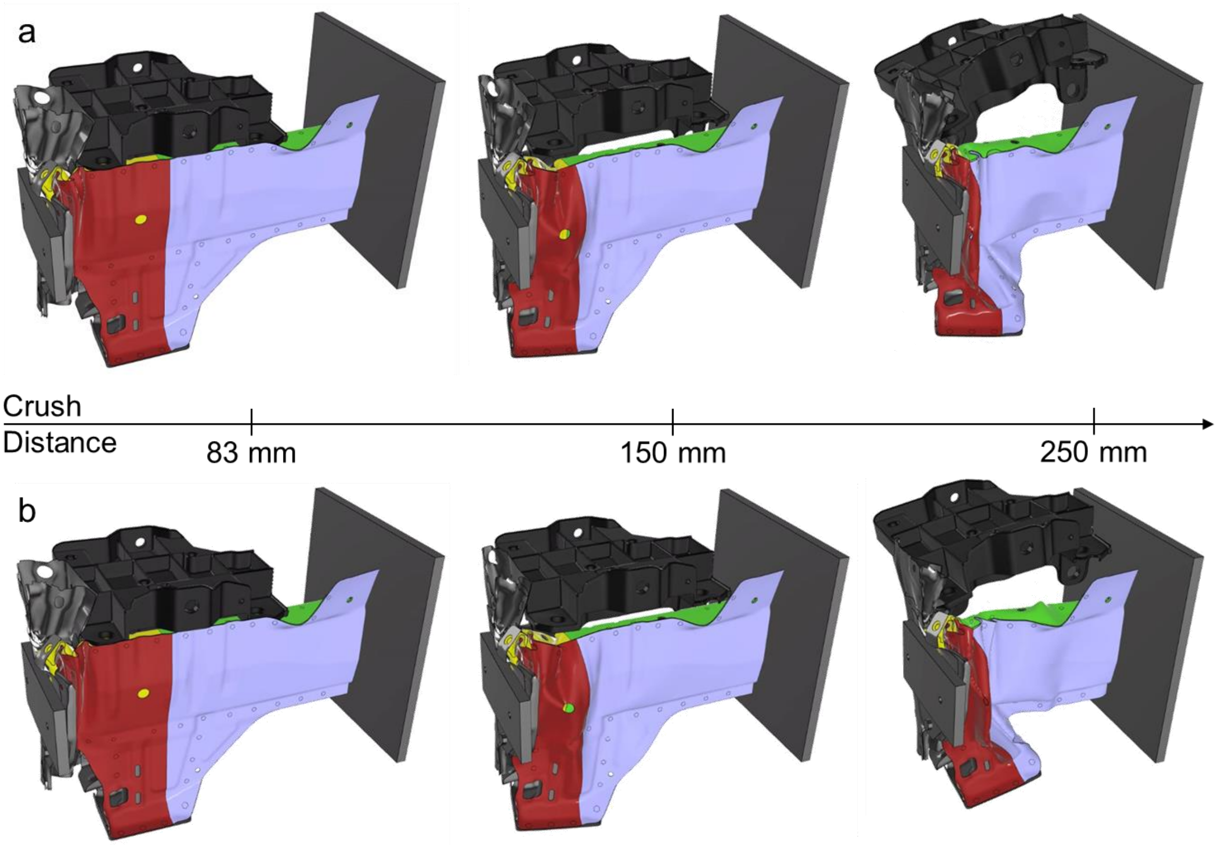

Figure 222. Predicted crush response, from the outboard isometric view, of the tailor-welded hot stamped crush tip **(a)** without the inclusion of thinning predictions (Trial 4019) and **(b)** with the inclusion of thinning predictions (Trial 4103).

The crush forces, determined from the reaction forces associated with the single point constraints (SPCs) located on the rigid reaction wall (non-impacted end) side of the steel mounting plate, for the tailor-welded hot stamped crush tip, with and without thinning predictions, are shown in Figure 223. It is observed in this figure that the crush forces are almost identical (with respect to general trend, peak forces and average force) up to 250 mm of crush distance for both crush tip configurations. After 250 mm of crush distance the crush forces deviate; however, this is not concerning because after this crush distance the crush tip begins to consolidate against the steel mounting plate, which changes the crush response, leading to skewed crush force predictions. In addition, at approximately 250 mm of crush distance, the large (220 mm by 220 mm) honeycomb is engaged, which rapidly decelerates the crash sled and reduces the strain rate on the structure.

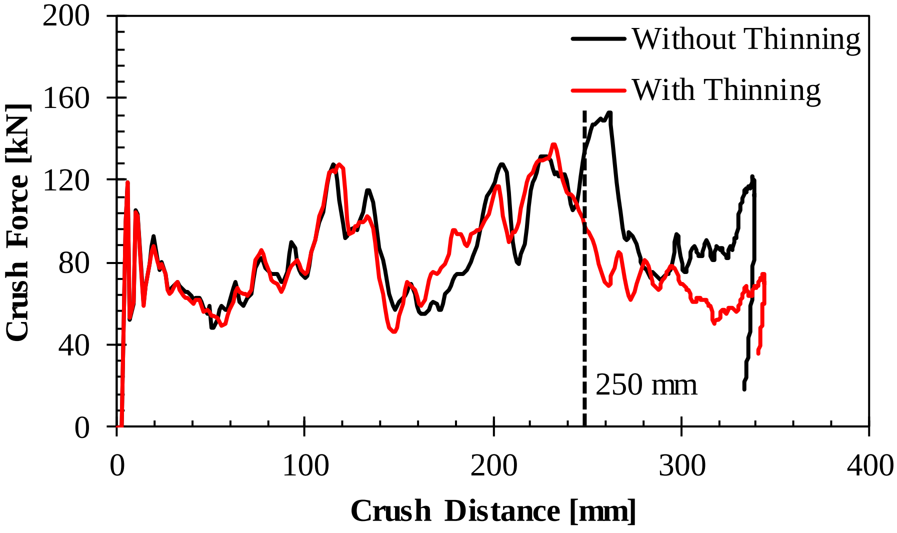

Figure 223. Predicted crush force of the tailor-welded hot stamped crush tip with (Trial 4103) and without thinning predictions (Trial 4019) accounted for.

The presented crush response and crush force predictions show that including the hot stamping simulation thinning predictions do not have a significant impact on the crash performance of the tailor-welded hot stamped crush tip. This result is not particularly surprising since the thickness change during forming is relatively low and largely confined to fold initiator locations. Future work should consider mapping of forming thickness changes on the entire side frame member (including the S-rail section).

6.3 Crash Performance Evaluation

The crash performance of the tailor-welded hot stamped crush tip, with thinning predictions included, is numerically evaluated against the baseline front end module (Bd-6 and Trial 1710), as well as the tailor-welded hot stamped side frame member (Trial 3920), within the front end module. Predications from the forming history study (section 6.2) showed that the tailor-welded hot stamped crush tip begins to consolidate between the crash sled and steel mounting plate at 250 mm of crash sled crush distance. It was observed that consolidation of the crush tip onto the mounting plate skews the crush response and crush force predictions obtained; therefore, evaluation of the tailor-welded hot stamped crush tip will only be considered up to 250 mm of crash sled crush distance.

The tailor-welded hot stamped crush tip is evaluated for crush response, particularly the consolidation of the crush tip section, velocity history, total crush force and extent of spot weld failure. Due to the shortened length of the tailor-welded hot stamped crush tip, relative to the full-length side frame member, buckle deformation modes in front and behind the shock tower support cannot be evaluated. In addition, the final crush distance and occupant compartment intrusion resistance cannot be assessed because of the shortened length of the crush tip.

6.3.1 Crush Response

The crush response of the tailor-welded hot stamped crush tip is shown alongside the baseline front end module and tailor-welded hot stamped side frame member in Figure 224. It is observed that controlled sequential folding is achieved as the crush tip consolidates in each of the model configurations shown. Though tighter radius folds are present in the baseline side frame member crush tip, the overall mode of consolidation in the tailor-welded hot stamped configurations are almost identical.

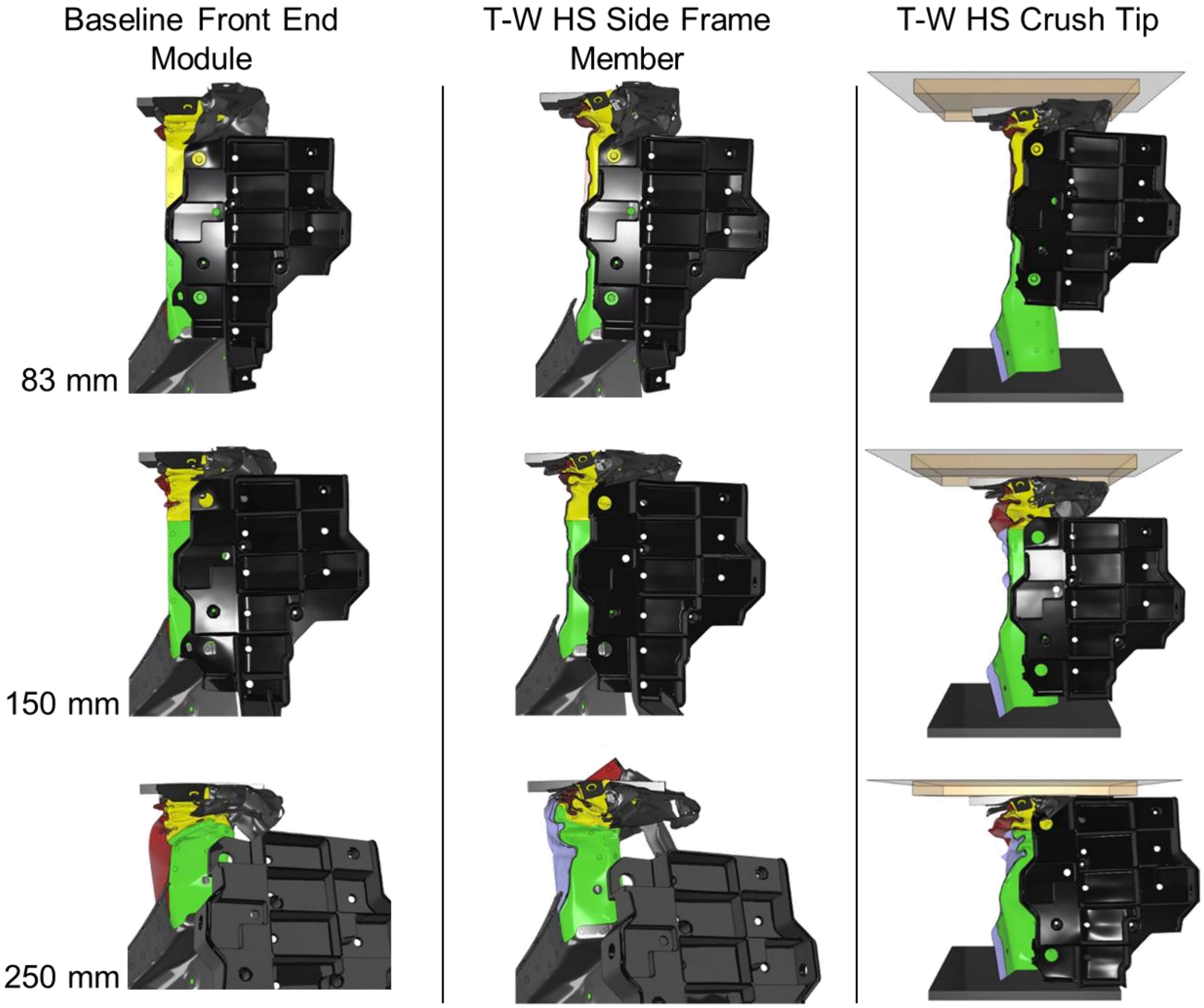

Figure 224. Predicted crush response of the tailor-welded hot stamped crush tip (Trial 4103) compared to the baseline front end module (Trial 1710) and tailor-welded hot stamped side frame member (Trial 3920), shown in the top view.

Parent metal fracture in the tailor-welded hot stamped crush tip is best visualized from contours of the maximum through thickness damage parameter (Figure 225). It is observed that there are very few locations at which the damage parameter is greater than 1 (red), which implies that parent material cracking is confined to local fold regions within the crush tip. In addition, catastrophic fracture propagation is not observed in the Ductibor® 1000 crush tip. It should be noted that at least 70% of the through thickness integration points must reach a damage parameter value of unity for an element to be deleted; therefore, locations of red contours do not necessarily imply that fracture initiates.

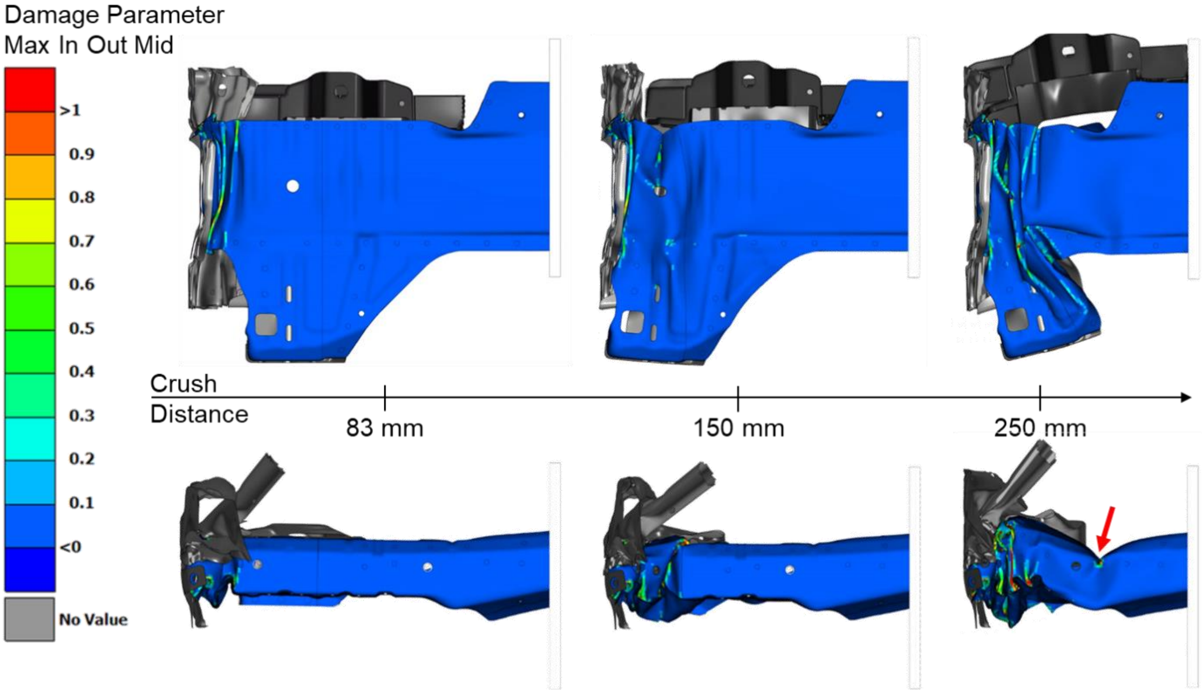

Figure 225. Maximum damage parameter contoured on the tailor-welded hot stamped crush tip (Trial 4103), shown from the outboard side view (top) and top view (bottom).

6.3.2 Velocity History

The predicted velocity history of the sled impacting the tailor-welded hot stamped crush tip is shown in Figure 226 and is compared to the velocity histories from the baseline front end module test (Bd-6) and model (Trial 1710), as well as the tailor-welded hot stamped side frame member model (Trial 3920). It is observed that up to 250 mm of crash sled crush distance, the velocity history of the tailor-welded hot stamped crush tip is almost identical to the baseline front end module and tailor-welded hot stamped side frame member. The velocity history is well within the ± 10% tolerance outlined in the design specification (Table 3). After 250 mm of crush distance the velocity history of the tailor-welded hot stamped crush tip deviates from the full-length structures. This deviation in velocity history is in part due to the activation of large honeycomb blocks (220 mm by 220 mm) to rapidly decrease the crash sleds kinetic energy, but is also due to the consolidation of the crush tip between the crash sled and steel mounting plate.

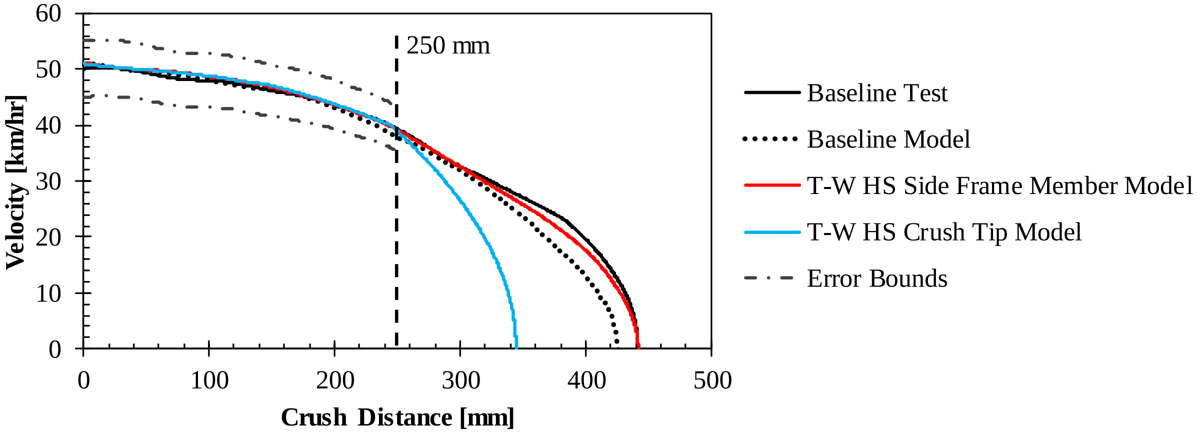

Figure 226. Velocity history for the baseline front end module test (Bd-6) and model (Trial 1710), tailor-welded hot stamped side frame member model (Trial 3920) and the tailor-welded hot stamped crush tip model (Trial 4103).

6.3.3 Crush Force

The total and total average crush forces are shown for the tailor-welded hot stamped crush tip, baseline front end module and tailor-welded hot stamped side frame member in Figure 227. It is observed that up to 250 mm of crash sled crush distance, the crush force histories for each configuration are very similar. The average total crush force of the tailor-welded hot stamped crush tip, tailor-welded hot stamped side frame member and baseline front end module are 87 kN, 86 kN and 108 kN, respectively. These values correspond to a 19% difference in average crush force between the tailor-welded hot stamped crush tip and baseline front end module, and a 1% difference in average crush force between the tailor-welded hot stamped crush tip and tailor-welded hot stamped side frame member, which are both within the ± 20% average crush force tolerance. The lower average force, which is observed in both the tailor-welded hot stamped side frame member and crush tip are attributed to the fact that many fold initiators are incorporated into the hot stamped designs, which are known to decrease peak forces in crush structures.

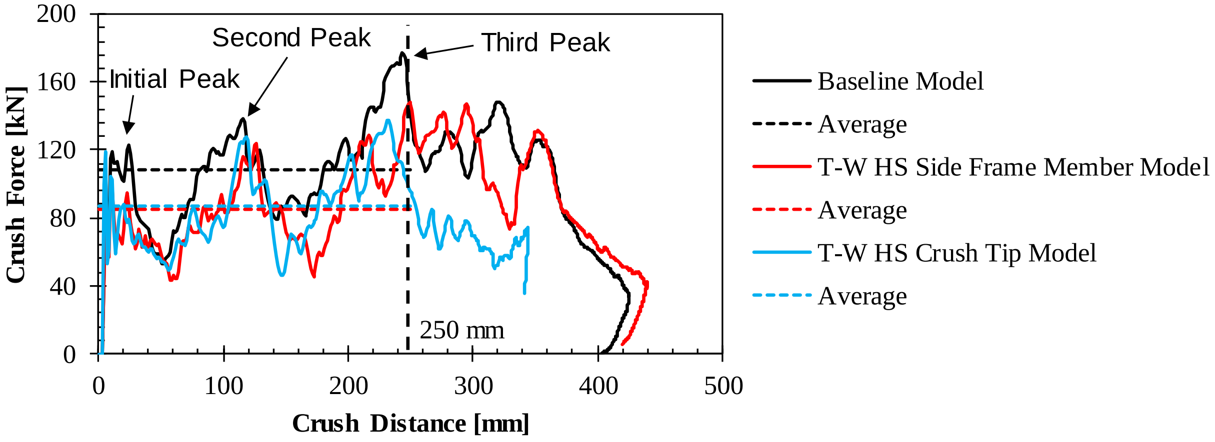

Figure 227. Predicted total force and average total force from the baseline front end module model (Trial 1710), the tailor-welded hot stamped side frame member model (Trial 3920) and the tailor-welded hot stamped crush tip model (Trial 4103).

The magnitudes of the three peak force locations of interest (pointed out with arrows in Figure 227) are plotted in Figure 228. In addition, the percent error for the baseline front end module compared to the tailor-welded hot stamped crush tip (values with arrows pointing the respective columns) and the tailor-welded hot stamped side frame member compared to the tailor-welded hot stamped crush tip (values inside of boxes) are also shown in Figure 228. In comparing the baseline front end module to the tailor-welded hot stamped crush tip it is observed that the peak forces match well with the exception of the third peak force, in which the tailor-welded hot stamped crush tip has a peak force 22% less than the baseline front end module. Comparing the tailor-welded hot stamped side frame member to the crush tip it is also observed that the peak force error is the highest at the third peak, in which the peak force predicted by the crush tip is 13% less than that of the tailor-welded hot stamped side frame member. The peak force is lower in the tailor-welded hot stamped crush tip at the third peak due to the plastic hinge that forms at approximately 250 mm of crash sled crush distance on the inboard side of the tailor-welded hot stamped crush tip, as shown in Figure 225 (red arrow). The formation of the plastic hinge transforms the crush response from a high energy absorbing sequential folding to a lower energy absorbing buckle-dominant response. This plastic hinge is trigger at a fold initiator and its severity is attributed to the shortened length of the crush tip and rigid mounting on the impact wall.

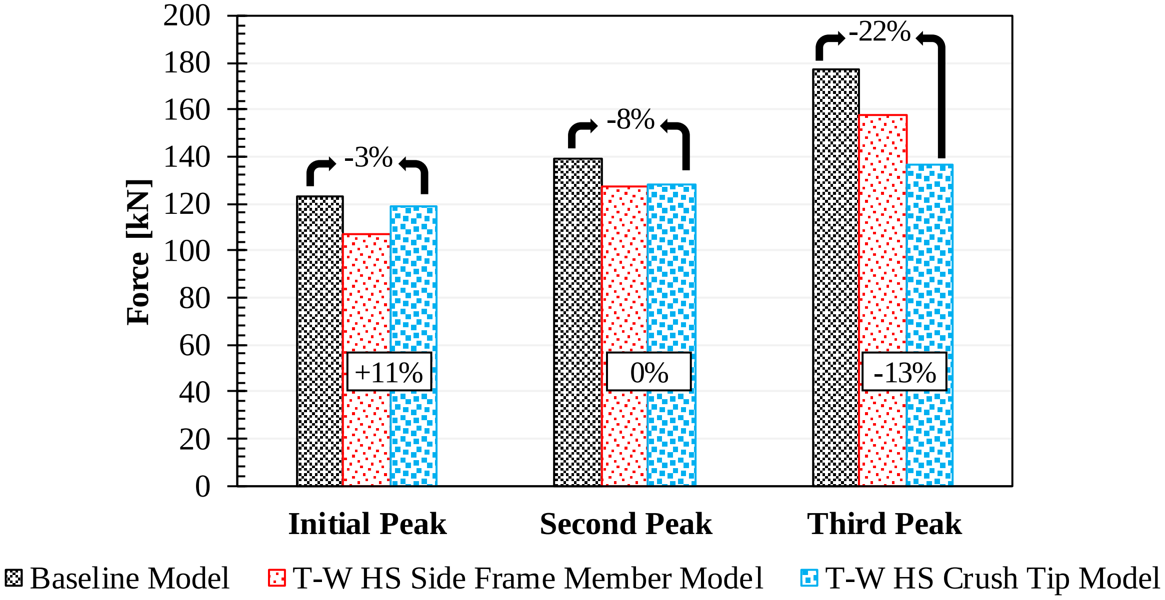

Figure 228. Predicted peak forces and associated percent error from the baseline front end module model (Trial 1710), the tailor-welded hot stamped side frame member model (Trial 3920) and tailor-welded hot stamped crush tip model (Trial 4103).

6.3.4 Extent of Spot Weld Failure

The location and number of spot weld failures along the top and bottom flange for the baseline front end module, tailor-welded hot stamped side frame member and crush tip are shown in Figure 229. Through monitoring the failure parameter, up to 250 mm of crash sled crush distance, it is observed that in the tailor-welded hot stamped crush tip 2 two additional spot welds initiate failure (1 more in the upper and lower flange) compared to the baseline front end module and 2 less spot welds initiate failure (2 less in the upper flange) occur than the tailor-welded hot stamped side frame member. The fact that fewer spot weld failures are observed in the upper flange of the tailor-welded hot stamped crush tip than in the tailor-welded hot stamped side frame member is likely due to the fact that only the first 250 mm of crush distance are considered when determining spot weld failures.

The crush response of the tailor-welded hot stamped crush tip is shown in Figure 230 from the outboard isometric view. It is observed in this figure that accordion-style sequential folding dominates the crush response of the crush tip. Furthermore, it is observed that the spot weld flanges of the crush tip maintain a controlled crush response, even though spot weld failures are occurring. Due to the fact that a controlled response is obtained, without spot weld flange "unzipping" occurring, it can be concluded that the spot weld failures that do occur are of low severity and do not cause catastrophic failure to the structure.

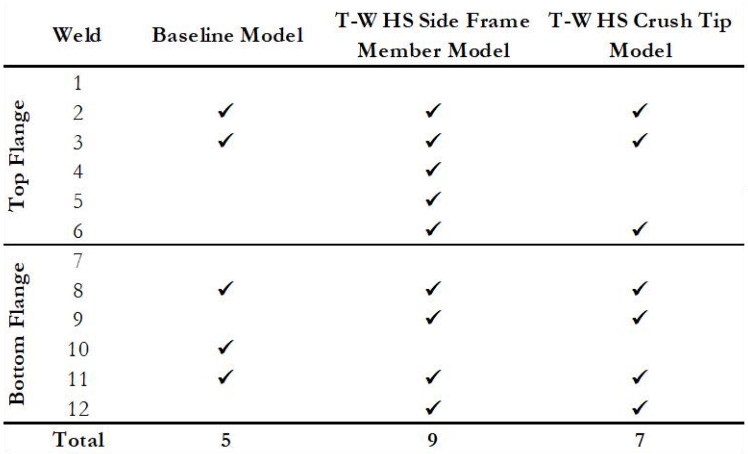

	Weld	Baseline Model	T-W HS Side Frame Member Model	T-W HS Crush Tip Model
Top Flange	1			
	2	✓	✓	✓
	3	✓	✓	✓
	4		✓	
	5		✓	
	6		✓	✓
Bottom Flange	7			
	8	✓	✓	✓
	9		✓	✓
	10	✓		
	11	✓	✓	✓
	12		✓	✓
	Total	5	9	7

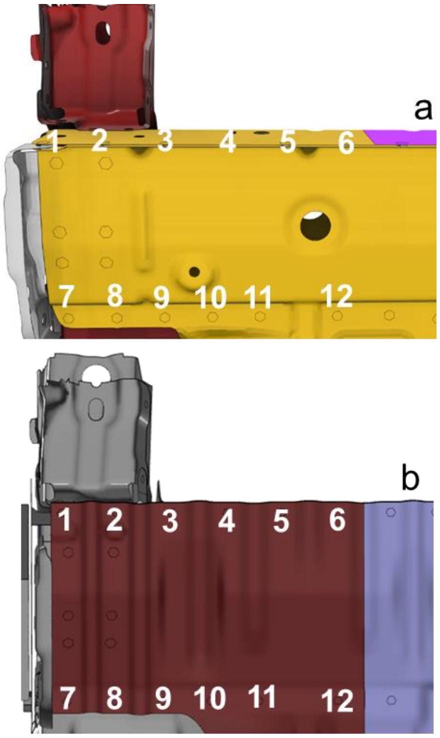

Figure 229. Predicted spot weld failure location and quantity occurring (monitored with the failure parameter) in the **(a)** baseline, **(b)** tailor-welded hot stamped side frame member and crush tip configurations.

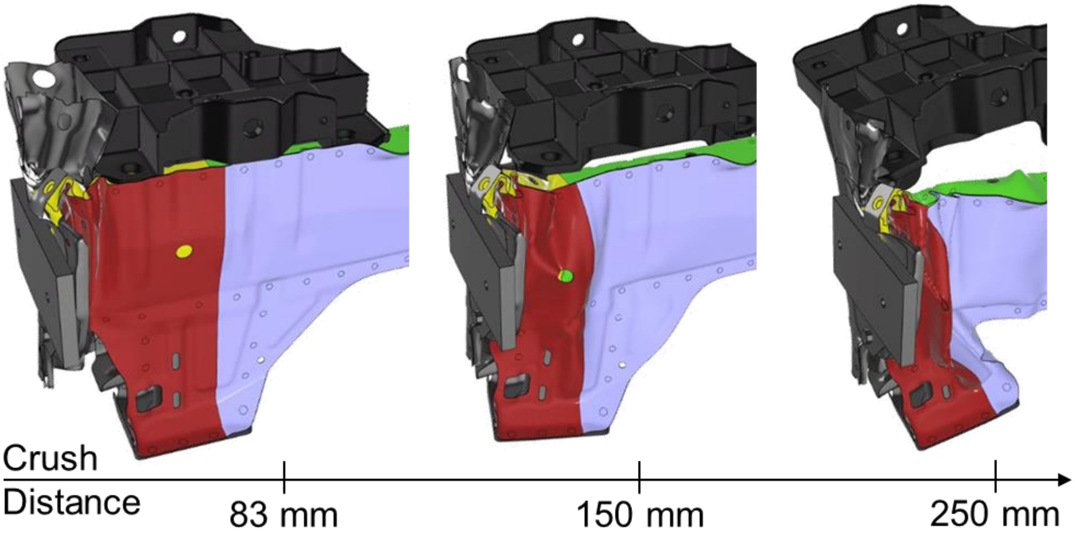

Figure 230. Outboard isometric view of the tailor-welded hot stamped crush tip demonstrating the low severity of spot weld failures.

6.3.5 Evaluation Summary

The crash performance of the proposed 491 mm long tailor-welded hot stamped crush tip is compared to the accepted baseline front end module (Bd-6 and Trial1710) and the tailor-welded hot stamped side frame member model (Trial 3920), as shown in Table 16. It is observed that the tailor-welded hot crush tip meets each of the design criteria, except for the peak force requirement, spot weld failure locations and total number of spot welds occurring in the crush tip section flanges.

Table 16. Evaluation of the proposed tailor-welded hot stamped crush tip, using the design specifications.

	Qualitative Quantitative	Target	Upper Bound	Lower Bound	T-W HS Crush Tip
Crush Response					
Consolidation of crush tip (Fig. 56)	Qualitative	Match	-	-	✓
Parent material fracture severity	Qualitative	Minimize	-	-	✓
Vehicle Decleration					
Velocity history	Quantitative	Match	+ 10%	- 10%	✓
Crush Forces					
Total Force (TF) - global trend	Qualitative	Match	-	-	✓
TF - peak forces (1st, 2nd, 3rd)	Quantitative	Match	+ 15%	- 15%	
TF - average force	Quantitative	Match	+ 20%	- 20%	✓
Extent of Spot Weld Failure					
Weld locations	Quantitative	Match	-	-	
Quantity	Quantitative	Match	-	-	
Severity	Qualitative	Minimize	-	-	✓

The peak force requirement is not met for the tailor-welded hot stamped crush tip when considering the third peak force location of interest. The third peak force occurs at approximately 250 mm of crash sled crush distance, which is the useful crush length of the tailor-welded hot stamped crush tip. After this amount of crush distance the large honeycomb block rapidly decreases the sleds kinetic energy and the crush tip begins to consolidate fully between the steel mounting plate and crash sled, skewing the crush response and force predictions. The initial and second peak forces are, however, well within the error tolerance; thus, it is suggested that the third peak not be considered during the tailor-welded crush tip evaluation, due to its occurrence at 250 mm of crush distance, which is the threshold of useful data.

The extent of spot weld failure does not meet the design requirement; however, the extent of spot weld failure is considered to be controlled and spot weld flange "unzipping" is not observed. Using hot stamped UHSS in crash applications it is difficult to avoid spot weld failure completely due to the heightened strength of the materials, thus subjecting the spot welds to greater loads. It is therefore deemed that a more important metric for spot weld failure is the effect a spot weld failure has on the structural integrity of the welded assembly. If for example, controlled sequential folding is observed after a spot weld failure, then the structural integrity of the welded assembly is not compromised and the weld failure severity is considered insignificant. Since the weld failures that occurred in the tailor-welded hot stamped side frame member had a low impact on the structural integrity of the welded assembly, it is considered to meet the spot weld failure criteria.

Ultimately, the tailor-welded hot stamped crush tip provides a far more simplified means (compared to the full-length side frame member) of evaluating the frontal crash performance of Ductibor® 1000-AS, within an actual automotive structure. Much of the difficulty with implementing hot stamped UHSS into frontal crush structures stem from parent metal fracture and spot weld failure. Though the tailor-welded hot stamped crush tip cannot be used to evaluate the intrusion resistance potential of Usibor® 1500-AS in the S-rail section of the side frame member, it can be used to evaluate parent metal fracture resistance, crush force and spot weld failure severity during crush. It is therefore concluded that the tailor-welded hot stamped crush tip is a suitable simplification to the tailor-welded hot stamped side frame for evaluating the front crash performance of Ductibor® 1000-AS in a realistic automotive structure.

Chapter 7 – Discussion, Conclusions & Recommendations

7.1 Discussion

The current work has increased our understanding of the potential to utilize hot stamped Ductibor® 1000-AS sheet within automotive front end crush applications. The scenario examined considered only full-frontal crash and a range of other load cases need to be considered. The current thesis closes with conclusions based on simulation studies, with some actual component hot stamping validation. The larger project within which this project is supported will continue, with fabrication and testing of the crush tip assembly presented in Chapter 6.

Hot stamped materials, such as Ductibor® 1000-AS (1000 MPa strength) and Usibor® 1500-AS (1500 MPa strength), are demonstrated to be potential replacements for JAC590R (590 MPa strength) in the commercial SUV side frame member axial crush and anti-intrusion zones, respectively. The increased strength level of these hot stamped materials over the current production JAC590R material allows for considerable sheet thickness down-gauging, which corresponds to a 27.6% (2.1 kg) weight reduction. Though significant weight savings are demonstrated through implementing the hot stamped materials into the side frame member, it has been shown in this thesis that a great deal of effort must also be devoted to designing the crush tip spot weld flanges and fold initiators so that the crush response and extent of spot weld failure are acceptable.

The balance of this section presents a number of discussion points and comparisons to previous work. Conclusions stemming from this research and recommendations for future research follow.

7.1.1 Comparison of Baseline Front End Module to Prior Crush Tip Results

It is of interest to compare the test results from the baseline front end modules to the production JAC590R crush tip sections tested by Peister [19]. The crush tip sections tested by Peister (Figure 231a) were , 340 mm long and were plasma cut from the same production JAC590R side frame member that the baseline front end module is fabricated from. A crash sled initial velocity of 27.1 km/hr with a sled mass of 855 kg was used for the crush tips, which is much less than the 51 km/hr used in the baseline front end module tests. It is observed that the front bulkhead structure, battery base and end plate used in the baseline front end module tests (Figure 231b) were not included in the crush tip sections.

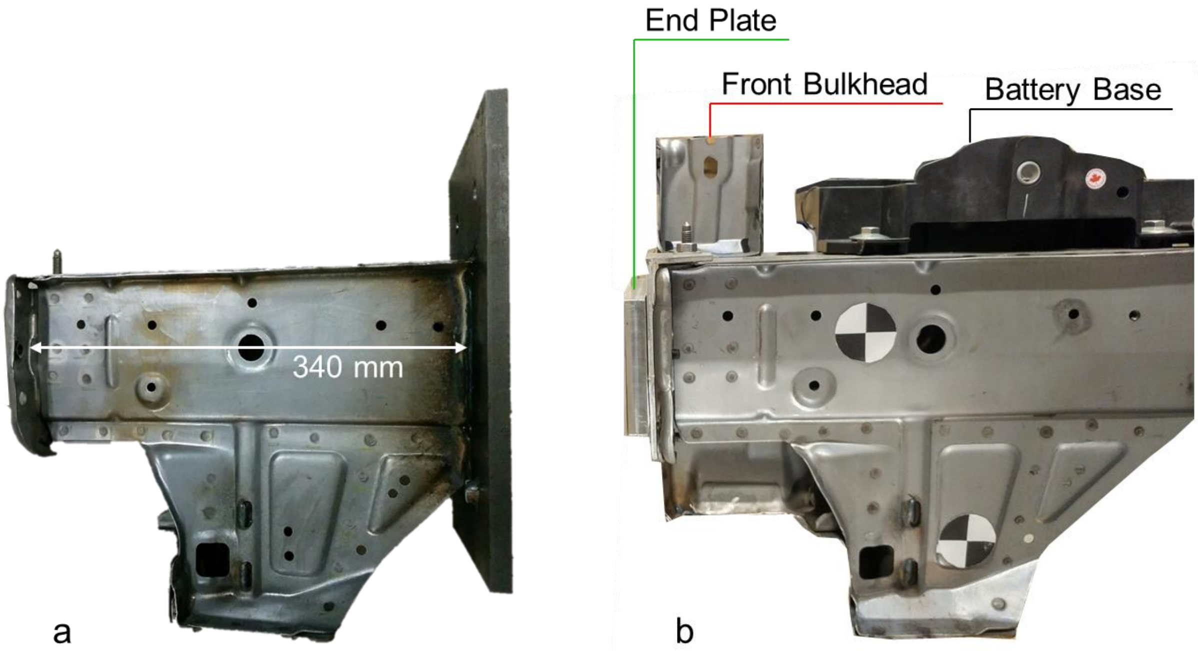

Figure 231. (a) Production JAC590R crush tips test by Peister [19] compared to the **(b)** baseline front end module, with production JAC590R side frame member.

In Figure 232 the measured crush forces from the baseline front end module tests (Bd-1, Bd-5, Bd-4, Bd-2, Bd-3, Bd-10 and Bd-9) and the average of all these tests are compared to the 5 left-hand JAC590R crush tips and their average, tested by Peister [19]. Note that the results from test Bd-7 are not included due to outlier force measurements, as well the results from test Bd-6 are not included due to missing load cell data. It is observed from the average crush forces that the global trend is relatively similar and definitely within the experimental scatter from both test series. The initial peak forces are 133 kN (at 29 mm of crush distance) and 120 kN (at 19 mm of crush distance) for the baseline front end module and crush tip, respectively.

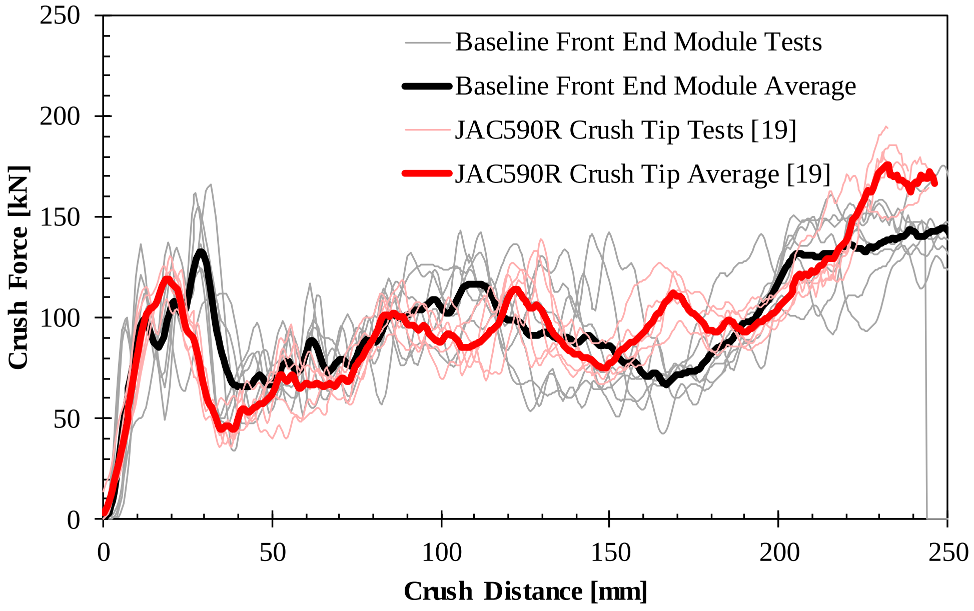

Figure 232. Crush forces from baseline front end module tests (Bd-1, Bd-5, Bd-4, Bd-2, Bd-3, Bd-10 and Bd-9) and their average compared to the 5 left-hand JAC590R crush tip sections, tested by Peister [19], and their average.

In Figure 233 the deformation of the crush tip sections at 120 mm of crash sled crush distance from the baseline front end module are compared to the crush tips tested by Peister [19] and to the crush tip section from the SUV model. A representative baseline front end module test from each end plate configuration has been selected to demonstrate the difference in crush modes achieved. Note that Bd-7, which used the 1” thick end plate is not included because the crush tip section was not captured by the outboard side view high speed camera. Specimen Bd-4 is representative of the tests that did not include an end plate, its crush response showed very little sequential folding. Specimen Bd-9 used the wedge shaped end plate and its crush response demonstrated very tight radius sequential folding. Bd-6 used the ½” thick end plate and demonstrates the closest crush tip section crush response to the SUV model, since it has relatively loose radius sequential folding. The crush tips tested by Peister show very tight radius sequential folding, which is not seen in the SUV model response.

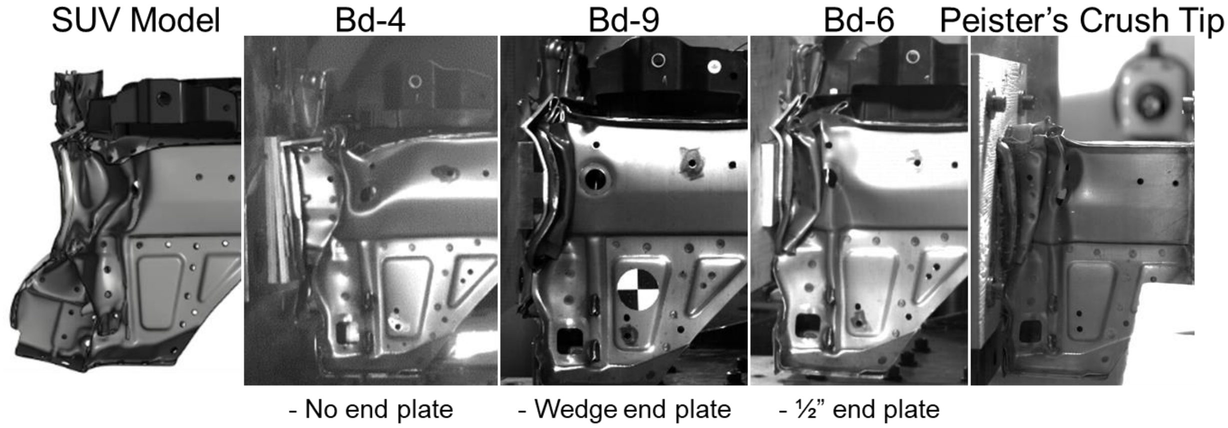

Figure 233. Deformation of the crush tip sections at 120 mm of crash sled crush distance from the baseline front end module tests with one of each end plate configurations (Bd-7 with the 1" thick end plate is excluded), the crush tips tested by Peister [19] and the SUV model.

7.1.2 Comparison of Ductibor® 1000-AS Crush Tips to Prior Crush Tip Results

The goal of this thesis is to determine the suitability of using Ductibor® 1000-AS in frontal crash applications. In light of this goal it is important to compare the crash performance of the tailor-welded hot stamped Ductibor® 1000-AS crush tips proposed in Chapter 6 to the tested JAC590R and modelled Ductibor® 500-AS crush tips due to Peister [19].

It is important to note some of the difference between the crush tip sections, test setups and modelling conditions used by the author of this thesis and those used by Peister. The tailor-welded hot stamped Ductibor® 1000-AS crush tips were modelled using a crash sled impact velocity of 51 km/hr, while those studied by Peister used an impact velocity of 27.1 km/hr. A length of 491 mm is used for the Ductibor® 1000-AS crush tip model, with the inclusion of the battery base, front bulkhead and end plate, as demonstrated in Figure 234b. The crush tips tested and modelled by Peister are 340 mm in length and do not include these additional components (Figure 234a). Figure 234 also compares the sheet material thicknesses between the JAC590R and Ductibor® 500-AS crush tips tested and modelled by Peister, to the tailor-welded hot stamped Ductibor® 1000-AS crush tips.

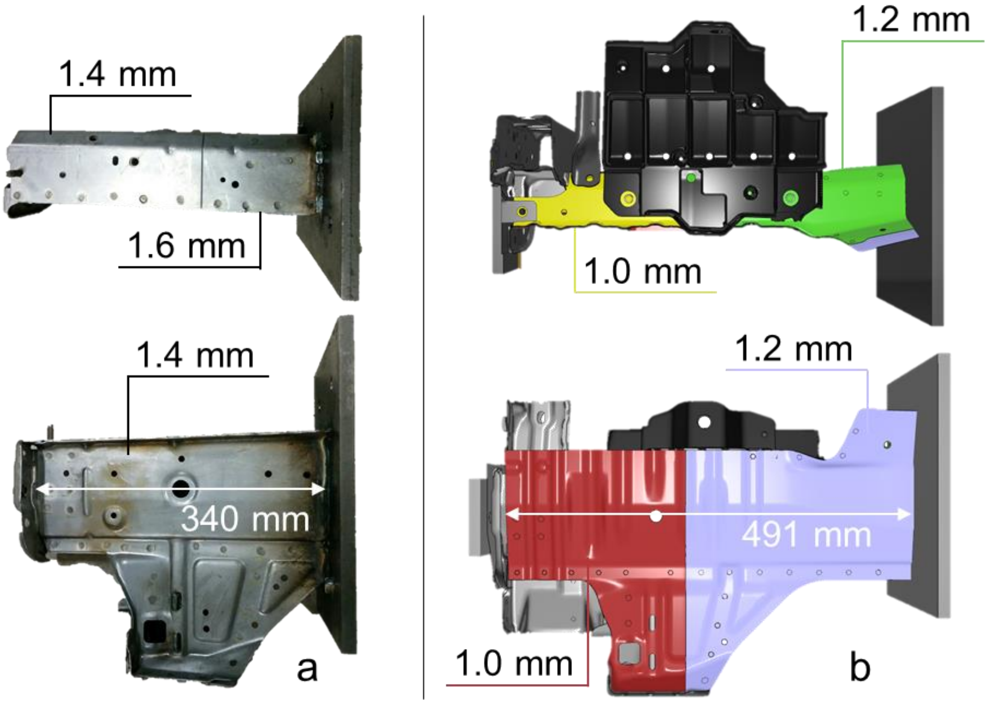

Figure 234. Comparison of the length, sheet material thicknesses and included parts between the **(a)** Peister's [19] tested JAC590R and modelled Ductibor® 500-AS crush tips, as well as the **(b)** modelled tailor-welded hot stamped Ductibor® 1000-AS crush tips.

The crush force and energy absorption for the modelled Ductibor® 1000-AS crush tips, the tested JAC590R crush tips and their combined average, as well as the modelled Ductibor® 500-AS crush tips are shown in Figure 235. It is observed that the global trend of the crush forces and energy absorptions correlate well with one another up to approximately 200 mm of crash sled crush distance. After 200 mm of crush distance the loads increase quite rapidly for the shorter crush tips (JAC590R and Ductibor® 500-AS) tested and modelled by Peister. The abrupt increase in crush force demonstrated by Peister's crush tips at 200 mm of crush distance is attributed to consolidation of the specimen between the crash sled and mounting plate. The crush tip specimen used by Peister are 151 mm shorter than the Ductibor® 1000-AS crush tip and will therefore consolidate earlier than the Ductibor® 1000-AS crush tip.

The initial peak forces for the Ductibor® 1000-AS, JAC590R and Ductibo® 500-AS crush tips are 114 kN, 119 kN and 128 kN, respectively, which are relatively similar in magnitude. The crush distance corresponding to the initial peak force, however is 13 mm different between the Ductibor® 1000-AS crush tips and those tested and modelled by Peister. The difference in peak force location is attributed to the fact that the crush tips tested by Peister did not have an end plate or battery base bolted on, nor did they include a front bumper beam extension plate, which would both serve to stiffen the impacted end, causing the peak force to more rapidly develop. The total energy absorption for the Ductibor® 1000-AS, JAC590R and Ductibor® 500-AS crush tips are 21 kJ, 23 kJ and 26 kJ, respectively.

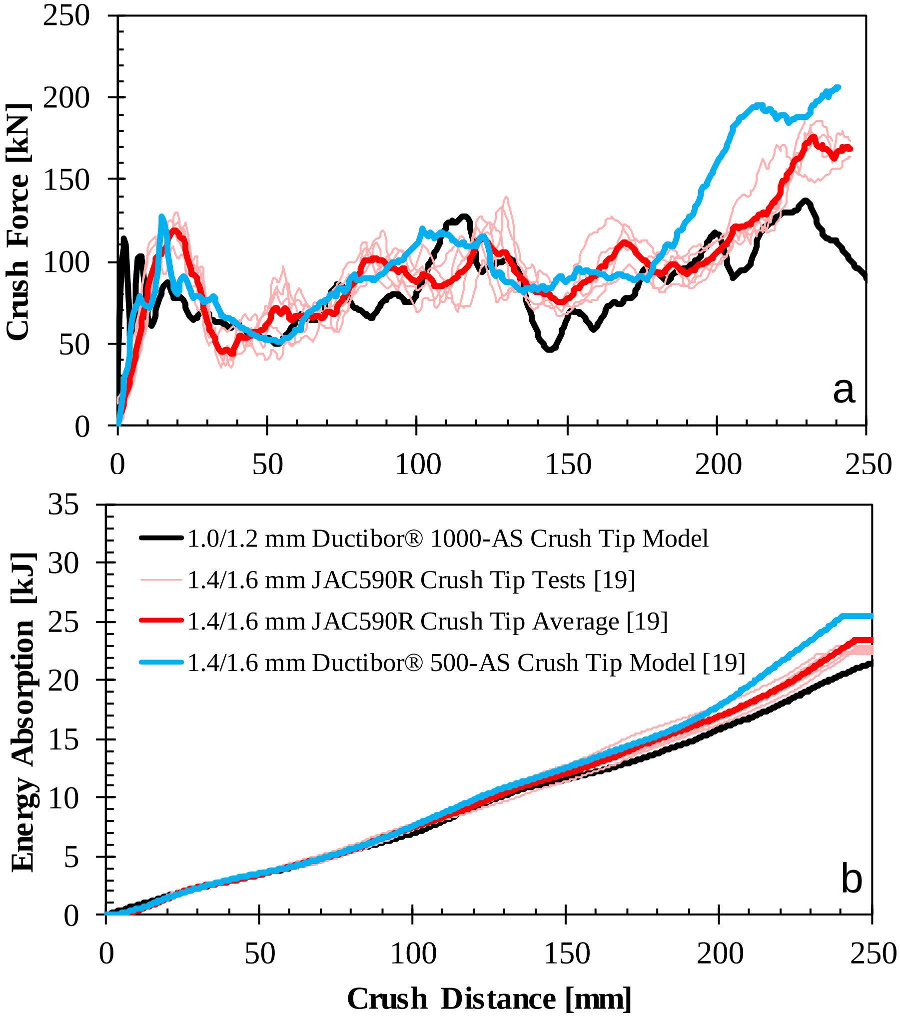

Figure 235. Comparison of the **(a)** crush force and **(b)** energy absorption for the Ductibor® 1000-AS crush tip model, JAC590R crush tips tests and their average due to Peister [19] and the Ductibor® 500-AS crush tip model due to Peister [19].

7.2 Conclusions

The work presented in this thesis aimed to demonstrate the suitability of hot stamped materials in frontal crash applications, as well as the weight savings that can be achieved through sheet material thickness down-gauging by using hot stamped materials. The following conclusions have been drawn from this research:

1. Baseline front end module tests Bd-2 and Bd-6 match the crash performance of the side frame member within the SUV model, as per the design specifications developed in this thesis (Table 3). In comparison

to the side frame member in the SUV model both of these tests (Bd-2 and Bd-6) exhibited a similar crush response (crush tip consolidation and plastic hinges forming in the right locations), velocity history, crush forces, resistance to passenger compartment intrusion and extent of spot weld failure. Baseline front end module specimen Bd-6 was selected as the "accepted baseline front end module" due to crush mode variability observed between Bd-2 and its identically configured tests Bd-3 and Bd-10.

2. Testing of the nine baseline front end modules resulted in three distinct deformation modes to be observed. In the first deformation mode consolidation of the crush tip section was quickly followed by the formation of a plastic hinge in front of the shock tower support, but the middle section of the side frame member remained composed. The second mode comprised of consolidation of the crush tip section followed by a plastic hinge forming behind the shock tower support, causing a global buckle dominant mode to follow. In the third deformation mode consolidation of the crush tip was followed by the formation of a plastic hinge in front and behind the shock tower support. It was concluded that the third deformation mode, demonstrated by Bd-2 and Bd-6, had the highest energy absorption potential and correlated well with the crush response and crash performance of the side frame member in the SUV model.
3. Simply substituting the thinner gauge and higher strength hot stamped materials (Ductibor® 1000-AS and Usibor® 1500-AS) into the production geometry side frame member, resulted in severe spot weld failures and spot weld flange unzipping in the side frame member crush tip, as well as an undesirable global crush response. The inclusion of enhanced, additional fold initiators into the tailor-welded hot stamped side frame member design greatly improved the crush response of the side frame member, making its response more similar to that of the accepted baseline front end module (Bd-6). Adding fold initiators to the production side frame did not however remedy the severe spot weld failures and flange unzipping that occurred.

4. Significant reduction in the extent and severity of spot weld failure in the tailor-welded hot stamped side frame member was only possible by changing the geometry of the crush tip section flanges from horizontally oriented to vertically oriented, in addition to removing an extra radius on the enclosure panel. This modification had the primary effect of changing the cross-section from a "double hat section" to a "single hat section". Spot weld unzipping long the upper and lower flanges was suppressed once the vertical flanges were implemented in the crush tip section, in combination with new, strategically located fold initiators.

5. The tailor-welded hot stamped side frame member was evaluated against the accepted baseline front end module (Bd-6). The evaluation showed that the tailor-welded hot stamped side frame member displayed a similar crush response, similar crush force, good passenger compartment intrusion

resistance. The hot stamped design also exhibited good resistance to parent metal fracture and a low spot weld failure severity. Ultimately, the proposed tailor-welded hot stamped side frame member was concluded to be a suitable replacement for the production JAC590R side frame member for the current load case. A further verification study was conducted, in which the tailor-welded hot stamped side frame member was inserted into the SUV model to replace the production driver's side frame member. The predictions from the SUV model further supported the use of hot stamped UHSS, such as Ductibor® 1000-A and Usibor® 1500-AS, in frontal crash energy management structures.

6. The proposed driver's side tailor-welded hot stamped side frame member is 27.6% (2.1 kg) lighter than the production JAC590R driver's side frame member. The thicknesses and materials used in the tailor-welded hot stamped side frame member by section are: 1.0 mm Ductibor® 1000-AS in the crush tip (was 1.4 mm JAC590R), 1.2 mm Ductibor® 1000-AS in the middle section (was 1.6 mm JAC590R) and 1.4 mm Usibor® 1500-AS in the S-rail section (was 1.8 mm JAC590R). In addition to weight savings, the proposed tailor-welded hot stamped side frame member consolidates the 3 component production side frame member into 2 components.

7. The complexities associated with forming the full-length tailor-welded hot stamped side frame member are greatly reduced by focusing on a smaller section of the side frame member instead. The section of interest is the 491 mm long tailor-welded hot stamped crush tip section. The tailor-welded hot stamped crush tip crash model predictions demonstrated a close match of the crush forces to the baseline front end module and full-length tailor-welded hot stamped side frame member. In addition it exhibited excellent resistance to parent metal fracture and a low severity of spot weld failures. The tailor-welded hot stamped crush tip is concluded to be a suitable simplification to the tailor-welded hot stamped side frame member, if it is being used to evaluate the resistance to spot weld failure and parent metal fracture, as well as crush forces and crush response within the crush tip section.

8. Forming the main rail and enclosure panel sections of the tailor-welded hot stamped crush tip was conducted using two separate crash form tools, with chilled water cooling channels. In the main rail part an average hardness of 368.5 HV and 401.2 HV was achieved in the 1.0 mm and 1.2 mm Ductibor® 1000-AS sections, respectively. In the enclosure panel part an average hardness of 412.8 HV and 392.8 HV was achieved in the 1.0 mm and 1.2 mm Ductibor® 1000-AS sections, respectively. Overall, good formability was observed in both of the parts, even in the locations identified from the hot stamping simulation to be at risk of splitting or material fold over.

9. Thinning predictions from the main rail and enclosure panel hot stamping models were mapped into the tailor-welded hot stamped crush tip crash model. The crush tip crash models with and without thinning predictions included were compared based on crush response and crush force. It was

concluded that the difference in response was observed to be insignificant due to the limited extent of thickness change during forming.

7.3 Recommendations

To build on the work that has been presented in this thesis the following recommendations should be considered:

1. Three different deformation modes were observed throughout testing of the baseline front end modules. The third deformation mode (full consolidation of the crush tip, followed by a buckle in front and behind the shock tower support) was determined to be the closest deformation mode to what is observed in the side frame member from the commercial SUV model. Only two of the nine baseline front end modules displayed the third crush mode and of those two tests the conditions were different. It is therefore recommended that more baseline front end modules be tested using the test configuration from Bd-6, so that the numbers of repeat samples displaying the third deformation mode can be increased.

2. Prior to testing, the crash sled was touched to the impacted end of each baseline front end module to ensure parallelism between the front bumper beam extension plate and the crash sled. Slight geometric differences were observed in each of the baseline front end modules, which could be attributed to part tolerances, fabrication tolerances and/or test setup. In the interest of making the numerical model best represent each test, a way of quantifying the geometric differences of each baseline front end module should be incorporated prior to testing each part.

3. The materials considered in the tailor-welded hot stamped side frame member are Ductibor® 1000-AS in the crush sections and Usibor® 1500-AS in anti-intrusion sections, which demonstrated a 27.6% weight reduction. To achieve further weight savings through material down-gauging, newer and higher strength materials, such as Usibor® 2000-AS, should be considered in anti-intrusion sections of the side frame member.

4. During the hot stamping process, austenitized blanks were removed from the furnace and placed onto the die set manually, using tongs. Though the manual process was conducted as consistently as possible, part-by-part variation still exists due to the additional human error associated with the manual process. An automated transfer system should be incorporated into the hot stamping process to eliminate this source of variability.

5. The hot stamping model uses an AutoForm default 22MnB5 material model to represent Ductibor® 1000-AS. The major problem with this assumption is that the final hardness levels

predicted by the model are much higher than hardness levels measured in the hot stamped main rail and enclosure panel parts. It is strongly recommended that the hot stamping simulations be re-run using an appropriate Ductibor® 1000-AS material model.

6. A study was conducted into the effect that forming history predictions had on the crash performance of the tailor-welded hot stamped crush tips. This study however only considered thinning predictions. In order to better represent the hot stamping – crash performance relationship, elemental hardness should also be considered. The local hardness achieved through hot stamping can be correlated to the local strength of the part, which can significantly impact crash performance.

7. Numerical simulation of the tailor-welded hot stamped crush tip has shown that Ductibor® 1000-AS is a suitable material in frontal crash energy management structures. It is strongly recommended that testing of the tailor-welded hot stamped crush tip assemblies be conducted to verify the modelling predictions.

8. It is acknowledged that there are drawbacks to evaluating the hot stamped side frame member with only the crush tip section. In the production JAC590R side frame member, thicker material is assigned to the S-rail section to prevent its collapse, which prevents components from the frontal crash structure intruding on the occupant compartment. In the tailor-welded hot stamped side frame member design, the S-rail section is intended to be comprised of Usibor® 1500-AS. By only evaluating the hot stamped crush tips, the suitability of Usibor® 1500-AS as a replacement for relatively thick JAC590R in the S-rail section cannot be validated. One of the crush modes highlighted in section 2.3 is the global buckling that occurs between the front and rear shock tower supports that serves to protect the S-rail section from being overloaded during the crash event. The crush tip section does not include this middle portion of the side frame member where this global buckling mode occurs and therefore it cannot be validated through the hot stamped crush tip.

9. The failure loads used in the spot weld model for Ductibor® 1000-AS is proprietary data that cannot be published in this thesis. Recent Ductibor® 1000-AS spot weld failure data, available from Tolton [100], should be considered in future modelling efforts to best represent the spot weld failures in the tailor-welded hot stamped crush tip. In addition, it is recommended that newer spot weld models and modelling techniques such as *MAT100_DA and the use of cohesive zone elements to represent spot welds, be considered in the tailor-welded hot stamped crush tip model.

10. In the tailor-welded hot stamped side frame member and crush tip, the average crush force was slightly lower (19%) than the production side frame member in the baseline front end module. Thickness selection for the Ductibor® 1000-AS and Usibor® 1500-AS sections was based on sheet

thicknesses available at the time; however, the sheet thickness can be fine tuned to better match the crush forces from the production side frame member. It is therefore recommended that the thicknesses of the Ductibor® 1000-AS and Usibor® 1500-AS sections be optimized to increase the crush force and energy absorption.

11. Through observing the predicted tailor-welded hot stamped crush tip deformation shown in Figure 226 it can be seen that the battery base has a high probability of becoming wedged between the crash sled and steel mounting plate. To mitigate this problem, it is recommended that a wedge profile be installed onto the mounting plate behind the battery base, so that the battery base is directed upwards and does not get stuck.
12. Only the US-NCAP Full Width Rigid Barrier SUV frontal crash test was considered in this thesis; however, many crash tests exist from crash safety regulatory bodies (IIHS, NCAP and FMVSS). It is strongly recommended that the tailor-welded hot stamped side frame member proposed in this thesis be evaluated in different crash configurations to further assess the suitability of hot stamped UHSS in frontal crash energy management structures.
13. The introduction of hot stamped UHSS into the commercial SUV side frame member design required topological changes, such as the addition of fold initiators and changes to the flange geometry, to capture the crush response and reduce spot weld failures. It is suggested that alternative ways of reducing spot weld failures in the side frame member be investigated including: using adhesive along the flanges in addition to spot welded joints, thermal softening of the spot weld flanges and multiple pulse tempering of spot welds to improve toughness.
14. Throughout this thesis no comment has been provided as to the corrosion resistance potential of Al-Si coated boron steel. Corrosion resistance is especially important for vehicle underbody applications (such as a side frame member) in which there exists potential for stone chipping and subsequent corrosion attack. It is suggested that the corrosion resistance potential of Al-Si coated boron steels be assessed further prior to the implementation of these materials in vehicle underbodies.

References

[1] National Highway Traffic Safety Administration, "NHTSA and EPA Set Standards to Improve Fuel Economy and Reduce Greenhouse Gases for Passenger Cars and Light Trucks for Model Years 2017 and Beyond," NHTSA, 2011.

[2] A. Bandivadekar, K. Bodek, L. Cheah, C. Evans, T. Groode, J. Heywood, E. Kasseris, M. Kromer and M. Weiss, "On the road in 2035 Reducing Transportation's Petroleum Consumption and GHG Emissions," MIT Laboratory for Energy and the Environment, Massachusetts, 2008.

[3] T. P. Hovorun, K. V. Berladir, V. I. Pervera, S. G. Rudenko and A. I. Martynov, "Modern Materials for Automotive Industry," *Journal of Engineering Sciences,* vol. 4, no. 2, pp. F8-F18, 2017.

[4] K. Mori, P. F. Bariani, B. A. Behrens, A. Brosius, S. Bruschi, T. Maeno, M. Merklein and J. Yanagimoto, "Hot Stamping of Ultra-High Strength Steel Parts," *CIRP Annuals - Manufacturing Technology,* vol. 66, pp. 755-777, 2017.

[5] M. Tisza and I. Czinege, "Comparative Study of the Application of Steels and Aluminum in Lightweight Production of Automotive Parts," *International Journal of Lightweight Materials and Manufacture,* vol. 1, no. 1, pp. 229-238, 2018.

[6] H. Karbasian and A. E. Tekkaya, "A review of hot stamping," *Journal of Materials Processing Technology,* vol. 210, pp. 2103-2118, 2010.

[7] American Honda Motor Co., "2016 Pilot: New Model Body Repair Information," June 2015. [Online]. Available: https://techinfo.honda.com/rjanisis/pubs/web/ABN01970.PDF. [Accessed 4 February 2019].

[8] S. Mackenzie, "History of Quenching," *Advanced Materials and Processing,* vol. 164, pp. 1-9, 2007.

[9] P. Hu, L. Ying and B. He, "Chapter 2 Hot Stamping Technology and the Main Equipment," in *Hot Stamping Advanced Manufacturing Technology of Lightweight Car Body*, Springer, 2017, pp. 19-44.

[10] American Honda Motor Co., "2016 Civic: New Model Body Repair Information," November 2015. [Online]. Available: https://www.civicx.com/threads/2016-civic-body-technology-construction-and-repair-bulletin.721/. [Accessed 1 February 2019].

[11] M. Merklein, M. Wieland, M. Lechner, S. Bruschi and A. Ghiotti, "Hot stamping of boron steel sheets with tailored properties: A review," *Journal of Materials Processing Technology,* vol. 228, pp. 11-24, 2016.

[12] J. Zhou, B.-y. Wang, M.-d. Huang and D. Cui, "Effect of Hot Stamping Parameters on the Mechanical Properties and Microstructure of Cold-Rolled 22MnB5 Steel Strips," *International Journal of Minerals, Metallurgy and Materials,* vol. 21, no. 6, pp. 544-555, 2014.

[13] L. ten Kortenaar, "Failure Characterization of Hot Formed Boron Steels with Tailored Mechanical Properties," Univeristy of Waterloo, Waterloo, 2016.

[14] A. Bardelcik, C. P. Salisbury, S. Winkler, M. A. Wells and M. J. Worswick, "Effect of Cooling Rate on High Strain Rate Properties of Boron Steel," *International Journal of Impact Engineering,* vol. 37, no. 6, pp. 694-702, 2010.

[15] A. Bardelcik, M. J. Worswick and M. A. Wells, "The Influence of Martensite, Bainite and Ferrite on the As-Quenched Constitutive Response of Simultaneously Quenched and Deformed Boron Steel - Experiments and Model," *Materials and Design,* vol. 55, pp. 509-525, 2014.

[16] K. Omer, R. George, A. Bardelcik, M. Worswick, S. Malcolm and D. Detwiler, "Development of a Hot Stamped Channel Section with Axially Tailored Properties - Experiments and Models," *International Journal of Material Forming,* vol. 11, no. 1, pp. 149-164, 2018.

[17] M. Merklein and T. Svec, "Transformation Kinetics of the Hot Stamping Steel 22MnB5 in Dependency of the Applied Deformation on the Austenitic Microstructure," in *International Deep Draw Research Group*, Graz, Austria, 2010.

[18] D. D. Munera, A. Pic, A. Khalil, F. Shmit and F. Pinard, "Innovative Press Hardened Steel Based Laser Welded Blanks Solutions for Weight Savings and Crash Safety Improvements," *SAE International,* vol. 1, no. 1, pp. 472-479, 2009.

[19] C. Peister, "Axial Crush Performance of Hot Stamped Tailor Welded Blanks," University of Waterloo, Waterloo, 2019.

[20] ArcelorMittal, "Laser Welded Blanks for Hot Stamping," ArcelorMittal, [Online]. Available: https://automotive.arcelormittal.com/tailored_blanks_home/LWB_home/LWB_types. [Accessed 21 05 2019].

[21] W. Ehling, L. Crettuer, A. Pic, R. Vierstraete and Q. Yin, "Development of a Laser Decoating Process for Fully Functional Al-Si Coated Press Hardened Steel Laser Welded Blank Solutions," in *Fifth International WLT-Conference on Lasers in Manufacturing*, Munich, 2009.

[22] M. Kang and C. Kim, "Laser Welding of Hot-Stamped Tailor-Welded Blanks with High-Strength Steel/High-Energy Absorption Steel," *Journal of Laser Applications,* vol. 26, no. 3, 2014.

[23] P. Samadian, M. A. Wells and M. J. Worswick, "Failure Characterization of Multi-Alloy and Multi-Gauge Hot-Stamped Tailor-Welded Blanks," in *37th International Deep-Drawing Research Group Conference*, Waterloo, Canada, 2018.

[24] T. L. Bergman, A. S. Lavine, F. P. Incropera and D. P. Dewitt, Fundementals of Heat and Mass Transfer, Hoboken, NJ: John Wiley & Sons, Inc., 2011.

[25] R. George, A. Bardelcik and M. J. Worswick, "Hot Forming of Boron Steels Using Heated and Cooled Tooling for Tailored Properties," *Journal of Materials Processing Technology,* vol. 212, no. 11, pp. 2386-2399, 2012.

[26] A. Barcellona and D. Palmeri, "Effect of plastic deformation on the hardness and continuous cooling transformations of 22MnB5 microalloyed boron steel," *Metallurgical and Material Transactions A,* vol. 40, no. 5, pp. 1160-1174, 2009.

[27] D. W. Fan and B. C. De Cooman, "Formation of an Aluminide Coating on Hot Stamped Steel," *The Iron and Steel Institute of Japan (ISIJ) International,* vol. 50, no. 11, pp. 1713-1718, 2010.

[28] I. Yakubtsov and R. Sohmshetty, "Evolution of Al-Si Coating Microstructure during Heat-Treatment of Usibor 1500," in *International Deep Drawing Research Group 37th Annual Conference*, Waterloo, Canada, 2018.

[29] S. Golling, R. Ostlund and M. Oldenburg, "Characterization of Ductile Fracture Properties of Quench-Hardenable Boron Steel: Influence of Microsturcture and Processing Conditions," *Materials Science and Engineering A,* vol. 658, pp. 472-483, 2016.

[30] R. Ostlund, S. Golling and M. Oldenburg, "Microstructure Based Modeling of Ductile Fracture Initiation in Press-Hardened Sheet Metal Structures," *Computer Methods in Applied Mechanics and Engineering,* vol. 302, pp. 90-108, 2016.

[31] S.-H. Lee, "Dynamic Axial Crush Response of Ductibor 1000-AS - Effect of Fold Initiator Pattern on Performance," in *7th International Conference Proceedings Hot Sheet Metal Forming of High Performance Steel*, Lulea, 2019.

[32] P. Samadian, C. Butcher and M. J. Worswick, "The Determination of the Fracture Behaviour of the Different Microstructures of Ductibor 500-AS Steel," in *7th International Conference Proceedings Hot Sheet Metal Forming of High Performance Steel*, Lulea, 2019.

[33] ArcelorMittal, "Steels for Hot Stamping - Usibor and Ductibor," [Online]. Available: https://automotive.arcelormittal.com/usibor_ductibor. [Accessed 24 05 2019].

[34] ArcelorMittal, "Stress-Strain Curves Hot Forming Steels - Usibor 1500 Treated," 2016. [Online]. Available: https://automotive.arcelormittal.com/files/Usibor1500--3a82a9aa69487763bbbba1a960151cc0.pdf. [Accessed 24 05 2019].

[35] ArcelorMittal, "Stress-Strain Curves Hot Forming Steels - Dutibor 1000 Treated," 2016. [Online]. Available: https://automotive.arcelormittal.com/files/Ductibor1000--42232ac6bc73f560a5c18a99582d6c56.pdf. [Accessed 24 05 2019].

[36] ArcelorMittal, "Stress-Strain Curves Hot Forming Steels - Ductibor 500 Treated," 2016. [Online]. Available: https://automotive.arcelormittal.com/files/Ductibor500--bac52373b9ba5e7cb8e80922dba4a6a4.pdf. [Accessed 24 05 2019].

[37] H. Kohei, K. Shinjiro and S. Kazuhiro, "Cold-Rolled and Galvannealed (GA) High Strength Steel Sheets for Automotive Cabin Structure," JFE Technical Report, 2013.

[38] P. Du Bois, C. C. Clifford, B. B. Fileta, T. B. Khalil, A. I. King, H. F. Mahmood, H. J. Mertz and J. Wilsmans, Vehicle Crashworthiness and Occupant Protection, Southfield, MI: American Iron and Steel Institute, 2004.

[39] H. K. Ibrahim, "Design Optimization of Vehicle Structures for Crashworthiness Improvement," Thesis: Concordia University, Montreal, 2009.

[40] D. A. Oliveira, "Interaction Between Forming and the Crash Response of Aluminum Alloy S-Rails," University of Waterloo, Waterloo, ON, 2007.

[41] J. M. Alexander, "An Approximate Analysis of the Collapse of Thin Cylindrical Shells Under Axial Load," *The Quarterly Journal of Mechanics and Applied Mathematics,* pp. 10-15, 1960.

[42] T. Wierzbicki and W. Abramowicz, "On the Crushing Mechanics of Thin-Walled Structures," *Journal of Applied Science,* vol. 50, pp. 727-734, 1983.

[43] M. D. White, N. Jones and W. Abramowicz, "A Theoretical Analysis for the Quasi-Static Axial Crushing of Top-Hat Thin-Walled Sections," *International Journal of Mechanical Sciences,* vol. 41, pp. 209-233, 1999.

[44] Y. Ohokubu, T. Akamatsu and K. Shirasawa, "Mean Crushing Strength of Closed-Hat Section Members," in *SAE Paper No. 740040*, 1974.

[45] W. Johnson, P. D. Soden and S. T. Al-Hassani, "Inextensional Collapse of Thin-Walled Tubes Under Axial Compression," *Journal of Strain Anlayis,* vol. 12, pp. 317-330, 1977.

[46] T. Wierzbicki and T. Akerstrom, "Dynamic Crushing of Strain Rate Sensitive Box Columns," in *Proceedings of the 2nd International Conference on Vehicle Structural Mechanics*, 1977.

[47] D. Kecman, "Bending Collpase of Rectangular and Square Section Tubes," *International Journal of Mechanical Science,* vol. 25, no. 9-10, pp. 623-636, 1983.

[48] T. H. Kim and S. R. Reid, "Bending Collapse of Thin-Walled Rectangular Section Columns," *Computers and Structures,* vol. 79, pp. 1897-1911, 2001.

[49] W. Abramowicz and N. Jones, "Transition from Initial Global Bending to Progressive Buckling of Tubes Loaded Statically and Dynamically," *International Journal of Impact Engineering,* vol. 19, no. 5-6, pp. 415-437, 1997.

[50] I. Eren, Y. Gur and Z. Aksoy, "Finite Element Analysis of Collapse of Front Side Rails with New Types of Crush Initiators," *International Journal of Automotive Technology,* vol. 10, no. 4, pp. 451-457, 2009.

[51] W. J. Witteman, "Improved Vehicle Crashworthiness Design by Control of the Energy Absorption," Thesis: Technische Universiteit Eindhoven, Eindhoven, 1999.

[52] S. Lee, C. Hahn, M. Rhee and J.-E. Oh, "Effect of Triggering on the Energy Absorption Capacity of Axially Compressed Aluminum Tubes," *Mechanical and Design,* vol. 20, pp. 31-40, 1999.

[53] S. J. Hosseinipour and G. H. Daneshi, "Energy Absorption and Mean Crushing Load of Thin-Walled Grooved Tubes Under Axial Compression," *Thin-Walled Structures,* vol. 41, pp. 31-46, 2003.

[54] H. Huh, K. P. Kim, S. H. Kim, J. H. Song, H. S. Kim and S. K. Hong, "Crashworthiness Assesment of Front Side Members in an Auto-Body Considering the Fabrication Histories," *International Journal of Mechanical Sciences,* vol. 45, pp. 1645-1660, 2003.

[55] D. A. Oliveira, M. J. Worswick, R. Grantab, B. W. Williams and R. Mayer, "Effect of Forming Process Variables on the Crashworthiness of Aluminum Alloy Tubes," *International Journal of Impact Engineering,* vol. 32, pp. 826-846, 2006.

[56] K. Omer, L. ten Kortenaar, C. Butcher, M. Worswick, S. Malcolm and D. Detwiler, "Testing of a Hot Stamped Axial Crush Member with Tailored Properties - Experiments and Models," *International Journal of Impact Engineering,* vol. 103, pp. 12-28, 2017.

[57] P. Akerstrom, "Modelling and Simulation of Hot Stamping," Thesis: Lulea University of Technology, Lulea, 2006.

[58] K. Sato, T. Inazumi, A. Yoshitake and S.-D. Liu, "Effect of Material Properties of Advanced High Strength Steels on Bending Crash Performance of Hat-Shaped Structure," *International Journal of Impact Engineering,* vol. 54, pp. 1-10, 2013.

[59] T. K. Eller, L. Greve, M. T. Andres, M. Medricky, A. Hatscher, V. T. Meinders and A. H. van der Boogaard, "Plasticity and Fracture Modelling of Quench-Hardenable Boron Steel with Tailored Properties," *Journal of Materials Processing Technology,* vol. 214, pp. 1211-1227, 2014.

[60] Y. Prajogo, "Hot Stamping of a Boron Steel Side Impact Beam with Tailored Flange Properties - Experiments and Numerical Simulations," Thesis, University of Waterloo, Waterloo, 2015.

[61] C. Peister, C. O'Keefe, J. Imbert, C. Butcher, M. J. Worswick, S. Malcolm, J. Dykeman, C. Yau, R. Soldaat and W. Bernert, "Dynamic and Quasi-Static Testing and Modelling of Hot Stamped Tailor-Welded Axial Crush Rails," in *18th International Conference on Experimental Mechanics*, Brussels, 2018.

[62] C. Peister, C. O'Keeffe, J. Imbert, C. Butcher, M. J. Worswick, S. Malcolm, J. Dykeman, C. Yau, E. deNijs, R. Soldaat and W. Bernert, "Crash Testing and Modelling of Hot Stamped Multi-Gauge Tailor-

Welded Automotive Axial Crush Structures," in *International Conference on Impact Loading of Structures and Materials*, Xi'an, China, 2018.

[63] N. Aknas, E. Ilhan, F. Varhol and S. Aslanlar, "Welding Time Effect on Mechanical Properties in Resistance Spot Welding of S235JR(Cu) Steel Sheets Used in Railway Vehicles," in *5th International Science Congress & Exhibition*, Lykia, 2015.

[64] V. H. Baltazar Hernandez, S. K. Panda, M. L. Kuntz and Y. Zhou, "Nanoindentation and microstructure analysis of resistance spot welded dual phase steel," *Materials Letters,* vol. 64, pp. 207-210, 2010.

[65] C. O'Keeffe, "Investigation of resistance spot weld failure in tailored hot stamped assemblies," Waterloo, Canada, 2018.

[66] C. O'Keeffe, J. Imbert-Boyd, M. J. Worswick, C. Butcher, S. Malcolm, J. Dykeman, P. Penner, C. Yau, R. Soldaat and W. Bernert, "Examination of Mode I Loading on Resistance Spot Weld Groups in Tailored Hot Stampings," in *DYMAT 23rd Technical Meeting Dynamic Fracture of Ductile Materials*, Trondheim, 2017.

[67] C. Tolton, C. O'Keeffe, M. J. Worswick, P. Penner, C. Yau, S. Malcolm, J. Dykeman, R. Soldaat and W. Bernert, "Investigation of Resistance Spot Weld Failure under Shear Loading in Die Quenched UHSS Assemblies," in *7th International Conference on Hot Sheet Metal Forming of High-Performance Steel*, Lulea, 2019.

[68] G. Bergman, "Modelling and Simulation of Simultaneous Forming and Quenching," Doctoral Thesis: Lulea University, Lulea, Sweden, 1999.

[69] Y. Chang, X. Tang, K. Zhao, P. Hu and Y. Wu, "Inverstigation of the Factors Influencing the Interfacial Heat Transfer Coefficient in Hot Stamping," *Journal of Materials Processing Technology,* vol. 228, pp. 25-33, 2016.

[70] P. Bosetti, S. Bruschi, T. Stoehr, J. Lechler and M. Merklein, "Interlaboratory Comparison for Heat Transfer Coefficient Identification in Hot Stamping of High Strength Steels," *International Journal of Material forming,* vol. 3, no. 1, pp. 817-820, 2010.

[71] A. Azushima, K. Uda and A. Yanagida, "Friction Behaviour of Aluminum-Coated 22MnB5 in Hot Stamping Under Dry and Lubricated Conditions," *Journal of Materials and Processing Technology,* vol. 212, no. 5, pp. 1014-1021, 2012.

[72] T. Olsson, "An LS-DYNA Material Model for Simulations of Hot Stamping Processes of Ultra High Strength Steels," in *7th European LS-DYNA Conference*, Salzburg, 2009.

[73] P. Akerstrom, G. Bergman and M. Oldenburg, "Numerical Implementation of a Constitutive Model for Simulation of Hot Stamping," *Modelling and Simulation in Materials Science and Engineering,* vol. 15, pp. 105-119, 2007.

[74] P. Maynier, J. Dollet and P. Bastien, "Hardenability Concepts with Applications to Steels," New York City, AIME, 1978, pp. 518-544.

[75] S. Graff, C. Pan, J. Lacues and F. Botz, "Process Monitoring of a Tailor Welded B-Pillar at Renault and Correlation between Forming Anlaysis and Simulation Results for Different Process Parameters," in *7th Internation Conference on Hot Sheet Metal Forming of High-Performance Steel*, Lulea, Sweden, 2019.

[76] J. Prajogo, K. Omer, A. Bardelcik, R. George, M. J. Worswick, N. Adam and D. Detwiler, "Development of a Hot Stamped Side Impact Beam and Axial Crush Member with Tailored Properties - Numerical Models," in *4th International Conference on Hot Sheet Metal Forming of High Performnce Steel*, Lulea, Sweden, 2013.

[77] M. Tummers, K. Omer, A. Abedini, C. Peister, C. Butcher, M. J. Worswick, S. Malcolm, C. Yau and R. Soldaat, "Introduction of a 1000 MPa Crush Tip within a Usibor 1500-AS Axial Crush Rail Using In-Die Heated Hot Stamping," in *37th International Deep-Drawing Research Group Conference*, Waterloo, Canada, 2018.

[78] C. Peister, M. J. Worswick, K. Omer, S. Malcolm, J. Dykeman, C. Yau, R. Soldaat and W. Bernert, "Numerical Modelling of the Crash Performance of Tailored Hot Stamped Crush Rails," in *6th International Conference on Hot Sheet Metal Forming of High Performance Steel*, Atlanta, Georgia, 2017.

[79] A. Bardelcik, M. J. Worswick, S. Winkler and M. A. Wells, "A Strain Rate Sensitive Constitutive Model for Quenched Boron Steel with Tailored Properties," *International Journal of Impact Engineering,* vol. 50, pp. 49-62, 2012.

[80] M. Basaran, S. D. Wolkerling, M. Feucht, F. Neukamm and D. Weichert, "An Extension of the GISSMO Damage Model Based on Lode Angle Dependence," in *LS-DYNA Awenderforum*, Bamberg, 2010.

[81] Y. Bai and T. Wierzbicki, "A New Model of Metal Plasticity and Fracture with Pressure and Lode Dependence," *International Journal of Plasticity,* vol. 24, pp. 1071-1096, 2008.

[82] H. Lee, P. Police, L. Koch, R. Komarivelli and B. Willis, "FEA Development of Spot Weld Modeling with Fracture Forming Limit Diagram (FFLD) Failure Criteria and Its Application to Vehicle Body Structure," *SAE International Journal of Passenger Cars - Mechanical Systems,* vol. 8, no. 1, pp. 59-64, 2015.

[83] S. Malcolm and E. Nutwell, "Spotweld Failure Prediction using Solid Element Assemblies," in *6th LS-DYNA Users Conference*, Gothenburg, Sweden, 2007.

[84] J. Saunders, M. J. Craig and J. Suway, "NHTSA's Test Procedure Evaluations for Small Overlap/Oblique Crashes," NHTSA.

[85] Seattle Safety, "Decelerator Sled Systems," [Online]. Available: http://www.seattlesafety.com/wp-content/uploads/2014/03/Decel_brochure_10.06.pdf. [Accessed 30 July 2019].

[86] Plascore, "Plascore CrushLite," [Online]. Available: https://www.plascore.com/download/datasheets/energy_absorption_documentation/PLA_AlumCrushLite_Sheet_7-8-2019.pdf. [Accessed 2 August 2019].

[87] A. M. Otkur, "Impact Modelling and Failure Modes of Composite Plywood," Texas Tech University, 2010.

[88] R. R. Ambriz and D. Jaramillo, "IntechOpen," 11 June 2014. [Online]. Available: https://www.intechopen.com/books/light-metal-alloys-applications/mechanical-behavior-of-precipitation-hardened-aluminum-alloys-welds. [Accessed 20 August 2091].

[89] R. Soldaat, *Private Correspondence: Available Hot Stamping Steel Sheet Thicknesses,* ArcelorMittal, 2019.

[90] A. Mohamadizadeh and P. Samadian, *Private Correspendance: Hardness of Ductibor 1000,* University of Waterloo, 2019.

[91] A. Abedini and P. Samadian, *Private Correspondance: Constitutive Behaviour of Ductibor 1000,* University of Waterloo, 2019.

[92] P. Samadian and S. Lee, *Private Correspondance: Ductibor 1000 Fracture Characterization,* University of Waterloo, 2019.

[93] P. Samadian, S. Lee, A. Abedini, C. Butcher and M. Tummers, *Private Correspondance: Ductibor 1000 Mesh Regularization,* University of Waterloo, 2019.

[94] C. Tolton, *Private Correspondance: Ductibor 1000-AS Spot Weld Failure Loads,* University of Waterloo, 2019.

[95] T. Belytschko and M. Tabbara, "H-Adaptive Finite Element Methods for Dynamic Problems, with Emphasis on Localization," *International Journal for Numerical Methods in Engineering,* vol. 36, pp. 4245-4265, 1993.

[96] A. Yanagida and A. Azushima, "Evaluation of Coefficients of Friction in Hot Stamping by Hot Flat Drawing Test," *CIRP Annuals - Manufacturing Technology,* vol. 58, pp. 247-250, 2009.

[97] J. Hansen and M. Hansen, *Private Correspondance: Splliting and Fold Over Criteria,* Cosma Die Technology, 2019.

[98] International Standard, *ISO 18265 Metallic Materials - Conversion of Hardness Values,* Switzerland: ISO, 2013.

[99] C. Yau, *Private Correspondance: Vickers Hardness Measurements,* Cosma International Promatek Research Centre, 2019.

[100] C. Tolton, *Private Correspondance: Failure Loads for Ductibor 1000-AS Spot Welds,* University of Waterloo, 2019.

Appendix A – Model Index

Table 17. Index of each numerical model used throughout this thesis.

Structure	Trial Number	Description
Baseline Front End Module	Trial 1101	Model representation of test Bd-1
	Trial 1202	Model representation of test Bd-5
	Trial 1301	Model representation of test Bd-4
	Trial 1402	Model representation of test Bd-7
	Trial 1501	Model representation of test Bd-2, Bd-3 and Bd-10
	Trial 1601	Model representation of test Bd-9
	Trial 1710	Model representation of test Bd-6
Tailor-Welded Hot Stamped Front End Module	Trial 3800	Base flange geometry, no initiators
	Trial 3809	Base flange geometry, initiators
	Trial 3900	Vertical flange geometry, no initiators
	Trial 3920	Vertical flange geometry, initiators
Tailor-Welded Hot Stamped Crush Tip	Trial 4019	Crush tip, no forming history
	Trial 4103	Crush tip, with forming history
SUV Model	Base NCAP	Baseline side frame member
	Trial 8000	Tailor-welded hot stamped side frame member